



**This electronic thesis or dissertation has been
downloaded from Explore Bristol Research,
<http://research-information.bristol.ac.uk>**

Author:

Kouzoumis, Konstantinos

Title:

Effect of biaxiality on engineering critical assessments

General rights

Access to the thesis is subject to the Creative Commons Attribution - NonCommercial-No Derivatives 4.0 International Public License. A copy of this may be found at <https://creativecommons.org/licenses/by-nc-nd/4.0/legalcode>. This license sets out your rights and the restrictions that apply to your access to the thesis so it is important you read this before proceeding.

Take down policy

Some pages of this thesis may have been removed for copyright restrictions prior to having it been deposited in Explore Bristol Research. However, if you have discovered material within the thesis that you consider to be unlawful e.g. breaches of copyright (either yours or that of a third party) or any other law, including but not limited to those relating to patent, trademark, confidentiality, data protection, obscenity, defamation, libel, then please contact collections-metadata@bristol.ac.uk and include the following information in your message:

- Your contact details
- Bibliographic details for the item, including a URL
- An outline nature of the complaint

Your claim will be investigated and, where appropriate, the item in question will be removed from public view as soon as possible.

Effect of biaxiality on engineering critical assessments

Konstantinos Kouzoumis



A dissertation submitted to the University of Bristol in accordance with the requirements for award of the degree of Doctor of Philosophy in the Faculty of Engineering, School of Civil, Aerospace and Mechanical Engineering.

November 2021

(47,000 words)

Abstract

Application of loads in two perpendicular directions, also known as biaxiality, has been recognized to have significant effects on the ability of a material to resist fracture, known as fracture toughness, normally defined for high-constraint conditions.

There are contradictory results in literature; most propose that biaxiality cannot drive fracture toughness below a minimum value found in specific geometries used for material characterization. This can allow for more lenient assessment of components and longer life expectancies. However, some research proposes that biaxiality could further decrease fracture toughness potentially leading to high financial costs and safety risks.

Initially historical data is used to investigate how biaxial loading could be analysed using standards that have been developed to assess the fitness for service of a component. These mostly use uniaxial fracture toughness data to assess the integrity of components, which is shown to be a safe and conservative practice for all biaxiality levels. Conservatism varies with flaw geometry and biaxiality, reaching zero for equibiaxially loaded through thickness cracks. Use of marginally higher fracture toughness values from different geometries or loading conditions result in potentially unsafe predictions and raise concern for this configuration.

Biaxiality in literature has mostly been studied experimentally in combination with surface flaws. To decouple the two effects an innovative experimental program is conducted here on through thickness flawed rectangular and cruciform specimens loaded in uniaxial and biaxial bending respectively. Crack propagation shows that biaxiality is captured, while specimens show varying plasticity levels with some including considerable ductile tearing.

Finite element analyses are conducted to analyse the tests. Biaxiality is shown to constrain the plastic flow and reduce fracture toughness in comparison to uniaxial loading. The fracture toughness values estimated with the application of experimental displacements to the models, for both geometries, are much higher than those for geometries used for material characterization denoting lower constraint levels than them.

Finally, it is concluded that the combination of thickness and crack geometry of the steel specimens tested here do not raise concern for the safety of a component in biaxial bending containing through thickness cracks. There is a potentially significant margin of

conservatism in assessing such a component with high constraint data and considerably higher fracture toughness values could be used instead.

Acknowledgements

This work could not have been possible without the guidance and expertise of both my industrial and academic supervisors, Isabel Hadley and Mahmoud Mostafavi. Isabel contributed towards not only shaping this work but also shaping my ideals by setting a great example of a role model and helping me adjust in a new life and a new country. Mahmoud helped me develop my capabilities, think outside the box and understand how to make my work appealing and marketable.

Additionally, I would like to thank all the academics, PhDs and postdocs of the Solid Mechanics Research Group (SMRG). Harry Coules, for being an excellent researcher, always giving me much needed feedback and being a wonderful person to affiliate with. My colleagues, Molly Probert, Megan Taylor, Unai de Francisco, Simon Tonge, Andy James, Nader Zentuti, Satyajit Dey, Andreas Andriotis and Derreck Van Gelderen for providing their valuable opinions on technical matters and for being there in difficult times of the PhD. The postdocs of the group, Haris Paraskeuoulakos, Martin McMillan, Dylan Agius and Abdullah Mamun for assisting me both in technical work and career progression. Lastly, our group's experimentalist Mehdi Mokhtarishirazabad who deserves a special thank you for his incredible talent in putting together novel experiments and his kindness and willingness to help even in times when he was overwhelmed with work. My sincere thanks is extended to Steve Harding and Peter Whereat, without who the cumbersome task of experiments would not have been possible.

An important part of this academic journey was completed within TWI and NSIRC where I was lucky enough to collaborate with great people and make friends for life. I would like to thank Jessica Taylor and Adrian Waka for being true to their character and for investing in our friendship, which I value greatly. Also want to thank the AFM group, Yin Jin Janin, Alex Pargeter, Matthew Haslett and Philippa Moore for making me feel welcome from the first moment in TWI and Cambridge.

I would also like to thank all the people in Bristol; Mitch Boulton, Evangelia Nikolaidou, Aggelos Stauroopoulos and Oona Oksanen for supporting me in the stressful times and giving me wonderful memories of a city that I will forever remember.

Also want to express my gratitude towards my friends that I left back in Greece but have not at all forgotten, Dimitris Roubos, Konstantinos Prountzopoulos, Manos Perisinakis, Nikolas Retoulas and Katianna Roubou who showed understanding throughout all my ups and downs, pride in my achievements and who made my time back home enjoyable beyond what I ever expected.

Additionally, want to thank my friend Maria Gkovedarou who supported me throughout our friendship, giving me wonderful memories and valuable insights on life, way of thinking and career progression.

A special thank you goes to my friend, alma-matter and collaborator Konstantina Traka who allowed our PhD journeys to intertwine and share the good and the bad experiences throughout.

Lastly, I would like to thank my family Matoula, Dimitris and Giorgos for their acceptance and understanding, even on the difficult days, as well as their unconditional love and support.

Authors declaration

I declare that the work in this dissertation was carried out in accordance with the requirements of the University's Regulations and Code of Practice for Research Degree Programmes and that it has not been submitted for any other academic award. Except where indicated by specific reference in the text, the work is the candidate's own work. Work done in collaboration with, or with the assistance of, others, is indicated as such. Any views expressed in the dissertation are those of the author.

SIGNED: DATE:.....

List of publications

1. K. Kouzoumis, I. Hadley, and M. Mostafavi, 'Effect of Biaxiality on Engineering Critical Assessments', *Procedia Structural Integrity*, vol. 17, pp. 347–354, Jan. 2019, doi: [10.1016/j.prostr.2019.08.046](https://doi.org/10.1016/j.prostr.2019.08.046).
2. K. Kouzoumis, I. Hadley, and M. Mostafavi, 'Validation of BS 7910; assessing the integrity of pipes containing axial flaws', *Procedia Structural Integrity*, vol. 13, pp. 868–876, Jan. 2018, doi: [10.1016/j.prostr.2018.12.165](https://doi.org/10.1016/j.prostr.2018.12.165).
3. K. Kouzoumis, I. Hadley, and M. Mostafavi, 'Validation of BS 7910 fracture assessment procedures; wide plates and cylinders', *International Journal of Pressure Vessels and Piping*, vol. 190, p. 104309, Apr. 2021, doi: [10.1016/j.ijpvp.2021.104309](https://doi.org/10.1016/j.ijpvp.2021.104309).

Table of contents

| | |
|--|----|
| Abstract | i |
| Acknowledgements | ii |
| Authors declaration | iv |
| List of publications | v |
| Table of contents | vi |
| List of Tables | ix |
| List of Figures..... | x |
| Chapter 1 Introduction | 13 |
| Chapter 2 Literature review | 19 |
| 2.1 Initial studies on biaxiality | 19 |
| 2.2 Biaxiality in elastic – plastic fracture mechanics | 26 |
| 2.3 Failure prediction models | 35 |
| 2.3.1 Dodds-Anderson toughness scaling model..... | 37 |
| 2.3.2 Weibull cleavage model..... | 39 |
| 2.3.3 Microstructure informed brittle fracture (MIBF) model | 41 |
| 2.3.4 Wallin, Saario, Törrönen (WST) model | 43 |
| 2.3.5 James Ford Jivkov (JFJ) model | 45 |
| 2.3.6 Seal and Sherry model | 47 |
| 2.4 Background to ECAs | 49 |
| 2.5 Biaxiality in ECAs | 52 |
| 2.5.1 Biaxiality in BS7910 | 52 |
| 2.5.2 Biaxiality in R6..... | 54 |
| 2.5.3 Biaxiality and plastic collapse..... | 55 |
| 2.6 Summary..... | 57 |
| Chapter 3 Analysis of existing experiments..... | 59 |

| | | |
|-----------|---|-----|
| 3.1 | Introduction | 59 |
| 3.2 | Application of BS 7910 on historical data | 60 |
| 3.2.1 | Introduction..... | 60 |
| 3.2.2 | Background to analyses | 61 |
| 3.2.3 | Tests analysed..... | 64 |
| 3.2.4 | Results | 68 |
| 3.2.5 | Summary | 76 |
| 3.3 | TWI biaxial experiments | 78 |
| 3.3.1 | Introduction..... | 78 |
| 3.3.2 | Tests analysed..... | 78 |
| 3.3.3 | Material properties..... | 80 |
| 3.3.4 | Assessment of tests | 83 |
| 3.3.5 | Summary | 97 |
| 3.4 | Conclusions | 98 |
| Chapter 4 | Biaxial and uniaxial experiments | 100 |
| 4.1 | Introduction | 100 |
| 4.2 | Material properties | 101 |
| 4.2.1 | Tensile properties..... | 102 |
| 4.2.2 | Fracture toughness..... | 103 |
| 4.2.3 | Metallography of material | 105 |
| 4.2.4 | Transition Curve..... | 107 |
| 4.3 | Design of experiments | 108 |
| 4.3.1 | Test setup..... | 108 |
| 4.3.2 | Testing the setup | 112 |
| 4.4 | Steel specimens..... | 114 |
| 4.5 | Test temperature..... | 115 |
| 4.6 | Fatigue pre-cracking | 116 |

| | | |
|-----------|--|-----|
| 4.7 | Instrumentation | 121 |
| 4.8 | Testing procedure | 123 |
| 4.9 | Experimental results | 126 |
| 4.9.1 | Room temperature tests | 126 |
| 4.9.2 | Lower shelf tests -160°C | 128 |
| 4.10 | Conclusions | 138 |
| Chapter 5 | Finite element analyses | 140 |
| 5.1 | Introduction | 140 |
| 5.2 | Model methodology | 141 |
| 5.2.1 | PMMA models | 141 |
| 5.2.2 | Steel models | 148 |
| 5.3 | Modelling results | 155 |
| 5.3.1 | PMMA models | 155 |
| 5.3.2 | Steel models | 160 |
| 5.4 | Conclusions | 169 |
| Chapter 6 | Conclusions | 171 |
| 6.1 | Conclusions | 171 |
| 6.2 | Future work | 173 |
| | List of References | 176 |
| | Appendix – 1: Experimental results | 185 |
| | Appendix – 2: Steel parametric FEA | 218 |
| | Appendix – 3: Steel FEA results | 227 |

List of Tables

| | |
|---|-----|
| Table 2.1: Biaxiality ratios of specimens tested in [18]..... | 20 |
| Table 3.1: Reference stress and Stress intensity factor solutions used for the assessments. | 62 |
| Table 3.2: Tests analysed | 67 |
| Table 3.3: Validity limiting parameters of BS 7910 solutions for cylindrical geometries, specimens which exceed them and their parameter values | 68 |
| Table 3.4: Cylinders assessed as Curved Shells..... | 68 |
| Table 3.5: Biaxiality and modelling error dataset | 75 |
| Table 3.6: Geometric Properties, Test Temperatures, and failure loads of specimens assessed | 80 |
| Table 3.7: Calculated Yield and Ultimate Tensile stresses (MPa) | 81 |
| Table 3.8: Fracture toughness values, K_{mat} (MPa \sqrt{m})..... | 82 |
| Table 3.9: Extracted stresses at points A, C | 90 |
| Table 3.10: Global Collapse Limit loads from FEA..... | 93 |
| Table 3.11: Structural constraint parameter (β) of specimens | 95 |
| Table 4.1: Chemical Composition of C-Mn steel Plate BS1501-224 28B [126] | 101 |
| Table 4.2: Tensile properties of BS1501-224 28B from [126] | 102 |
| Table 4.3: BS1501-224 28 fracture toughness measurements for fatigue pre-cracked specimens | 104 |
| Table 4.4: Upper limit K values for fatigue pre-cracking..... | 118 |
| Table 4.5: Loads used for fatigue pre-cracking | 119 |
| Table 4.6: Experimental database..... | 128 |
| Table 4.7: Experimental matrix of Uniaxial specimens | 130 |
| Table 4.8: 5-point bend failure conditions..... | 134 |
| Table 4.9: Experimental matrix of Biaxial specimens..... | 135 |
| Table 5.1: J values (MPa mm) at each contour calculated at Z_{Max-J} depth | 154 |
| Table 5.2: PMMA elastic compliance in mm/kN..... | 156 |
| Table 5.3: Fracture toughness values for PMMA specimens in MPa \sqrt{m} | 159 |
| Table 5.4: Structural parameter β values calculated for PMMA specimens in MPa \sqrt{m} | 160 |
| Table 5.5 : Steel specimens simulated | 162 |
| Table 5.6: Steel tests elastic compliance in mm/kN | 163 |
| Table 5.7: Structural parameter β values calculated for steel specimens in MPa \sqrt{m} | 163 |
| Table 5.8: FEA parameters and results | 167 |

List of Figures

| | |
|--|-----|
| Figure 2.1: Fracture Trajectories of biaxially loaded 4 mm thick PMMA specimens [18]..... | 20 |
| Figure 2.2: Effect of plasticity on the crack-tip stress fields: (a) small-scale yielding, (b) elastic-plastic conditions, and (c) large-scale yielding.[27] | 29 |
| Figure 2.3: Cruciform specimen geometry, showing the in and out of plane components of stress during biaxial testing [33] | 30 |
| Figure 2.4: Modified boundary layer analysis, an area around the crack tip is studied remotely with the loading of Equation 2.15 applied at the boundary [27]..... | 33 |
| Figure 2.5: Sensitivity to biaxiality for Q-stress based on different stress criteria, [9] | 38 |
| Figure 2.6: Contours of stresses with increasing J-values, [9] | 39 |
| Figure 2.7: Graphical presentation of an ECA | 49 |
| Figure 2.8: Example of tearing resistance (R-curve) assessment..... | 51 |
| Figure 2.9: Modelling error in ECAs | 52 |
| Figure 3.1: Yield Stress De-rating for C-Mn Steels. Adapted from [1, Fig. 7.10] | 63 |
| Figure 3.2: Wide Plate Tests Geometry | 65 |
| Figure 3.3: Flaw geometries for cylindrical specimens | 67 |
| Figure 3.4: FAD of wide plate test data..... | 70 |
| Figure 3.5: FAD of specimen 2518 | 70 |
| Figure 3.6: Comparison between BS7910 2013 and BS7910 2019 in assessing axially flawed cylinders..... | 72 |
| Figure 3.7: FAD of axially flawed cylinders (assessed with BS 7910 2019 version)..... | 72 |
| Figure 3.8: FAD of specimen a)1602, b)2113 | 73 |
| Figure 3.9: FAD of circumferentially flawed cylinders | 73 |
| Figure 3.10: Modelling error at different levels of biaxiality for tests on a) 20MnMoNi55 b) NiMoCr - Melt and c) API 5L X56 steels | 76 |
| Figure 3.11: Geometry of of (a) biaxially loaded, (b) uniaxially loaded specimens..... | 79 |
| Figure 3.12: Tensile properties at various temperatures..... | 81 |
| Figure 3.13: Option 1 and Option 3 assessments of specimens #15 (k=0) and #16 (k=1) | 86 |
| Figure 3.14: FEA mesh of specimen #15 and #16 | 87 |
| Figure 3.15: Visual of stress extraction points | 89 |
| Figure 3.16: Option 1, A & B assessments | 91 |
| Figure 3.17: FE mesh of quarter of (a) biaxially, (b) uniaxially loaded specimens | 93 |
| Figure 3.18: Option 3 FAD – Through thickness TWI plates..... | 95 |
| Figure 3.19: Constraint modified Option 3 FALs – Through thickness TWI plates | 96 |
| Figure 4.1: BS1501-224 28B - Tensile properties at different temperatures..... | 103 |
| Figure 4.2: Microstructure of face A, Plate 2 | 106 |
| Figure 4.3: Microstructure of face B, Plate 2 at (a) the surface, (b) quarter thickness, (c) mid-thickness | 106 |
| Figure 4.4: Microstructure of face C, Plate 2 at (a) the surface, (b) quarter thickness, (c) mid-thickness | 107 |
| Figure 4.5: BS1501-224 28B Charpy test results & Transition Curve | 108 |
| Figure 4.6: Basic setup of 3 Point bend..... | 109 |
| Figure 4.7: Basic setup of 5 Point bend..... | 109 |
| Figure 4.8: Engineering drawing of a rectangular specimen..... | 110 |

| | |
|--|-----|
| Figure 4.9: Engineering drawing of a cruciform specimen..... | 110 |
| Figure 4.10: Hollow cylinder base of experimental rig | 111 |
| Figure 4.11: roller of rig | 111 |
| Figure 4.12: semi-spherical punch of rig | 111 |
| Figure 4.13: 3 Point Bend Specimen (dimensions in mm) | 112 |
| Figure 4.14: 5 Point Bend Specimen (dimensions in mm) | 112 |
| Figure 4.15: PMMA Uniaxial - 3PB specimen - Post fracture | 113 |
| Figure 4.16: PMMA Biaxial - 5PB specimen - Post fracture..... | 113 |
| Figure 4.17: Experimentally measured Load - CMOD for PMMA specimens..... | 114 |
| Figure 4.18: Setup of Fatigue pre-cracking a rectangular shaped specimen | 117 |
| Figure 4.19: Crack growth as observed from camera | 117 |
| Figure 4.20: Maximum stress intensity factor values during pre-cracking of rectangular specimens | 120 |
| Figure 4.21: Maximum stress intensity factor values during pre-cracking of cruciform specimens | 120 |
| Figure 4.22: Schematic showing the thermocouple positions on a 3PB specimen..... | 121 |
| Figure 4.23: Schematic showing the thermocouple positions on a 5PB specimen..... | 122 |
| Figure 4.24: Knife edges to attach COD gauge..... | 122 |
| Figure 4.25: 3PB specimen with holes for the knife edge attachment | 123 |
| Figure 4.26: Photographs of experimental setup (a) face view with open chamber (b) face view with closed chamber and (c) side view | 124 |
| Figure 4.27: Post fracture (a) image of the fracture surface (b) digitised fatigue pre-crack..... | 125 |
| Figure 4.28: Specimen 5PB 6B1 post testing (a) top view (b) bottom view | 126 |
| Figure 4.29: Load-CMOD of room temperature tests | 127 |
| Figure 4.30: Load - CMOD of 3PB 1_U_2 | 129 |
| Figure 4.31: Load-CMOD of 3PB tests | 130 |
| Figure 4.32: 3PB 1_U_2 post-fracture surface (a) as taken (b) with highlighted ductile tearing zones. | 131 |
| Figure 4.33: 3PB 1_U_2 post-fracture surface | 132 |
| Figure 4.34: Load-CMOD curve of elastic 3PB tests | 132 |
| Figure 4.35: Load-CMOD curve of plastic 3PB tests | 133 |
| Figure 4.36: Load-CMOD of 5PB 3_B_2 | 134 |
| Figure 4.37: Load-CMOD of 5PB tests | 135 |
| Figure 4.38: 5PB 3_B_2 post-fracture surface (a) as taken (b) with highlighted ductile tearing zones. | 136 |
| Figure 4.39: Load-CMOD curve of elastic 5PB tests | 137 |
| Figure 4.40: Load-CMOD curve of plastic 5PB tests | 137 |
| Figure 4.41: Post fracture pictures of (a) 5PB 1_B_1 and (b) 5PB 1_B_2..... | 138 |
| Figure 5.1: PMMA 3PB FEA Assembly | 141 |
| Figure 5.2: PMMA 5PB FEA Assembly | 142 |
| Figure 5.3: Displacement at centre of specimen vs # of elements | 142 |
| Figure 5.4: Meshed instances of PMMA models (a) 3PB specimen (b) 5PB specimen (c) boundary surface | 144 |
| Figure 5.5: Crack-tip mesh of PMMA specimens | 146 |
| Figure 5.6: Boundary conditions of 3PB PMMA specimen | 147 |
| Figure 5.7: Boundary conditions of 5PB PMMA specimen | 147 |

| | |
|--|-----|
| Figure 5.8: Meshed instances of steel models (a) 3PB specimen (b) 5PB specimen | 149 |
| Figure 5.9: Effects of element choice on (a) Load-CMOD (b) J-integral at failure calculation for specimen 3PB 5_U_2 | 150 |
| Figure 5.10: Effects of element choice on (a) Load-CMOD (b) J-integral at failure calculation for specimen 5PB 5_B_2..... | 151 |
| Figure 5.11: BS1501-224 28B Stress Strain Curve recreated from [126]..... | 152 |
| Figure 5.12: Crack-tip mesh of steel specimens..... | 153 |
| Figure 5.13: Uniaxial PMMA FEA and Experimental Load-CMOD..... | 156 |
| Figure 5.14: Biaxial PMMA FEA and Experimental Load-CMOD | 157 |
| Figure 5.15: Uniaxial PMMA FEA - J-integral along crack front..... | 157 |
| Figure 5.16: Biaxial PMMA FEA - J-integral along crack front | 158 |
| Figure 5.17: Uniaxial PMMA FEA - T-stress along crack front | 158 |
| Figure 5.18: Biaxial PMMA FEA - T-stress along crack front | 159 |
| Figure 5.19: Specimen 5PB 1_BB_2; Experimental and FEA Load-CMOD curve | 161 |
| Figure 5.20: Specimen 3PB 5_U_2 (a) FEA and Experimental Load-CMOD curve, (b) J-integral along the crack front, (c) T-stress from elastic analysis | 165 |
| Figure 5.21: Specimen 5PB_5_B_2 (a) FEA and Experimental Load-CMOD curve, (b) J-integral along the crack front, (c) T-stress from elastic analysis | 166 |
| Figure 5.22: FEA derived fracture toughness values of the specimens analysed | 168 |
| Figure 5.23: FEA derived fracture toughness values in J-Q space [135] | 169 |

Chapter 1 Introduction

During the manufacturing or operation of an engineering structure, crack-like flaws might be formed. The nature of the formation of such flaws is not of interest at this point, however their effect on the integrity of the structure, which has concerned the engineering community greatly, is focused on here. Cases of catastrophic failures under low loads and no warning, in terms of deformation, generated the motive for studying the effect of such crack-like flaws. In light of this, the fracture mechanics field was developed within solid mechanics and continues to constitute a major area of interest and research activity in recent years.

Fitness for service (FFS) procedures (e.g. BS7910, API 579/ASME FFS-1, R6) [1]–[3] are developed for the assessment of the integrity of an engineering component against different failure modes, namely:

1. fracture and plastic collapse
2. fatigue
3. creep and creep fatigue
4. leakage of containments
5. corrosion and/or erosion
6. environmentally assisted cracking

7. instability (buckling)

FFS procedures, based on continuum mechanics theory and literature, conduct engineering critical assessments (ECA), which result in a quantitative measure of the structural integrity of a component containing a flaw.

Better understanding of complex features which affect the structural integrity of a component (e.g. residual stress distribution, strength mismatch), help advance FFS procedures. It is important to note that such advancements can be both in terms of exploring new features and variables that affect the structural integrity and revisiting and enhancing existing methods for improvement of accuracy in the analyses. The combination of

- the initially high safety margins included in the procedures,
- the fact that FFS usage has over the years shifted from assessing existing flaws to designing flaw tolerant structures and thus the need for better estimation of the lifespan of structures [4], [5]
- the need for better repair guidance of ageing structures in service, whose number constantly increases, with more of them qualifying as fit for service beyond their initial design life
- the increase in computational abilities and understanding of the phenomena

generate motive for increased accuracy.

The precision of the procedures relies upon several variables included in an assessment. The number of variables, as well as their values, depend on the,

1. Geometry of component
2. Geometry of flaw
3. Material Properties
4. Loads imposed on the component
5. Loading history – residual stresses

The above parameters may be studied individually; however, they are connected. For instance, in a case of misalignment in the connection between two components (e.g. girth

weld in a pipe) the geometry of the component, incorporating the apparent misalignment, will influence the imposed load by an added bending stress.

From the large variety of phenomena that can affect the behaviour of a flawed component, this work focuses on the study of multiaxial loading and its effect, which has been recognized to be significant [6]–[9]. Multiaxial loads regard to the application of loads in different (perpendicular) directions and are an issue especially in structures like nuclear reactor pressure vessels, piping systems and storage tanks, where a biaxial state of loading is met. The effects of biaxiality, i.e. application of loads in two (perpendicular) directions, are imprinted on the stress field tensor in the vicinity of the crack tip, with biaxiality increasing the level of stress triaxiality also defined as crack tip constraint, and decreasing the plastic zone around the crack tip [10].

Here it should be explained that a metal's ability to resist fracture, i.e. fracture toughness, exhibits temperature and geometry/stress triaxiality dependence. Both temperature and constraint affect the plastic strain development and consequently the material's resistance to failure. Depending on the temperature at which a component or structure is functioning, the effect of constraint will be of different severity on the component's behaviour.

In the lower shelf-transition region, experimental work studying the behaviour of biaxially loaded components [6], [7], [9], [11], shows that the existence of an increase biaxiality decreases the critical values of the energy release rate - J with increasing constraint.

Here it is worth defining J as a way to calculate the strain energy release rate, per unit fracture surface area, in a material. For isotropic, perfectly brittle, linear elastic materials, the J -integral can be directly related to the fracture toughness if the crack extends straight ahead with respect to its original orientation, whilst J remains valid representation of fracture toughness in nonlinear (power law hardening) elastic-plastic materials where the size of the plastic zone is small compared with the crack length.

In other words an increase in biaxiality/triaxiality is translated as a decrease in fracture toughness values. J eventually reaches the values measured from testing high constraint specimens (e.g. Single Edge Notched Bending - SENB, Compact tension-CT) [9] or falling below them [11]. While the structure is loaded, plasticity starts flowing and the constraint/stress triaxiality level reduces, allowing for more elastic/plastic strain energy to be consumed by the specimen prior to fracture, leading to an increase in fracture

toughness. This could also be expressed as a drop in the stresses and strains over the fracture region resulting from plasticity elsewhere.

These observations prompted a surge of interest in analysing and predicting fracture resistance behaviour across different levels of constraint as well as unifying fracture toughness values with the use of micromechanics interpretations of the cleavage fracture process. In light of this, probabilistic models incorporating weakest link statistics [12], [13], which attempt to describe the coupling of the (local) fracture stress/behaviour with the remote loading, were employed. Such models allowed the comparison between components with different levels of constraint, thus unifying the cleavage fracture toughness values. Successful implementation of such methodologies ([14], [15]) led to their incorporation (indirectly) in the latest editions of FFS procedures (e.g. Annex N in BS7910:2013) allowing for constraint effects to be included in the assessment. Even though such methods can be used they require caution in how they are implemented.

Regarding a structure operating in the ductile-to-brittle transition (DBT) region, there is uncertainty concerning the type of failure that might occur, i.e. ductile failure or unstable fracture by transgranular cleavage are both potential scenarios. However, during ductile fracture there is a flow of plasticity which decreases crack tip triaxiality, while more energy is consumed by the material to have a larger area plastically deforming and higher values of fracture toughness are expected, compared to cleavage fracture of the same geometry/material/temperature. Hence, in the transition region, where there is uncertainty over the type of failure that might occur and constraint favours a less ductile behaviour, concern is focused on the avoidance of cleavage fracture.

As elaborated so far, biaxiality is an important factor in the lower shelf and transition region, however, many structures, such as offshore pipelines carrying hot fluid under a combination of high internal pressure and axial strain, experience biaxial loads whilst in the collapse dominated-upper shelf area. Experimental evidence focusing on biaxiality effects on plastic collapse [7], [8], [16] strongly suggest a connection between variation of limit load/strain capacity/plasticity flow and biaxiality. Considering this many researchers studied the load bearing capability of components under biaxial (or combinations of) loading.

This work focuses mostly on the exploration of the effect of biaxiality on the initiation fracture toughness, since components are mostly designed to avoid initiation rather than

facing crack propagation (e.g. crack arrest). In particular the decoupling of crack depth and biaxiality is attempted as described in later chapters.

Following the scope of the work described until now, Chapter 2 provides a detailed literature review on the studies of biaxiality and the approaches that have been developed to include constraint effects.

In pursuit of better understanding the current capabilities of the existing FFS procedures, Chapter 3 includes engineering critical assessments (ECAs) on experimental databases with a variety of biaxiality ratios. From the analysis of historical data that do not specifically target biaxiality it shows that basic ECAs can, safely and conservatively estimate the fitness for service of a component and prove the importance of a targeted experimental database. The analysis on biaxiality related oriented experiments show a trend between biaxiality and limit loads. Additionally, more advanced assessment procedures on biaxial tests raise concern on the conservatism in the fracture toughness values used especially on through thickness flawed components. Cases of components with such a flaw geometry appear to be incorrectly assessed when non-conservative fracture toughness values are used.

An innovative experimental program is explained in Chapter 4. In pursuit of decoupling biaxiality and flaw depth as well as by following the findings of its preceding chapter, the program in Chapter 4 focuses on uniaxially and equibiaxially loaded plate geometries with through thickness flaws. The loading applied is in uniaxial and biaxial bending, and the experimental layout is first validated with the use of a PMMA brittle thermoplastic material. Following, a C-Mn ferritic steel is tested at a single lower shelf temperature. The results show both geometries tested exhibit varying levels of plasticity with some tests exhibiting significant plasticity. Overall, biaxiality is captured by the setup however the combination of biaxiality and specimen thickness do not achieve high levels of constraint.

Subsequent to the experimental program, Chapter 5 includes finite element analyses (FEA) that of the specimens tested. For the linear elastic PMMA tests, structural constraint parameters calculated from the FEA, show the constraint increase in the case of the biaxially loaded specimens. The modelling of the steel specimens is conducted on the tests that exhibit cleavage fracture during failure and provide qualitative results, showing a trend of decreasing fracture toughness with biaxiality and further supporting that the experimental program of Chapter 4 does not achieve high levels of constraint.

Finally, Chapter 6 summarises the findings of this work and recommends further steps of action that can be taken.

Chapter 2 Literature review

2.1 Initial studies on biaxiality

Original research at the time of the 1970's focused on further understanding the physical quantities that had a non-negligible effect in the calculation of the stresses around the crack tip and predicting the stability, morphology and the trajectory of the crack.

Up to that point, common practice was to consider cases of uniaxial stress, in which the crack would propagate either by fatigue or quasi static loading in the direction normal to the load, following the path of the maximum tangential stress. According to Leever et al ([17], [18]), the assumption of the stresses parallel to the crack having a negligible effect on the crack opening/propagation was an oversimplification, since such stresses had been shown to affect the fracture toughness of the structure [19]. The deterrents for the hitherto analysis, were the lack of a theoretical framework and a biaxial testing machine/setup. In light of the latest, an experimental setup was proposed [17], capable of applying uniform normal boundary stresses on each side of a square plate specimen. With the use of this experimental setup on quasi-brittle polymer plates (PMMA - polymethyl methacrylate), Leever examined in the context of linear elastic fracture mechanics, the propagation of the crack and its trajectory in relation to the biaxiality ratio [18] defined in Equation 2.1.

$$k = \frac{P_2}{P_1} = \frac{\text{Load parallel to crack}}{\text{Load perpendicular to crack}} \quad \text{Equation 2.1}$$

From experimental results included in [18] it was demonstrated that the crack propagation trajectories were straight at low biaxiality ratios (k), while taking the form of an "S" shape at higher ones. In particular, for specimens loaded with the biaxiality ratios shown in Table 2.1, the crack path changed in accordance with biaxiality, reaching an angle of almost 90° at the highest k , as shown in Figure 2.1. These results provided further support to the notion that the crack changes its propagation path to perpendicularly align to the most intense stress.

Table 2.1: Biaxiality ratios of specimens tested in [18]

| Specimen No. | k | Specimen No. | k |
|--------------|------|--------------|------|
| 1 | 0 | 7 | 1.45 |
| 2 | 0 | 8 | 2.10 |
| 3 | 0 | 9 | 2.10 |
| 4 | 0.95 | 10 | 2.78 |
| 5 | 0.97 | 11 | 2.78 |
| 6 | 1.43 | 12 | 2.79 |

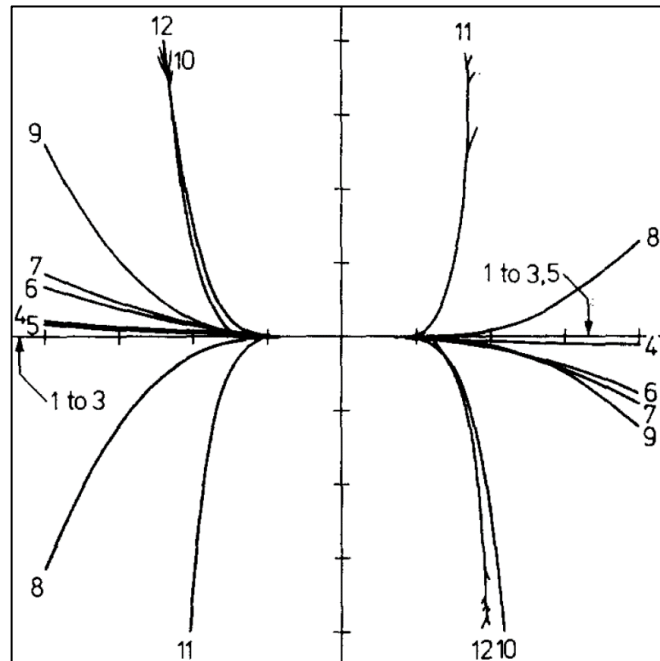


Figure 2.1: Fracture Trajectories of biaxially loaded 4 mm thick PMMA specimens [18]

In pursuit of interpreting this behaviour, the stress field around the crack was given by Williams' [20] and Irwin's [21] analyses concerning plane stress, in the form of Equation 2.2, where x is the parallel and y the perpendicular direction to the crack.

$$\left\{ \begin{array}{l} \sigma_{xx} = Kr^{-1/2}f_{xx}(\theta) + T + \dots \\ \sigma_{yy} = Kr^{-1/2}f_{yy}(\theta) + \dots \\ \sigma_{xy} = Kr^{-1/2}f_{xy}(\theta) + \dots \end{array} \right\} \quad \text{Equation 2.2}$$

Where:

- $f_{xx,yy,xy}(\theta)$: functions of geometry of the crack and angle at which the stresses are calculated
- r : the distance from the crack tip
- K : the stress intensity factor
- T : the uniform stress acting parallel to the crack

In Equation 2.2, higher order terms were not considered, while the stress acting parallel to the crack (T) was expressed in terms of the biaxiality ratio ($k = \sigma_{xx}/\sigma_{yy}$) as follows,

$$T = (k - 1) \sigma_{yy} \quad \text{Equation 2.3}$$

With the above in mind, Leever's [18] set focus on producing an analytical solution able to meet the following requirements,

- characterization of the trajectory in terms of initially determinable parameters
- determination of the stress intensity factor at the instability point, from which fracture toughness will be calculated
- a quantification of the effect of stress biaxiality at the instability point, denoting its effect on toughness

The S-shaped cracks, i.e. not having a straight-line propagation path, observed experimentally were approached either as bent or curved cracks and a model was employed for each of these cases, based on projecting the crack and conducting calculations based on its projected length and angle. The curved crack model attempted to represent the right-hand tip of the crack by treating it as a part-circular crack. This was implemented by the superimposition of the mode I and mode II stress intensity factors calculated for,

- the crack projection on the y axis

- the crack projection on the x axis

The general form of the stress intensity factor formulae invoked in the superimposition were,

$$\begin{cases} K_I = F_{1y}(\alpha)p_y(\pi\alpha_y)^{1/2} + F_{1x}(\alpha)p_x(\pi\alpha_x)^{1/2} \\ K_{II} = F_{2y}(\alpha)p_y(\pi\alpha_y)^{1/2} + F_{2x}(\alpha)p_x(\pi\alpha_x)^{1/2} \end{cases} \quad \text{Equation 2.4}$$

Where:

- K_I, K_{II} : the mode I and mode II stress intensity factors accordingly
- $F_{1x,1y,2x,2y}(\alpha)$: functions of geometry and angle of the crack
- p_y : applied uniform stress at the y direction
- p_x : applied uniform stress at the x direction
- α_x : half of the projected length ($2\alpha_x$) on the x axis
- α_y : half of the projected length ($2\alpha_y$) on the y axis

After determining a way for calculating the stress intensity factors, a path prediction model was developed based on Erdogan & Sih's analysis of the stresses in the vicinity of the crack [22]. According to their assumptions and in agreement with the experimental data, it was argued that the crack propagates in the plane perpendicular to the direction of the greatest tension, i.e., in the direction of the maximum tangential stress. Hence, setting the first derivative of the tangential stress as zero resulted in the formula calculating the difference in angle between the crack tip and the maximum tangential stress, Equation 2.5.

$$(K_{II}/K_I)(3\cos\theta^* - 1) + \sin\theta^* = 0 \quad \text{Equation 2.5}$$

The above, in combination with the assumption that the crack path does not deviate significantly during each step of propagation, were translated as a need for K_{II} to be zero. Setting this condition in Equation 2.4 (b) and taking into account the finite width corrections, the following formula which expresses the gradient of the propagation direction, was produced:

$$dy/dx = 1.145k^2[F_T(2y/W)/F_T(2x/W)]^2(y/x) \quad \text{Equation 2.6}$$

Where:

- F_T : finite width corrections

- x, y : Cartesian coordinates from the center of the crack
- k : the biaxiality ratio

Equation 2.6 showed good agreement between with the experimental results and supported the conclusion that the path of the crack positions itself normal to the maximum applied load [18].

Supplementary work done by Radon, Leever & Culver [23] pursued the study of the effect of biaxial loading on the fracture toughness of the material. The fracture toughness values calculated diverged insignificantly from those of uniaxial tests, leading to the conclusion that fracture toughness stayed the same and regardless of biaxiality.

Further research on the effects of biaxiality was done by Eftis et al. [24]. As in [17], [18], it was argued that for strictly symmetrical and anti-symmetrical biaxial loadings with respect to the axis of crack length, the one parameter representation of the elastic stress and displacements was qualitatively unacceptable. The analysis in [24] concerned an isotropic solid in plane stress, or plane strain with no body forces exerted. The stress function under these conditions was represented by the Airy's stress function ($U(r, \theta)$), which due to the condition of stress compatibility was required to satisfy the biharmonic equation.

$$\left\{ \begin{array}{ll} U(r, \theta) = r^{\lambda+1} F(\theta), & \text{Assumed form of the Airy's Stress Function} \\ \nabla^2 U = 0, & \text{Biharmonic Equation} \end{array} \right\} \quad \text{Equation 2.7}$$

Where:

- $F(\theta)$: the eigenfunctions of the partial differential equation
- λ : the eigenvalues of the partial differential equation
- r : the radial distance from the crack tip
- θ : the angle from the axis on which the crack length lies

The solution of the system in Equation 2.7 invoked Williams' solution [20] in terms of a series of eigenfunctions. This was commonly implemented with keeping only the first term of the series, judging the rest to have a negligible effect. In this case the series was expanded up to the third term, keeping only what was of order higher than $r^{1/2}$. The final equations included three parameters, K_I , K_{II} and A , which were determined from the traction boundary conditions applied. Overall, it was illustrated that,

- close to the crack tip the first term dominated quantitatively

- the second terms were independent of radial distance, hence when studying the stresses very close to the crack tip they improved calculative accuracy in an inconsequential way

Thus, for direct stress calculation, the second terms might have been insignificant, but when attempts were made to calculate other stress related quantities such as the maximum shear or strain energy, the existence of the second terms was of significant qualitative nature. The stress intensity factor, expressed as a complex function, was shown to be independent of the second and higher order terms and not affected by them.

The boundary conditions, after specifying the problem as a biaxially loaded plate with a centre crack, were:

$$\begin{cases} \sigma_{yy}(\infty) = \sigma \\ \sigma_{xx}(\infty) = k \\ \sigma_{xy}(\infty) = 0 \end{cases} \quad \text{Equation 2.8}$$

With the additional assumption that loading could not cause buckling (thickness dimension could be assumed to be large enough to prevent this) and further analysis with the boundary conditions known, the parameters K_I , K_{II} and A , mentioned before, were expressed as,

$$\begin{cases} K_I = \sigma\sqrt{(\pi a)} \\ K_{II} = 0 \\ A = -(1 - k)\sigma \end{cases} \quad \text{Equation 2.9}$$

While the crack border stresses were calculated by the following equations,

$$\begin{cases} \sigma_{xx} = \frac{K_I}{\sqrt{2\pi r}} \cos\left(\frac{\theta}{2}\right) \left[1 + \sin\left(\frac{\theta}{2}\right) \sin\left(\frac{3\theta}{2}\right)\right] \\ \sigma_{yy} = \frac{K_I}{\sqrt{2\pi r}} \cos\left(\frac{\theta}{2}\right) \left[1 - \sin\left(\frac{\theta}{2}\right) \sin\left(\frac{3\theta}{2}\right)\right] - (1 - k)\sigma \\ \sigma_{xy} = \frac{K_I}{\sqrt{2\pi r}} \sin\left(\frac{\theta}{2}\right) \cos\left(\frac{\theta}{2}\right) \cos\left(\frac{3\theta}{2}\right) \end{cases}, \text{ for } 0 < \frac{r}{a} \leq 1 \quad \text{Equation 2.10}$$

Where:

- K_I : the mode 1 stress intensity factor
- K_{II} : the mode 2 stress intensity factor
- k : the biaxiality ratio
- σ : the stress acting perpendicularly to the crack line

- θ, r : angle and distance from the crack tip

It was observed that the single term approximation of Williams' eigenfunction expansion was adequate to the two-term approach only in the case where $k=1$, i.e. equiaxial loading. The case of $k=0$, i.e. uniaxial loading, studied in [24], illustrated that even in uniaxial loading the displacement relating to the Poisson ratio effect (perpendicular to the loading) was not taken into account with the single term approximation, as opposed to the two-term solution, in which the second term incorporated this effect.

Additionally, a single term characterization was shown to disregard the boundary loading and its effect on the stress patterns close to the crack tip as seen during comparison with the isochromatic fringe patterns, which resembled the maximum shear stress trajectories. Since plastic deformation related to maximum shear, plastic yield and its extent were directly affected by the boundary loading.

In this mindset Eftis et.al, as Leever et al., studied the crack propagation trajectory. The extension of the crack based on the maximum normal stress criterion was mathematically expressed as:

$$\left\{ \begin{array}{l} [\sigma_{\theta\theta}]_{\theta_0} > 0 \\ \left[\frac{\partial \sigma_{\theta\theta}}{\partial \theta} \right]_{\theta_0} = 0 \\ \left[\frac{\partial^2 \sigma_{\theta\theta}}{\partial \theta^2} \right]_{\theta_0} = 0 \end{array} \right\} \quad \text{Equation 2.11}$$

The single term approximation of the solution gave only one path for crack propagation by allowing a solution of $\theta = 0$ or 2π disregarding boundary conditions that concerned loading. As expected this was not the case observed in actual experiments and retaining the second term gave rise to two possible solutions, namely

- for $k \leq 1$, the only permitted solution was $\theta = 0$
- for $k > 1$, the angle of the crack path repositioned itself. In the extreme case where $k \rightarrow \infty$, the crack oriented itself perpendicularly to the horizontal loading which reached infinity, i.e. $\theta = \frac{\pi}{2}$

Additional, analysis conducted in [24], [25] attempted to understand the effect of biaxiality on the relationship between the stress intensity factor and global and local elastic strain energy rates in the case of symmetric stresses ($K_{II} = 0$). The global and local elastic strain

energy rates were important values since they provided a measure of the energy available for an increment of crack extension.

Concerning the local elastic strain energy density (Φ) it was calculated using the stress and strain equations retaining the second terms, Equation 2.10, thus Φ depended on both the biaxiality factor (k) and Poisson's ratio (ν). An interesting observation was that an increase in Poisson's ratio degenerated the solution to the equibiaxial loading condition/single term solution.

The local elastic strain energy rate ($\dot{\Phi}$) was calculated with the integration of the elastic strain energy at a point (φ), over a circular region originating from the crack tip. It was shown that $\dot{\Phi}$ was dependent on the second terms of the series expansion, which were of major importance for the calculation of elastic strain energy rate locally since they accounted for the loading horizontally of the crack.

As for the global elastic strain energy rate (\dot{G}), a load applied horizontal to the crack and consequently the second term of Williams' series expansion, appeared to have no effect. A valid question as to why that happened is expressed in [24], [25] without further explanation.

Concerning the effects of biaxiality beyond elastic behaviour, non-linear analysis was conducted by Liebowitz et al. [26], with the use of a Ramberg-Osgood stress strain relation. It was illustrated that the non-linear energy rate (\dot{G}) and J-integral were affected by biaxiality and had the same trend in value change. The size of the plastic zone behaved in a similar way; as expected, it increased with an increase in the applied load or a rise in the value of the biaxiality ratio k .

2.2 Biaxiality in elastic - plastic fracture mechanics

Research up to the 1980's had mostly focused on the analysis of the crack tip stress field and the material's fracture toughness within the scope of linear elastic fracture mechanics. Such an approach was valid only to the extent where non-linear material deformation was confined to a small region around the crack tip [27], which was not necessarily the case in real structures.

In a ductile material, the inelastic zone does not necessarily remain contained in a small area. This led to the development of elastic-plastic fracture mechanics (EPFM), where the

material behaviour was treated as non-linearly elastic [27], [28]. Within this context the non-linear energy release rate, J , can be expressed as a path-independent line integral [29]. Assuming a Ramberg-Osgood power hardening law relationship, Hutchison, Rice and Rosengren (HRR) showed that the path independency stands, as long as there was a (plastic) zone around the crack tip governed by a $r^{-1/(n+1)}$ singularity, where n was the hardening coefficient of the material. EPFM was based on the assumption of small strain theory and was valid in accordance to the J -dominance over a region, i.e. validity of the J path independence in that region. Path independence means that any closed path has a J value of zero and that any path around the crack will result in the same J calculated. It should be emphasized that the HRR solution is one of the possible solutions that translate the J path integral to a characterization of crack tip conditions, hence an HRR singularity was efficient but not necessary for J -dominance over a region. Additionally, path independence of J -integral required proportional¹, monotonically applied loading, in the case of multiaxial loading conditions, the load path could be non-radial, i.e. the direction of the principal stress could change in any load increment.

As plasticity developed further with increased loading, assuming ductile behaviour, the crack tip blunted (large strains) and reduced stress triaxiality locally, whilst the plastic zone grew to a considerable size. Once the plastic zone was big enough, J could not uniquely characterize the stress distribution in front of the crack tip and was affected by geometry.

It would be prudent to sum up the above explanations concerning the validity limits of LEFM and EPFM, illustrated in Figure 2.2. The former is not accurate when the plastic zone is significant in regard to in-plane dimensions, i.e. approximately 1/15 times larger than the crack length or ligament, whilst J -integral lacks validity as a single crack tip characterization parameter as large-scale yielding is approached, i.e. this is where the plastic zone extends to start interacting with a free surface in the component/structure. The size of this area and consequently the region of J -dominance, vary according to the geometry/loading and hardening coefficient of the component [31].

¹ Proportional loading: Loading is proportional when the applied load on one axis is always equal to that on another axis multiplied by a constant [30], hence all components of the stress tensor change proportionally

2.2.1 Two parameter fracture mechanics

As mentioned, single parameter fracture mechanics could not quantify the stress field around a crack when there was excessive plasticity. In light of this, two-parameter crack-tip constraint modified fracture mechanics approaches, which pursued the characterization of the material whilst considering the geometrical properties and/or complex loading conditions that affected the plasticity flow [32], were developed.

It was apparent to researchers that the crack tip triaxiality/constraint was dependent on geometrical aspects (e.g. thickness), load conditions (e.g. bending loads that restrict the plasticity flow) or material properties (e.g. ductile or brittle behaviour at operating temperature) [13], [32]–[34]. Even though some work was originally done by O'Dowd & Shih ([35], [36]) on developing a two parameter approach which would address these effects of constraint, validation of such approaches was mostly done within the Oak Ridge National Laboratory, where extensive research was conducted for the better assessment of reactor pressure vessels (RPV), [37]–[42].

It was noticed that fracture in such components began from shallow flaws, which were under a state of biaxiality due to the internal pressure, that created both a hoop stress and an out of plane stress at the caps of the vessel. In this direction, tests were conducted on A533B steel, in the transition region of the toughness curve. The geometries of the tested specimens were:

- Single edge notched bend specimens (SENB), with shallow or deep cracks
- Bend cruciform specimens, containing a surface crack in the centre, which were loaded uni-axially or bi-axially

The latter [37] had a similar specimen geometry to that used in the PMMA studies [17], however in this case a surface-breaking rather than a through thickness flaw is introduced, as seen in Figure 2.3.

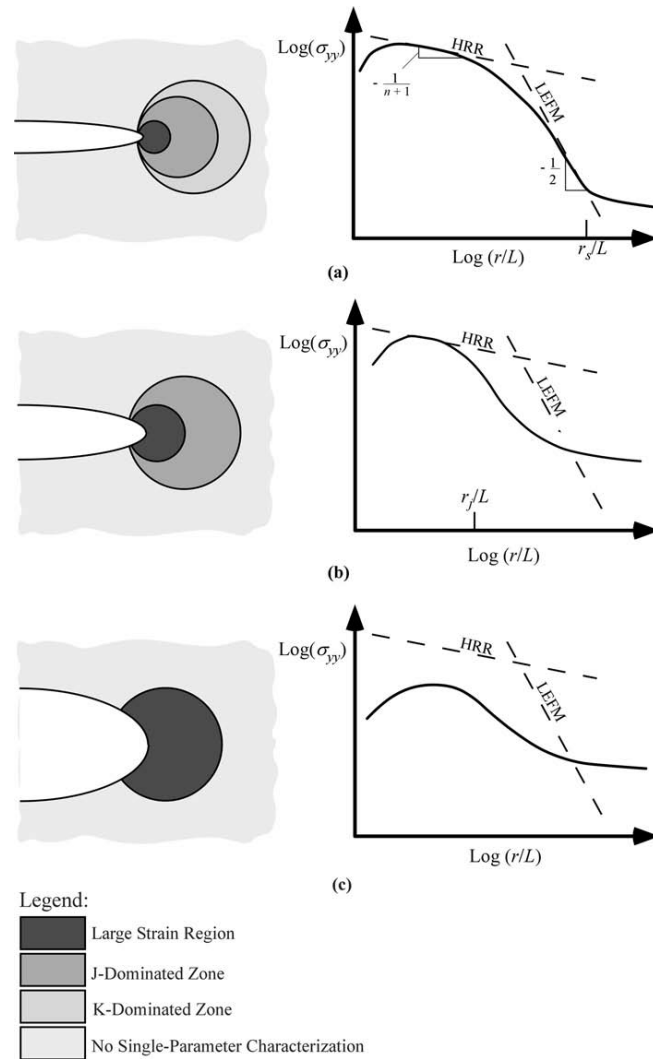


Figure 2.2: Effect of plasticity on the crack-tip stress fields: (a) small-scale yielding, (b) elastic-plastic conditions, and (c) large-scale yielding.[27]

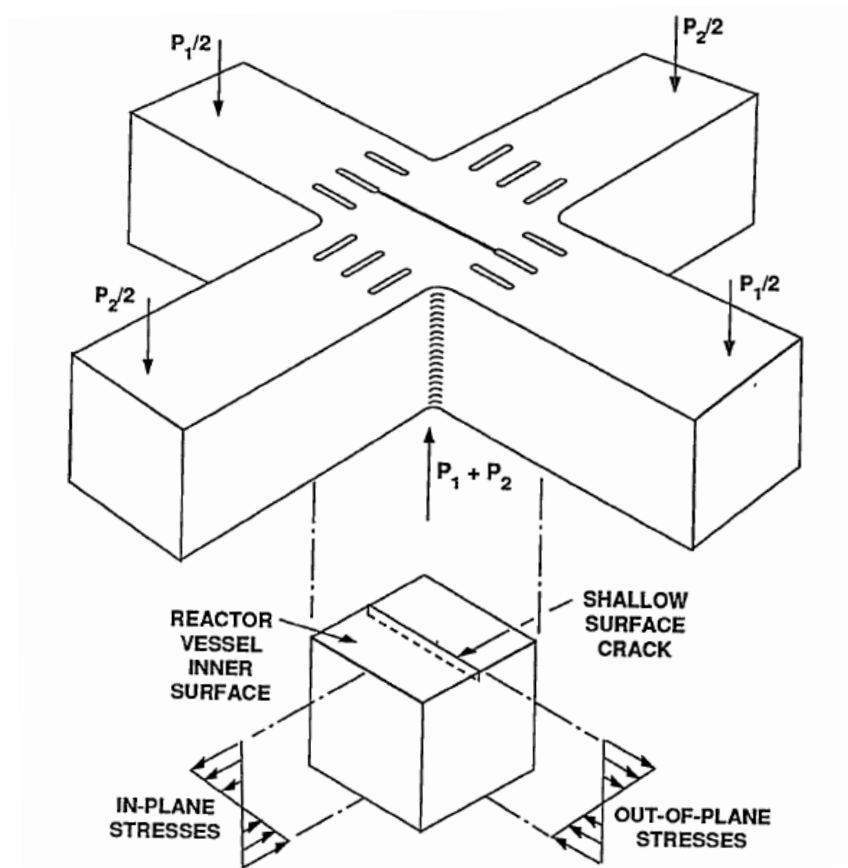


Figure 2.3: Cruciform specimen geometry, showing the in and out of plane components of stress during biaxial testing [33]

Concerning the SENB specimens, it was observed that the shallow cracked specimens had an increased fracture toughness compared with the deeply flawed. For the tests on cruciform specimens, biaxial loads resulted in lower fracture toughness compared to uniaxially loaded cruciform or SENB specimens. It should be noted that, even though the critical loads for uniaxial and biaxial loading of the cruciform specimen were close, a significantly higher amount of deflection (plastic strain) was withstood during uniaxial loading, leading to an interpretation of biaxial loading as reducing the ductility, which was also supported by more recent experiments [7].

Comparison between the uniaxially loaded cruciform and the SENB specimens demonstrated similar values of fracture toughness [38]. This can be explained physically by the effect of constraint. In the SENB specimens, deeper cracks would encounter higher crack tip constraint, due to plane strain conditions governing the material behaviour around the centre of the crack at the mid-thickness position. In other words, out of plane surfaces of the specimen would be displaced towards the centre of the specimen as a result

of the contraction which follows volume retention. This, in combination with the nature of the loading (i.e. bending, which also constraints the flow of plasticity) increased crack tip triaxiality and lowered fracture toughness.

In the case of the uniaxially loaded cruciform specimen, fracture toughness tended to approach the (lower bound) fracture toughness of SENB specimens, as expected due to their similar geometrical and loading effects on constraint. However, when biaxiality was introduced, the existence of a far-field out-of-plane stress (stress parallel to the crack plane) further increased stress triaxiality (constraint) resulting in a decrease in fracture toughness.

Here it is prudent to explain that constraint evolved in accordance with the flow of plasticity in the material, which could reach up to fully yielded conditions. If constraint was to remain constant throughout the loading procedure (initiation - failure), then yielding would have stayed contained in a relatively small area and two parameter fracture mechanics would not be necessary. However, the development of plasticity raised concern regarding the way in which the material would fail. To distinguish between the stress-induced fracture² (brittle fracture, where opening mode stress exceeds a critical value over a finite length with little or no ductile deformation of the material around the crack tip) and the strain-induced fracture (ductile tearing, where crack tip strains exceed the stress-state-dependent ductility of the material and often results in a stable and predictable mode of fracture in which crack growth can only occur under an increasing applied load) the crack tip stresses were studied as a result of two stress fields [34]. In particular, the stress tensor, Equation 2.12,

$$\sigma = \begin{bmatrix} \sigma_{11} & \sigma_{12} & \sigma_{13} \\ \sigma_{21} & \sigma_{22} & \sigma_{23} \\ \sigma_{31} & \sigma_{32} & \sigma_{33} \end{bmatrix} = \begin{bmatrix} \sigma_{xx} & \sigma_{xy} & \sigma_{xz} \\ \sigma_{yx} & \sigma_{yy} & \sigma_{yz} \\ \sigma_{zx} & \sigma_{zy} & \sigma_{zz} \end{bmatrix} = \begin{bmatrix} \sigma_{xx} & \tau_{xy} & \tau_{xz} \\ \tau_{yx} & \sigma_{yy} & \tau_{yz} \\ \tau_{zx} & \tau_{zy} & \sigma_{zz} \end{bmatrix} \quad \text{Equation 2.12}$$

was divided into two tensors, namely:

- Hydrostatic Stresses: a volume changing stress tensor, Equation 2.13, its matrix is diagonal and is composed of equal stresses at each of the axes of a Cartesian system. Change in orientation of the system studied will not alter the stresses [44]. This tensor

² Brittle fracture is interpreted as a stress-based failure; however, it does rely on plastic strain since sufficient plastic strain is needed to nucleate a microcrack. [43]

contributes directly to the opening mode tensile stress and influences crack tip constraint but does not directly influence yielding or crack tip blunting

$$\sigma_{\text{Hyd}} = \begin{bmatrix} \sigma_{\text{Hyd}} & 0 & 0 \\ 0 & \sigma_{\text{Hyd}} & 0 \\ 0 & 0 & \sigma_{\text{Hyd}} \end{bmatrix}, \quad \sigma_{\text{Hyd}} = \frac{1}{3} \text{tr}(\sigma) = \frac{1}{3} \sigma_{kk} \quad \text{Equation 2.13}$$

- Deviatoric Stresses: part of the stress tensor that tends to distort the body, Equation 2.14. It is what is left after the removal of the hydrostatic stresses from the stress tensor [44] and includes all shear stresses. The shear stresses govern the yielding and consequently plastic deformation and crack-tip blunting

$$\sigma' = \sigma - \sigma_{\text{Hyd}} = \begin{bmatrix} \sigma_{11} - \sigma_{\text{Hyd}} & \sigma_{12} & \sigma_{13} \\ \sigma_{21} & \sigma_{22} - \sigma_{\text{Hyd}} & \sigma_{23} \\ \sigma_{31} & \sigma_{32} & \sigma_{33} - \sigma_{\text{Hyd}} \end{bmatrix} \quad \text{Equation 2.14}$$

Hence, an increase in the hydrostatic stress tensor under stress-controlled conditions (brittle material/behaviour) would directly increase the likelihood of fracture by cleavage. However, such an increase would also (indirectly) affect a strain-controlled fracture by increasing the crack tip stresses, which, if not combined with additional yielding or crack tip blunting (increase in the shear stress components of the stress tensor) would lead to further strain on an already yielded area and consequently strain concentration and ductile tearing.

2.2.1.1 K-T stress

Similar to the analysis conducted for the study of the crack trajectory in biaxially loaded PMMA specimens (Section 2.1), the Williams' eigenfunction expansion was used here to incorporate constraint. The second term of the expansion was found to have a significant effect on the plastic zone shape and the stresses deep inside it [27]. The stress distribution, from maintaining the first and second terms of the eigenfunction expansion, was expressed as [27], [45]:

$$\sigma_{ij}^e(\mathbf{r}, \theta) = \frac{K}{\sqrt{(2\pi a)}} \cdot f_{ij}(\theta) + \mathbf{T}_{\text{stress}} \cdot \delta_{i1} \cdot \delta_{1j}, \text{ for } \mathbf{r} \ll \mathbf{a} \quad \text{Equation 2.15}$$

Where:

- σ_{ij}^e : the elastic stresses around the crack tip
- K : the elastic stress intensity factor
- $f_{ij}(\theta)$: geometry related correction

- δ_{ij} : Kronecker delta functions
- θ, r : polar coordinates originating from the crack tip
- a : half of the crack length

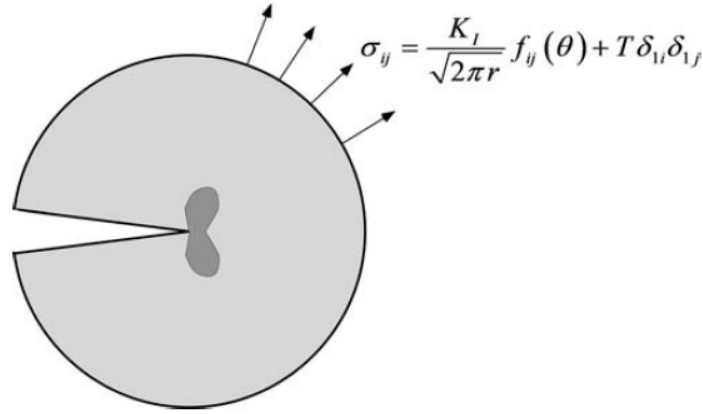


Figure 2.4: Modified boundary layer analysis, an area around the crack tip is studied remotely with the loading of Equation 2.15 applied at the boundary [27]

By applying this stress distribution as a boundary condition in a modified boundary layer analysis (MBL), which is essentially the focus on a part of the material around the crack tip studied as a free body, Figure 2.4, the effects of the T-stress were studied. Some important conclusions of this study were:

- a $T = 0$ stress was equivalent to the small-scale yielding limit, i.e. when the size of the plastic zone is considered negligible in regard to the geometrical dimensions (crack length, body size). This was expected considering the form of Equation 2.15
- negative T stresses caused a decrease of the σ_{11} and σ_{33} stresses of the overall stress tensor. This could be interpreted as a decrease in constraint and divergence from the small-scale yielding condition
- $T = 0$ did not match the HRR solution, since the latter took higher order plastic terms into account
- T stress could be used as a quantitative index of constraint effects

It should be noted that the T-stress approach was valid only when plasticity was contained in a small area and the material around it behaved elastically, since it derived from analytical equations that originated from the elastic theory. Hence, T-stress loses its physical meaning and does not provide accurate results under fully plastic conditions.

2.2.1.2 J-Q Theory

O'Dowd and Shih [35], [36] developed a methodology which quantified constraint as plastic flow progressed from well contained yielding up to fully yielded conditions.

Initial observations made with the use of the T-stress were that the different crack tip stress fields caused by different levels of triaxiality (different T-stress) could be organized into a family of crack tip fields. In other words, the effect of geometry and constraint effects on the crack tip stress field could be parametrized, albeit only in conditions of small-scale yielding.

To overcome the limitation of the small-scale yielding, a plane-strain family of self-similar stress fields was derived, albeit this time from plasticity analysis. Assuming small strains and a power law hardening material, the asymptotic expansion solution expressed in terms of a power series, had the HRR solution as the first order term, while all the higher order terms were grouped into a collective term, i.e. the “difference field”. This difference field designated as “ Q ” expressed the divergence of the crack tip stress field from a reference one ($(\sigma_{ij})_{\text{reference}}$), which was the HRR solution in this case. Apart from the HRR solution another reference stress field used was the T -stress = 0 field, which related to small scale yielding.

With the use of an MBL analysis (on an elastic power law hardening material) the forward sector of the crack within the annulus of $J/\sigma_0 < r < 5J/\sigma_0$ was investigated, since all the microstructurally significant effects concerning both brittle and ductile fracture were encompassed in this zone [32]. It was noticed that the stress field was not highly dependent on the distance and angular position ($\sigma_{rr}, \sigma_{\theta\theta} \approx \text{constant}$) and that the shear components of stress in this field were of much lower magnitude than the hydrostatic stresses ($\sigma_{rr} \ll \sigma_{\theta\theta}$). Hence Q was defined as a spatially uniform (approximately), normalized, hydrostatic stress tensor of adjustable magnitude, which shifted the stresses in front of the crack tip to lower or higher levels depending on the constraint during loading. Q was defined at a distance of $r = 2J/\sigma_0$ and was expressed as:

$$Q = \frac{\sigma_{\theta\theta} - (\sigma_{\theta\theta})_{\text{reference}}}{\sigma_0}, \text{ at } \theta = 0, r = 2J/\sigma_0 \quad \text{Equation 2.16}$$

Where:

- $\sigma_{\theta\theta}$: the hydrostatic stress at the θ direction

- $(\sigma_{\theta\theta})_{\text{reference}}$: the reference stress field
- δ_{ij} : Kronecker delta functions
- σ_0 : the yield stress of the material

The near-tip stress field with the use of the J-Q theory was expressed by Equation 2.17.

$$\sigma_{ij} = (\sigma_{ij})_{\text{reference}} + Q\sigma_0\delta_{ij} \quad \text{Equation 2.17}$$

In general, the maximum stress and stress distribution were determined by Q, which scales the stress level relative to a reference state that regarded high triaxiality, while J adjusted the size of the process zone over which the large stresses and strains developed [35], [36]. Negative Q values expressed a reduction of hydrostatic stress (and consequently stress triaxiality), whilst positive Q values expressed an increase, by $Q\sigma_0$ from the $Q = 0$ high triaxiality state. For instance, if a constant value of J was considered, a negative Q ($Q < 0$) value would be met in low constraint geometries along with more crack tip blunting in comparison to positive or zero values of Q ($Q \geq 0$) and less blunting met in high-constraint geometries. It should be noted that during excessive crack-tip blunting, the J-Q dominance was valid in a region not much bigger than the annulus where J-dominance existed. Additionally, when excessive blunting or specific loading conditions (e.g. bending) were introduced, the distance independence of Q weakens, and it changed linearly with the distance r, in dependence on remote load and crack geometry.

It should be noted that J-Q theory was not applicable to growing cracks, since Q quantified both opening and mean (hydrostatic) stress, in terms of the crack tip constraint, it provided a description of the “competition” between fracture by cleavage (controlled by the opening stress [46]) and ductile tearing (controlled by the void growth/interaction/coalescence, which relied on the mean stress [46])[32]. It is worth noting here that the validity of these methods relies on the compliance of the material tensile properties to a Ramberg Osgood law. In non-ideal power-law hardening materials, as are most, additional contours further away from the crack tip need to be used for accurate calculation of properties.

2.3 Failure prediction models

In pursuit of relating the crack tip fields to fracture toughness, a need for micromechanical failure criteria was developed. A simplified mechanical failure criterion, connecting the

local crack behaviour to the macroscopically applied loads, was the commonly used (cleavage) fracture toughness (K_c) measured from high constraint specimens (e.g. Single edge notched bending - SENB). In particular, the measured value of K_c for a specimen, which maintained high constraint throughout loading, acted as a minimum value of fracture toughness. This ensured that any structure of the same material would have at least this minimum fracture toughness, at any level of constraint. From the point of view of statistics, this could be interpreted as the lowest limit of the fracture toughness, where the possibility of the material exhibiting a value lower than that was approximately zero. It was apparent that the above criterion provided conservatism since cracks were not always under such high constraint and crack tip triaxiality was reduced as plasticity flowed with load increase.

Determination of the fracture toughness of a structure, with loss of constraint taken into account, would require fracture toughness testing on specimens that match the structure in terms of constraint. While this decreased conservatism in assessing such a structure it increased the amount and cost of experiments. To satisfy the demand for fewer and less costly experiments many researchers attempted to develop criteria that would unify fracture toughness as a material parameter and detach it from geometric and loading configuration. Some of the criteria developed concerned ductile fracture [47], [48], however for constraint related cases, the majority focused on cleavage. The reason behind this was that prior to ductile fracture there was a flow of plasticity, which decreased crack tip triaxiality and its effect on the crack tip stress field. During plasticity flow the energy dissipated in the material did not seem to be affected by biaxiality according to Ostby & Hellesvik [7], where the values of J and the crack growth resistance seemed to be insignificantly influenced by biaxial loading. Here it should be noted that even though biaxiality might not influence ductile behaviour; constraint and especially crack depth related induced constraint, can have an effect on the J developed [49], while this effect varies with different crack depths. Here, in the transition region, where there was uncertainty over the type of failure that might occur and constraint favoured a less ductile behaviour, higher concern was raised with regard to failure by cleavage.

In this direction, many micromechanical criteria have been developed and calibrated against experimental data. Validation of such criteria was intensively conducted within pressure vessel related work, a high fraction of which was conducted at the Oak Ridge Laboratory [9], [50], [51]. This work aimed to correlate fracture toughness and biaxiality by

using micromechanical failure criteria. Several of the criteria covered by the latest work, along with additional ones, were revisited at a later time within the context of the VOCALIST project [45], [52], which was launched to provide an overview of the effects of constraint on the cleavage fracture toughness and the existing methodologies assessing it. From the failure criteria presented in the literature two of the most used, concerning cleavage fracture, are explained in the following paragraphs.

2.3.1 Dodds-Anderson toughness scaling model

This model developed by Dodds & Anderson (D&A) concerned (transgranular) cleavage fracture and derived from weakest link model which assumed that cleavage fracture was controlled by a particle which is most favourable, either by its orientation or size, to have fracture initiating from it [13], [53]. The triggering effect included an instability of a microcrack forming at the particle, where a critical stress was reached in the vicinity of the microcrack. The geometry and position of the microstructural feature that triggered the microcrack directly affected the fracture toughness value and its scatter.

The probability of finding a triggering microfeature ahead of the crack tip was related to the volume of the zone in front of the crack where the stress exceeded a limiting value, that sufficed to initiate cleavage. Hence, the probability of fracture was expressed as,

$$F = F[V(\sigma_t)]$$

Where:

F: the failure probability

σ_t : the cleavage triggering stress at a point

$V(\sigma_t)$: volume ahead of the crack tip over which the stress was equal to or higher than σ_t

The D&A model hence assumed that when the critically stressed volumes ahead of the crack were equal then the cleavage fracture had the same probability of happening. Using two parameter fracture mechanics, the stress tensor in front of the crack tip (dependent on constraint through Q) and the size of the area with stresses higher than a critical stress, could be calculated. In this respect, the D&A model did not attempt to predict a value for the fracture toughness (J_c), but rather to correlate changes in fracture toughness with changes of constraint effects by comparing to a reference condition. This reference

condition was the small-scale yielding condition, which represented an upper margin on constraint.

The implementation of the method started with the calculation of the area enclosed within a specific contour, where the stress (σ_t) had a value equal or higher than a critical stress (σ_c). Let the area for the small-scale yielding (infinite body) be represented by A_0 and the J-value for which such a stress distribution was created by J_0 . In the same way, for the finite body the area was denoted as A_f and J-value as J_f . The ratio of J_f/J_0 for which $A_0(\sigma_t) = A_f(\sigma_t)$ quantified the effect of constraint on fracture toughness. It is worth noting that the brittle fracture models (at least those presented here) adopt a weakest link assumption when determining the failure probability.

Concerning the σ_t stress, it could be interpreted in different ways. In the initial analysis, the model was validated against SENB specimens and a plane strain analysis was conducted, where thickness was disregarded [50]. At that stage, σ_t stress was set as the opening mode stress (σ_3), which provided valid results for the two-dimensional loadings of the SENB specimens. However, in the case of biaxial loadings, the far-field out-of-plane bending stresses had an impact in the hydrostatic stress tensor, which was not imprinted on the opening mode stress. It was shown in [9] that the insensitivity to the far-field out-of-plane bending stresses was alleviated with the use of the hydrostatic stress (σ_H) as a failure criterion, illustrated in Figure 2.5, where increase in the biaxiality ratio had no effect on the opening mode stress (σ_3), presented as σ_{zz} in the figure; however, there was an apparent shift in the hydrostatic stress (σ_H).

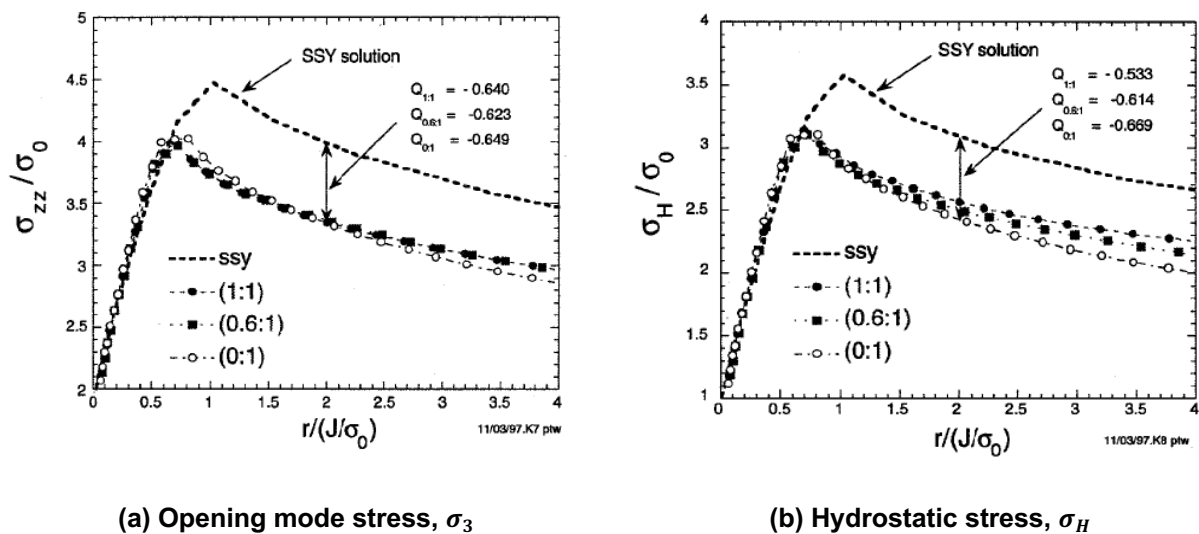


Figure 2.5: Sensitivity to biaxiality for Q-stress based on different stress criteria, [9]

This can also be seen in Figure 2.6, where the stress contours for both stress criteria were presented with increasing J-values. In the case of σ_3 , uniaxial and biaxial loadings produced similar stress contours for all levels of J; however, use of σ_H included the effect of biaxiality, with stress contours having been larger for biaxial loading. This in its turn denoted a larger critically stressed volume and thus higher probability of cleavage fracture, which was expected according to the experimental data in [9], thus rendering σ_H as a more accurate stress criterion.

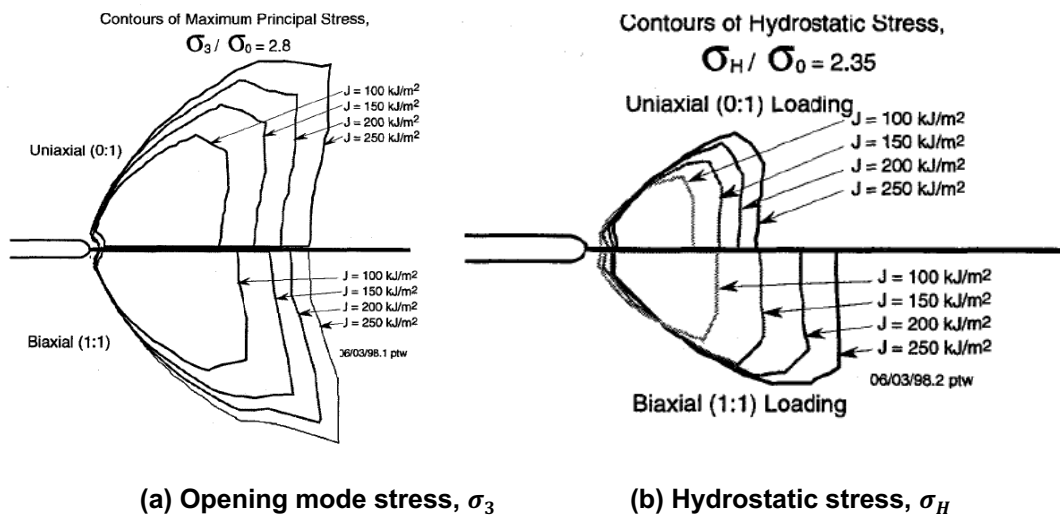


Figure 2.6: Contours of stresses with increasing J-values, [9]

2.3.2 Weibull cleavage model

Another widely used local fracture criterion is the Weibull cleavage model. This was initially developed by the Beremin group [12], who argued that there is a need for statistical treatment of the fracture toughness data due to their scatter. Their study was theoretically based on the same assumptions as the ones for the D&A model, i.e. the critically stressed volume in front of the crack was directly related to the probability of fracture. Thus, effort was put towards the approximation of the distribution of microcracks that would have sufficient length to initiate fracture. This sufficient length was related to a critical stress (σ_c) with the use of the Griffith model, which denoted the energy required for a crack to start propagating (i.e. sufficient potential energy was available to overcome the surface energy of the material). The latter was approximated in [12], with use of Equation 2.18.

$$\sigma_c = \sqrt{\frac{2E\gamma}{\pi(1-\nu^2)l_0}} \quad \text{Equation 2.18}$$

Where:

- σ_c : the critical stress
- γ : surface energy
- ν : Poisson's ratio
- l_0 : length of the microcrack

The analysis assumed a volume V_0 , which should be large enough to have an acceptable probability of including a microcrack with sufficient length and could be divided into smaller volumes. Each fraction of the volume was treated as statistically independent from the rest and the overall probability of failure was defined as the aggregation of the probability of each of the volume fractions. After expressing the crack length with the use of Equation 2.18 in terms of critical stress and combining this with the assumption of a constant stress over V_0 the probability of failure became:

$$P_R = 1 - \exp \left[- \left(\frac{\sigma_w}{\sigma_u} \right)^m \right] \quad \text{Equation 2.19}$$

$$\sigma_w = \sqrt[m]{\sum_j (\sigma_1^j)^m \frac{V_j}{V_0}} \quad \text{Equation 2.20}$$

It is clear that Equation 2.19 represented a Weibull distribution [54], where:

- P_R : the probability of failure
- σ_w : Weibull stress. This was a fracture parameter that showed the damage of the material in the vicinity of the crack tip [14]
- σ_u : scaling stress (scaling factor), a material parameter
- m : Weibull modulus
- σ_1^j : maximum principal stress
- V_j : volume of the j^{th} element experiencing the maximum stress σ_1^j
- V_0 : a reference volume; should be small enough for stress gradients to be approximately zero and large enough to incorporate a non-negligible probability of including a microcrack of appropriate length

Concerning the applied stress in Equation 2.20, there were different criteria that could be used to evaluate the stress that was to reach a critical value for failure. The one applied in Equation 2.20 was the “Maximum Principal Stress”. However, as in the case of the Anderson & Dodd scaling model, the use of the hydrostatic stress as a failure criterion provided higher accuracy in the application of the Weibull model [15].

A three parameter Weibull cleavage model had also been developed with the introduction of parameter designated as $\sigma_{w-\min}$, as seen in Equation 2.21 . This third parameter cancels out any non-zero probabilities of failure when loads were very close to zero and acted as lower-bound strength [55].

$$P_R = 1 - \exp \left[- \left(\frac{\sigma_w - \sigma_{w-\min}}{\sigma_u - \sigma_{w-\min}} \right)^m \right] \quad \text{Equation 2.21}$$

Another important observation was that the Weibull distribution did not consider the effect of plastic strains on cleavage fracture initiation. Although final fracture was still stress-controlled, the attainment of a necessary critical plastic strain level invalidated Equation 2.19, which did not recognize the effect of plastic strain in the cleavage process. The stress-only description of cleavage inherently implied that all potential nucleators (e.g. carbide microcracks) were created at the onset of plasticity and that their number kept constant with further plastic deformation [43], which did not necessarily correspond to real behaviour.

2.3.3 Microstructure informed brittle fracture (MIBF) model

A microstructurally informed model was developed by Vincent et al. [56]. In their work fracture followed the same assumptions as the Beremin model, i.e. in a representative volume V_0 , micro-cracks initiate for a certain level of plastic strain and then propagate when a local stress reaches a critical value. However, this model is microstructurally informed and can accommodate a heterogeneous stress field.

In particular, the probability to find a maximum principal stress higher than a given value σ_I in one area out of a polycrystalline aggregate submitted to an average maximum principal stress $\langle \sigma_I \rangle$ and an average von Mises stress $\langle \sigma_{MISES} \rangle$, was microstructurally dependent and expressed as shown in Equation 2.22 [56].

$$P(\sigma^* > \sigma_1) = 1 - \exp \left[-\exp \left(-\left(\frac{\sigma_1 - \langle \sigma_1 \rangle}{\alpha_1 \langle \sigma_{Mises} \rangle + \beta_1} + \gamma_1 \right) \right) \right] \quad \text{Equation 2.22}$$

Where $\alpha_1, \beta_1, \gamma_1$ are parameters describing the distributions of the maximum principal stresses (assumed to follow a Gumbull distribution) . These distributions have been produced from microstructural (crystal plasticity) modelling. Even though in this work these parameters are shown for different irradiation conditions, constraint effects from loading conditions can also be expressed with the different values of these parameters.

Following a Griffith type criterion, the fracture stress of a representative volume is given by Equation 2.23.

$$\sigma_f = \sqrt{\lambda \frac{E \gamma_f}{r}} \quad \text{Equation 2.23}$$

Where,

- λ : is a micro-crack shape factor
- E : the Young's modulus
- γ_f : the fracture surface energy and
- r : is the size of the micro-defect which becomes instable (i.e. propagates) under the local stress σ_f

The micro-cracks that cause fracture are mainly produced by the cracking of the carbides. In this work the probability of failure, $P_f(v, \Sigma)$, of a volume v containing 1 carbide under loading Σ , is calculated by integrating the probability density of the carbide size weighted by the probability that the local stress will be higher than the fracture stress. This carbide size distribution is taken from literature. Integrating the carbide sizes amplified the failure probability density beyond what the Beremin model could calculate [56].

Further assuming weakest link theory, i.e. failure of a representative volume is due to the first unstable micro-crack, the failure of a representative volume V_0 is the product of the probabilities of failure of the N number of v elements that V_0 comprises.

Taking this one step further, the probability of failure $P_f(V_p)$, a macroscopic plastic volume V_p which consists of many V_0 volumes can again be calculated with weakest link statistics.

A similar model that incorporated the local approach to fracture, i.e. incorporated the inherent stress heterogeneity was used by Forget et al [57] assuming that stresses and carbide sizes both follow Weibull distributions.

The model was applied to the “Euro Material A” (22 NiMoCr 3 7) data set [58]. The material had a Master Curve reference temperature $T_0 = -91^\circ\text{C}$. The test data that was simulated was selected to have failed by cleavage fracture with a ductile crack extension less than 0.2 mm. Analyses included C(T) tests conducted at lower shelf and lower transition temperatures, with a variety of thicknesses.

For all the different combinations of temperature and thickness, there was very good agreement between experimental and FEA calculated fracture toughness values, with the specimens that showed less ductile tearing having the best agreement regardless of thickness.

One of the most interesting observations of this work is that the MIBF models have such flexibility that they can include several other mechanisms in the probability of fracture calculations such as intergranular failure, competing populations of nucleation sites and extremely rare particles [57].

2.3.4 Wallin, Saario, Törrönen (WST) model

As in previous models described; the work of Wallin et al. [59], [60] assumed that the material in front of the crack contains a distribution of possible cleavage fracture initiation sites i.e. cleavage initiators. The cumulative probability distribution for a single initiator being critical could be expressed as $P_r\{I\}$ and it is a complex function of the initiator size distribution, stress, strain, grain size, temperature, stress and strain rate, etc.

The WST model assumes that the shape and origin of the initiator distribution is not important if a sharp crack is ensured, while local interaction between initiators is permitted and a cluster of cleavage initiations may be required for macroscopic initiation.

It also considers the conditional events of

- A particle failing but not being capable to initiate cleavage because it blunted and formed a void
- An initiated cleavage crack not being able to propagate through the matrix to produce failure (crack arrest)

With the above in mind a probability tree of cleavage fracture is created. Assuming that cleavage fracture process zone is essentially restricted to the region of high tensile stresses and plastic strains and that the self-similarity of the stress field remains unaffected by loading (small scale yielding), a two-dimensional calculation is allowed where a slice through the thickness is representative of the whole volume.

The WST model expresses conditional probability of cleavage initiation $P_r\{I/O\}$ as the integral of the product of the particle failure and survival probabilities to compensate for the previously broken particles which do not contribute to the cleavage. The probability of particle fracture is described by a Weibull expression accounting for particle size and particle stress.

The particle size distribution was formulated so that it was fully described by the average particle size and the shape factor. While for the particle stress, since the particle is elastic and the stress in the particle equals approximately to the product of matrix stress and strain, it is expressed in terms of strain energy density. Hence, the effect of matrix strain is introduced into the new version of the WST model [60] through the particle stress.

As also seen in the three parameter Beremin model the authors here address the scenario of infinitesimal stress intensity factor values leading to a finite failure probability with the incorporation of conditional crack propagation criterion, that introduces a lower limiting K_{min} value, below which cleavage fracture is impossible. This cancels out any non-zero probabilities of failure when loads were very close to zero and addresses the need for propagation in relation to initiation for cleavage fracture to happen. The total cumulative failure probability was expressed as shown in Equation 2.24

$$P_f = 1 - \exp \left[- \frac{B \cdot A}{B_0 \cdot K_0^4} (K_I - K_{min})^4 \right] \quad \text{Equation 2.24}$$

Where:

- K_{min} : the steepest possible stress distribution enabling propagation, calculated under the assumption that a microcrack of size U must have an increasing dK/dU ratio for propagation to be possible.
- A : the propagation probability of a uniform stress state
- B : thickness
- B_0, K_0 : interrelated normalization parameters

This model was applied on a test dataset of C(T) sampled made out of A508 Cl.3 German pressure vessel steel which has been used in various programs [52], [61], [62]. This material was extremely well characterized and allowed for the strain energy density (and thus particle stress), particle size distribution and distance of initiation site from the crack tip to be included in the WST model. Distance of initiation sites in combination with the fracture toughness allowed to express a normalized initiation distance which is needed since the stress and strain distributions in front of the crack scale in a similar way.

Through FEA work the stresses and strains in front of the crack tip were calculated qualitatively. These FEA results were used in the WST model, which was successful in qualitatively predicting the local cleavage initiation probability in front of a crack. Quantitative discrepancies were argued by the authors to be due to uncertainties in the fractography, or to the fact that the cleavage initiation might be controlled by something other than the carbides [59], [60].

2.3.5 James Ford Jivkov (JFJ) model

In the work of James et al. [63] the authors attempted to compare the predictive capabilities between a variety of existing models at a single temperature and proposed a model whose terms will not vary with temperature or constraint levels.

The authors initially argued that the parameters of the Beremin model changed with different temperatures or constraint conditions. This meant that the Weibull fitting parameters (m , σ_u) of the Beremin model, calibrated for geometries with high constraint would not lead to accurate predictions under lower constraint conditions or at higher temperatures. Additionally, it was stated that methodologies that attempt to cross-calibrate these parameters were valid up to temperatures below the reference temperature. This denoted that the link between physics and mechanics did not adequately capture the effects of high levels of plasticity.

This work laid out the basic two assumptions of local approaches, which were:

- The local mechanical fields were defined under the assumption of a macroscopically homogenous material and provided an ‘individual’ probability of failure on each of the micro-crack initiators
- Individual failure events were independent, allowing weakest-link statistic to be applied for calculating the global failure probability

Following these assumption the JFJ model was developed in [63]. JFJ agreed with WST [60] that the probability of failure was based also on the particle size. This was explained considering that larger particles had higher probability of failure than smaller particles under identical mechanical conditions, and the larger particles released more energy when they failed, so were more likely to rupture the surrounding matrix and cause cleavage fracture.

In the developed model principal strains in the intact particle, which were elastic, were set equal to the total principal strains in the surrounding matrix. This together with the plastic incompressibility condition, connected the principal stresses in the particle to the principal stresses and principal plastic strains in the matrix. The principal stresses could then be given in a form that expresses plastic overload on the particle.

For the JFJ model the probability of a particle rupturing was calculated from subtracting the survival probability of a particle from unity. This survival probability was calculated from the energy lost during rapture. It was considered that the survival probability must decrease with increasing work of rupture. The final formulation was dependent on the matrix stresses and strains and thus incorporated the effects of plastic strain and stress triaxiality.

A very interesting concept in this work was to account for the reduction in crack driving force due to plastic dissipation in the matrix (i.e. crack tip blunting) through the definition of an effective critical micro-crack size criterion which incorporated crack tip blunting. This was a developed by modifying the Griffith criterion to include a “fictional”- crack whose size depended on the original microcrack size, and the plastic strains developed. This connection was made under the assumption that the crack opening displacement of the initial microcrack equalled its size multiplied by the plastic strains.

The developed JFJ model was compared with the

- original Weibull model
- modified Beremin allowing for the effect of constraint, improving the ability to apply the model to geometries other than the calibration geometry
- WST model compensating for the particle size and previously broken particles cleavage initiators which do not contribute to the cleavage

- Bordet Model [64], which is another modification of the Beremin model accounting for the effects of strain rate and temperature

The comparison was conducted on data from an RPV 22NiMoCr37 ferritic steel, known as Euro Material A, for which the mechanical and fracture toughness properties at a number of temperatures and irradiation states within the lower shelf and in DBT were available from [58]. Additionally, this material had gone through comprehensive metallographic examination which provided the number density of carbides and allowed a fit for the probability density of particle sizes. The test specimens that were included from this dataset and modelled in the work of JFJ regarded Charpy V notch (PCCV) specimens in three-point bending.

In general, all the models compared showed little difference between them and the cleavage fracture predictions they made were in good agreement with experimental data.

Regarding calibration of the models, the Weibull model was the simplest as it requires calibration of three individual terms. The JFJ model along with the WST model required calibration only of two microstructurally informed values, i.e. rupture energy density scale and surface energy value. While the remaining two models required calibration of multiple parameters which did not relate to measurable values and couldn't easily be taken from experimental results or literature

It should be noted that the JFJ model required a simple set of experimental data for calibration: size distribution and density of the cleavage initiating particles from metallography and a limited range of positions of cleavage initiation sites from fractography. Furthermore, even though calibration was performed at a single temperature the JFJ model results showed good agreement with experimental data at a range of different irradiation and constraint conditions and any change in toughness calculations arose only from the changing deformation properties.

2.3.6 Seal and Sherry model

The work of Seal and Sherry [65] attempted to combine the D&A scaling model with the Beremin modified Rice and Tracey [66] model to predict the benefit of constraint loss to fracture toughness.

The Rice and Tracey [66] model predicted that void growth is a function of the stress state and plastic strain increment, while it assumed that critical void size is a material property.

The need to know this property was a drawback for its application to a variety of materials, however the authors argued that this could be overcome by using an equivalent scaling method to the Anderson and Dodds method but this time including contours of equal void growth ratios, i.e. Rice and Tracey contours. It was argued that if the areas defined by different Rice and Tracey contours could be shown to scale proportionally in both the low and high constraint cases, then the ratio of the effective fracture toughness for a low constraint structure to the high constraint toughness would be independent of the Rice and Tracey parameter chosen.

Using an MBL model multiple parametric studies describing different constraint states were run. These models considered a variety of materials, that represent a wide range of ferritic steels. The models were run for a combination of applied K and T -stress, several areas enclosed by iso-stress and iso-Rice and Tracey contours. For the D&A parameters the area enclosed by iso-stress contour for the small-scale yielding was determined from the $T=0$ analyses while for the actual constraint level from each of the T -stresses in the range tested and allowed the calculation of the benefit to fracture toughness. This in turn allowed parametrization of the benefit in α and k terms as they are used in BS7910 and R6 described later in Section 2.5. The validity window of the results was expressed in terms of the size of the plastic zone being smaller than $1/5$ of the radius of the model.

The predicted benefit to ductile initiation fracture toughness from the use of different Rice and Tracey parameter contours was independent of the choice of critical Rice and Tracey parameter and was argued that the benefit to ductile initiation fracture toughness could be predicted from any sensible Rice and Tracey parameter, thus eliminating the need to determine the critical value for the individual steel of interest. However, the iso-Rice and Tracey contours showed loading path dependence which and was argued that this was expected since the presence of a hydrostatic stress field accelerates the growth of voids. In light of this the benefit on ductile fracture predicted by the α, k values shown here should be used only indicatively.

Comparing against three point bend data from literature [67]–[69] the model developed by Seal and Sherry [65] showed good promise for predicting the influence of constraint on both cleavage and ductile initiation fracture toughness.

2.4 Background to ECAs

An ECA is represented graphically with the use of the Failure Assessment Diagram (FAD). This consists of a failure assessment line (FAL) and the assessment point of the component analysed. The FAL divides the diagram into two zones, i.e. underneath/inside the FAL and outside the FAL. The zone inside is considered as the “acceptable/safe region” while the one outside is the “unacceptable/potentially unsafe region”. Depending on where the assessment point lies, the flaw is deemed as acceptable, i.e. the component can withstand the loading conditions modelled, or unacceptable, i.e. its integrity cannot be guaranteed. A graphical representation of a FAD can be found in Figure 2.7.

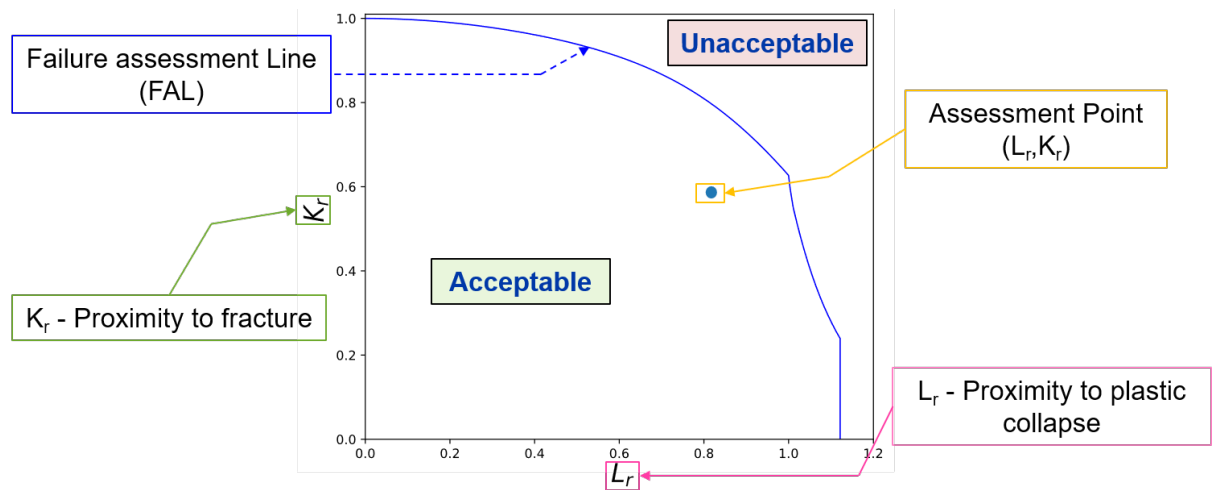


Figure 2.7: Graphical presentation of an ECA

There are three assessment options (Option 1 – 3); with increasing option number the FAL is more accurate and less conservative but requires a higher amount of information for its calculation. The easiest to conduct are Option 1 assessments due to the limited data required. The Option 1 FAL requires knowledge of the yield stress (σ_y) and tensile strength (σ_{UTS}) of the material as well as its yielding behaviour (continuous/discontinuous yielding), i.e. whether a Luders strain is included in the tensile curve. The latter isn't important when large complex deformations happen while it shows a higher effect on smaller (test specimens). In many cases where σ_y , σ_{UTS} are not available at the test/operating temperature, they are determined following the guidance the standard

provides for calculation of the tensile properties at different temperatures, for BS 7910 this is included in clause 7.1.3.4 [1] background for this clause is provided in [70].

The assessment point is plotted with an abscissa designated L_r , considered as proximity to plastic collapse, and an ordinate of K_r , proximity to fracture. L_r is cut-off at the average between the yield and UTS stresses (L_r^{\max}), while yield discontinuity should be included as the standard advises in accordance to tensile properties.

For BS 7910 assessments, their values are calculated from the following equations,

$$L_r = \frac{\sigma_{ref}}{\sigma_y} \quad \text{Equation 2.25}$$

$$K_r = \frac{K_I^p + K_I^s}{K_{mat}} + \rho \quad \text{Equation 2.26}$$

Where:

- σ_{ref} : the reference stress calculated in accordance with BS 7910:2019 (Annex P)
- K_I^p, K_I^s : the elastic stress intensity factor at the current crack size due to primary and secondary stresses respectively, calculated in accordance with BS 7910:2019 (Annex M)
- ρ : a function of primary and secondary loads that account for plasticity interaction effects, calculated according to BS 7910:2019 (Annex R), this approach has been amended in later versions of R6
- K_{mat} : the ‘characteristic’ (i.e. lower bound) fracture toughness. This is given directly in terms of a critical stress intensity factor (MPa√m), or J-integral (kJ/m²) value converted to stress intensity factor (K_J); in many cases it is estimated from Charpy measurements (J), using the guidance of BS 7910:2019 (Annex J)

In some cases, where the material of the tested specimen exhibits tearing under increasing load, resistance curves (R-curve) can be used. In these instances, various amounts of ductile tearing are postulated (from 0.2 to 2 mm) and L_r and K_r are calculated at different flaw sizes equivalent to the initial flaw length plus the postulated amount of crack growth. The fracture ratio (K_r) is calculated using an enhanced K_{mat} which corresponds to the postulated amount of tearing. This results to each specimen having a series of L_r , K_r value pairs as a function of increasing flaw size. These are plotted on the FAD as a line consisting of the locus of the assessment points that derive from the different flaw lengths. An example of what an assessment

including ductile tearing resistance (R-curve) looks like is given in Figure 2.8, where the locus of assessment points lies in the unsafe zone of the FAD.

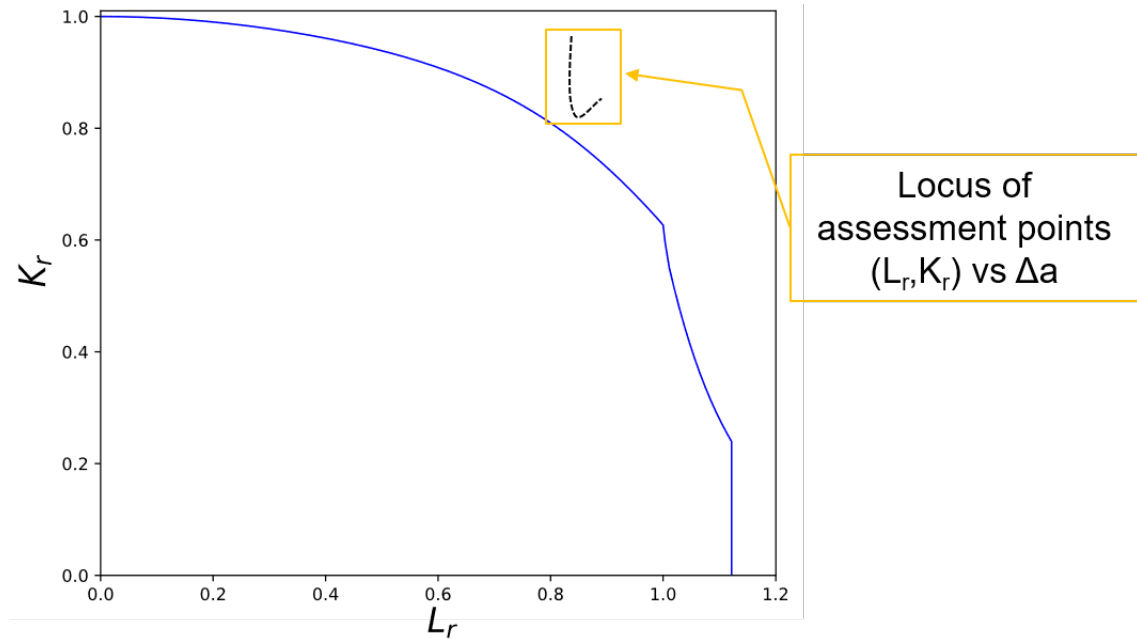


Figure 2.8: Example of tearing resistance (R-curve) assessment

If there is no conservatism and the assessment methodology is representative, then the distribution of failure will equally straddle the FAL for a 50% toughness value (when using mean tensile properties etc) but should then be mostly outside the FAD when using a 5% toughness (but mean properties) and would be expected to be fully outside if using lower bound properties and lower bound toughness. Hence, a completely accurate assessment of a specimen whose failure is certain would have the assessment point lying outside of the FAL, at a distance relative to the estimate of fracture toughness used.

In order to estimate the conservatism of the assessment a line is drawn between the start of the axes and the assessment point, as shown in Figure 2.9, then the modelling error is calculated as the ratio of the distance from the start of the axes to the assessment point, divided by the distance from the start of the axes to where the line meets the FAL, distance OB to OA in Figure 2.9. It is worth noting that this definition of modelling error encapsulates secondary stresses in K_r but due to relaxation point B could potentially not be aligned to the original angle from the origin. This is not of concern in this collection of experimental data since all but three specimens experienced secondary stresses. Additionally, the vast majority of specimens have been loaded to high values of L_r where the secondary stresses would have been washed out by the plasticity developed.

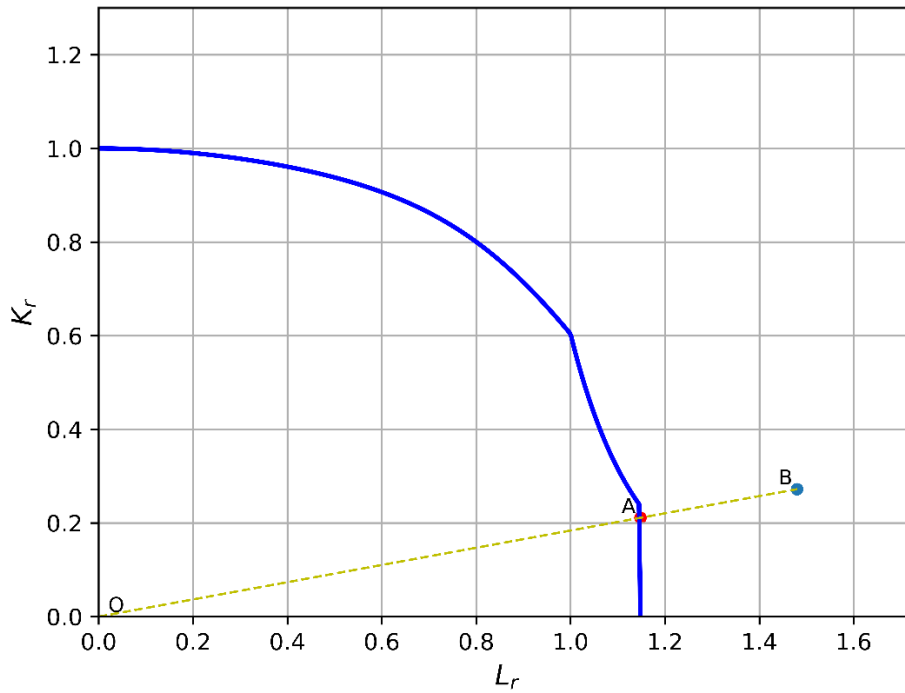


Figure 2.9: Modelling error in ECAs

2.5 Biaxiality in ECAs

2.5.1 Biaxiality in BS7910

Biaxiality and its effects are at the stage of this work not incorporated in the reference stress solutions and stress intensity factors, of BS 7910 [71]. However, the standard has a clause (Annex N) which deals with constraint effects. Since the fracture toughness values used in the assessments, defined in Section 2.4, are already a conservative lower bound from the measured values³, Annex N provides guidance on exploiting the increased fracture toughness values, due to the relaxation of constraint, for the assessment of a structure. The level of constraint in the structure is expressed with either the elastic T-stress, recommended for $L_r \leq 1$, or the hydrostatic parameter Q , generally recommended for $L_r > 1$. It should be noted that small-scale yielding effects can have a significant impact on plasticity at the crack-tip are typically seen for $0.6 < L_r < 1$ and Q could be used from lower values than 1 of L_r . Whichever parameter is adopted for the expression of constraint

³ fracture toughness values are measured with deeply cracked bend specimens designed to ensure high constraint conditions and can be treated as lower bound material property

is then translated to a structural constraint parameter designated as β , with the formulae in Equation 2.27.

$$\left\{ \begin{array}{l} \beta = \frac{T}{L_r \sigma_y}, \text{ when calculated with the T-stress} \\ \beta = \frac{Q}{L_r}, \text{ when calculated with the Q parameter} \end{array} \right\} \quad \text{Equation 2.27}$$

BS 7910 offers a compendium of β solutions, together with the reference stress solutions used for their calculation. Concerning biaxiality, only a single reference stress- β solution in this compendium relates to biaxial loading (of a centre-cracked plate). In addition, it is not clear from the procedure whether the reference stress solutions used for the calculation of β should also be used for the calculation of the L_r abscissa of the assessment point. This is a current issue being researched and is discussed in the later paragraphs.

Moving forward, once β was calculated it can be used for estimating the constraint related fracture toughness (K_{mat}^c) in three ways, namely

- Using material constraint parameters α and k
- Using the Master Curve transition temperature
- Using low constraint testing which corresponds to the structure's level of βL_r

From the three ways of measuring K_{mat}^c the standard focuses mostly on the first, i.e. using α and k . These parameters can be either calculated or invoked directly from tables included in the standard. The values presented in tabular form derive from the work done by Sherry et al. [72], [73] within the framework of VOCALIST [45]. Sherry et al. with the aid of FEA and the Weibull cleavage fracture model, produced K_{mat}^c/K_{mat} —constraint ($T/\sigma_0, Q$) points, where the probability of cleavage failure would remain the same between different levels of constraint. It was observed from the results that fracture toughness ratios (K_{mat}^c/K_{mat}) between two different constraint levels were approximately the same for any probability of cleavage failure. This effectively meant that fracture toughness ratio (K_{mat}^c/K_{mat}) — constraint points could be bounded from below with the same curve regardless of the cleavage failure probability.

In this direction, lower bound curves in the form of Equation 2.28, were created as a function of the parameters α and k , for a range of

- E/σ_y
- Hardening coefficients (n)

- Weibull parameters m

$$\left\{ \begin{array}{ll} K_{\text{mat}}^c = K_{\text{mat}} \left[1 + \alpha(-T/\sigma_y)^k \right], & T/\sigma_y < 0 \text{ when calculated with the T-stress} \\ K_{\text{mat}}^c = K_{\text{mat}} \left[1 + \alpha(-Q)^k \right], & Q < 0 \text{ when calculated with Q parameter} \end{array} \right\} \quad \begin{array}{l} \text{Equation} \\ \mathbf{2.28} \end{array}$$

With the use of this method, the increased fracture toughness can be applied to the assessment with two ways, namely

- Modification to the FAD, i.e. for $\beta < 0$ the FAL has the form:

$$K_r = f(L_r) \left[1 + \alpha(-\beta L_r)^k \right]$$

- Modification to K_r , where the denominator changes from K_{mat} to K_{mat}^c

Overall, the influence of constraint relaxation included in the standards is,

1. in the cleavage/brittle regime: fracture toughness increases with decreasing constraint (as βL_r became more negative)
2. in the ductile regime: the magnitude of the constraint effect on ductile tearing initiation depends on the yield and strain hardening of the material in question while after crack growth the fracture toughness increases with decreasing (more negative βL_r) constraint
3. in the transition region: as constraint decreases the transition curve shifts towards lower temperatures

2.5.2 Biaxiality in R6

BS 7910 [71] and R6 [3] use the same underlying method to account for constraint effects, and consequently biaxiality. The integration of constraint in an assessment with R6, follows the same steps as in BS 7910. The former provides guidance on incorporating constraint in Section III.7, where the calculation steps are described, while the compendium of β solutions and the reference stresses used for their calculation are included in Section IV.5. It should be noted that R6 states directly that “the particular value of β required for application of Section III.7 should use the same limit load as that used in the determination of L_r ” [3]. Additionally, it is advised in cases that no limit load/reference stress solution are provided for the calculation of the constraint development (β) for a particular geometry, one of the available β solutions of Section IV.5

should be calculated with the use of its respective reference stress solution and scaled with the ratio of the reference stress solution used to calculate β to the reference stress solution (limit load in R6) used for the assessment of the specific geometry. The approach described is for primary loads and this differs slightly in BS7910 when adding the contribution from secondary stresses.

2.5.3 Biaxiality and plastic collapse

Even though biaxiality is an important factor in the fracture dominated zone, many structures, such as offshore pipelines carrying hot fluid under a combination of high internal pressure and axial strain, experience biaxial loads whilst in the collapse dominated area. Procedures deal with the effect of biaxiality mostly in the context of fracture toughness variation due to changes in constraint, however, do not explicitly address the effect of biaxial loading on the reference stress/limit load solutions.

Experimental evidence showing biaxiality effects on the upper shelf-collapse dominated zone are available in the literature [7], [8], [16]. The data strongly suggests a connection between differences in limit load/strain capacity/plasticity flow and biaxiality.

Researchers have put effort towards producing reference stress/limit load solutions, for a variety of geometries and crack configurations, which incorporate biaxiality and its consequent effects on the load bearing capability of the structure/component. This effect can be important in reducing conservatism in high plasticity situations.

Such an analyses can be found in the work by Meek and Ainsworth [74], who studied the effects of biaxial loads on the limit load of a centre cracked plate under plane strain conditions. Using lower and upper bound solutions^{4,5}, as well as FE analyses, they produced limit load solutions and concluded that accurate estimates of limit load enable accurate estimates of J under biaxial loading. These solutions are used later in this chapter for assessing fracture test data.

In pursuit of evaluating the J-integral values on a surface cracked plate under biaxial loading, Miura and Takahashi [75], proposed the use of the “extended reference stress

⁴ Lower Bound Limit Load solutions are generated by the assumption of a stress distribution which satisfies equilibrium

⁵ Upper Bound Limit Load solutions are generated by the assumption of a deformational pattern which equates internal and external work

method”. Their method was based on the accurate evaluation of the reference stress/limit load of a geometry under uniaxial loading and the multiplication of the uniaxial-load with a factor which connects the yielding between uniaxial and biaxial loads based on the Von Mises yielding criterion (a hypothesis defining the limit of elasticity in a material and the onset of plastic deformation).

Using the Von Mises yielding criterion, Lei and Budden [76], studied how the combination of biaxial and cross-thickness bending affects the net collapse limit loads of surface cracked plates. Ignoring stress concentration near the crack tip region, they studied a rectangular section including a rectangular crack. They provided different solutions according to:

- Stress distribution: two distributions were studied, the first had the maximum - tensile stress perpendicular to the crack, being applied in the front part of the crack ligament while the second had the minimum - compressive stress at the front part
- Crack geometry: a crack located wholly in one stress zone was designated as “shallow crack” if it crosses both stress zones it was designated as a “deep crack”. Hence, even though crack depth in this study won’t affect stress concentration, which is not considered, it still is an important factor that will affect the position of the neutral axis and the choice of solution

Relating to plates with surface cracks under biaxial loading, the work of Madia et al. [77], focused on the load bearing capacity of a plate with a semi elliptical crack. The capacity was studied in terms of the “reference yield stress”, which acts as a limit load, translated to stress and corresponds to an L_r value of 1. Reference yield stress solutions were given for the deepest and the near surface points of the crack and for bending, uniaxial and biaxial loads. In the case of the latter loading, solutions using maximum principal or equivalent (Von Mises) stress were generated.

Additional work by Lei et al. [78], [79] focused on the effect of the combination of internal pressure, axial forces and bending moments on the limit loads of thick cylinders with circumferential flaws. The analysis follows the same principle and criteria as in [76], with the minor differences regarding crack face contact. Lei et al. produce different solutions according to the stress distribution and the positioning of the crack regarding the stress field.

2.6 Summary

The preceding sections have given a chronological picture of how biaxiality was accounted for in the failure mode and fracture toughness values and how current FFS standards address this. Whilst such effects were initially disregarded under the assumption of linear elasticity, that changed over time with the introduction of a second parameter in the stress functions calculating the crack tip fields, that addressed non-linear material deformation. These parameters quantified the concept of constraint, the suppression of plasticity around the crack tip, imposed by different temperature, geometric and loading conditions.

Building on the two parameter fracture mechanics, multiple methods were developed attempting to predict fracture toughness values in relation to constraint, by connecting the local crack behaviour to the macroscopically applied loads. Methods focusing on cleavage fracture firstly assumed that the material in front of the crack contains a distribution of possible cleavage fracture initiation sites, i.e. cleavage initiators and the probability of finding a triggering microfeature ahead was related to the volume of the zone in front of the crack where the stress exceeded a limiting value. Additionally, the fraction of the volume was treated as statistically independent from the rest and the overall probability of failure was defined as the aggregation of the probability of each of the volume fractions allowing for weakest link statistics. Overall, a variety of statistical and mathematical tools were invoked to describe the probability of finding a micromechanical feature capable of being a cleavage initiator, as well as the critical stress needed stress needed to initiate crack.

Most methods were calibrated against C(T) and three-point bend test datasets to quantify/predict out of plane and shallow flaw effects on constraint. Even though, these methods showed great promise, at the time of writing, such methods have not yet been applied to experimental datasets that solely focus on biaxiality.

The current capability of the ECA procedures is quite fundamental and requires knowing the sensitivity of fracture toughness with constraint. This is translated in a need for a wide variety of tests to be conducted. Another drawback is that the available structural parameter β (T-stress) solutions in the standards refer to limited geometries and loading conditions and in the case of biaxial loading they do not differentiate shallow flaw effects and biaxiality.

Considering the above, it is important to create a consistent biaxiality centred experimental database on which failure prediction models could be applied. Such a database that decouples shallow flaw effects from biaxiality does not yet exist and has thus not been used by any of the models described here. Implementing failure prediction models on such data could allow biaxiality to be included separately from shallow flaws in ECAs without requiring lots of experiments.

Chapter 3 Analysis of existing experiments

3.1 Introduction

To decide on the focus of the work, this chapter studies the current, at the time of writing, capabilities of the Fitness for Service standards (FFS) in assessing biaxiality. FFS Procedures, like BS 7910 [1] and R6 [3] are built upon sound fracture mechanics principles and engineering data, and have been implemented by the engineering community for many decades. They provide guidance on conducting Engineering Critical Assessments (ECAs) for purposes ranging from defect-tolerant design to life extension of safety-sensitive components.

Firstly, an exercise, where ECAs with BS 7910 are conducted on hundreds of fracture tests including wide plate and cylindrical geometries with different levels of biaxiality. This exercise, is conducted to validate the safety and accuracy of the standards, providing advice to the procedure where applicable and secondly to recognize any trend between the assessment results of uniaxially loaded wide plates and biaxially loaded pipes.

Subsequently, the analyses conducted on specimens from an experimental program conducted within TWI are presented. These analyses include a combination of FEA, with

analytical solutions to check the usability and robustness of the standards' constraint specific clauses. The biaxiality ratios in these analyses vary from $k=0$ to $k=2$.

3.2 Application of BS 7910 on historical data

3.2.1 Introduction

The aim of this exercise was, firstly to update cases concerning full scale tests which had been studied in the past with earlier versions of BS 7910 [80]–[83], and check the soundness of the latest, at the time, version [71], as well as to investigate whether structures that experience different biaxial loadings could reveal a trend when analysed with the basic option of BS 7910 and how such loading conditions should be incorporated in the analyses, which is one of the aspects of validation not hitherto considered in any detail.

The formulae used for the necessary calculations during an ECA can vary in terms of accuracy between different procedures and especially when considering the wide variety of applications that each of them must cover. To ensure that the FFS procedures can provide acceptable results in all these different applications they need to be validated regularly. Validation is achieved by applying them in situations in which the failure conditions are known. For example, a large-scale test, in which the loading history, geometric parameters and mechanical properties, are known, could be used. Assessments of such tests with the use of an FFS procedure demonstrate if it is reliable and can help trace potential inadequacies or room for improvement.

Validation is therefore an important tool that is applied to standards to improve their existing accuracy and to safely incorporate new additions to them, e.g. consideration of the effect of constraint on failure [84]. Validation against experimental data ensures that standards encapsulate best practice that's calibrated to real cases, nevertheless validation is often done using FEA [85], [86] or a combination of FEA and experiments [87].

Experimental validation work for FFS standards is very limited in the public domain. Even though updated versions of standards are usually followed by overview papers explaining the newest alterations [88]–[93], widely used standards like R6 [3] (Chapter V). In the cases where information is included in other sources these are usually in bulletins/reports [80], [94], [95] and not in the public domain.

To update the limited experimental validation data available in the public domain, to evaluate the accuracy of the procedure and to recognize trends in regard to biaxiality, a validation exercise of BS 7910, including analysis of several hundred large-scale fracture tests from the literature, has been conducted.

The exercise was initially carried out with the use of the 2013 version of the standard [71], which was the most recent at the time, while all assessments in this study are Option 1 assessments, as explained in detail in Section 2.4.

An important result of the analyses with 2013 version was to investigate an aspect for modification for the newest version (2019) of BS 7910 [1]. This concerned the proximity to plastic collapse (L_r) of a pipe (or curved shell) containing an axial flaw, either surface-breaking or through thickness. Namely, the reference stress solutions used for the calculation of L_r were found to be overconservative, due to a multiplication factor. As explained in [96], this factor provides added conservatism thus not being necessary for a safe assessment and has been omitted in the 2019 version of BS 7910 [1]. Detailed assessments with and without this factor can be found in Appendix 1 of the report that contains all original assessments [97].

This exercise focused on the stress based assessment of full scale tests on plates as well as pressure vessels and pipelines (cylinders/curved shells), some of which have been studied in the past with earlier versions of BS 7910 [80]–[83]. For the cases that have been assessed in previous work, all original sources mentioned were assessed directly and reanalysed when possible, while where the original reports were not available the data was selected from previous validation work [82], [83], [98].

In pursuit of conciseness an overview of the work conducted is presented in this chapter, whilst the Appendix 1 of the TWI member report [97] with all the detailed analyses is available upon request in case the reader required further details.

3.2.2 Background to analyses

The geometries studied in this exercise were wide plates and closed cylinders/pipes, the latter experiencing different loadings (tensile, pressure, bending) and thus biaxiality ratios ranging from $k=0$ to $k=2$. Table 3.1 includes the subclauses of the annexes the reference stress and stress intensity factor solutions were obtained from, while further information concerning the origin of the solutions can be found in [99]. In Table 3.1 “closed cylinders”

refers to the geometry of pipes/closed cylinders (i.e. cylindrical pressure vessels), while curved shells to flat plates with curvature. It should be noted that several of the tested pipes had geometrical features which exceeded the validity margins of the stress intensity factor solutions for closed cylinders and were assessed as curved shells.

Table 3.1: Reference stress and Stress intensity factor solutions used for the assessments.

| Component Geometry | Flaw Geometry | | Reference Stress Solution | Stress Intensity Factor solution |
|--------------------|---------------------------------------|-------------------------|---------------------------|----------------------------------|
| Wide Plate | Surface Cracked Tension (SCT) | | P.5.1 | M.4.1 |
| | Centre Cracked Tension (CCT) | | P.4.1 | M.3.1 |
| | Extended Surface Crack Tension (ESCT) | | P.5.2 | M.4.3 |
| Closed Cylinder | Axial Flaws | External Surface (AES) | P.8.4 | M.7.2.4 |
| | | Through Thickness (ATT) | P.8.1 | M.7.2.1 |
| | Circumferential Flaws | External Surface (CES) | P.9.4 | M.7.3.4 |
| | | Through Thickness (CTT) | P.9.1 | M.7.3.1 |
| Curved Shell | Axial Flaws | Internal Surface (AIS) | P.8.2 | M.6 |
| | | External Surface (AES) | P.8.4 | M.6 |
| | Circumferential Flaws | Internal Surface (CIS) | P.9.2 | M.6 |

Concerning the reference stress solutions used for the assessment of axially flawed cylinders or curved shells (Clause P.8.1, P.8.2, P.8.4), the 2013 version of BS 7910 included a multiplication factor of 1.2 on the membrane stresses. As explained in [96], this factor is empirical and was most likely transferred as a measure of consistency from plate solutions where it was initially used. It provides added conservatism thus not being necessary for a safe assessment and is omitted in the 2019 version and here from the reference stress solutions implemented in the analyses of axially flawed cylindrical geometries. Detailed assessments with and without this factor can be found in [97].

Regarding tensile properties they were in many cases given at room temperature rather than the temperatures at which the specimens were tested. BS 7910 (Clause 7.1.3.4) provided guidance for the estimation of the properties at the correct temperatures and was used as follows.

- For tests conducted above room temperature the yield stress de-rating graph shown in Figure 3.1 combined with the yield stress to ultimate tensile strength ratio were used to calculate the corresponding properties. This is considered as a safe

assumption in high temperatures given the materials in this study it does not however fully mirror reality

- For tests conducted below room temperature the yield stress and ultimate tensile strength were translated from the room temperature properties using Equation 3.1 and Equation 3.2 respectively

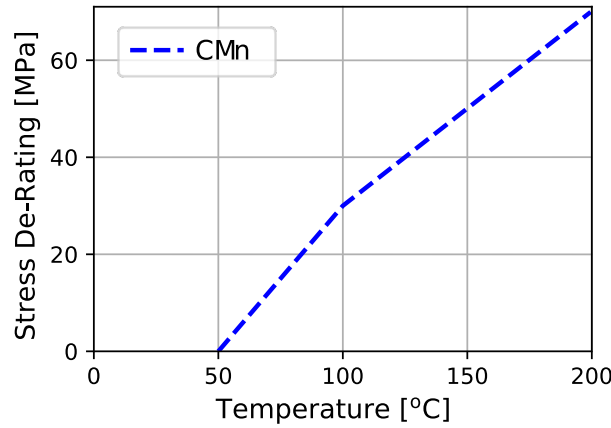


Figure 3.1: Yield Stress De-rating for C-Mn Steels. Adapted from [1, Fig. 7.10]

$$\sigma_y (\text{Test temperature}) = \sigma_y (\text{room temperature}) + \frac{10^5}{(491 + 1.8T)} - 189 \quad \text{Equation 3.1}$$

$$\sigma_{UTS} (\text{Test Temperature}) = \sigma_{UTS} (\text{room temperature}) \times \left(0.7857 + 0.2423 \exp \left(-\frac{T}{170.646} \right) \right) \quad \text{Equation 3.2}$$

Where T was the temperature (in °C) at which the properties were calculated. This guidance is of empirical nature and supporting evidence for its origin and validity are given in [70].

Some of the original reports of the axially flawed pipes provided Charpy impact test values rather than valid fracture toughness measurements. A conservative estimate of K_{mat} can be calculated from Charpy measurements with the use of Annex J, where equations based on the empirical correlation of the two are given. The equations used from the annex in this study are given here as Equation 3.3 and Equation 3.4, while background for these can be found in [70] and [100]. The latter was used for low sulphur steels on the upper shelf and provided a fracture toughness estimate at 0.2mm of ductile crack extension, thus calculating $K_{mat0.2}$.

$$K_{mat} = 0.54C_v + 55 \quad \text{Equation 3.3}$$

$$K_{mat0.2} = K_{J0.2} = \sqrt{\frac{E(0.53C_{Vus}^{1.28})(0.2^{0.133}C_{Vus}^{0.256})}{1000(1 - \nu^2)}} \quad \text{Equation 3.4}$$

Where C_v was the lower bound Charpy V-notch impact energy at the temperature for which K_{mat} was calculated, C_{Vus} was the upper shelf energy.

In the cases where residual stresses were included, these were treated according to the guidance of BS7910 (Clause 7.1.10). In five analyses, where there were enough information available, non-uniform residual stress profiles were included with the use of the annex that provided guidance on residual stress profiles for assessing flaws in as-welded joints (Annex Q). The rest of the welded specimens were studied assuming a uniform stress profile. For the as-welded specimens, the residual stresses were calculated with Equation 3.5, while for the post-weld heat-treated (PWHT) they were estimated with respect to flaw orientation and heat treatment parameters from Clause 7.1.10.3, which dealt with residual stresses of PWHT structures. Further explanation of the guidance the standard provided on residual stresses can be found in [101].

$$Q_m = \min \left[\sigma'_Y, \left(1.4 - \frac{\sigma_{ref}}{\sigma'_f} \right) \sigma'_Y \right] \quad \text{Equation 3.5}$$

Where Q_m was the membrane residual stress, σ'_Y and σ'_f were the yield stress and flow strength of the parent material respectively and σ_{ref} was the calculated reference stress.

The current exercise validated all the above parameters that were calculated during ECA as well as their synergy with each other. It is worth noting that this exercise shows the validity of the procedure and builds confidence in using it, however, it is expected that the conservative estimation of many of the parameters (e.g. Charpy fracture toughness) can dominate the outcome. More detailed and accurate assessments would require better material characterization testing and fracture testing, which is not available for the steels studied here and did not allow for Option 2/3 assessments to be made.

3.2.3 Tests analysed

The assessments in this study have been conducted on wide plates and closed cylinders from a variety of steels. All the wide plates were loaded in tension. The cylinders were in most cases closed with end caps and loaded under internal pressure, while in other cases

had tensile or bending loads applied. The flaw geometries included in the study consist of surface breaking flaws and through thickness flaws. A schematic of the wide plate test geometries can be found in Figure 3.2, while the cylinder flaw geometries are shown in Figure 3.3.

Wide plates and cylinders under tension were considered uniaxially loaded with a biaxiality ratio of $k=0$. Cylindrical geometries with circumferential flaws and axial flaws loaded only with pressure had biaxiality ratios of $k=2$ and $k=0.5$ accordingly, while when bending was also applied with pressure k was between 0 and 0.5.

Each test analysed has been given an ID which is in line with the overall validation exercise conducted within TWI. A summary of the tests analysed and their respective IDs, is shown in Table 3.2, where the tests have been categorized by specimen geometry and source from which their data was gathered. The test data was collected from the original reports, where possible, while for some cases for which the reports could not be retrieved, it was taken as reported in previous validation work [3],[4],[98].

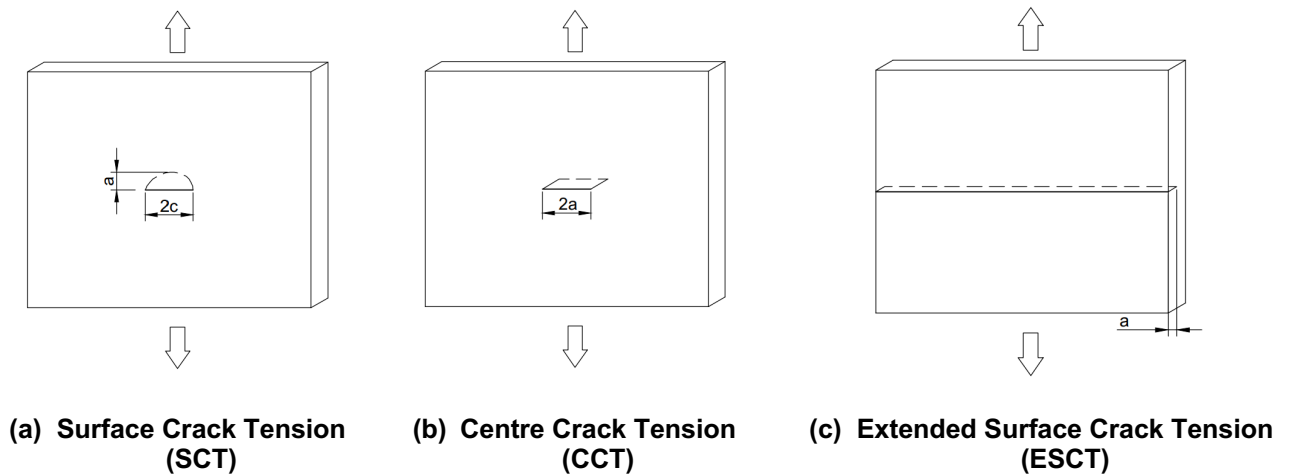


Figure 3.2: Wide Plate Tests Geometry

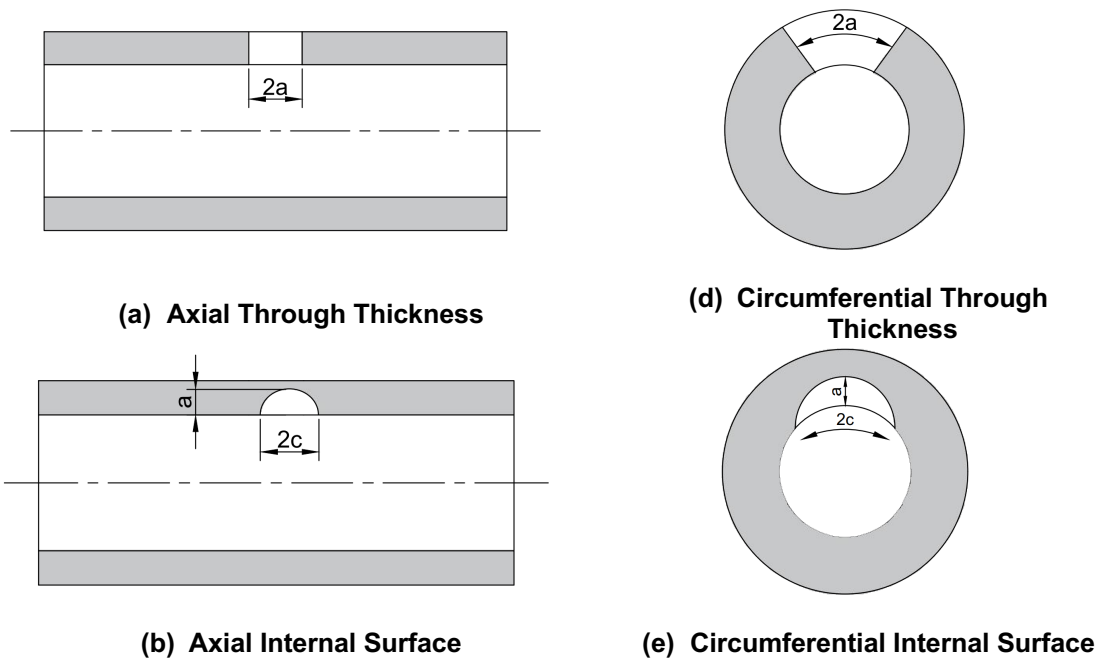
Overall, there were 212 tests included in the analyses. Thirty-seven (37) of the tests concerned wide plates while the rest of the specimens (175) were of cylindrical geometry.

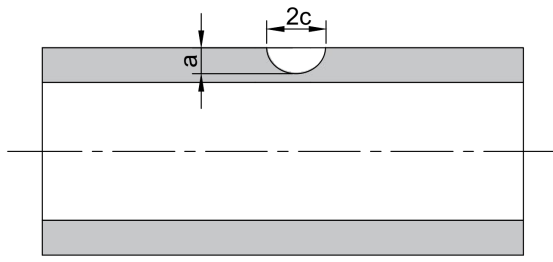
In some cases, the geometry of the pipe laid outside the geometrical limits of K solutions for cylinders, given in BS 7910. These limits concern either the component or flaw dimensions and margins vary according to flaw orientation. In these cases, curved shell solutions were used instead. For each flaw geometry and respective cylinder equation, the

limiting validity parameters and the specimens which did not comply with the margins along with the parameter value of these specimens are shown in Table 3.3, where B and r_i refer to the thickness and the internal radius of the specimens respectively. Oriented per ID and reference, Table 3.4 includes the cylindrical specimens which were assessed as curved shells.

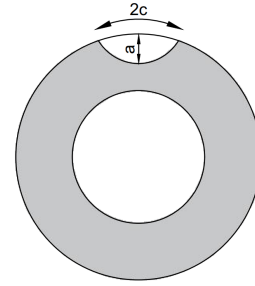
It should be noted that, out of the 37 wide plate tests analysed, 12 did not reach failure during testing and one was not certain to have failed, however they have been included in the analyses.

Further details about each set of tests examined including, their material, geometric properties and loading conditions, as well as the interpretation and implementation of this data is given in the member report [97] where all the original assessments are included. It is pointed out that the original report includes data that would have been more properly analysed with the newest addition of Annex V of the standard that includes a strain-based assessment technique. Given that this exercise was initially done with the 2013 version that data has been filtered out here. This filtering has excluded all specimens whose applied stress to yield stress ratio was higher than 1.1.





(c) Axial External Surface



(f) Circumferential External Surface

Figure 3.3: Flaw geometries for cylindrical specimens

Table 3.2: Tests analysed

| Specimen Geometry | Reference | ID | Flaw Geometry | No. of Specimens Analysed |
|-------------------|-------------|------------------------|-----------------------------------|---------------------------|
| Wide Plate | [102] | 302-306 | SCT | 1 |
| | | | CCT | 2 |
| | | | ESCT | 2 |
| | [103]-[106] | 702-716 | SCT | 6 |
| Closed Cylinder | [107] | 2507-2548 | SCT | 24 |
| | [108]-[110] | 721-728 | Axial-External Surface | 8 |
| | [83] | 1001-1003 | Axial-External Surface | 3 |
| | | | Axial-Internal Surface | 2 |
| | [83] | 1101-1107 | Axial-External Surface | 3 |
| | | | Axial-Internal Surface | 2 |
| | | | Axial-Through thickness | 1 |
| | [111] | 1201-1212 | Axial-Through thickness | 12 |
| | [112] | 1501-1503 | Axial-External Surface | 3 |
| | [113] | 1601-1604 | Axial-External Surface | 4 |
| | [102] | 2101-2102 | Axial-External Surface | 1 |
| | | | Axial-Through thickness | 1 |
| | [114] | 2103-2114 | Axial-External Surface | 7 |
| | | | Axial-Internal Surface | 1 |
| | | | Axial-Through thickness | 4 |
| | | 2116-2133 | Circumferential-External Surface | 6 |
| | | | Circumferential-Internal Surface | 1 |
| | | | Circumferential-Through Thickness | 3 |
| | [115] | 2201-2292 2301-2345 | Axial-Through thickness | 88 |
| | | | Axial-External Surface | 33 |

Table 3.3: Validity limiting parameters of BS 7910 solutions for cylindrical geometries, specimens which exceed them and their parameter values

| Flaw geometry | Cylinder Equation | Limiting parameter | Parameter value | Specimens exceeding limits |
|----------------------------------|-------------------|---------------------------|-----------------|--|
| Axial-External Surface | M.7.2.4 | $0.1 \leq B/ri \leq 0.25$ | 0.02-0.08 | 722-728, 1501-1503, 1601-1604, 2101, 2301-2345 |
| | | $a/B \leq 0.8$ | 0.80-0.81 | 2106, 2112, 2114 |
| | | $0.05 \leq a/c \leq 1$ | ≈ 0.048 | 2107, 2108, 2110 |
| Axial-Internal Surface | M.7.2.2 | $a/B \leq 0.8$ | 0.81 | 2109 |
| Circumferential-Internal Surface | M.7.3.2 | $0.1 \leq a/c \leq 1$ | 0.05 | 2125 |

Table 3.4: Cylinders assessed as Curved Shells

| ID | Reference | Flaw Geometry | Specimens Analysed |
|-----------------------------|-------------|----------------------------------|--------------------|
| 722-728 | [108]–[110] | Axial-External Surface | 7 |
| 1501-1503 | [112] | Axial-External Surface | 3 |
| 1601-1604 | [113] | Axial-External Surface | 4 |
| 2301-2345 | [115] | Axial-External Surface | 33 |
| 2101 | [102] | Axial-External Surface | 1 |
| 2106-2108, 2110, 2112, 2114 | [114] | Axial-External Surface | 6 |
| 2109 | | Axial-Internal Surface | 1 |
| 2125 | | Circumferential-Internal Surface | 1 |

3.2.4 Results

The following sections contain the results from all 212 analyses. They are divided in two categories according to the component geometry, i.e. wide plates and cylinders. Each category includes 37 and 175 specimens analysed, respectively. The assessments were made with a single value of fracture toughness or with the use of a tearing resistance curve (R-curve), depending on the available data.

Each different material, and each test temperature, correspond to a different set of σ_y , σ_{UTS} values. Given that an FAL corresponds to a specific set of σ_y , σ_{UTS} values, this would

result in a high number of FALs and FADs. In pursuit of brevity, the FADs presented in this section include two curves which correspond to the upper and lower limit of all the FALs of the specimens included in the graph. These were calculated by extracting from all the FALs, at each value of L_r , the maximum and minimum value of K_r that was calculated. There was no distinction between continuous and discontinuous yielding in these graphs since the main aim was to show that the assessment points of failed specimens lied outside the safe zone of the FALs.

Following the assessment results is the comparison of modelling error for different levels of biaxiality as that was calculated for the different tests. Modelling error calculations were conducted with the use of each specimen's FAL.

Detailed reporting of the results of the analyses, the calculated values for the assessments and separate FADs for each set of tests can be found in [97].

3.2.4.1 Wide Plates

The results of the wide plate assessments are shown in Figure 3.4, where the blue and red markers refer to specimens which had surface flaws and through thickness flaws, respectively. The wide plates came from a variety of experimental programs and steels, while as explained previously some of the specimens included in the analyses, were either reported to not have reached failure or it was not clear whether the last values recorded during testing corresponded to failure, these were given as “unfailed specimens” and “uncertain failure” respectively.

In Figure 3.4, all the assessment points lied outside the minimum Option 1 FAL, while specimens which didn't fail during testing showed a clear trend of being closer to the safe zone. There was a single specimen (ID:2518), that has been annotated and circled in Figure 3.4, which lied inside the maximum FAL. To address any initial concern regarding this specimen, Figure 3.5 gives the FAD containing the FAL that derives from the tensile properties of the material of 2518 at the respective test temperature. Figure 3.5 shows that it was assessed safely with the specimen lying outside the FAL in the unsafe zone.

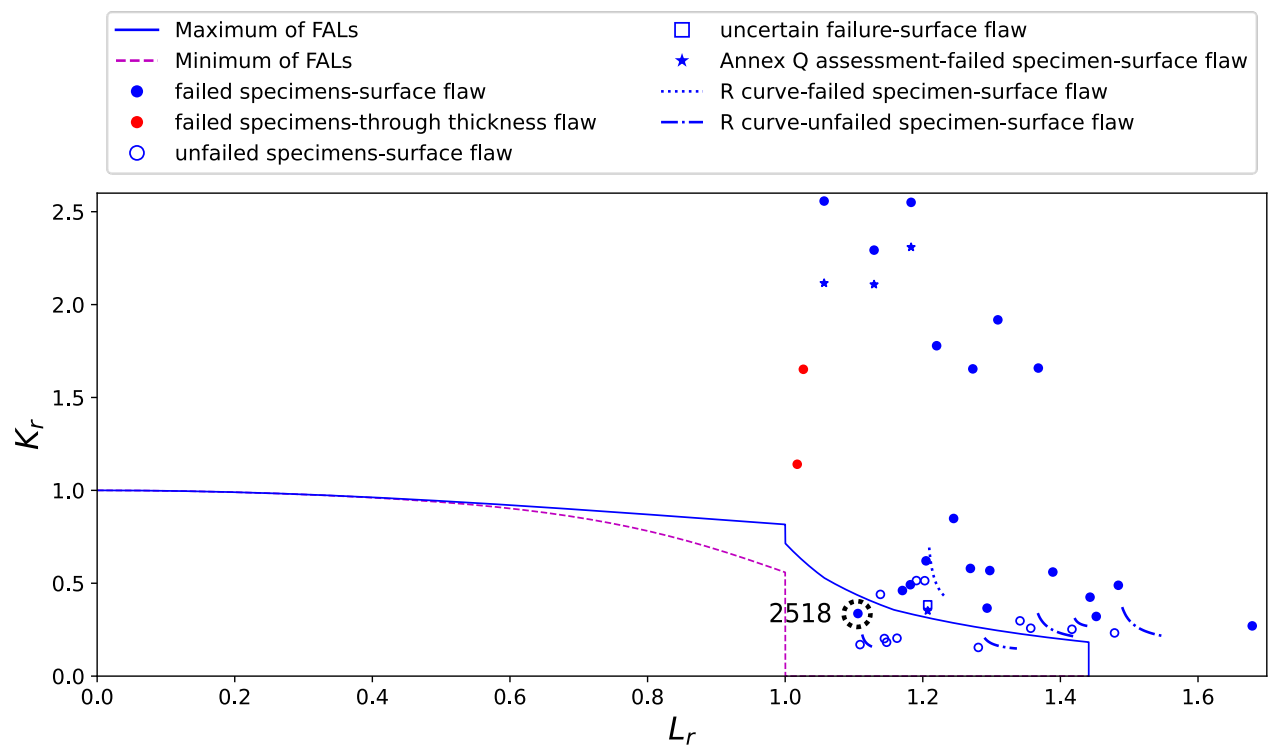


Figure 3.4: FAD of wide plate test data

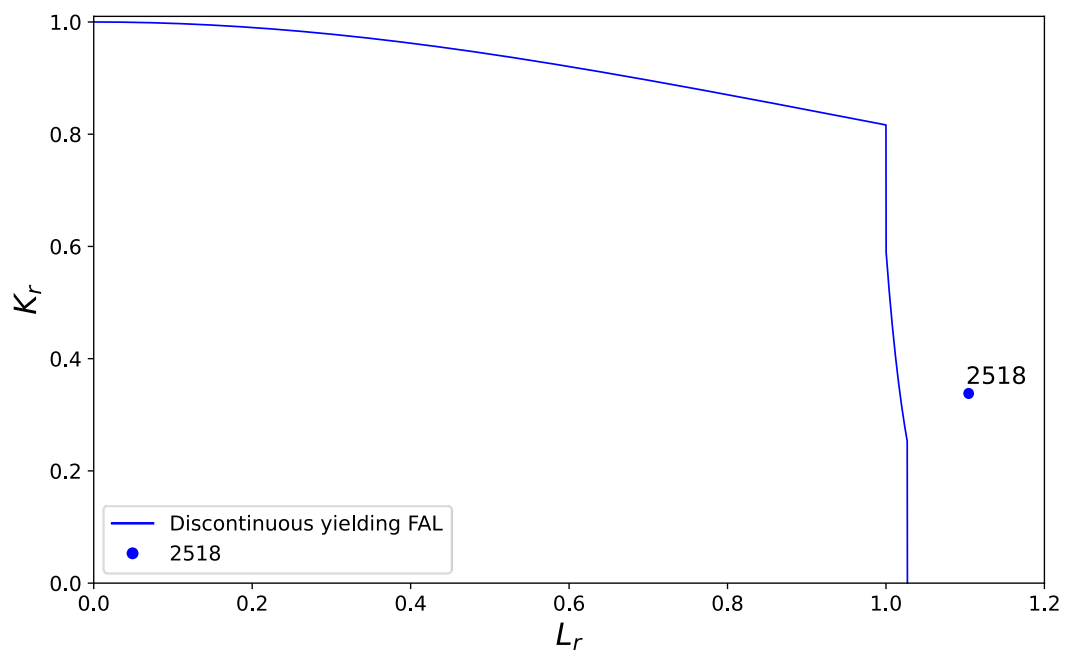


Figure 3.5: FAD of specimen 2518

3.2.4.2 Cylinders

3.2.4.2.1 Axially flawed

The assessment of all the axially flawed components has been conducted with the use of the reference stress equations of the 2019 version of the standard [1]. A comparison between the results using the equations from the 2013 and 2019 revisions of BS 7910 is given here in Figure 3.6, showing the decrease of conservatism between the different solutions, with the 2019 assessment points shifting closer to the FAL but remaining on the “unacceptable/unsafe” zone of the FAD. The decrease in conservatism comes from the decrease of the calculated L_r by approximately 20%, while the exact difference varies with the different values of K_r . This comparison can be seen in more detail in [96], [97].

Figure 3.7 includes the results of this set of assessments conducted with the 2019 version of the standard. There, the blue and red points correspond to surface breaking and through thickness flawed specimens, respectively. Additionally, the open and closed points, denoted as “Charpy” and “ K_{mat} ” indicate whether fracture toughness values came from the use of Charpy measurements or fracture toughness testing, respectively. Following the conservatism in the formula used to calculate fracture toughness from Charpy measurements, it is observed in Figure 3.7 that the majority of Charpy based fracture toughness assessments lie further out from the FAL, in comparison to those based on fracture toughness testing.

In Figure 3.7 there is a single (circled) point lying in between the minimum and maximum of the FALs, which corresponds to specimen I602. This point together with the single R curve, of specimen 2113, lying very close to the FAL are given in Figure 3.8 a and b respectively. Figure 3.8 shows the assessment of the two specimens, i.e. I602 and 2113, made using their respective tensile properties, where the assessment point/line lie outside both continuous and discontinuous yielding FALs. All of the above rendered the assessment procedure with the updated equations/reference stress solutions for pipes/curved shells, included in the 2019 version of the standard, safe.

Using curved shell SIF for cylinders, that lay outside the geometrical limits of the latter’s K solutions is also supported in [99]. It appears from the results presented here that this action gave safe results without any trend of added conservatism. This could be an incentive to further research whether the limitations of the cylindrical geometry equations

could be relaxed and still give safe results, however this would require a further parametric numerical and experimental study.

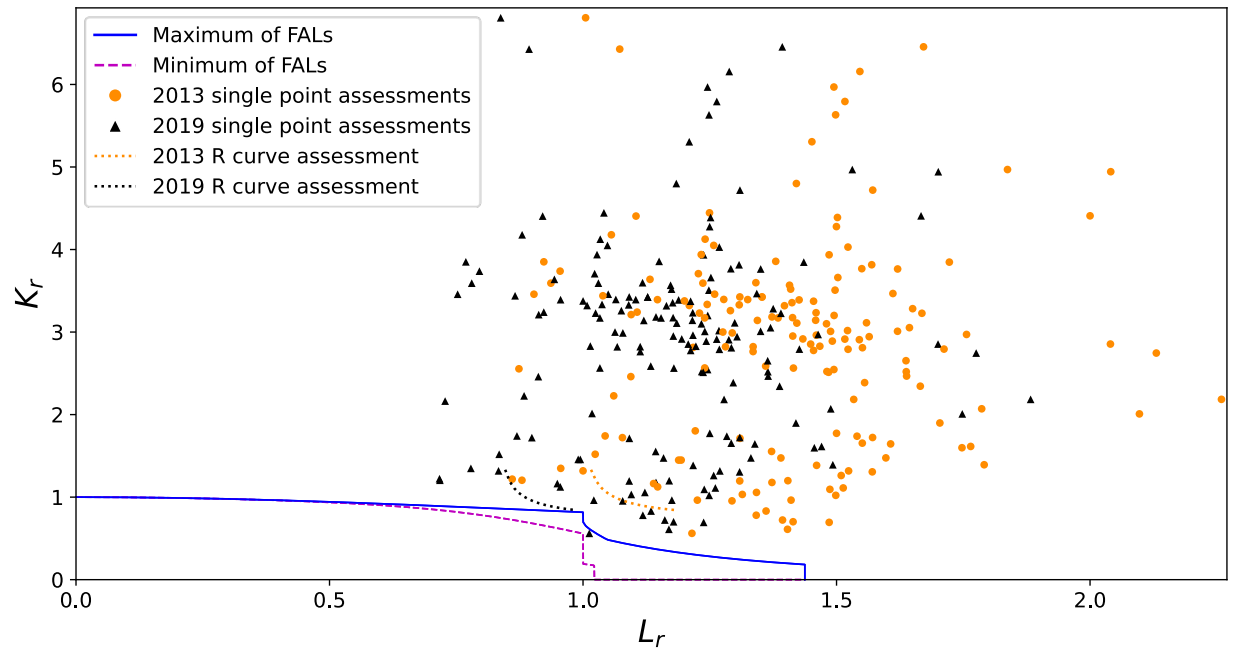


Figure 3.6: Comparison between BS7910 2013 and BS7910 2019 in assessing axially flawed cylinders

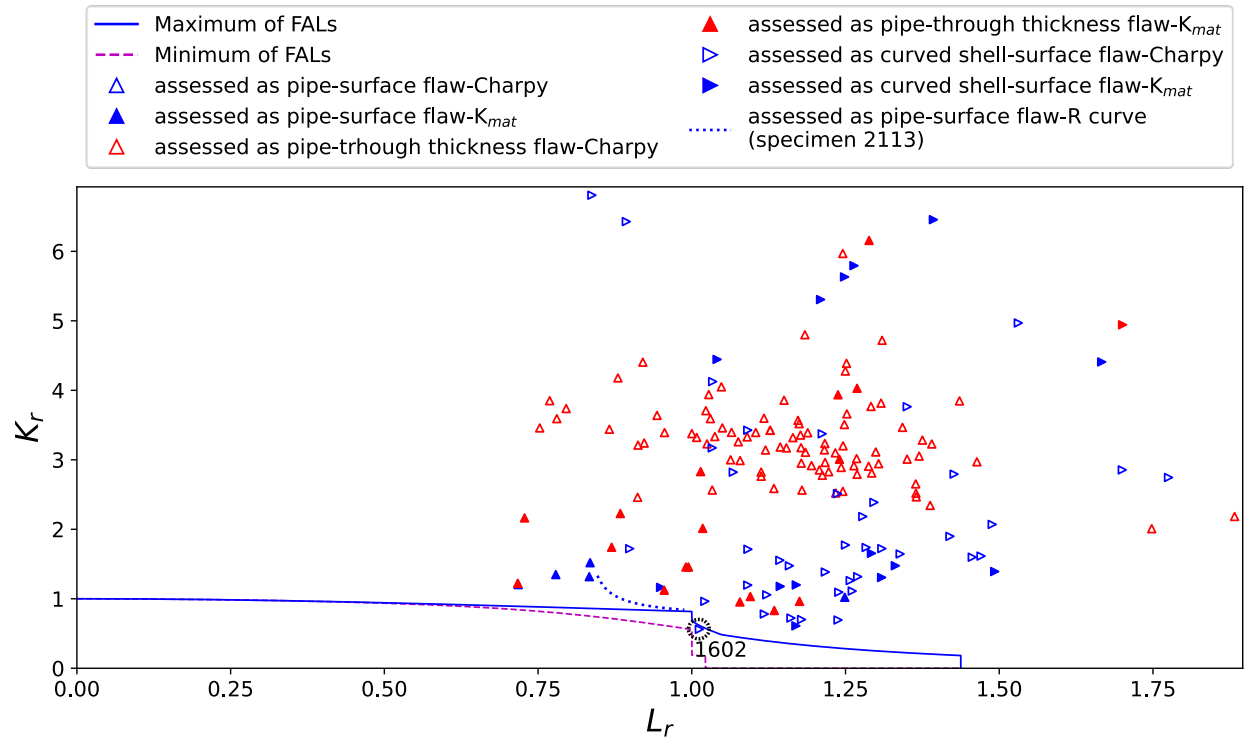


Figure 3.7: FAD of axially flawed cylinders (assessed with BS 7910 2019 version)

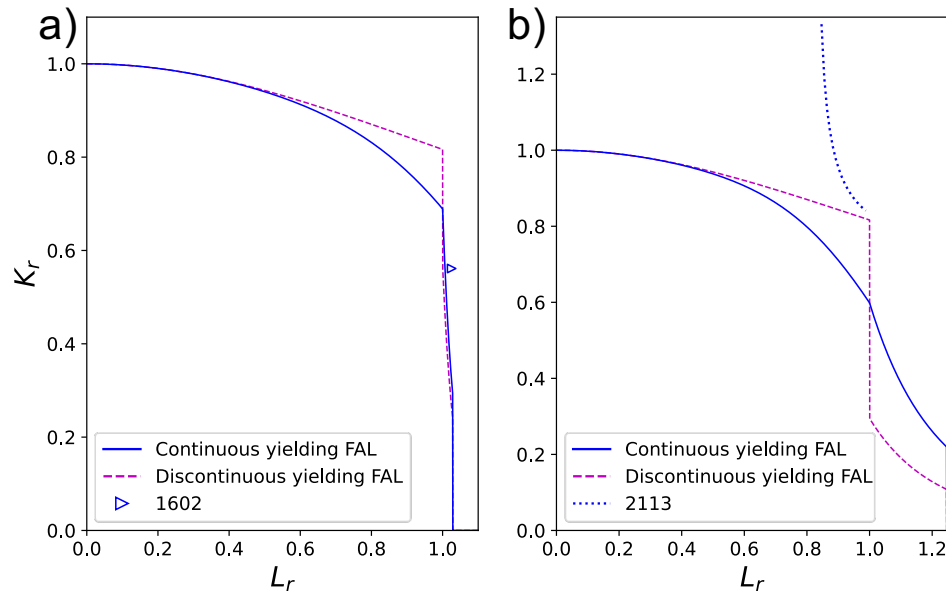


Figure 3.8: FAD of specimen a)1602, b)2113

3.2.4.2.2 Circumferentially flawed

The assessment results of the circumferentially flawed cylinders are shown in Figure 3.9, where again the blue and red coloured loci of points correspond to surface flawed and through thickness flawed specimens, respectively. Here all the assessments were made using tearing resistance curve data, which resulted in a locus of assessment points in the form of a line, as explained in Section 2.4. Again, all the assessment points/lines lied outside the FALs.

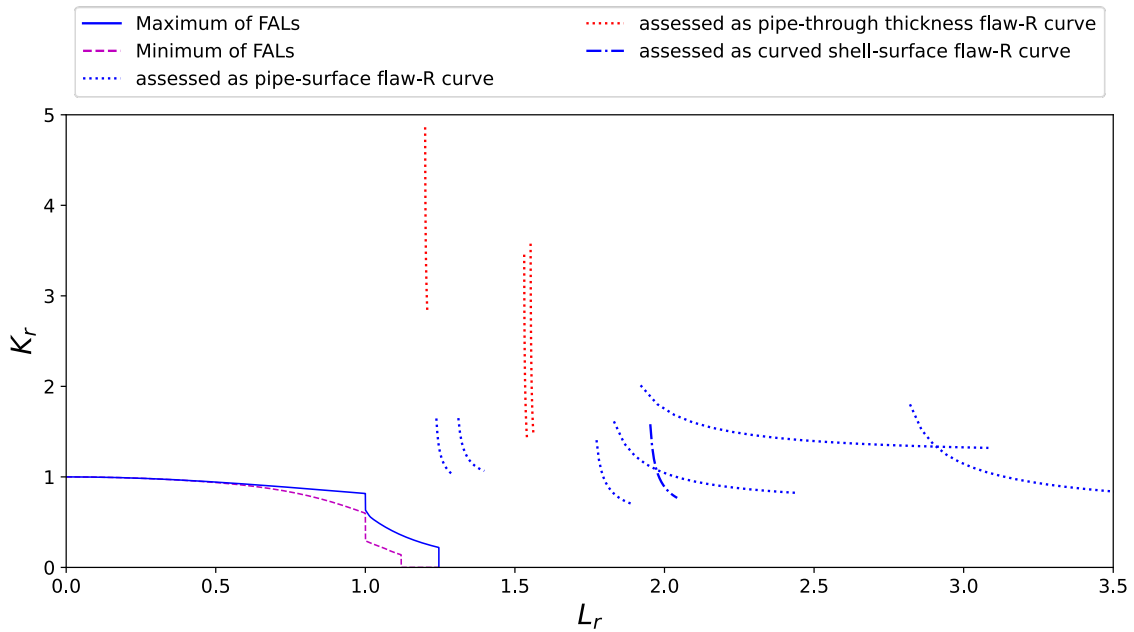


Figure 3.9: FAD of circumferentially flawed cylinders

3.2.4.3 Biaxiality-modelling error

At this part of the exercise the modelling error throughout different biaxiality ratios was calculated, as explained in Section 2.4 and graphically presented in Figure 2.9.

It was expected that there would have been a consistent trend between error and biaxiality, which would in its turn allow for an investigation of the source of the error and the potential of using historical data to better calibrate the existing equations.

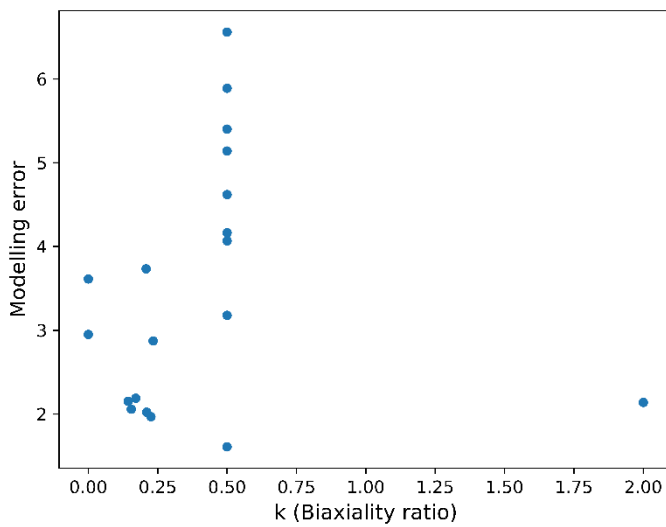
The experimental dataset was originally filtered so that comparisons could be made only between the same material, given the material dependency of plasticity constraint. This significantly reduced the amount of available data for comparison since multiple of the original sources focused on a single geometry with different flaw sizes, or different materials with a specific geometry and flaw size. The dataset now included 36 tests whose ID, material and biaxiality ratios are shown in Table 3.5. The dataset comprised three different materials whose biaxiality versus modelling error are given in Figure 3.10.

There is a lot of inherent scatter for all three materials. This is explained to a certain degree from the nature of fracture testing which includes scatter as well as the pooling of different flaw orientations (e.g. surface and through thickness) together. More importantly though this is due to the nature of the failure itself varying. Here comparisons have included specimens which failed with considerably more plasticity and/or stable crack propagation as well as tests where there was cleavage/brittle fracture. This affected the modelling error significantly as the closer the failure is to plastic collapse the more prominent the role of the reference stress solutions and thus L_r is. The opposite happens for brittle fractures, where the stress intensity factor solutions and K_r play a more important role on the modelling error. Overall, the error calculated for 20MnMoNi 55 and NiMoCr-Melt is widely scattered with values ranging from 2 to 6, thus rendering the data for these materials not trustworthy to capture biaxiality effects.

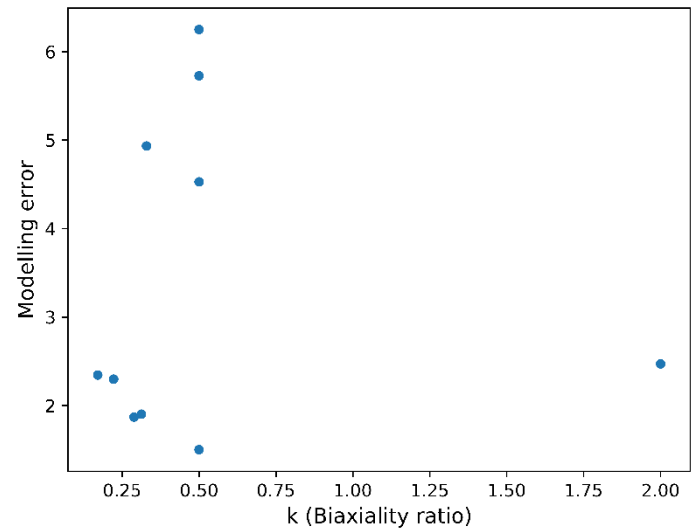
For the API 5L X56 steel, further filtering could be applied to distinguish between the assessment points that lied in the collapse and the fracture dominated region, however this would allow for a maximum of 4 points of the dataset to be plotted. This number of points would be significantly low for any conclusion to be drawn.

Table 3.5: Biaxiality and modelling error dataset

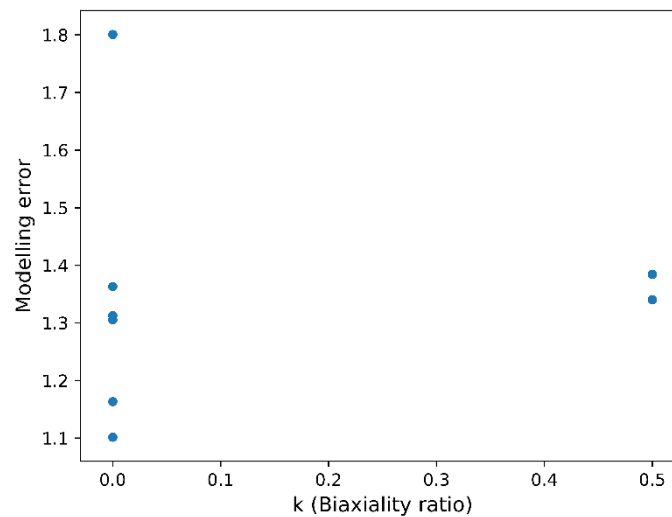
| ID | Ref. | Material | Specimen Geometry | Loading | Biaxiality ratio k | Modelling Error |
|------|--------------------------|--------------|-------------------|-----------------------------|--------------------|-----------------|
| 722 | [108], [114] | 20 MnMoNi 55 | Closed Cylinder | Internal Pressure | 0.5 | 1.61 |
| 2103 | | | | | 0.5 | 3.18 |
| 2104 | | | | | 0.5 | 4.16 |
| 2105 | | | | | 0.5 | 4.07 |
| 2106 | | | | | 0.5 | 5.14 |
| 2107 | | | | | 0.5 | 6.56 |
| 2108 | | | | | 0.5 | 5.40 |
| 2109 | | | | | 0.5 | 4.62 |
| 2110 | | | | | 0.5 | 5.89 |
| 2116 | | | | | 2 | 2.14 |
| 2119 | | | | Bending | 0 | 2.95 |
| 2120 | | | | | 0 | 3.61 |
| 2121 | | | | Internal Pressure + Bending | 0.21 | 3.73 |
| 2122 | | | | | 0.14 | 2.15 |
| 2123 | | | | | 0.23 | 2.87 |
| 2124 | | | | | 0.15 | 2.06 |
| 2125 | | | | | 0.17 | 2.19 |
| 2126 | | | | | 0.21 | 2.02 |
| 2127 | | | | | 0.23 | 1.97 |
| 301 | [82], [102], [116] | API 5L X56 | Wide Plate | Tension | 0 | 1.10 |
| 302 | | | | | 0 | 1.31 |
| 303 | | | | | 0 | 1.36 |
| 304 | | | | | 0 | 1.80 |
| 305 | | | | | 0 | 1.16 |
| 306 | | | | | 0 | 1.31 |
| 2101 | | | Closed Cylinder | Internal Pressure | 0.5 | 1.34 |
| 2102 | | | | | 0.5 | 1.38 |
| 2111 | [116] | NiMoCr-Melt | Closed Cylinder | Internal Pressure | 0.5 | 6.25 |
| 2112 | | | | | 0.5 | 4.53 |
| 2113 | | | | | 0.5 | 1.50 |
| 2114 | | | | | 0.5 | 5.73 |
| 2117 | | | | | 2 | 2.47 |
| 2129 | | | | Internal Pressure + Bending | 0.33 | 4.93 |
| 2130 | | | | | 0.22 | 2.30 |
| 2131 | | | | | 0.17 | 2.34 |
| 2132 | | | | | 0.29 | 1.87 |
| 2133 | | | | | 0.31 | 1.90 |



a) 20MnMoNi55



b) NiMoCr-Melt



c) API 5L X56

**Figure 3.10: Modelling error at different levels of biaxiality for tests on a) 20MnMoNi55
b) NiMoCr - Melt and c) API 5L X56 steels**

3.2.5 Summary

From the results presented, BS 7910 and in particular its most conservative procedure, i.e. Option 1, can safely, albeit conservatively, estimate the fitness for service of a component and can predict failure. The level of this conservatism is something that might not be desired but is necessary for the procedure to be used in a fast manner, and multifunctionality of the procedure is mirrored in the high variation, between cases, of distance between the assessment point and the FAL.

It is important for procedures to be validated against experimental data, so they are calibrated against real cases. A characteristic example of the benefits of validating can be noted in this exercise. That was the pattern of unnecessary conservatism that had been observed on the reference stress solutions concerning cylinders/curved shells with axial through thickness, internal/external flaws. This regarded a multiplication factor of 1.2 which was included in the previous version of the standard [71] and has been amended to 1 in the latest one [1], leading to a decrease of the calculated L_r by approximately 20%, while the exact difference in conservatism values varied with the different values of K_r . In this study the latest version of the reference stress solutions has been used, i.e. the factor has been 1. Further explanation of the history of this factor and the respective solutions included in other standards can be found in [96], while comparative results including both factors can be found in [96], [97].

Regarding the trend of modelling error with varying biaxiality ratios, the experimental database studied was not found to be consistent enough to be able to capture the phenomenon. Different sources included combinations of failure modes (collapse vs fracture), materials, testing temperatures and flaw geometries (surface, internal/external flaws) leaving very limited instances for comparison after careful filtering of the data. This together with the inherent scatter of testing itself did not make for a trustworthy basis on which a conclusion could be drawn. Nevertheless, this proved the importance of analysing a consistent database with specific biaxiality related oriented experiments, included in the following section.

One of the most important tasks accomplished here was re-gathering the experimental data. The data used here had been tracked back to the original reports in most cases. As expected, some reports were either unavailable or did not provide all the data needed, and data from earlier validation work was used and/or assumptions were accordingly made. Given the limited availability of such studies in the public domain an experimental database like the one constituted here is of very high value since it can be used for validation of future versions of both existing FFS standards and their constituents as well as new additions to them.

3.3 TWI biaxial experiments

3.3.1 Introduction

In pursuit of better understanding and more accurately assessing the effects that biaxial loading has on the integrity of a structural component, biaxial and uniaxial tests conducted previously in TWI [8] are analysed. This test database is much more suitable to capture the current capabilities of FFS on biaxiality, in comparison to the historical data analysed before, given the tests are conducted on a single material, are high in number, include both surface breaking and through thickness flaws and have been tested throughout a spectrum of temperatures, biaxiality ratios and thicknesses. [117]

3.3.2 Tests analysed

Overall, 20 large scale tests including uniaxial and biaxial loading had been previously conducted on A533B pressure vessel steel plates by TWI. From these tests, six that failed in the fracture dominated region of the FAD are analysed here. Two of these tests have surface breaking and the remaining four have through thickness cracks.

The geometry of the biaxially loaded plates was that of a cruciform specimen, while the geometry of the uniaxially loaded was similar with the two loading legs of the specimen removed; a schematic of the specimens is shown in Figure 3.11.

The tests' numbering from the original reports [118]–[121] and the one used in previous analyses and here [94], [117] are shown in Table 3.6, along with the thickness, crack size values of each specimen, test temperatures, biaxiality ratios and failure loads.

The two tests with surface breaking flaws, were originally numbered as M01-30, M01-40 [121] and are here referred to as #15 and #16 accordingly. These were conducted at approximately -160°C , at the lower shelf of the fracture toughness, according to the information provided in [94], with the surface cracks having been introduced with a fatigue pre-cracked EDM notch. The testing of each specimen comprised sequential loading and unloading at successfully lower temperatures; however the original report denoted that no plastic deformation or warm-pre stress effects have occurred prior to the failure that occurred with the final loading [121]. Thus, the analyses consider only the final loading and temperature. The interest in analysing these tests is mainly their difference on K_r shown in [94], where they were analysed using BS 7910 Option 1 assessments and

the standard's SIF an reference stress solutions for uniaxially loaded plates. Their study thus mainly aims to answer whether the difference on K_r can be explained with the effect of biaxiality.

Additionally, four wide plate tests with through thickness cracks are included in this work. These are referred to here and in [94] as #40, #41, #41(a)1 and #41a(2). They were tested at -100°C which corresponds to the end of the lower transition of region of fracture toughness. The four results comprise three discrete tests, since #41a did not reach failure during initial loading [#41a(1)], where a biaxiality ratio $k=2$ was applied, and was reloaded to failure with a ratio $k=0.5$ [#41a(2)]. The failure load reported in Table 3.6 for $k=2$ corresponds to the maximum load prior to unloading. For through thickness cracks the easily applied limit load solutions proposed in Meek et al and BS 7910 [71], [74] that incorporate biaxiality are also used. Hence, one aspect of the analysis of these tests was to also test these solutions and compare it with the FEA analyses to check its validity. Additionally, at this temperature (-100°C), a fracture toughness - constraint curve was available, which allowed for constraint corrected assessments according to BS 7910 : Annex N [71].

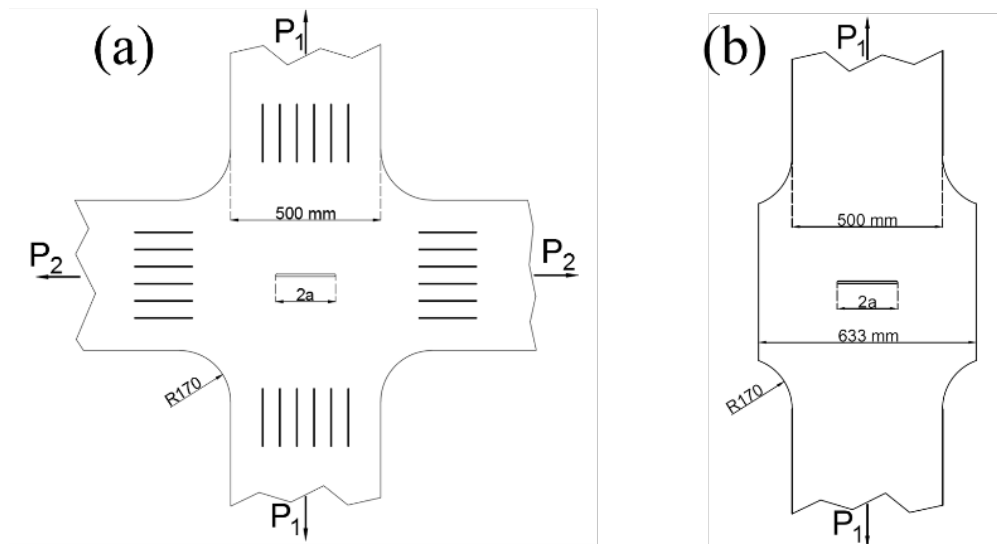


Figure 3.11: Geometry of (a) biaxially loaded, (b) uniaxially loaded specimens

Table 3.6: Geometric Properties, Test Temperatures, and failure loads of specimens assessed

| ID in [94] | ID, original work | Crack Type | Crack Size (ax2c or 2a), mm | Nominal Thickness, mm | Test Temp., °C | Biaxiality Ratio, k | P_1 at failure (kN) |
|------------|-------------------|-------------------|-----------------------------|-----------------------|----------------|-----------------------|-----------------------|
| #15 | M01-30 | Surface | 24x144.6 | 50 | -157 | 0 | 10747 |
| #16 | M01-40 | | 22.7x135.9 | 50 | -163 | 1 | 11189 |
| #40 | M01-26 | Through thickness | 203 | 50 | -100 | 1 | 5686 |
| #41 | M01-28 | | 200 | 50 | -100 | 0 | 8718 |
| #41a(1) | M01-27 | | 202.4 | 50 | -104 | 2 | 6380 |
| #41a(2) | M01-27 | | 202.4 | 50 | -104 | 0.5 | 6296 |

3.3.3 Material properties

Tensile properties

Tensile properties for the tested plates were originally measured only at +70°C. The yield stress and ultimate tensile strength values required for the Option 1 assessments, were calculated in accordance with the standard approach of BS 7910:2013 and are shown in Table 3.7, while the elastic modulus was taken as 212GPa.

Option 3 analyses require full tensile curves to produce the FAL. In this case full tensile curves were only given at +70°C [8]. In later work assessing specimens of this material at lower temperatures [94] the stress strain curve was shifted upwards, following the increase of yield strength value as temperature decreases, to a temperature of -95.5°C. This curve, as presented in [94], is used for the Option 3 assessments of all specimens tested at -100°C, while for those tested at -160°C the same methodology of shifting the curve upwards is used to offset to the yield stress, as calculated following the BS 7910 guidance at that temperature. The original stress-strain curve at +70 °C along with the shifted curves are shown in Figure 3.12.

Table 3.7: Calculated Yield and Ultimate Tensile stresses (MPa)

| ID | Biaxiality Ratio, k | Test Temp., °C | σ_y , at T_{fail} (MPa) | σ_{UTS} , at T_{fail} (MPa) |
|---------|-----------------------|----------------|----------------------------------|--------------------------------------|
| #15 | 0 | -157 | 774 | 843 |
| #16 | 1 | -163 | 800 | 855 |
| #40 | 1 | -100 | 616 | 738 |
| #41 | 0 | | | |
| #41a(1) | 2 | -104 | 623 | 744 |
| #41a(2) | 0.5 | | | |

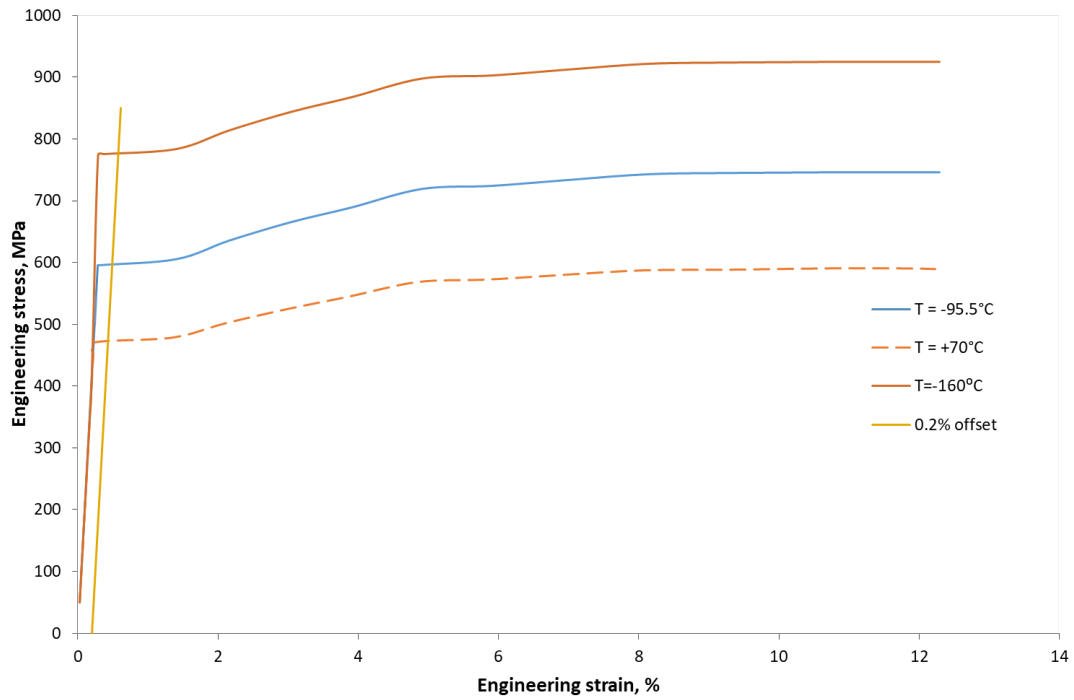


Figure 3.12: Tensile properties at various temperatures

Fracture toughness

Fracture toughness (K_{mat}) for this material had been measured from a variety of specimen geometries (e.g. C(T) and Charpy) thicknesses and temperatures. The analysis of the existing fracture toughness data in [94] allows for a Master Curve approach. The reference temperature of the Master Curve, $T_0 = -151.3^\circ\text{C}$, is used to calculate fracture toughness that correspond to the 5% and 20% probability, i.e. a 5% and 20% probability of the toughness

to be lower. As advised by BS 7910 for lower shelf transitional behaviour based on the Master Curve, the 5% values are used for the Option 1 assessments while for the more detailed Option 3 assessments 5% and 20% are both used for comparison. All the values included in the assessments are shown in Table 3.8.

Table 3.8: Fracture toughness values, K_{mat} (MPa√m)

| Temperature | -157°C (#15) | -163°C (#16) | -100°C (#40,#41) | -104°C (#41(a)1,41(a)2) |
|-------------------------|-----------------|-----------------|---------------------|----------------------------|
| 20% Master Curve | 48.2 | 45.3 | 138.2 | 129.8 |
| 5% Master Curve | 62.1 | 57.9 | 100.9 | 95.1 |
| MOTE | - | - | 107.9 | 94.8 |

For the specimens tested at -100°C, the relationship between fracture toughness and constraint was presented in terms of a curve which best fit high and low constraint experimental data, which were SENB specimens of different thickness, in [122] and is used here for the constraint modified Option 3 FALs of all four specimens tested at -100°C and -104°C. The curve follows Equation 3.6

$$\frac{K_{mat}^c}{K_{mat}} = [1 + \alpha_1(-\beta L_r)^{k_1}] \quad \text{Equation 3.6}$$

where K_{mat}^c is the constraint corrected fracture toughness, K_{mat} is the fracture toughness determined from standard high constraint tests, α_1 , k_1 are material and temperature dependent constants ($\alpha_1=1.97$, $k_1=2.36$) and β is the structural constraint parameter, which remains constant throughout the load (load independent), and is calculated as,

$$\beta = \frac{T}{L_r \sigma_y} \quad \text{Equation 3.7}$$

T denotes the T-stress which was extracted with ABAQUS from the elastic model of each specimen.

3.3.4 Assessment of tests

The assessments include FALs created with Option 1, which requires knowledge of the yield stress and ultimate tensile strength as well as with Option 3 which is a tailor made FAL corresponding to the material and geometry studied and is generated via FEA. In addition to the Option 3 FALs, for the tests at -100°C a constraint modified Option 3 FAL is created for all specimens that experience constraint relaxation.

Option 1 assessments

The basic Option 1 FAL is based on the tensile properties from Table 3.7 and yielding is taken as discontinuous. The assessments have L_r and K_r calculated with the use of the analytical solutions included in BS 7910 and R6, while for the through thickness cracked plates an additional solution, partly included in the standards, is implemented.

Option 3 assessments

An option 3 failure assessment line is given by Equation 3.8.

$$f(L_r) = \sqrt{\frac{J_e}{J_{el-pl}}} \quad \text{Equation 3.8}$$

where J_e is the value from the J-integral from the elastic analysis and J_{el-pl} is the value from the J-integral from the elastic-plastic analysis. For the calculation of these variables, FEA is invoked. Overall, three FEA are run for each specimen, these include:

- an elastic analysis, with an elastic modulus of 212GPa and a Poisson ratio of 0.3, for J_e
- an elastic plastic analysis, containing the whole tensile curve included in Figure 3.12, for J_{el-pl}
- an elastic perfectly plastic, with the properties of Table 3.7, for the limit load, which was extracted from the last step of loading where a plastic hinge would be created and model would stop converging

The values of L_r are calculated by dividing the applied load at failure by the elastic perfectly plastic FEA derived limit load and K_r by dividing the elastic K calculated from FE with the respective fracture toughness.

Following, the analyses and their results are given for each different set of temperature/flaw geometry tests.

3.3.4.1 Surface breaking flaws | -160°C

Option 1 assessments

For the calculation of L_r , Option 1 assessments use the local collapse R6 limit load solutions for plates with surface breaking flaws (Section IV.1.7.2 in [3]). Additionally, for the calculation of K_r the stress intensity factor K_I is calculated using the solutions for surface flaws in plates included in BS 7910 (Section M.4.1). The cruciform specimen is assessed as a plate with a width of 500mm and a thickness of 50 mm, whilst the uniaxially loaded specimen ($k=0$) is treated as a 633mm wide plate of similar thickness.

To assess the specimens as plates, the applied stress used for the Option 1 assessments corresponds to the average opening stress at the central area of the biaxial specimen. That stress was given in [121] both as it was calculated by the biaxial strain gauge measurements as well as with its calculation with use of a calibration factor, the latter is used in the Option 1 assessments here. As explained in [117], this calibration factor correlated the applied load at the ends of the specimen to the stress experienced at the middle of the specimen and was validated with the use of experiments conducted at higher temperatures. It is interesting to note that this calibration factor shows a trend of the biaxially loaded centre having lower stresses perpendicular to the crack, as shown below.

- For equibiaxial loading: $\sigma_{plate} \left(\frac{N}{mm^2} \right) = 27.3 \times \text{load in arm (MN)}$
- For uniaxial loading: $\sigma_{plate} \left(\frac{N}{mm^2} \right) = 31 \times \text{load in arm (MN)}$

The above equations show that a uniaxially loaded specimen will translate an applied load to a higher crack opening stress in the central area of the specimen. The results of the assessments are shown in Figure 3.13. In this figure only the Option 1 FAL of specimen #15 is provided, given that there were minor differences between that and the one of specimen #16.

Option 3 assessments

To create the Option 3 FAL, FEA are carried out with the use of ABAQUS. Due to the double symmetry of the specimens a quarter of each is modelled, as shown in Figure 3.14.

The models are loaded in uniaxial or biaxial tension according to the geometry and the biaxiality ratio of the experiment. The loads are applied on the loading arms in the form of a homogeneous stress that is calculated by dividing the applied load from the

experiment by the surface, at the end of the loading arm, i.e., the thickness multiplied by the width of the loading arm. The models were done with incremental plasticity, i.e. using the whole tensile curve provided. Since not a lot of deformation happened prior to the failure of the tests this was considered accurate enough while the Abaqus parameter NLGeom was not applied.

The J integral is calculated automatically by ABAQUS using a domain integral method. To aid the contour calculation a spiderweb mesh with concentric circles of elements is created around the crack tip and extruded throughout the crack length. The first elements are wedge elements, originally hexahedral elements collapsed to wedges. The nodes at the crack tip are constrained to move as a single node in the elastic analyses, and as duplicate nodes in the elastic-perfectly plastic and elastic plastic analyses. The singularity is accounted for by moving the mid-side nodes of second order elements, at the crack edge, towards the crack tip at a distance of $\frac{1}{4}$ of the element edge, as suggested for elastic and elastic-plastic analyses with a hardening material [123], while the midsize node is placed at $\frac{1}{2}$ the distance of the element for elastic perfectly plastic analyses. J-integral is calculated over 7 contours, whilst J values, even on the highest plasticity levels, converges from the third contour onwards. For instance, in the elastic-plastic model of #16, on the node depth where the maximum J-integral was met, the first contour calculated a J of 36.01 whilst from the third onwards the values converged to 36.42. The first contour was calculated at 1 mm from the crack tip gradually extending to 9 mm.

The biaxially loaded specimen's model comprises 29764 C3D8, 2310 C3D20 and 38030 C3D10 elements, while the uniaxial model comprises 20354 C3D8, 2310 C3D20 and 42138 C3D10 elements. These types of elements were assumed to be able to capture the plasticity developed accurately. In particular collapsed wedge of full C3D20 elements were used to mesh the crack tip, C3D10 elements were used to transfer the stress and strains from the crack tip to the rest of the specimen, while C3D8 elements were used to account for the simple loading of the specimen.

The models are validated with the comparison of the experimentally measured and modelled stresses at the centre of the specimen. The creation of the FAL follows the same steps described previously [117]. J_{el} and J_{el-pl} are extracted from the deepest point of the modelled crack, given that the crack driving force in both the uniaxial and biaxial models is highest there.

The calculation of L_r uses the limit load calculated from the elastic-perfectly plastic FEA, while for K_I the stress intensity factor calculated from the elastic FEA is used. The results of the assessments are shown in Figure 3.13.

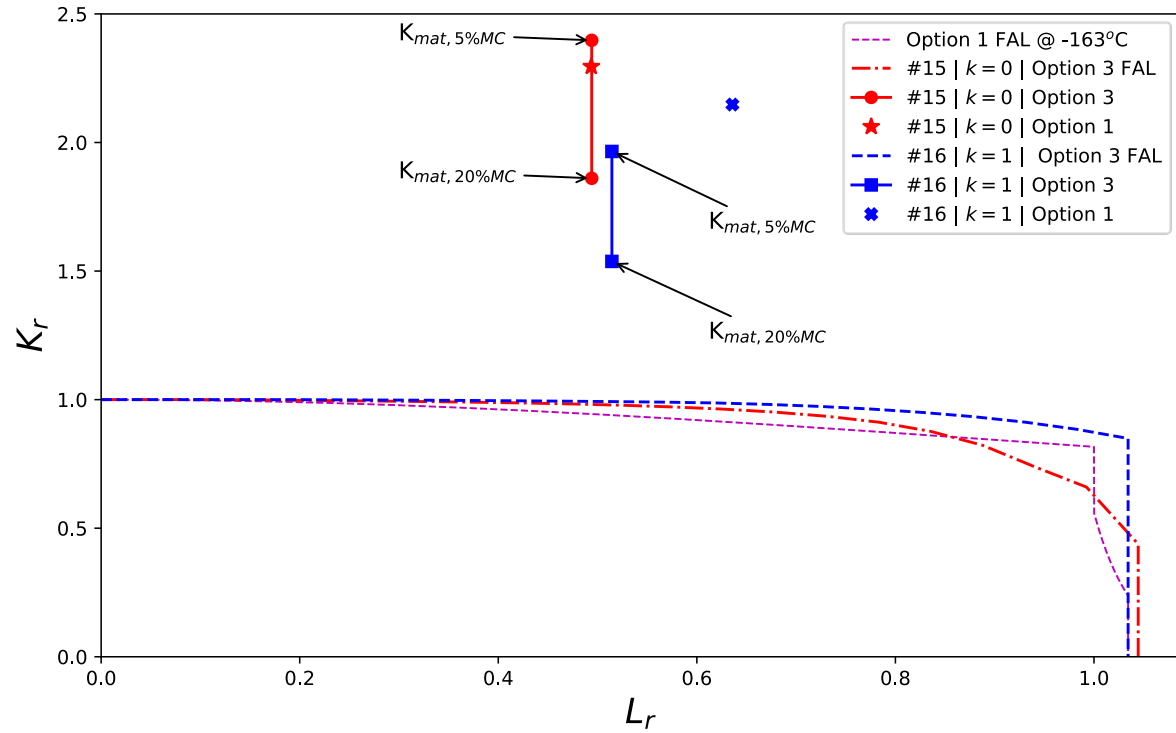
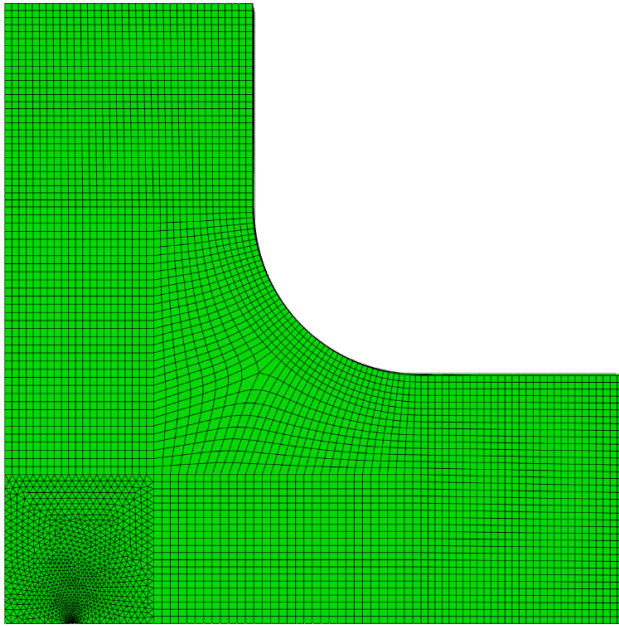
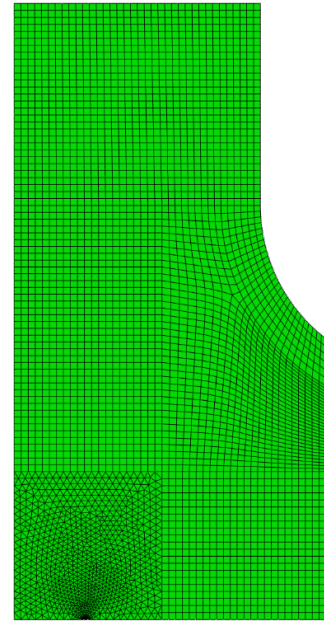


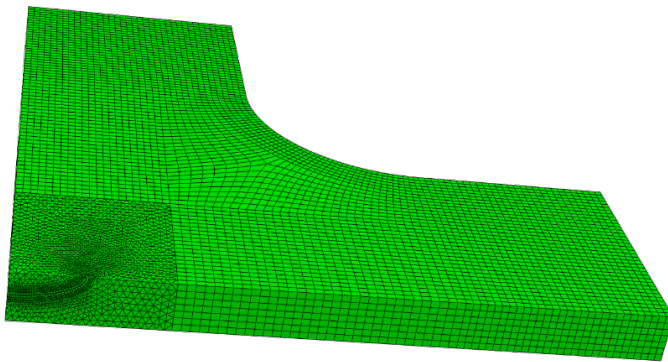
Figure 3.13: Option 1 and Option 3 assessments of specimens #15 ($k=0$) and #16 ($k=1$)



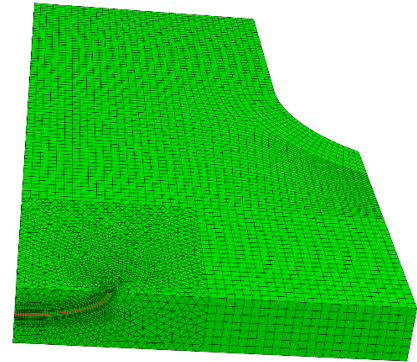
(a) FEA - Specimen #16 (top view)



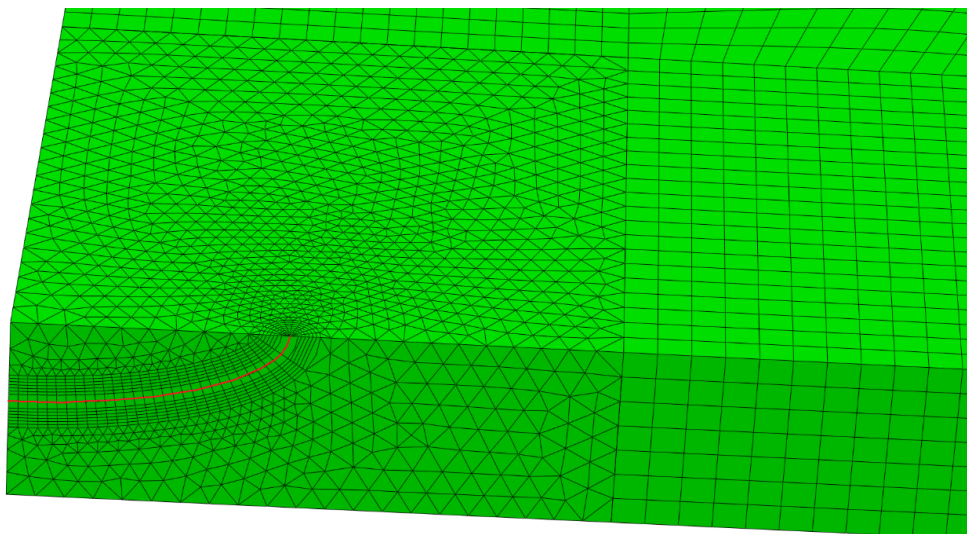
(b) FEA - Specimen #15 (top view)



(c) FEA - Specimen #16 (angled view)



(d) FEA - Specimen #15 (angled view)



(e) FEA - Crack region

Figure 3.14: FEA mesh of specimen #15 and #16

From the Option 3 FALs in Figure 3.13 the biaxially loaded specimen has a flatter curve denoting the effect of the biaxial loading on the constraint. In other words, J_{el-pl} is closer to the values of J_{el} in the case of the biaxially loaded specimen (#16) in comparison to the uniaxial specimen where plasticity could develop.

Regarding L_r , for the uniaxially loaded specimen (#15) the R6 local collapse solution and the FEA derived limit load values essentially provide the same results. This is expected firstly because the geometry of specimen #15 is that of a plate and thus the R6 solution is accurately used and secondly because both FEA and analytical solutions address a uniaxially loaded specimen.

On the other hand, for the equibiaxially loaded specimen (#16) the R6 solution provides a lower limit load than that of the FEA and thus higher L_r values. Even though this difference could be due to the geometry of the specimen not being exactly that of a wide plate, as is the one of the analytical solutions, it is argued to be mostly due to the analytical solution not considering the load parallel to the crack. This is supported by literature [124] where the limit load increases non monotonically as biaxiality increases from $k=0$ to $k=1$; and it is argued that this trend is the one observed here, with the FEA derived limit load for $k=1$ being higher than the analytical R6 limit load for $k=0$. A limit load that includes the out of plane component could be used to assess these tests, however these were analysed to investigate the difference in K_r and would be out of scope.

Additionally, the K_r values for the biaxially loaded specimen (#16) are lower than those of the uniaxial specimen (#15), showing that the elastic SIF (stress intensity factor) developed in the former is the lowest between them. That is explained partly by the equibiaxially loaded specimen having a shorter and shallower flaw ($a \times 2c=22.7 \times 135.9 \text{ mm}$) than the uniaxial specimen ($a \times 2c=24 \times 144.6 \text{ mm}$) but most importantly by the lower stresses experienced in the centre of the biaxial specimen. The latter argument might seem contradictory with the failure loads recorded during testing, since the biaxially loaded specimen had a higher failure load, however the difference in the loading conditions results to both experimentally and FEA calculated crack opening stresses to be lower in the centre of the equibiaxially loaded specimen. As explained earlier the stresses calculated by the two directional strain gauge measurements recorded during the experiments [121] show higher stress values in the uniaxially loaded specimen in comparison to the equibiaxially loaded specimen. This trend is also seen in the FEA of the two specimens

where the average crack opening stress in the uniaxial specimen is larger than the equibiaxially loaded specimen.

To further understand this trend of biaxiality decreasing the crack opening stress, an additional FEA of specimen #16 is run. This time the cruciform specimen is loaded with the same (failure) load (11.2 MN) but only at one direction, i.e. it is loaded uniaxially. This aims to clarify whether the difference in stresses is due to the slight difference in geometry between #15 and #16 or is indeed an effect of biaxiality.

The analysis is run assuming an elastic material. The average stresses presented here are extracted from the unnotched side of the specimen at points A and C which are shown in Figure 3.15. The opening stresses (σ_{yy}) calculated at the points are shown in Table 3.9.

From Table 3.9 the previously observed trend of crack opening stresses decreasing when moving from a uniaxially loaded to an equibiaxially loaded specimen is confirmed. This in its turn explains the difference in K_r values between specimens #15 and #16.

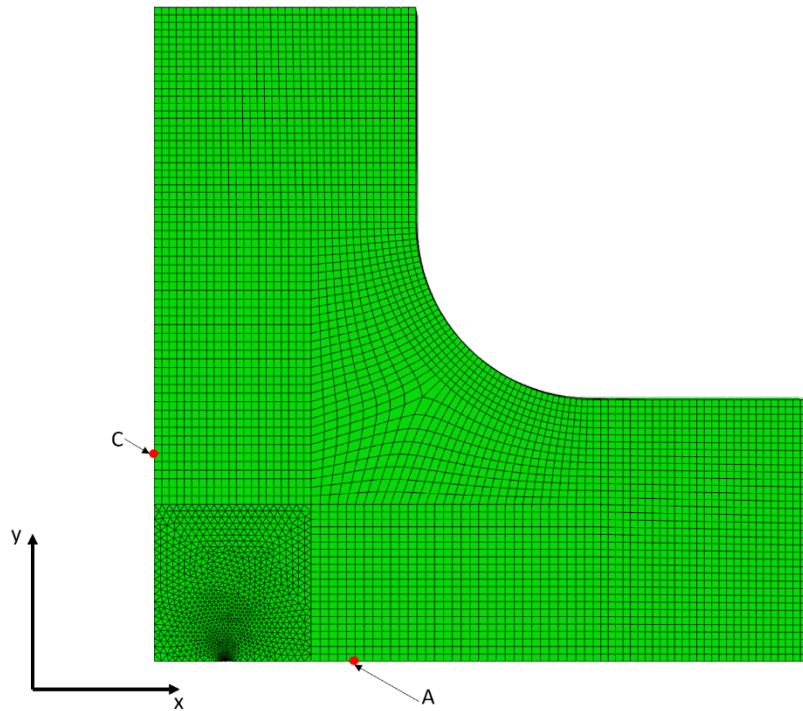


Figure 3.15: Visual of stress extraction points

Table 3.9: Extracted stresses at points A, C

| Point A ($y=0$, $x=165$) | | Point C ($y=166$, $x=0$) | |
|--------------------------------|-------|--------------------------------|-------|
| σ_{yy} – uniaxial (MPa) | 305.2 | σ_{yy} – uniaxial (MPa) | 379.8 |
| σ_{yy} – biaxial (MPa) | 262.2 | σ_{yy} – biaxial (MPa) | 312.9 |

3.3.4.2 Through thickness flaws | -100°C

Option 1 assessments

As before, the basic Option 1 FAL is based on the tensile properties from Table 3.7 and yielding is taken as discontinuous. The assessments have L_r and K_r calculated with the use of the handbook solutions included in BS 7910 and R6. From the available solutions the ones used here concern a plate with a through thickness flaw loaded in uniaxial tension.

For the calculation of L_r , two solutions for the limit load exist, the first one corresponds to failure under plane stress using either the Tresca or Von Mises failure criterion (or plane strain with the use of Tresca). The second solution corresponds to failure under plane strain with the use of the Von Mises criterion. Even though, BS 7910 highlights the first (Mises-plane stress) solution given its more conservative results, the plane strain solution can be invoked from the strength mis-match limit load solutions assuming a plate made wholly out of parent material. Given the thickness of the plates assessed here (50 mm) plane strain conditions are expected in the middle of their thickness and thus the Von Mises plane strain solution is used. The stress intensity factor solutions for the calculation of K_r are essentially the same between the two procedures. The difference between them is considered negligible and the stress intensity factor from BS 7910 is used. The fracture toughness values used for the Option 1 assessments are the 5% Master Curve values shown in Table 3.8. These assessments are designated as assessments “A”.

For the biaxially loaded tests, an additional assessment is made, where K_r is calculated as previously and L_r is calculated using the lower bound plane strain von Mises limit load solution (given in terms of limit stress) invoked in [125] and given here as Equation 3.8. These assessments are designated as assessments “B”.

It should be noted that Equation 3.8 gives the same results with the reference stress solution used in the constraint effect associated clauses of BS 7910 (Annex N) and R6 (Section IV.5), for both centre-cracked equibiaxially and uniaxially loaded plates. In the

uniaxial case it is also equivalent to the Von Mises plane strain solution used for the A assessment of $k=0$.

$$(\sigma_2)_L^{lb} = \frac{2\sigma_y}{\sqrt{3}} \min \left[\frac{1}{|k|}, \frac{(1 - a/W)}{|1 - k(1 - a/W)|} \right] \quad \text{Equation 3.9}$$

where k is the biaxiality ratio, a is half of the crack length and W is half width of the plate.

As for the surface breaking flawed specimens; here the cruciform specimens are assessed as plates with a width of 500mm and a thickness of 50 mm, whilst the uniaxially loaded specimen ($k=0$) is treated as a 633mm wide plate of similar thickness. The failure stresses invoked for the assessments are the average stresses that had been calculated from the strain gauge measurements of the original reports.

In the case of $k=1$ the failure stresses experimentally measured are very low and do not seem to be fully responsible for the failure of the specimen. According to the original report the specimen had an inhomogeneous temperature field across the crack vicinity, which was assumed to have resulted in secondary thermal stresses of 110 MPa magnitude, this secondary stress is included in the analyses here. The results of the Option 1 basic assessments are shown in Figure 3.16, where the different tests are annotated with their applied biaxiality ratio. More information on their specific ID and properties can be found in Table 3.6.

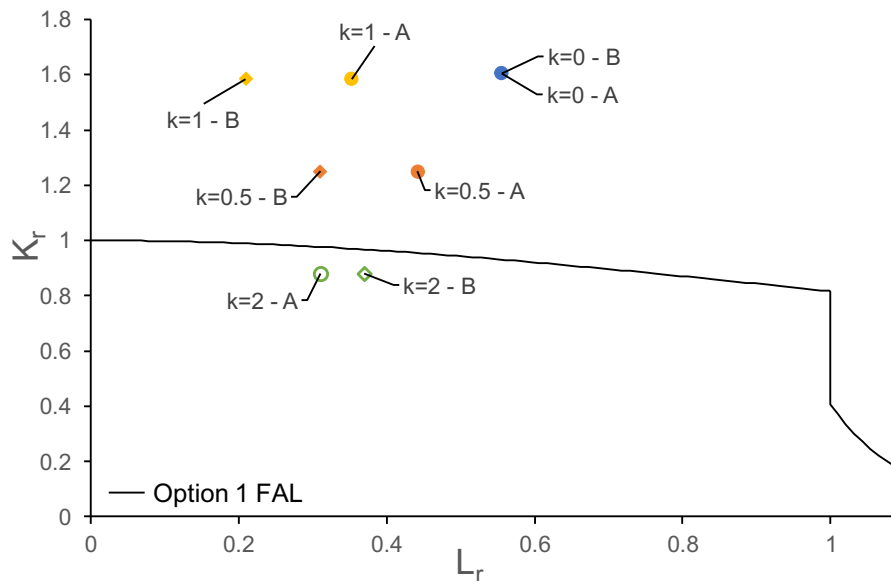


Figure 3.16: Option 1, A & B assessments

For biaxiality ratios of $k=1$ and $k=0.5$ the B assessments significantly decreases values of L_r , while for $k=2$ L_r increases. The latter case causes concern, since the limit load for a uniaxially loaded plate might not give safe results and would be worth exploring further if there are experimental data that capture failure at $k=2$.

Overall, apart from the specimen loaded with a ratio of $k=2$, which did not fail during testing (plotted with open symbols in Figure 3.16), all the failed specimens are safely predicted to be in the unsafe zone of the FAD. This supports the use the conservative 5% Master Curve values for the calculation of K_r in Option 1 assessments that disregard biaxiality. Given that all assessment points lie in the fracture dominated zone and above the FAL there cannot be a definitive conclusion about Equation 3.9 and it there is value in testing the limit load equation applied on the B assessments on tests conducted in the collapse dominated zone (high values of L_r).

Option 3 assessments

Given that the crack run throughout the thickness of the specimen and that the specimens were thick enough to be under plane strain in the middle, two-dimensional plane strain FE models are invoked. Due to symmetry, a quarter of the specimens is modelled.

The modelling strategy is like that of the surface breaking flaw models. As before, the load is applied as a homogeneous stress on the loading arms and the mesh around the crack tip is concentric circles, with the first line of elements being hexahedrons collapsed into wedges. The nodes at the crack tip are constrained to move as a single node in the elastic analyses, and as duplicate nodes in the elastic-perfectly plastic and elastic plastic analyses. The singularity is accounted for by moving the mid-side nodes of second order elements, at the crack edge, towards the crack tip at a distance of $\frac{1}{4}$ of the element edge, as suggested for elastic and elastic-plastic analyses with a hardening material [123], while the midsize node is placed at $\frac{1}{2}$ the distance of the element for elastic perfectly plastic analyses. J-integral is calculated over 7 contours, whilst the J values, converge from the third contour onwards. Following are the J-integral values (Mpa mm) calculated over the contours of the elastic-plastic model of $k=1$ when loaded to the cut-off value of L_r .

| | | | |
|-------------------|-------------------|-------------------|-------------------|
| Contour 1 - 683.5 | Contour 2 - 693.3 | Contour 3 - 696.8 | Contour 4 - 696.9 |
| Contour 5 - 697.0 | Contour 6 - 697.0 | Contour 7 - 697.1 | |

The cruciform and the uniaxial quarter models comprise 3042 and 2632 CPE8 elements respectively, a schematic of the modelled quarters is given in Figure 3.17.

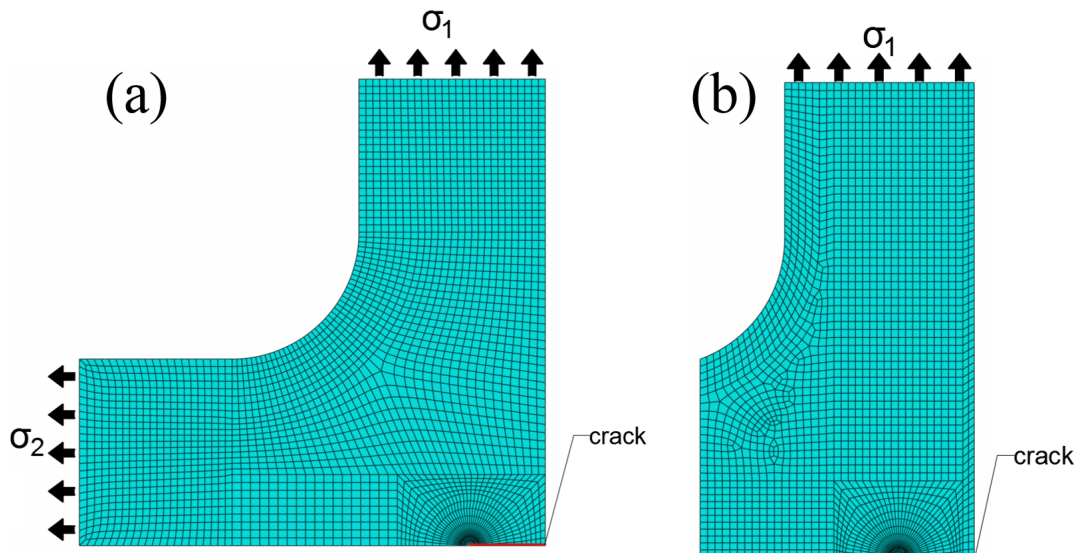


Figure 3.17: FE mesh of quarter of (a) biaxially, (b) uniaxially loaded specimens

The limit load values correspond to global collapse, the calculated values for each specimen/biaxiality ratio are shown in Table 3.10.

Table 3.10: Global Collapse Limit loads from FEA

| $k=0$ | $k=0.5$ | $k=1$ | $k=2$ |
|----------|---------|----------|---------|
| 17.12 MN | 19.4 MN | 19.87 MN | 9.93 MN |

The experimental failure loads, shown in Table 3.6, are applied to each model to calculate J_{el} at failure. In addition to the applied load, the equibiaxially loaded specimen ($k=1$) experienced an inhomogeneous temperature field during testing, which was assumed in previous assessments to have resulted in a stress field of 110MPa magnitude. To produce a stress field of this magnitude at the centre of the specimen a stress of 164 MPa is applied at the end of the loading beams. Whilst the factor ρ is also calculated and added to K as proposed in BS 7910.

Overall, the values of L_r are calculated by dividing the applied load by the FEA limit load and K_r by dividing the elastic K calculated from FE, which includes both primary and

secondary loads, by K_{mat} . The resulting Option 3 FALs with their respective assessment points are shown in Figure 3.18. The assessment points from the FEA provide safe results for all biaxiality ratios when the 5% probability of fracture Master Curve toughness is used, while using the 20% Master Curve toughness leads to $k=0.5$ lying in the safe zone.

Regarding the failure assessment lines, when k exceeds 1, the distribution of the load throughout the applied spectrum (0 - $L_{r,max}$) shows geometry dependence and is not applied consistently on the crack front. This means that plasticity evolves much more at the fillet of the cruciform specimen causing loads to be redistributed and J_{el-pl} to increase with a slower rate, acquiring slightly lower values than the corresponding J_{el} . Hence, even though for $k=2$ the FAL reaches values of K_r higher than one, this reflects geometry dependence.

Disregarding the aforementioned geometry dependence, it is observed for values of L_r approximately higher than 0.5, that as biaxiality increases and so do the limiting values of K_r given by the FAL. This means that as the biaxiality ratio increases, the energy release rate calculated from an elastic and an elastic plastic analysis deviate less thus denoting higher constraint of plasticity. The fact that higher in plane constraint (higher k) gives an Option 3 FAD with a larger safe zone seems counterintuitive with the perception that constrained plasticity favours brittle fracture and was expected at lower values of J . Even though this is excused by the nondimensionalization of J_{el} with J_{el-pl} , both of whose values decrease with increasing biaxiality, it is also due to assessing high and low constrained specimens with the use of the same lower bound fracture toughness, K_{mat} . To address this, constraint corrected assessments are developed using the guidance of BS 7910's Annex N.

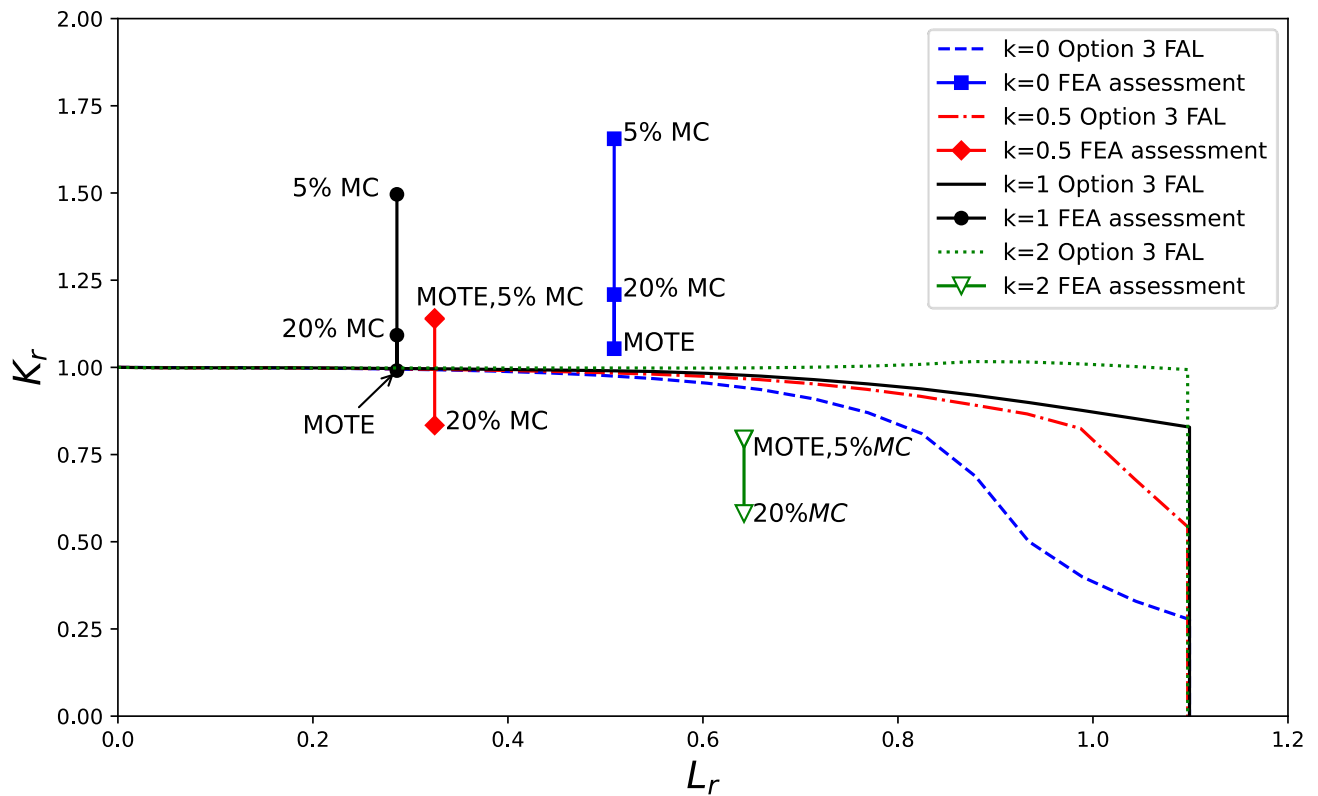


Figure 3.18: Option 3 FAD – Through thickness TWI plates

Option 3 – Constraint Corrected

A constraint corrected FAL is generated according to Equation 3.10.

$$K_r = f(L_r) \cdot [1 + a(-\beta L_r)^{k_1}]$$

Equation 3.10

BS 7910 and R6 contain analytical solutions for β and L_r in the case of uniaxially and equibiaxially loaded plates, however the current cruciform and cut cruciform geometry does not directly relate to a plate and the T- stress and L_r values calculated from FEA are used for the determination of β and consequently Equation 3.10. These values are shown in Table 3.11.

Table 3.11: Structural constraint parameter (β) of specimens

| Biaxiality ratio | $k=0$ | $k=0.5$ | $k=1$ | $k=2$ |
|------------------|--------|---------|--------|-------|
| β - FEA | -1.154 | -0.633 | -0.051 | 0.551 |

From Table 3.11, biaxiality increases the constraint relaxation decreases, i.e. β becomes less negative, leading to positive T-stresses and no constraint relaxation at a ratio of $k=2$. The resulting graph with Option 3-constraint corrected FALs along with the FEA derived assessment points are shown in Figure 3.19.

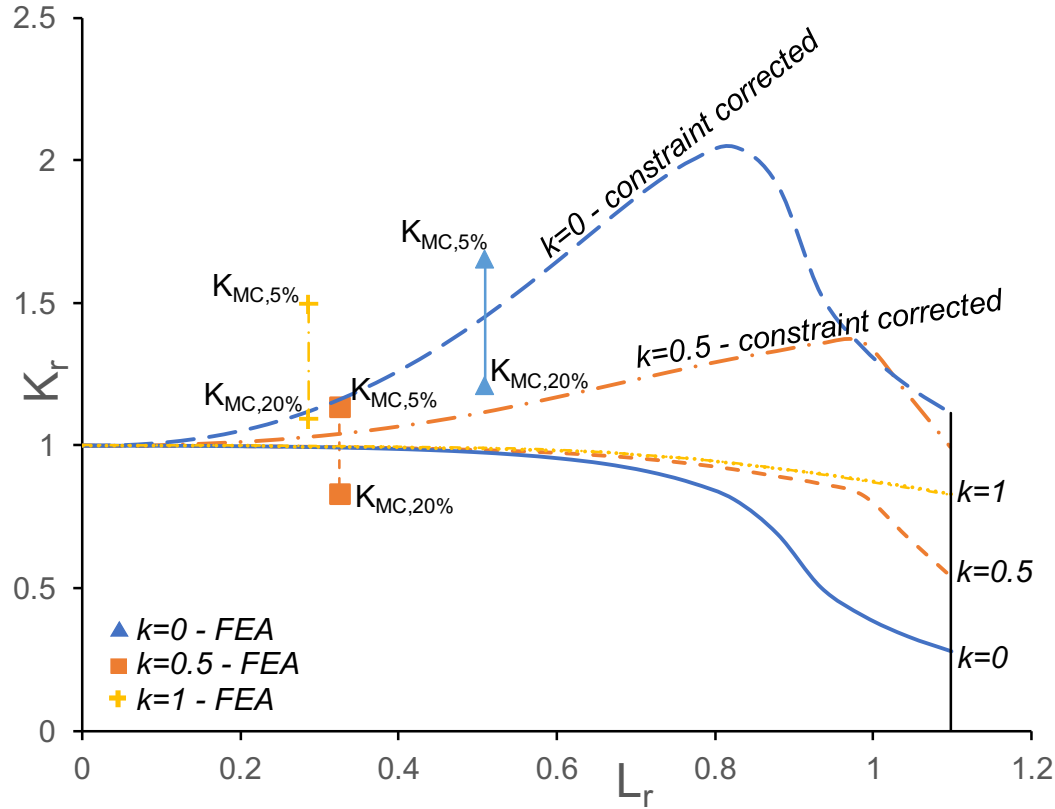


Figure 3.19: Constraint modified Option 3 FALs – Through thickness | TWI plates

Given that for $k=2$ no constraint relaxation is experienced, that specimen is not included in this analysis and in Figure 3.19. Additionally, for $k=1$ constraint relaxation is almost insignificant, and the constraint modified FAL lies on the original Option 3 FAL. For biaxiality ratios of $k=0.5$ and $k=0$ the constraint correction widely increases the safe zone of the FAD in accordance with k . Using a very conservative estimate of fracture toughness, i.e. the 5% probability Master Curve value, gives safe results for all the biaxiality ratios. However, with the 20% Master Curve toughness values both $k=0$ and $k=0.5$ assessment points lie in the safe zone. This could be due to assumptions included in the definition of the constraint dependent fracture toughness curve or the limited dataset out of which the Master Curve originated. It should be noted that the α and k values used are high in comparison to what Seal and Sherry [65] proposed, and future use of mean data may be useful. In any case it raises concern over the use of advanced methods in assessing a

component without a high number of fracture toughness tests or a conservative definition of K_{mat} .

3.3.5 Summary

Biaxially and uniaxially loaded cruciform tests conducted at the lower shelf of the fracture transition curve were analysed in accordance with the current BS 7910 and R6 fracture assessment procedures as well as with the use of tailor made FEA analyses.

Option 1 assessments showed that high constraint fracture toughness data can provide safe, albeit conservative results. The amount of conservatism depended on both the biaxiality and thus constraint and the geometry of the plates analysed here being different than the one of the analytical solutions used.

Use of alternative limit load solutions, for through thickness flawed plates, that incorporate biaxiality gave safe results while raising concern on the case of $k=2$ where L_r increased with biaxiality. The trends noticed in the analytical solutions followed those derived from the FEA developed here, however direct comparison between the limit load values of the two could not be made directly as the geometry of the cruciform specimens affected plastic collapse significantly. Such robust solutions that include biaxiality showed promise, however this study only preliminarily addressed this, as plastic collapse was not the governing failure mechanism in these tests and no definitive conclusion could be drawn.

For surface flaws the FEA confirmed the experimentally observed trend of crack opening stresses decreasing when moving from a uniaxially loaded to an equibiaxially loaded specimen. In other words, a decreased stress field was needed to develop around the crack for the equibiaxially loaded specimen to fail.

The FEA derived Option 3 assessments provided safe results for a conservative definition of K_{mat} . The Option 3 FALs showed that for biaxiality ratios lower than one, as biaxiality increased so did the limiting values of K_r with increasing L_r . This essentially expressed the suppression of plasticity experienced in higher constraint/biaxiality ratios. However, for through thickness flawed specimens, with higher values of biaxiality ($k > 1$) the FAL reached values of K_r higher than one, capturing geometry dependence and the creation of a plastic arc between the crack and fillet, rather than the biaxiality effect.

For the tests conducted at -100°C , Annex N of BS 7910 was followed to generate a constraint corrected Option 3 FALs which accounted for the change of fracture toughness in relation to constraint. As expected with increasing biaxiality the constraint relaxation was less, leading to the FAL for a biaxiality ratio of $k=1$ having a minimal change and for $k=2$ having none. For the biaxiality ratios of $k=0.5$ and $k=0$ the constraint correction widely increased the safe area below the FAL and non-conservative estimates of fracture toughness values provided unsafe results. This suggested that a conservative value of fracture toughness or a high number of tests should always follow the use of a more advanced procedure, such as that of Annex N, to ensure safety.

3.4 Conclusions

The capabilities and accuracy of FFS standards (BS 7910, R6) to assess uniaxial and biaxial specimens have been validated against a large experimental database.

From assessing historical data on commonly tested geometries that include wide plates and pressurised vessels from past experimental programs, the following conclusions are drawn:

- BS 7910 Option 1, can safely, albeit conservatively, estimate the fitness for service of a component and can predict failure
- The importance of validating against experimental data allows for calibration of the procedure and its clauses. Here this was manifested with recognizing a pattern of unnecessary conservatism on the reference stress solutions concerning cylinders/curved shells with axial through thickness, internal/external flaws. This was included in the previous version of the standard [71] and has been amended in the latest one [1], leading to a decrease of the calculated L_r by approximately 20%
- Experimental programs that do not focus on biaxiality cannot provide for a consistent database (material, test temperatures, loading conditions) to observe trends of biaxiality but instead prove the importance of analysing a consistent database with specific biaxiality related oriented experiments

Following this, fracture tests on biaxial and uniaxial specimens from a previously conducted program within TWI were assessed. The key conclusions of these analyses are:

- Option 1 assessments using high constraint fracture toughness data and uniaxial plate solutions provide safe and conservative results
- Plastic collapse loads show a trend of increasing from uniaxial ($k=0$) to equibiaxial loadings ($k=1$), while decreasing again for higher biaxiality ratios ($k>1$)
- Use of robust analytical limit load solutions that incorporate biaxiality show promise and agree with FEA limit load trend. Further validation of such solutions with data of specimens failing by plastic collapse is needed to draw a definite conclusion
- FEA of surface breaking flaws show that equibiaxial loading results in crack opening stresses reducing from the case of uniaxial loading at similar failure loads.
- Option 3 assessments provide safe results with high constraint fracture toughness values
- Option 3 FALs reveal the direct effect of biaxiality on the elastic plastic J-integral, which approximates its linear counterpart as biaxiality increases up to equibiaxial loading ($k=1$). For biaxiality ratios higher than that ($k=2$) the FAL captures geometry dependence making the role of geometry prominent
- Constraint corrected Option 3 FALs, result in safe assessments for all cases when conservative 5% Master curve fracture toughness values are used, however slightly higher values of fracture toughness can lead to unsafe predictions for through thickness cracks loaded in equibiaxial tension
- Caution is needed on the amount of data or the conservatism in fracture toughness values used in more advanced assessment procedures

Chapter 4 Biaxial and uniaxial experiments

4.1 Introduction

As explained in the previous chapters biaxiality has been studied mostly in combination with flaw depth. Even though this is a logical approach, given they are mostly found together in practice, it is difficult to quantify the extent of each of the two parameters on constraint, especially in a way that could be implemented in an ECA. In other words, it is considered beneficial to separate the two constituents found in practice so that future FFS standards can include a “fix” for biaxiality that can disregard the effects of crack depth.

In order to achieve de-convoluting the effects of flaw depth and biaxiality, the experimental program designed for this work includes uniaxial and biaxial bends on two different geometries, i.e. rectangular and cruciform specimens, accordingly, which include through thickness cracks. In this way no shallow flaw effects will be captured during testing. Details of the specimens and the rig design are given in Section 4.3. The through thickness cracks were created with fatigue cycles in tension, as described in detail in Section 4.6. The experimental layout was validated on its capability to capture biaxiality with conducting initial tests on PMMA specimens, explained in Section 4.3.2.

As highlighted by the analyses of Chapter 3, capturing the effect of biaxiality needs a very well characterized material and a consistent experimental database. The available experimental data in literature do not disclose all the needed information for additional investigations to be made, while the materials tested are not available for further characterization. Available plates of BS1501-224 28B C-Mn steel previously studied in [126]–[128] will be used to create test specimens. Details of the material used in this work and the existing mechanical properties data can be found in the Section 4.2.

Since toughness and failure mode are functions of both temperature and loading [14], the experimental program aims to test the specimens throughout a temperature spectrum which covers from lower transition to upper shelf behaviour. In detail, the effect of biaxial loading on crack tip triaxiality is expected to be negligible at extremely low temperatures that any loading would result to a minimum and unaffected fracture toughness. Thus, elastic response indicates that the temperature of testing is too low to capture a biaxial loading effect [41]. As temperature increases, pure cleavage behaviour is outweighed by accumulated plasticity and a balance can be found at which constraint and thus biaxiality effects on toughness can be evaluated, however at a very high temperature only its effect on plastic collapse might be able to be investigated. Further explanation on the testing temperatures can be found in Section 4.5.

Lastly, the results of the fracture tests are given for the different geometries tested in Section 4.9.

4.2 Material properties

The material used for the tests is extracted from BS1501-224 28B steel plates. The material properties are collected from [126]. This C-Mn ferritic steel comprises 79% Ferrite and 21% Pearlite. The chemical composition of the material is shown in Table 4.1.

Table 4.1: Chemical Composition of C-Mn steel Plate BS1501-224 28B [126]

| C | Si | Mn | Al | P | S |
|----------|-----------|-----------|-----------|----------|----------|
| 0.15 | 0.28 | 1.27 | 0.022 | 0.007 | 0.005 |

4.2.1 Tensile properties

The tensile properties for the BS1501-224 28B plate were measured in [126] for both the transverse and longitudinal orientations. The results for the different temperatures tested are shown in Table 4.2 and graphically in Figure 4.1.

Table 4.2: Tensile properties of BS1501-224 28B from [126]

| Specimen | Test Temperature (°C) | Yield Strength (MPa) | Tensile Strength (MPa) | Young's Modulus (GPa) |
|----------|--------------------------|-------------------------|---------------------------|--------------------------|
| S3A01 | -120 | 471.77 | 628.5 | 200.26 |
| S3A02 | -160 | 602.73 | 730.89 | 202.1 |
| S3A03 | -80 | 392.26 | 578.11 | 193.21 |
| S3A04 | -100 | 426.45 | 595.03 | 200.58 |
| S3A05 | -120 | 457.17 | 626.35 | 201.8 |
| S3A06 | -140 | 512.45 | 680.01 | 202.73 |
| S3A07 | -160 | 614.83 | 726.68 | 207.09 |
| S3A08 | -100 | 425.93 | 604.06 | 178.16 |
| S3A09 | -160 | 595.03 | 698.98 | 224.28 |
| S3A10 | -120 | 482.13 | 645.04 | 185.82 |
| S3A11 | -80 | 387.49 | 582.73 | - |
| S3A12 | 20 | 303.12 | 487.01 | 197.41 |
| S3B01 | -160 | 596.76 | 723.1 | 194.99 |
| S3B02 | -140 | 534.4 | 677.09 | 204.95 |
| S3B03 | -120 | 479.88 | 640.76 | 192.53 |
| S3B04 | 20 | 326.08 | 485.64 | 193.51 |
| S3B05 | -160 | 615.08 | 726.39 | 210.94 |
| S3B06 | -80 | 381.89 | 593.25 | 213.1 |
| S3B07 | -120 | 465.94 | 628.26 | 200.02 |
| S3B08 | 20 | 322.91 | 482.9 | 185.15 |
| S3B09 | -100 | 438.45 | 613.23 | 189.88 |
| S3B10 | -140 | 530 | 683.3 | 187.92 |
| S3B11 | -160 | 602.42 | 719.65 | 186.6 |
| S3B12 | -120 | 444.48 | 627.34 | 199.79 |

Additionally, full tensile stress-strain curves were provided in previous work ([126]–[128]), at -160 °C, -120 °C and room temperature.

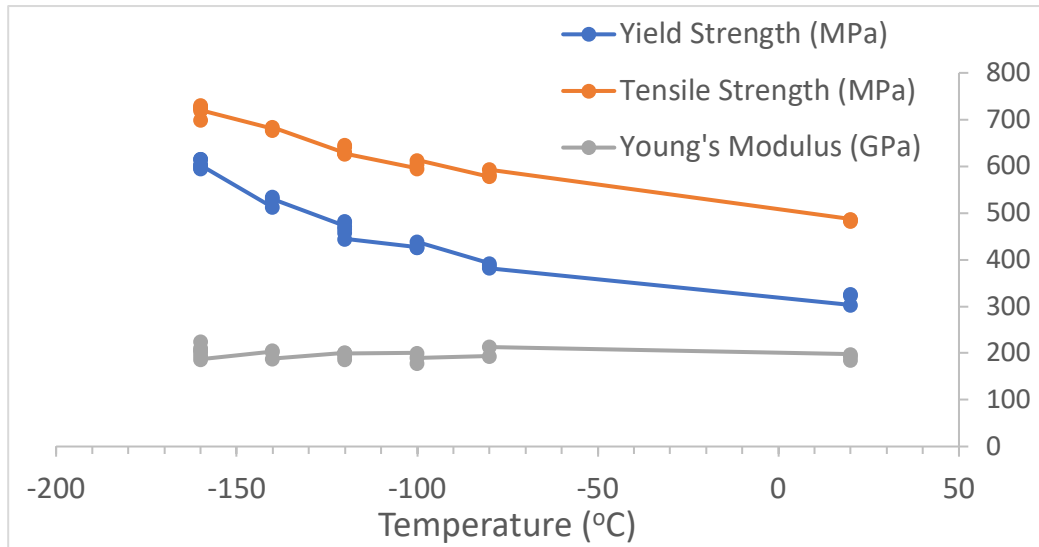


Figure 4.1: BS1501-224 28B - Tensile properties at different temperatures

4.2.2 Fracture toughness

In regard to fracture toughness values, previous work ([126]–[128]) includes multiple fracture toughness test results. The tests were conducted on,

- 25 mm thick compact tension (C(T)) specimens, that were either EDM-notched or fatigue pre-cracked
- 10 mm thick single edge bend (SE(B)) specimens, that were fatigue pre-cracked

Concerning the C(T) specimens testing temperatures varied from -160°C to room temperatures for the EDM-notched specimens, while fatigue pre-cracked C(T) specimens were tested at -160°C and -120°C. The majority of C(T) specimens were tested approximately at -160°C. SE(B) specimens were only tested at -157°C. The nominal crack length to specimen width ratio (a/W) was approximately 0.5 for both C(T) and SE(B) specimens.

An overview of the fracture toughness values calculated for fatigue pre-cracked specimens at [126]–[128] is given in Table 4.3.

Table 4.3: BS1501-224 28 fracture toughness measurements for fatigue pre-cracked specimens

| Reference | Specimen No. | Test Temperature (°C) | K _{JC} (MPa√m) |
|----------------------------|------------------------------------|-----------------------|-------------------------|
| | 1T (25mm) C(T) fatigue pre-cracked | | |
| Derreck Van Gelderen [126] | S3A04 | -160 | 57 |
| | S3A07 | -160 | 64.1 |
| | S3B07 | -160 | 35.43 |
| | S3A03 | -120 | 129.9 |
| | S3A06 | -120 | 158.68 |
| | S3B01 | -120 | 128.92 |
| Karin Rosahl [127] | 10 | -140 | 90.2 |
| | 11 | -140 | 85.2 |
| | 14 | -140 | 75.5 |
| | 17 | -140 | 96.4 |
| | 22 | -140 | 78.1 |
| | 24 | -140 | 53 |
| | 26 | -140 | 50.8 |
| | 29 | -140 | 61.9 |
| Balart & Knott [128] | 1 | -157 | 37.4 |
| | 2 | -157 | 38 |
| | 3 | -157 | 39.9 |
| | 4 | -157 | 41 |
| | 5 | -157 | 41.4 |
| | 6 | -157 | 44.3 |
| | 7 | -157 | 44.9 |
| | 8 | -157 | 49.5 |
| | 9 | -157 | 51.1 |
| | 10 | -157 | 53.3 |
| | 11 | -157 | 53.6 |
| | 12 | -157 | 57.9 |
| | 13 | -157 | 58.8 |
| | 14 | -157 | 61.1 |
| | 15 | -157 | 61.2 |
| | 16 | -157 | 64 |
| | 17 | -157 | 71.2 |

| 0.4T (10mm thick) SEN(B) – fatigue pre-cracked | | |
|--|------|------|
| 1 | -157 | 39.2 |
| 2 | -157 | 44.1 |
| 3 | -157 | 44.9 |
| 4 | -157 | 52.4 |
| 5 | -157 | 53.5 |
| 6 | -157 | 54.5 |
| 7 | -157 | 56.7 |
| 8 | -157 | 57.5 |
| 9 | -157 | 58.4 |
| 10 | -157 | 58.7 |
| 11 | -157 | 58.8 |
| 12 | -157 | 60 |
| 13 | -157 | 61.9 |
| 14 | -157 | 63.7 |
| 15 | -157 | 67.4 |
| 16 | -157 | 68.8 |

The results of these tests were used in [126] to calculate the reference temperature (T_0) and draft a Master Curve according to ASTM E1921 [129]. For the wire EDM-notched specimens $T_0 = -175$ °C while for fatigue pre-cracked specimens $T_0 = -131$ °C. This in combination with the transition curve developed for this material in Section 4.2.4 are used to decide on the testing temperatures of the biaxial and uniaxial bend tests of this study.

4.2.3 Metallography of material

The existing BS1501-224 28 plates that are used for this experimental program had been cut, in the past, in a rectangular shape, thus not making it easy to distinguish between the rolling and the transverse direction. Fractography results obtained from Rosahl [127] showed that grains were fairly uniform in arrangement and in size in both directions and was thus expected that performing fracture toughness experiments on L-T and T-L specimens would not yield any significant differences in fracture.

Additional investigation carried out by Van Gelderen [126], which included fracture toughness and tensile tests on specimens from both directions of the plate and from different plates supported this. The results of fracture toughness tests on fatigue pre-

cracked specimens and tensile tests showed that there is no trend of mechanical properties being different with orientation [126, p. 418] [126, p. 384].

Additional metallographic work is conducted in this work, with small samples being taken from the three different surfaces of each plate, i.e. A,B,C, as shown in Figure 4.5. The samples were grinded and polished before being placed under the optical microscope. All six plates exhibit the same microstructure. Here only the images of plate 2 are presented in Figures 4.1 – 4.3. The figures show there is no clear indication regarding rolling direction and that pearlite bands are more prominent towards the middle of the specimen. In light of the latter, test specimens are extracted from near the surfaces to ensure microstructural homogeneity.

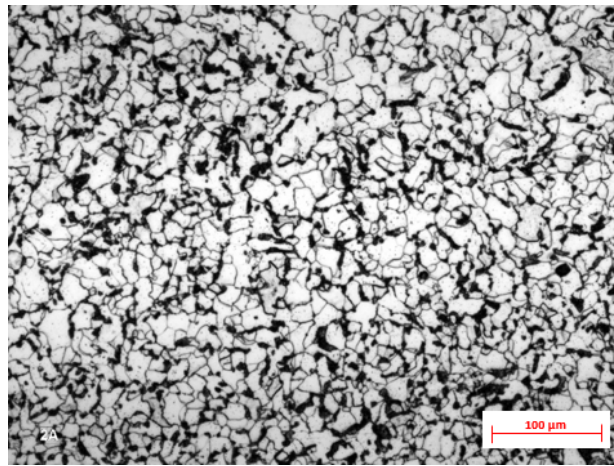


Figure 4.2: Microstructure of face A, Plate 2

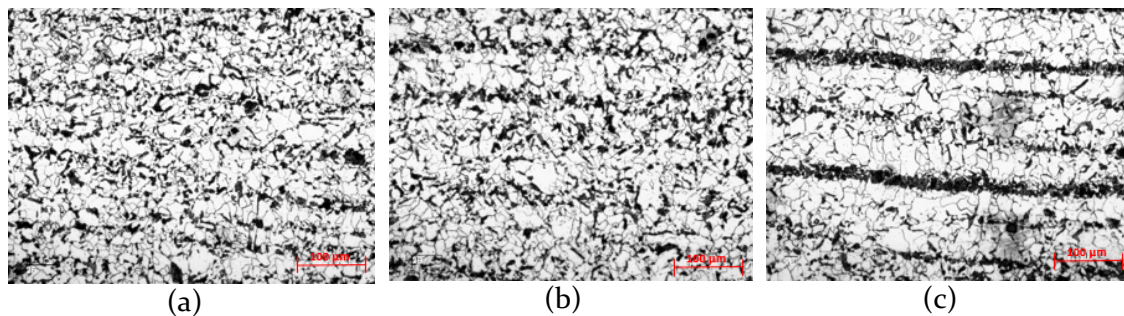


Figure 4.3: Microstructure of face B, Plate 2 at (a) the surface, (b) quarter thickness, (c) mid-thickness

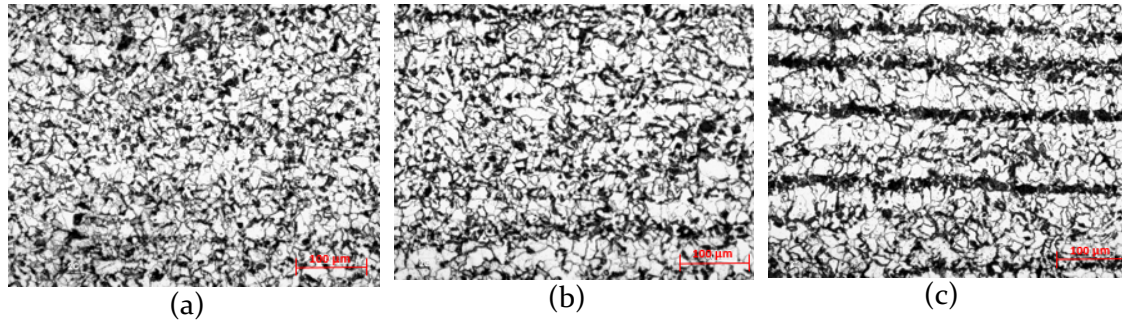


Figure 4.4: Microstructure of face C, Plate 2 at (a) the surface, (b) quarter thickness, (c) mid-thickness

4.2.4 Transition Curve

4.2.4.1 Charpy specimen design

Given the constraint phenomena that are addressed in this work, it is crucial to have a clear image of the ferritic steel's transition curve. To obtain this small Charpy V-notch specimens were extracted from one of the BS1501-224 28B plates (plate number 2).

The specimens complied to BS EN ISO 148-1:2010 [130] and were designed according to its specifications.

Charpys were extracted from near the top and bottom surfaces of the plate where the microstructure is similar as shown in Section 4.2.3. The Charpy notches all had the same orientation in regard to the rolling direction, however it is not certain, due to the lack of information whether their orientation is L-T or T-L.

The specimens were handed to TWI Ltd. for testing, where they were tested at various temperatures to obtain the transition curve of the steel. Overall, 20 specimens were cut and tested. This provides a means to correlate the toughness in the later interpretations of Chapter 5, to see how reliable that data is.

4.2.4.2 Charpy test results - Transition curve

The results of Charpy tests are presented graphically along with a transition curve that was fitted using a Burr distribution, as advised in [131], in Figure 4.5.

From Figure 4.5 the lower shelf is reached at approximately -100°C , while the fracture mode is transitioning from brittle to ductile between -100 and -40°C .

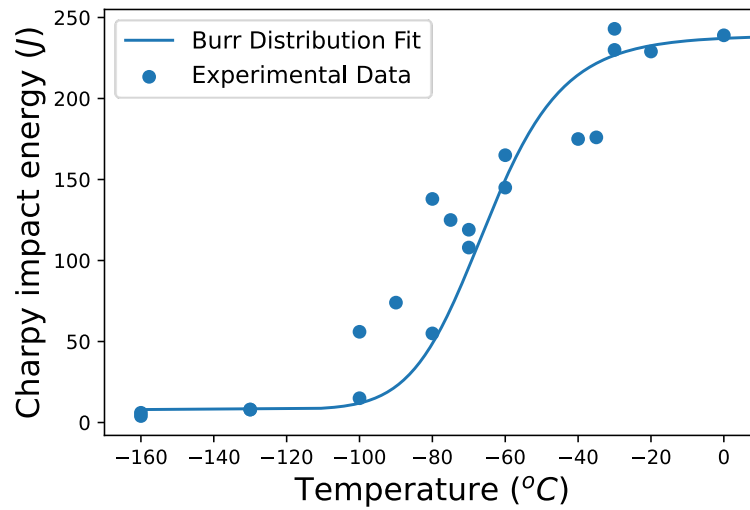


Figure 4.5: BS1501-224 28B Charpy test results & Transition Curve

4.3 Design of experiments

4.3.1 Test setup

To capture solely the effect of biaxiality, uncoupled from any shallow flaw effects this experimental program includes uniaxial and biaxial bending applied to specimens with through thickness cracks of rectangular and cruciform sections, respectively.

The experimental rig with a cruciform/5 Point Bend (5PB – equibiaxially bent) specimen and a rectangular/3 Point Bend (3PB - uniaxially bent) specimen are shown in Figure 4.6 and Figure 4.7 respectively. Their engineering drawings with dimensional details are shown in Figure 4.8 and Figure 4.9. The initial thickness of the specimens was designed to be 25 mm, same as the specimen thickness of the PMMA samples that were used to test the rig, shown in Section 4.3.2, however the limited material available allowed for 10 mm thick specimens to be cut. The nominal width (W) of the specimens is considered as that of the central area tested, i.e. disregarding the loading legs of the cruciform specimens and equal to the width of the rectangular specimens which was 50 mm. All specimens, both rectangular and cruciform, are designed to contain a through thickness with a desired crack length to nominal width ratio ($2a/W$) of 0.5. Details on the preparation of the samples and the fatigue pre-cracking of the steel specimens are given in Sections 4.4 and 4.6.

Regarding the experimental rig, it consists of:

- a base, in the shape of a hollow cylinder, shown in Figure 4.10
- 4 smaller solid cylinders lying on the indentations of the base and on which the specimens will be placed, allowing relative rotation to their central axis, Figure 4.11
- a semi-spherical punch, which will apply the load, shown in Figure 4.12

After the specimens are placed on the base as shown in Figure 4.6 for the rectangular shaped specimens and Figure 4.7 for the cruciform specimens, the punch is pushed downwards from the hydraulic press generating a three-point bend in the case of the rectangular shaped specimens and a five-point bend in the case of the cruciform ones. The biaxiality ratios (k) included in this study are controlled by the geometry of the setup and are $k = 0$, i.e. uniaxial, for the rectangular shaped 3PB specimens and $k = 1$, i.e. equibiaxial, for the case of the cruciform 5PB specimens.

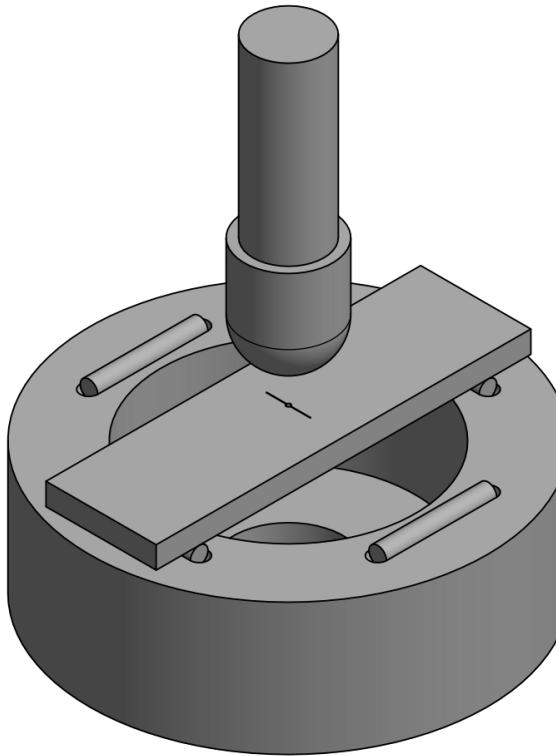


Figure 4.6: Basic setup of 3 Point bend

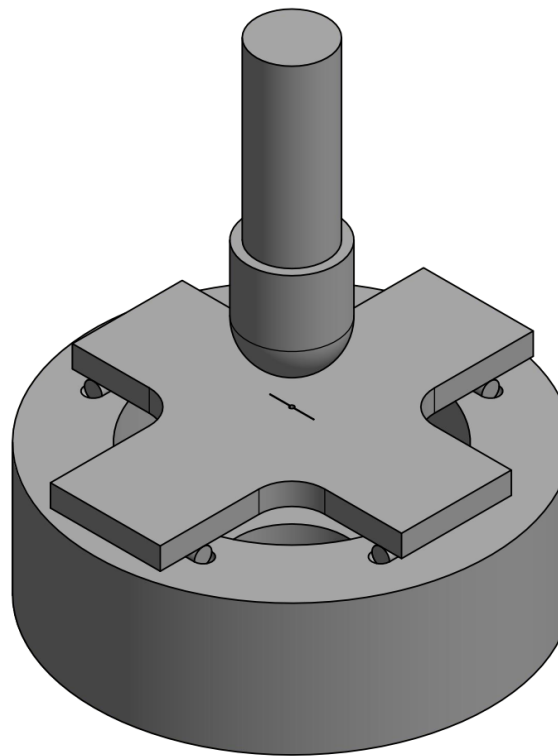


Figure 4.7: Basic setup of 5 Point bend

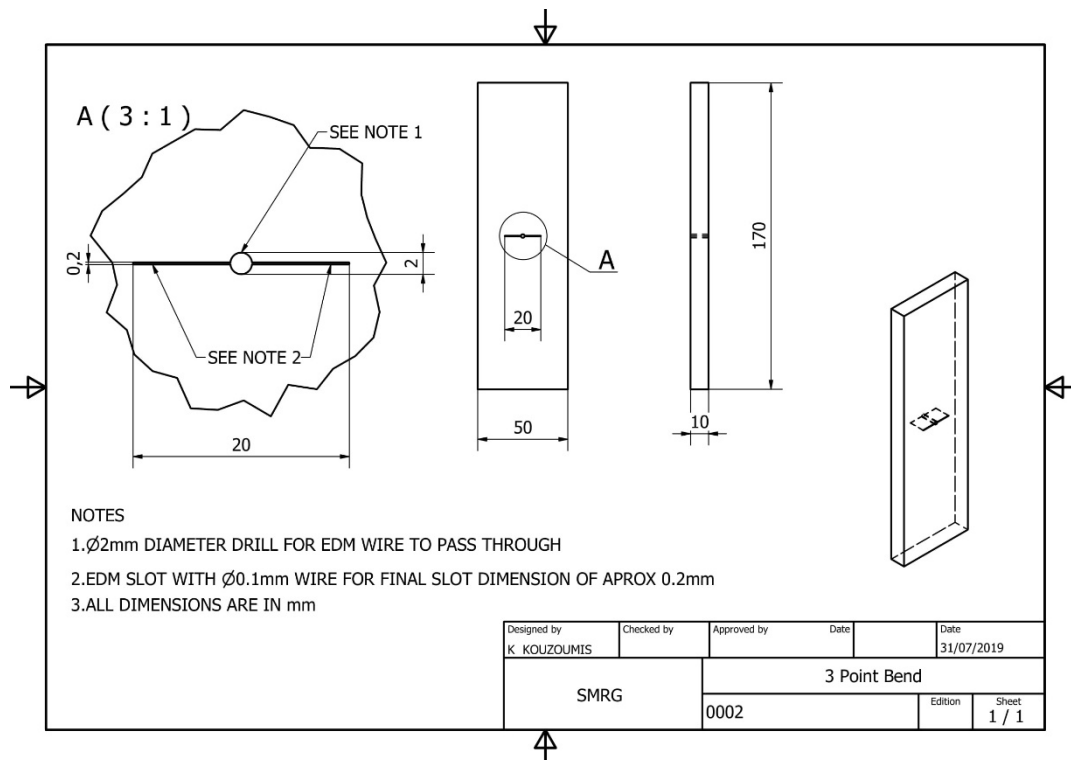


Figure 4.8: Engineering drawing of a rectangular specimen

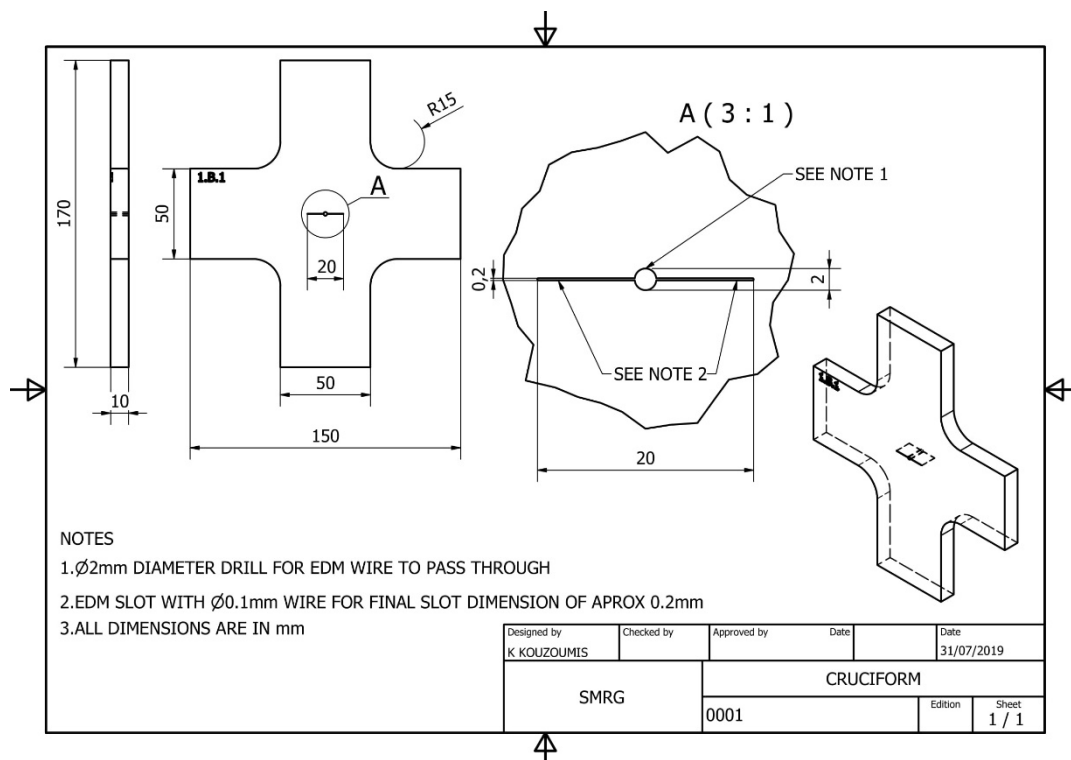


Figure 4.9: Engineering drawing of a cruciform specimen

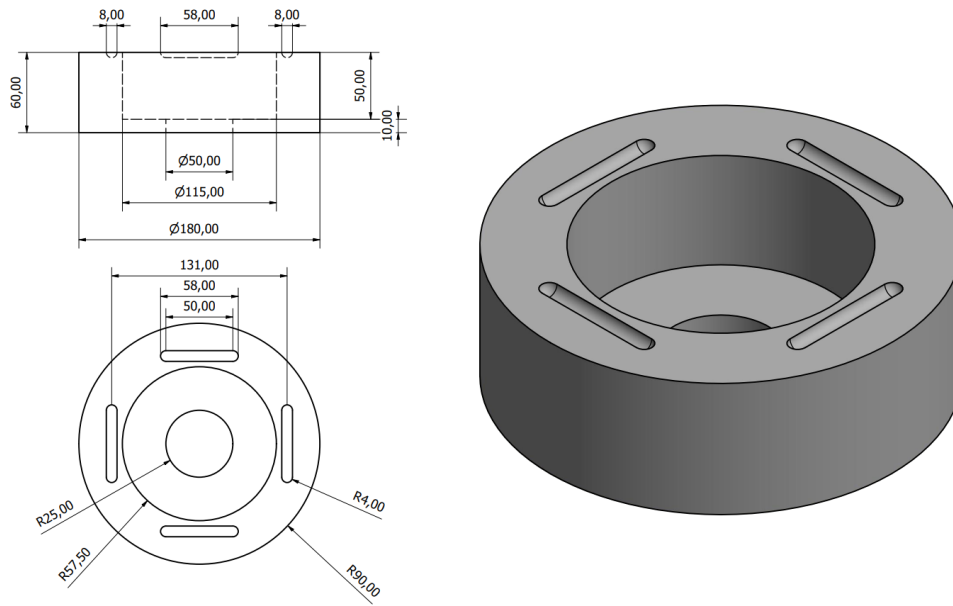


Figure 4.10: Hollow cylinder base of experimental rig

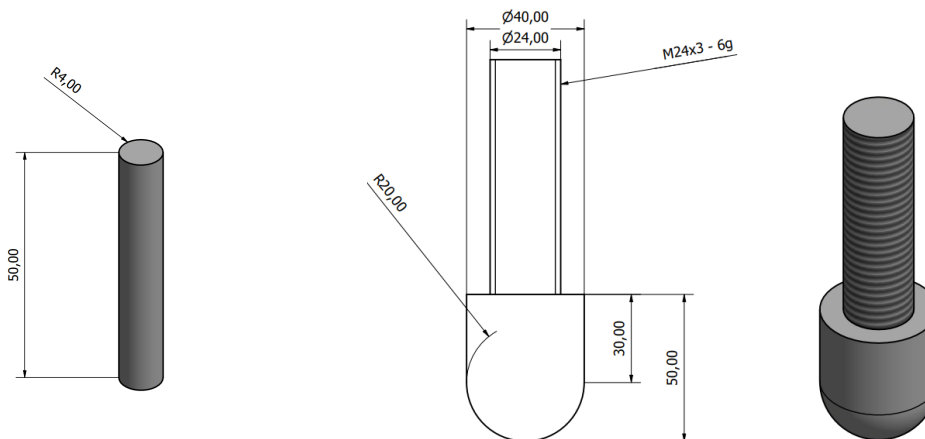


Figure 4.11: roller of rig

Figure 4.12: semi-spherical punch of rig

It should be noted here that the punch, the rig and the rollers were all used in earlier research and were not fully redesigned from scratch. Even though the punch has a relatively small diameter the low temperature of testing was expected to create a brittle behaviour allowing for minimum indentation before fracture. Additionally preliminary FEA had ensured that the fillet of the cruciform specimens had a radius which ensured no stress concentration there higher than the crack area.

4.3.2 Testing the setup

The experimental setup was initially tested with the use of PMMA samples, expecting that its linear elastic behaviour approximates that of the steel in the lower transition region and the crack propagation between the PMMA and the steel specimens will be similar when fracture happens in brittle manner, i.e. when no significant ductile tearing occurs.

The setup was the same as that described in the previous section for the steel specimens. The tests were conducted at room temperature using a 250kN Instron machine. The measured values during testing were the load and displacement recorded by the Instron machine as well as the crack mouth opening displacement measured by a CMOD (Crack Mouth Opening Displacement) gauge. The CMOD gauge was placed on knife edges that were glued on the specimens at a distance of approximately 8 mm either side of the crack mouth.

The PMMA specimen database comprises two rectangular shaped specimens which have the geometry of Figure 4.13 and two cruciform specimens with the geometry of Figure 4.14. The specimens were loaded in displacement control (0.2 mm/min) to the point of fracture.

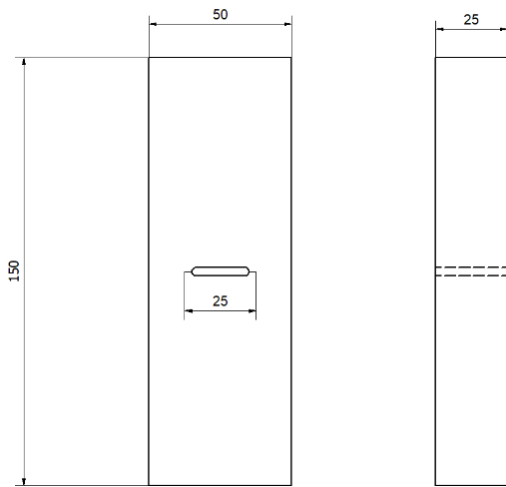


Figure 4.13: 3 Point Bend Specimen (dimensions in mm)

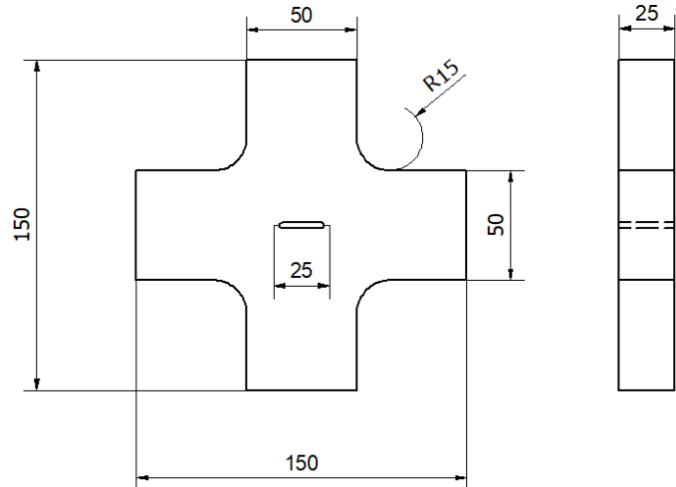
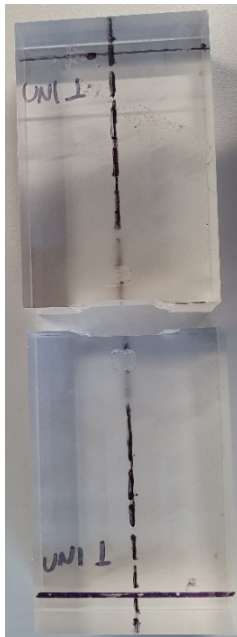


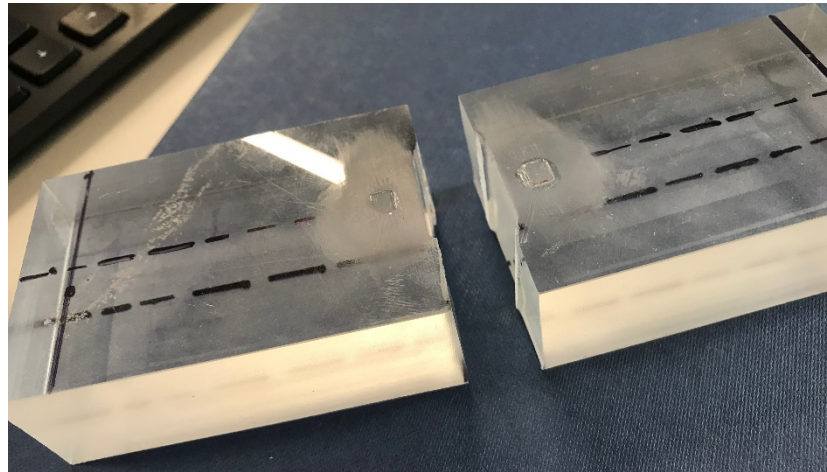
Figure 4.14: 5 Point Bend Specimen (dimensions in mm)

Figure 4.15 shows a uniaxial specimen post fracture and Figure 4.16 shows a biaxial specimen. It is observed in the latter that the fracture trajectory has an “S” shape, this effect of the curved crack has been noted in literature [18] as an effect of biaxiality. Hence, the trajectory of the crack observed in these specimens provides confidence that the current setup captures biaxiality. Additionally, the Load-CMOD curves captured during

the experiments for all 4 specimens are shown in Figure 4.17, where only linear elastic behaviour was met during the test and the fracture was purely brittle.

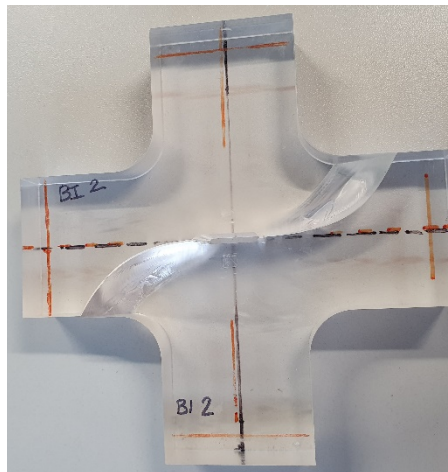


a) Base view

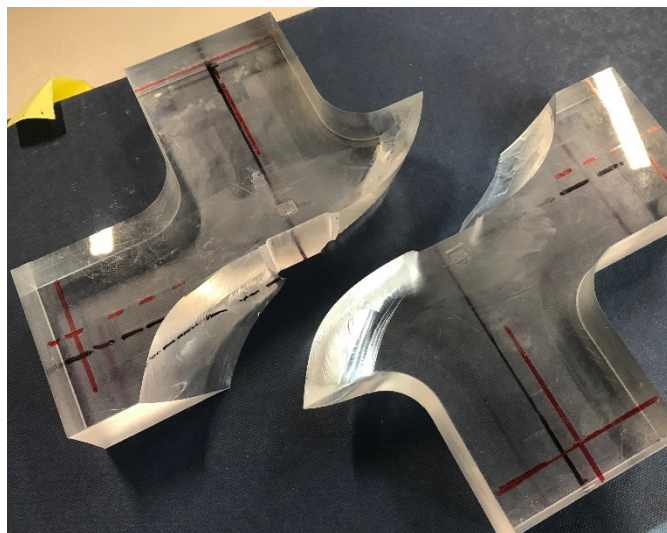


b) Projected view

Figure 4.15: PMMA Uniaxial - 3PB specimen - Post fracture



a) Base view



b) Projected view

Figure 4.16: PMMA Biaxial - 5PB specimen - Post fracture

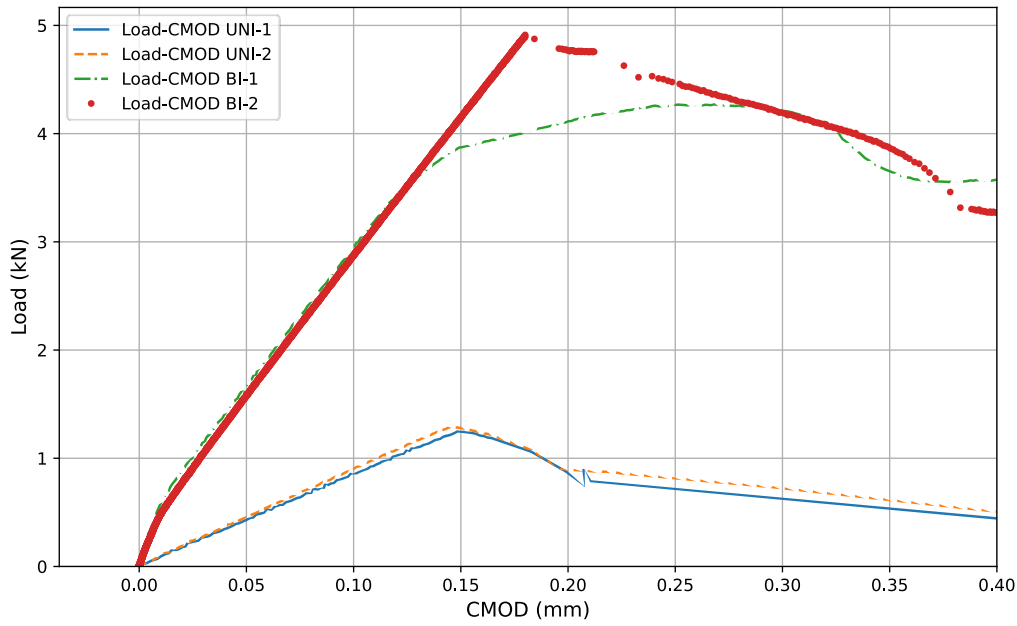


Figure 4.17: Experimentally measured Load - CMOD for PMMA specimens

It is apparent from Figure 4.17 that the cruciform specimens require higher loads to fracture in comparison to the uniaxially loaded specimens. This can be partly explained by the fact that the uniaxial specimens have smaller width, however this is mostly due to the biaxially loaded specimen being loaded in a 5-point bend. In other words, a significant fraction of the load applied by the punch is consumed for the in-plane loading.

4.4 Steel specimens

As denoted in Section 4.3.1 the thickness of the steel specimens was 10 mm. The specimens were extracted from near the surface of the plates to ensure microstructural consistency between the samples, similarly to the extraction of the Charpy specimens in Section 4.2.4.1. An engineering drawing of the rectangular and cruciform specimens can be seen in Figure 4.8 and Figure 4.9 respectively.

All specimens, both rectangular and cruciform, contain through thickness EDM notches of 20mm length, made with a 0.1 mm EDM wire, which are then fatigue pre-cracked to ensure a sharp crack is developed. The initially desired crack length to nominal width ratio ($2a/W$) was 0.5. Details on the preparation of the samples and the fatigue pre-cracking are given in Section 4.6.

4.5 Test temperature

As observed in [14] toughness is a function of both temperature and biaxial loading, i.e. as temperature increases, uniaxially loaded specimens experience a loss of constraint and consequently high toughness values. However, biaxially loaded specimens keep their high constraint levels up to the higher temperatures [14]. To capture constraint effects due to biaxiality during testing, the tests should be conducted at temperatures which are:

1. Low enough, at the lower region of the transition curve, so that plasticity does not develop throughout the ligament, leading to its plastic collapse but instead a small-scale yielding condition is approached
2. High enough for some plasticity to be developed so that its relationship with constraint and how it affects it can be studied

This experimental program originally attempted to capture the effect that biaxiality has on the plastic collapse load and the change of the governing failure mechanism from small scale yielding to plastic collapse. It was the intention of the author for three different temperatures varying from lower shelf to upper shelf to be tested. Unfortunately, COVID-19 restrictions did not allow for enough experimental cycles to be conducted and only a single temperature was decided to be tested.

The test temperature would need to be one at which experimental data already existed and be close to the lower shelf but allowing for limited amounts of plasticity. The existing fracture testing data of [126] were used as guidelines. In particular, the material had a reference temperature was $T_0 = -131^\circ\text{C}$, calculated with the data of full thickness (25 mm) C(T) pre-cracked specimens that were tested between -160°C and -120°C . It was seen from the Load-CMOD curves of the -160°C and -120°C pre-cracked C(T) specimens, shown in [126, p. 342] and [126, p. 345] respectively, that almost fully elastic behaviour was observed at -160°C while some plasticity was developed at -120°C . Since the specimens tested here are thinner and have lower out-of-plane constraint some plasticity can be expected at -160°C . This in addition with the high number of data available (fracture toughness, tensile properties) at -160°C designated this temperature as appropriate for testing, where the toughness values from the literature varied from 35 to 71 $\text{MPa}\sqrt{\text{m}}$.

To achieve testing at cryogenic temperatures the rig is placed inside a well-insulated Zwick cooling chamber of 1170 mm length 595 mm width and 800 mm depth with a wall

thickness of 80 mm. At the opening of the chamber Thermalfleece Cosywool is used to seal the two parts, while inside, surrounding the rig, polystyrene rings and blocks are added. The setup of the chamber is presented visually with the chamber open and closed in Figure 4.26 (a) and (b) respectively. Cooling is achieved with the use of liquid nitrogen that is provided to the chamber shown in Figure 4.26 (c). A Eurotherm controller is used to control the temperature. To ensure that all the specimen has reached the desired temperature and that no thermal gradients exist, once its surface reaches that temperature, it is left for another 30 mins in the chamber before testing commences.

4.6 Fatigue pre-cracking

From fabrication the specimens have a 20 mm long through thickness notch made with wire EDM cutting using a wire of 0.1 mm radius. To grow a sharp crack from the EDM notch prior to fracture testing, the specimens are fatigue pre-cracked in tension. The fatigue pre-cracking setup of a rectangular shaped specimen can be seen in Figure 4.18.

There are two stages included in fatigue pre-cracking the specimens. The first one is specimen preparation. The specimens are first polished using a hand polisher until a good surface finish is achieved. The specimens have an appropriate surface finish only from the one side, hence only one side can be polished and prepared for visual observation of the fatigue pre-cracking. Following, at a distance from each end of the EDM notch two lines are scratched using a scribe. The first of these lines represents the crack length ($a=11.5\text{mm}$) at which the load will be adjusted to avoid creating a plastic wake ahead of the crack during pre-cracking and the second one represents the desired crack length ($a=12.5\text{ mm}$).

The second stage is the stage of the actual fatigue pre-cracking. The specimen is clamped at both legs, that are perpendicular to the crack, by the machine and is loaded in load controlled cyclic tension. To monitor the crack growth a high-resolution camera is used to observe the crack opening. Loading continues until the crack reaches the scribed lines adjusting the load as needed during the procedure. The scribed lines and crack growth as observed by the camera can be seen in Figure 4.19.

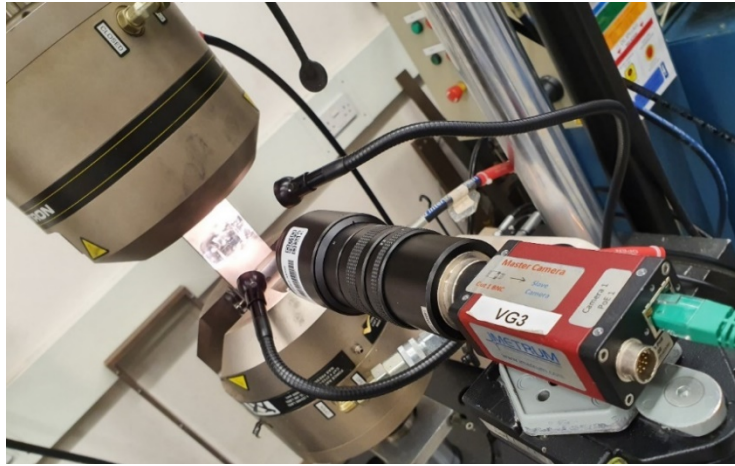


Figure 4.18: Setup of Fatigue pre-cracking a rectangular shaped specimen

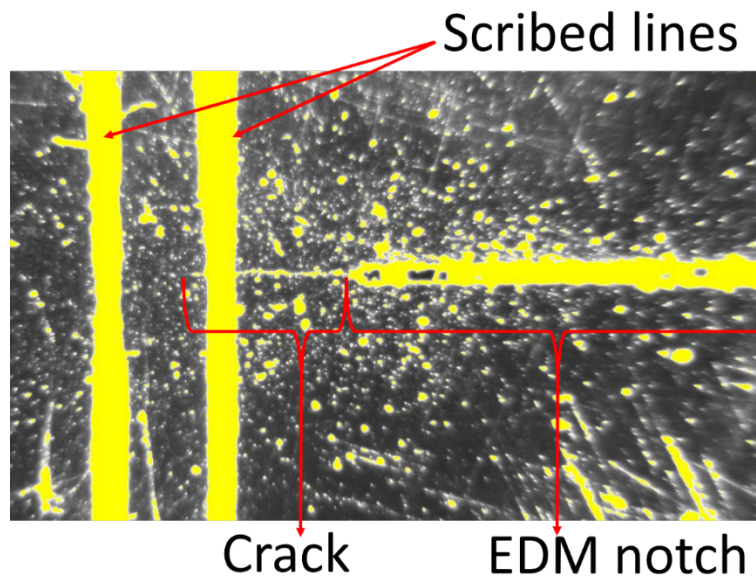


Figure 4.19: Crack growth as observed from camera

The frequency of loading was restricted by the hydraulic system at 15Hz.

The applied loads for fatigue pre-cracking are calculated using the guidance of ASTM-E399 [132]. To ensure that a sharp crack is being tested Annex 8.3.3 advises that a minimum fatigue produced crack length is reached. This length for the case of notches ending in a hole is

$$\max (0.5D, 1.3 \text{ mm})$$

With D being the diameter of the hole. The EDM notch is created using a wire of 0.1mm diameter, and the end hole is considered of 0.2mm diameter. This means that the fatigue

pre-crack length should be larger than 1.3 mm, hence the desired length of 2.5mm satisfies the condition.

Additionally, Annex 8.4.2 and 8.4.3 of ASTM-E399 [132] suggest that the for main duration of the procedure the maximum stress intensity factor (K_{max}) reached during the cycling loading should be lower than 80% of the fracture toughness (K_Q) of the material, while for the latest stages K_{max} should be reduced to $<0.6 K_Q$. However, Annex 8.4.4 suggests that if fatigue pre-cracking is conducted at a temperature T_1 and testing is to be conducted at a temperature T_2 then $K_{max(T_1)}$ shall not exceed the limits of Equation 4.1.

$$K_{max(T_1)} < 0.6 (\sigma_{ys(T_1)}/\sigma_{ys(T_2)}) K_{Q(T_2)} \quad \text{Equation 4.1}$$

where σ_{ys} is the yield stress at the respective temperature. The latter condition is used to calculate the maximum loads that are applied during fatigue pre-cracking. Even though testing is done at different temperatures, the properties of the lowest temperature (-160°C) are used for the calculations of the fatigue pre-cracking loads. There are no existing fracture data for the specimen geometries that are fatigue pre-cracked/tested here, however previous work on the same batch of material [126], [128] includes fracture toughness values that have been calculated from testing C(T) and SEN(B) specimens at -160 °C (-157°C). Additionally [126], [128] include tensile properties at -160 °C and room temperature, which are used for the calculations. The yield stress at the two temperatures is,

- $\sigma_{ys(RT)} = 317 \text{ MPa}$ at room temperature
- $\sigma_{ys(-160)} = 532 \text{ MPa}$ at -160 °C

Table 4.4 shows the values of fracture toughness for the two specimen configurations and the maximum allowable stress intensity factors that are calculated for them ($K_{max} C(T)$, $K_{max} SEN(B)$) according to [132].

Table 4.4: Upper limit K values for fatigue pre-cracking

| Specimen Type | average K_Q [128] (MPa $\sqrt{\text{m}}$) | $K_{max} < 60\% (\sigma_{ys(RT)}/\sigma_{ys(-160)}) K_Q$ (MPa $\sqrt{\text{m}}$) |
|---------------|--|---|
| SEN(B) | 56.3 | $K_{max} SEN(B) = 15.8$ |
| C(T) | 44.3 | $K_{max} C(T) = 20.1$ |

To translate applied load to stress intensity factor values, the BS 7910 [71] stress intensity factor solution for a centrally cracked plate in tension is used. This is also given here as Equation 4.2.

$$K_I = P_m [\sec(\pi a/W)]^{0.5} \sqrt{\pi a} \quad \text{Equation 4.2}$$

Where P_m is the applied tensile load. The specimen width W is considered as 50 mm for the rectangular specimens and 150 mm for the cruciform specimens. The maximum fatigue pre-cracking loads (P_{\max}) are selected so that they won't exceed neither of $K_{\max} C(T)$ and $K_{\max} SEN(B)$ at any stage of crack growth.

Higher loads are initially used up to a crack length of $a=11.5\text{mm}$. Then the load is decreased and cycling loading continues until a length of $a=12.5\text{mm}$ is reached. The maximum (P_{\max}) and minimum (P_{\min}) loads applied during pre-cracking as well as their load ratio ($R = P_{\min}/P_{\max}$) are shown in Table 4.5.

Table 4.5: Loads used for fatigue pre-cracking

| | Rectangular specimens | |
|-----------------|-----------------------|-----------------------------|
| | For $a \leq 11.5$ | For $11.5 \leq a \leq 12.5$ |
| P_{\max} (kN) | 36 | 30 |
| P_{\min} (kN) | 3.6 | 3 |
| $R=$ | 0.1 | 0.1 |
| | Cruciform specimens | |
| | For $a \leq 11.5$ | For $11.5 \leq a \leq 12.5$ |
| P_{\max} (kN) | 40 | 35 |
| P_{\min} (kN) | 4 | 3.5 |
| $R=$ | 0.1 | 0.1 |

The stress intensity factor value of the maximum load ($K_e(P_{\max})$) calculated at each crack length is shown together with $K_{\max} C(T)$ and $K_{\max} SEN(B)$ in Figure 4.20 and Figure 4.21 for the rectangular and cruciform specimens respectively. The resulting pre-fatigue crack shape is identified later in Chapter 5 as it will be used for the FEA analyses.

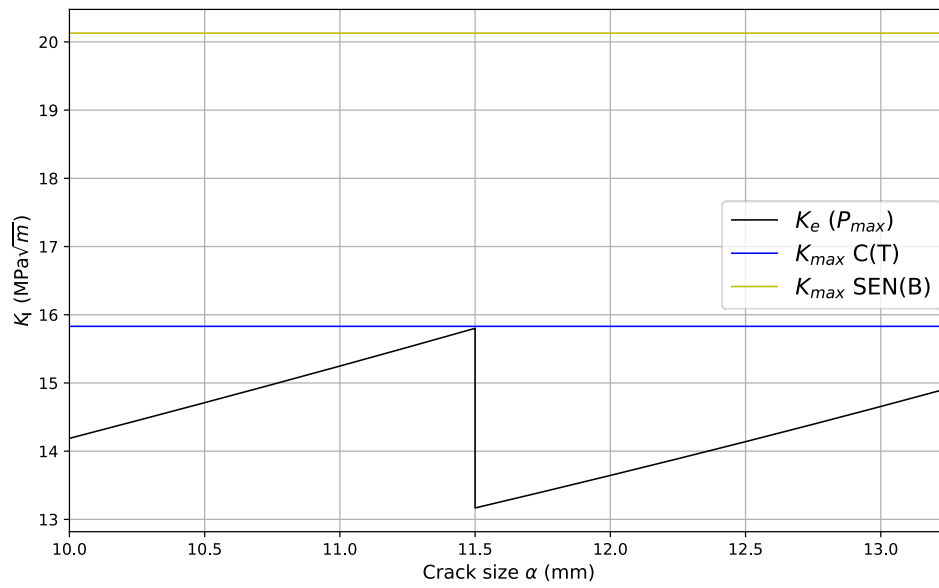


Figure 4.20: Maximum stress intensity factor values during pre-cracking of rectangular specimens

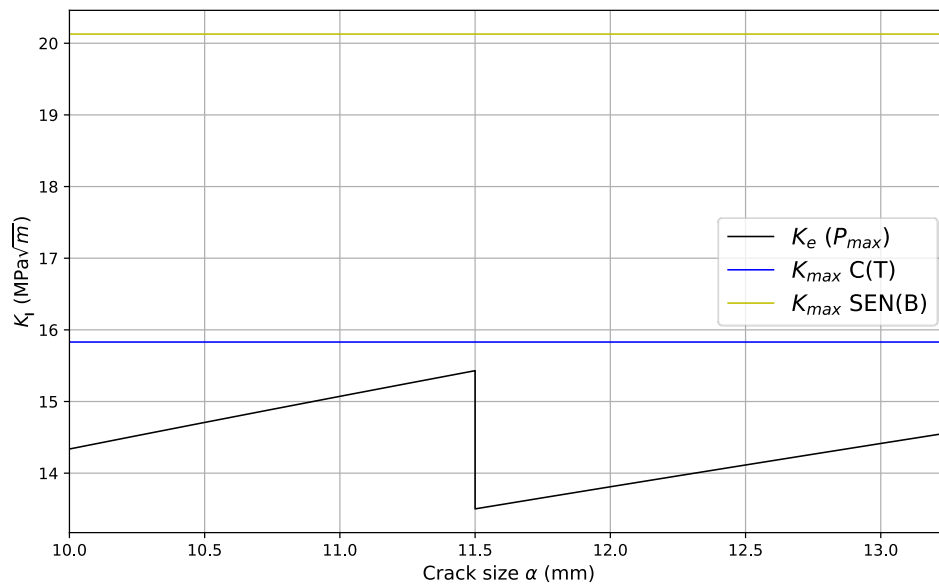


Figure 4.21: Maximum stress intensity factor values during pre-cracking of cruciform specimens

4.7 Instrumentation

During testing four different physical quantities are measured, i.e.

1. Displacement
2. Load
3. Temperature
4. CMOD

Load and displacement values are recorded directly from the Dartech 500 kN machine that is used. The remaining two quantities are measured from separate instruments and all of the values are gathered using a Vishay System 5000 data acquisition system.

Temperature is measured with the use of type K thermocouples (Chromel-Alumel). Type K thermocouples can measure temperatures from -200 to 40°C. They comprise a nickel-chromium positive leg and a nickel-aluminium negative leg which are twisted, and spot welded at their end. Each specimen has 2 thermocouples whose end is spot welded on the specimen. A representative sketch of a uniaxial 3PB and biaxial 5PB specimen and the places where the thermocouples are attached is shown in Figure 4.22 and Figure 4.23 respectively.

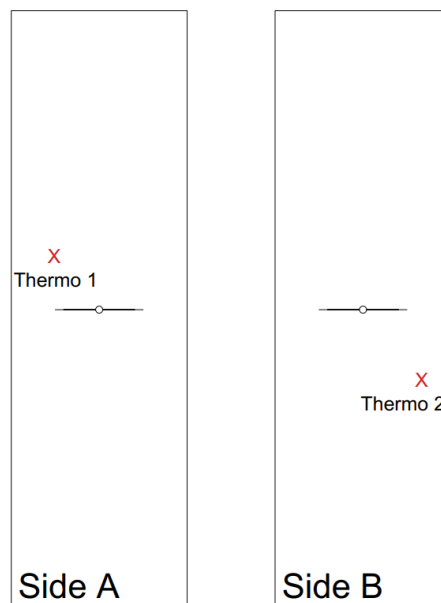


Figure 4.22: Schematic showing the thermocouple positions on a 3PB specimen

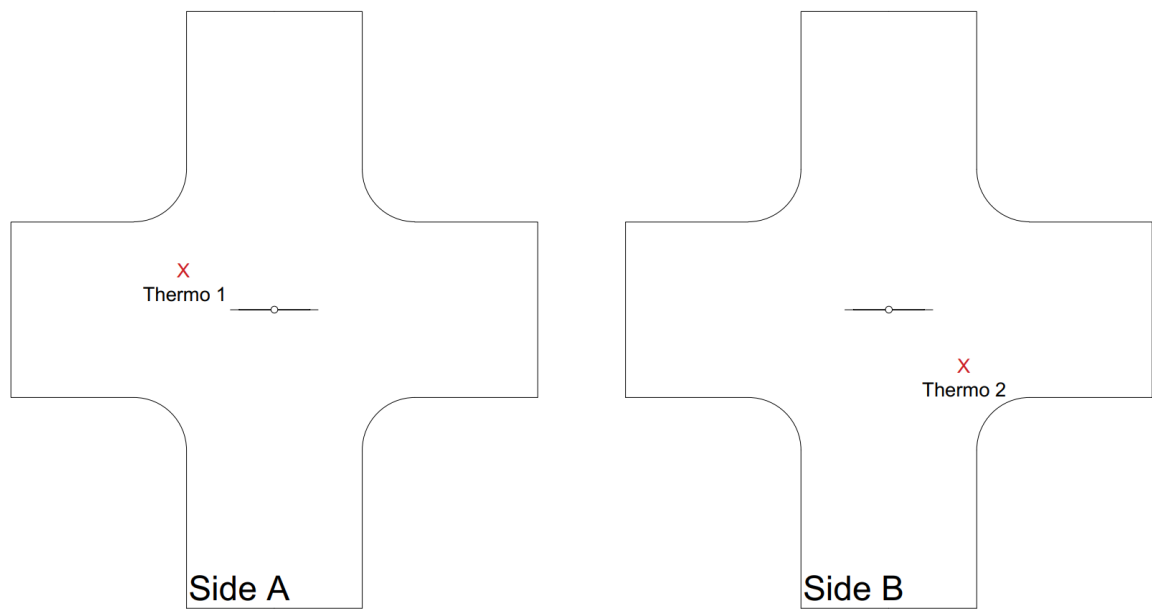


Figure 4.23: Schematic showing the thermocouple positions on a 5PB specimen

CMOD values were measured using an Epsilon 3541 – 005M – 120M – LT COD gauge. This has an initial gauge length of 5 mm and can measure accurately between 100 and -270°C . To attach the clip gauge on the specimens knife edges are designed following the guidance of [132]. A schematic of the knife edges can be seen in Figure 4.24. To attach the knife edges on the specimens, the latter are drilled and taped on each side of crack notch, as shown in Figure 4.25 for the 3PB specimens.

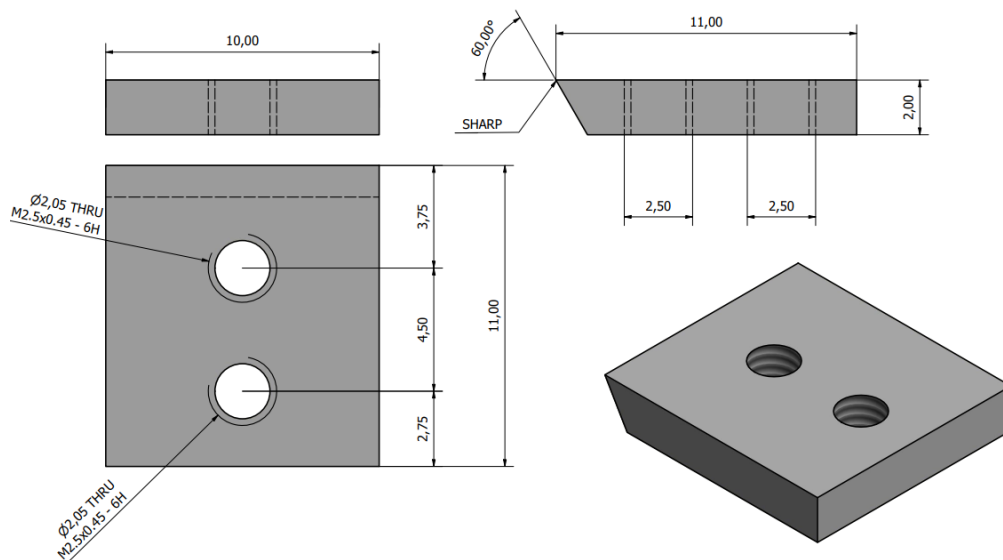


Figure 4.24: Knife edges to attach COD gauge

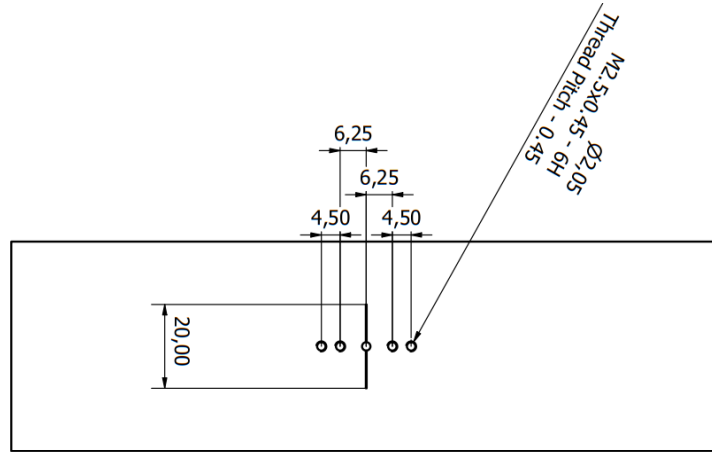


Figure 4.25: 3PB specimen with holes for the knife edge attachment

4.8 Testing procedure

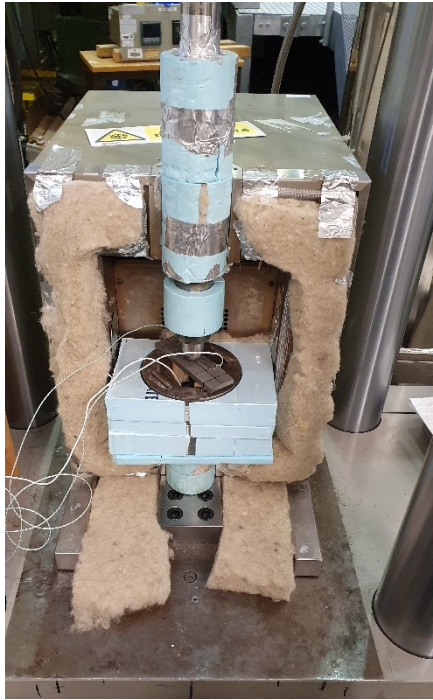
Each test began with the spot welding of the thermocouples on the specimen. Then the knife edges were screwed on each side of the crack. Following the semi-spherical punch was lubricated using a low temperature bearing lubricant and mechanical grease.

The CMOD gauge was then attached at the knife edges and the specimen was placed on the rig. Alignment of the specimen with the punch was accomplished by visual observation and markings on the specimen and the polystyrene insulation blocks. The final setup of a uniaxial experiment with the chamber open is shown in Figure 4.26 (a).

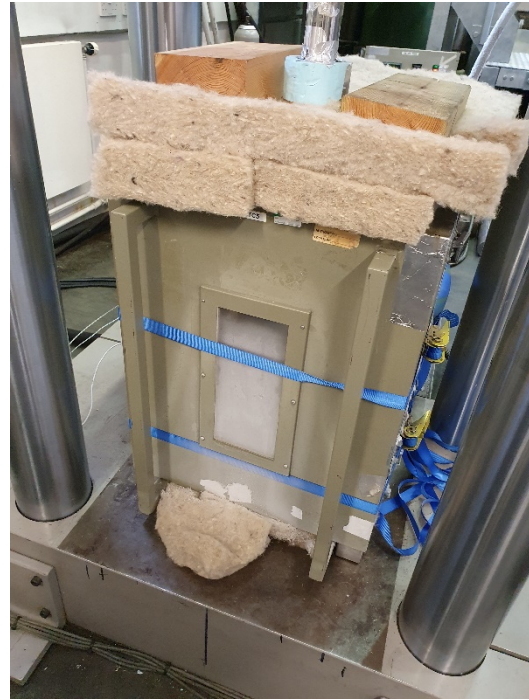
Once alignment was assured, the wiring from the CMOD gauge and the thermocouples was guided out through the side of the chamber and the chamber was shut. To ensure proper sealing of the chamber two straps were used to keep it firmly shut, as seen in Figure 4.26 (b), while aluminium tape was placed at the “lips” of the chamber to avoid any leaks. The liquid nitrogen supply was then opened, and the temperature controller was set to -160°C.

Once the thermocouples read a steady temperature of approximately -160°C the specimen was left for an additional 30 minutes at this temperature. This time sufficed to ensure no temperature gradients through its thickness.

Finally, the crosshead was moved to meet the specimen and the test began. Testing was conducted under displacement control at a rate of 0.2 mm/min.



(a)



(b)

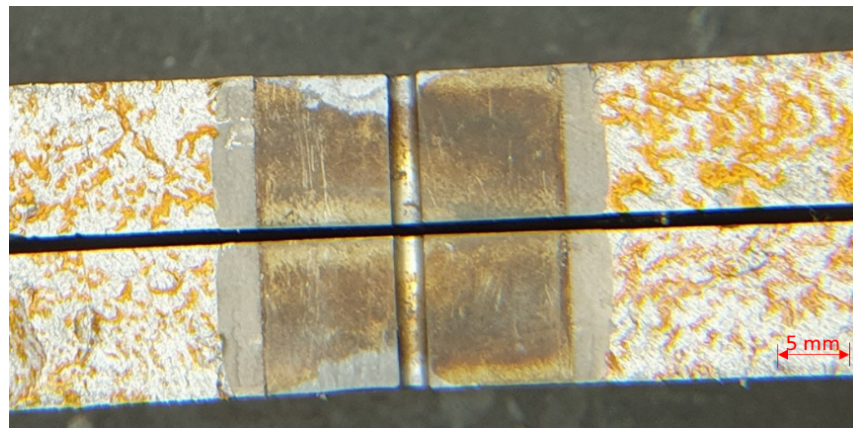


(c)

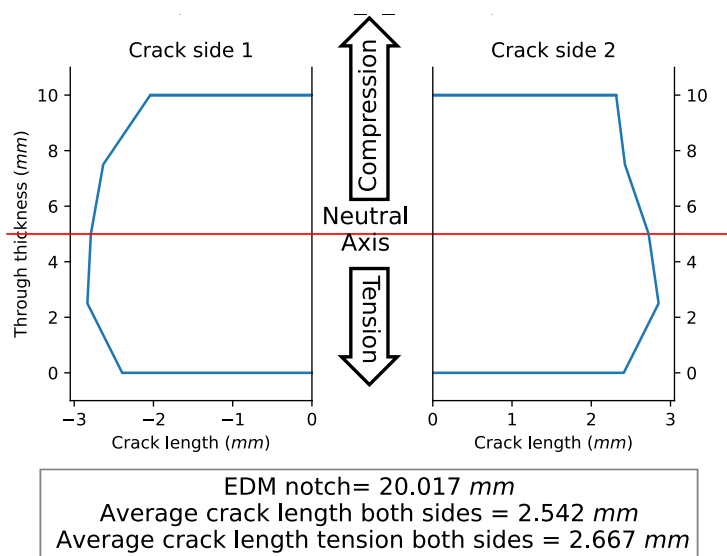
Figure 4.26: Photographs of experimental setup (a) face view with open chamber (b) face view with closed chamber and (c) side view

After the end of each experiment the post fracture surfaces were photographed using an optimax stereoscope and the exact length of the fatigue pre-crack was measured. The latter was then digitised using a python code. An example of a post fracture surface and its digitised counterpart is shown in for equibiaxially loaded specimen 5PB 4_B_1 in Figure

4.27 (a) and (b) respectively. In the latter, the measured EDM notch length, as well as the average fatigue crack length throughout the thickness and the average fatigue crack length on the tensile side of the bend are noted.



(a)



(b)

Figure 4.27: Post fracture (a) image of the fracture surface (b) digitised fatigue pre-crack

4.9 Experimental results

4.9.1 Room temperature tests

Overall, two room temperature tests were conducted, both on cruciform specimens. The first test aimed to check the soundness of the setup. It was conducted on specimen 5PB 3_BB_1 which was rejected for proper testing due to a thickness gradient from its fabrication and was not fatigue pre-cracked. The test was stopped at a CMOD value of approximately 1 mm after clearly entering the plastic zone of the Load-CMOD curve.

Once this test was completed, a fatigue pre-cracked specimen, i.e. 5PB 6_B_1, was tested to check the shape of the Load-CMOD produced with this layout. This test was loaded to a much higher CMOD however was stopped after a certain amount of applied displacement due to the punch being too low and the rollers that support the specimen potentially being shot off the rig. Specimen 5PB 6_B_1 is shown post testing in Figure 4.28.

The results of the two tests are presented in Figure 4.29. As expected, also shown with the experiments in the work of [126], at this temperature the difference of the notch tip acuity plays an important role and changes the shape of the Load-CMOD curve, with the EDM-notched specimen reaching much higher loads for the same crack mouth opening.

The limitation of being able to further load the specimen and the shape of the curve in Figure 4.29, which does not show a clear maximum, did not allow for further room temperature tests to be conducted.

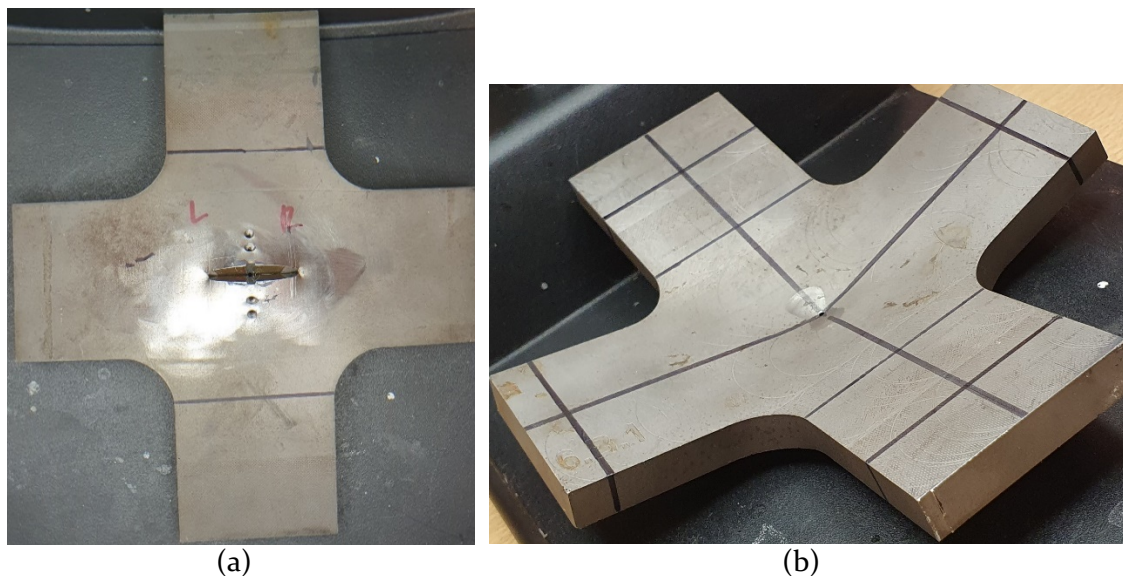


Figure 4.28: Specimen 5PB 6B1 post testing (a) top view (b) bottom view

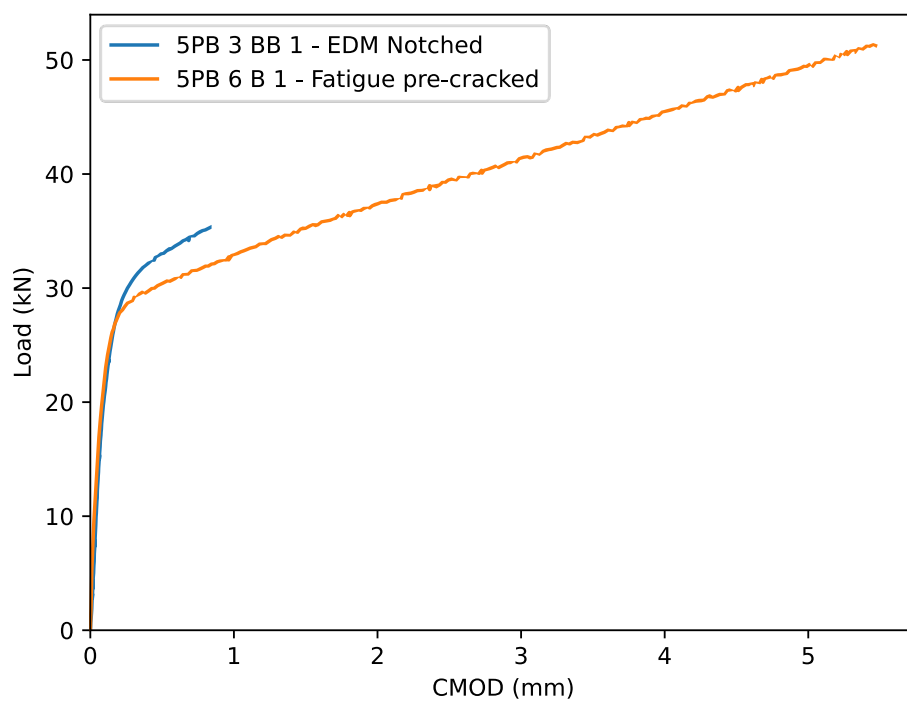


Figure 4.29: Load-CMOD of room temperature tests

4.9.2 Lower shelf tests | -160°C

This section includes the results of all the remaining specimens, not rejected from the fatigue pre-cracking phase, which were tested at -160°C. This temperature corresponds to lower shelf fracture toughness. A matrix of the experimental database is given in Table 4.6.

Table 4.6: Experimental database

| Specimen ID | |
|-------------------------|------------------------|
| Uniaxial - 3 Point bend | Biaxial - 5 Point bend |
| 3PB_1_U_1 | 5PB_1_B_1 |
| 3PB_1_U_2 | 5PB_1_B_2 |
| 3PB_1_B_1 | 5PB_1_BB_1 |
| 3PB_3_U_1 | 5PB_1_BB_2 |
| 3PB_3_U_2 | 5PB_3_B_1 |
| 3PB_3_B_1 | 5PB_3_B_2 |
| 3PB_4_U_1 | 5PB_3_BB_2 |
| 3PB_4_B_1 | 5PB_4_B_1 |
| 3PB_4_B_2 | 5PB_4_B_2 |
| 3PB_5_U_1 | 5PB_4_BB_1 |
| 3PB_5_U_2 | 5PB_4_BB_2 |
| 3PB_5_B_1 | 5PB_5_B_2 |
| 3PB_6_U_1 | 5PB_5_BB_1 |
| 3PB_6_U_2 | 5PB_5_BB_2 |
| 3PB_6_B_1 | 5PB_6_B_2 |
| | 5PB_6_BB_1 |
| | 5PB_6_BB_2 |

Overall, 15 3-point bend tests were conducted on rectangular specimens and 17 5-point bend tests on cruciform specimens. Throughout the testing at low temperatures many specimens exhibited some form of friction. This can be seen in the Load-CMOD graph of specimen 3PB_1_U_2 shown in Figure 4.30. Additionally, during experiments the window of the chamber became frosty, as shown in Figure 4.26, prohibiting visual observation and not allowing for the exact source of the friction to be traced. It is speculated that the friction came between the rollers and the specimens or the hollow cylinder base. Unfortunately, no visual accessibility and complexity of the experimental layout did not allow for a more detailed understanding of the source of friction.

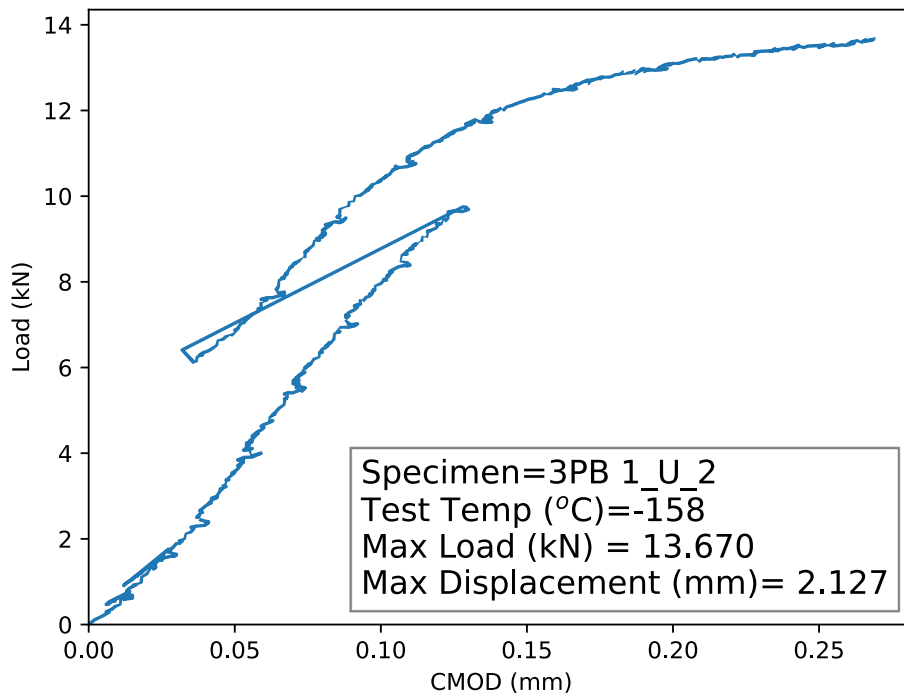


Figure 4.30: Load - CMOD of 3PB 1_U_2

4.9.2.1 Uniaxial fracture tests

From the 15 3-point bend tests, two were rejected (3PB_4_U_1, 3PB_6_U_1) due to very high friction. The remaining 13 are presented in Figure 4.31 while the experimental matrix including the average test temperature, the failure loads, the post fracture average crack length calculated throughout the thickness and the average crack length for the tensile side is given in Table 4.7.

Figure 4.31 shows that some tests exhibited a Load-CMOD curve going way past linearity into the plastic zone. In light of this the tests were separated into two categories, the ones that failed elastically, i.e. without lots of ductile tearing, and those which had considerable plasticity.

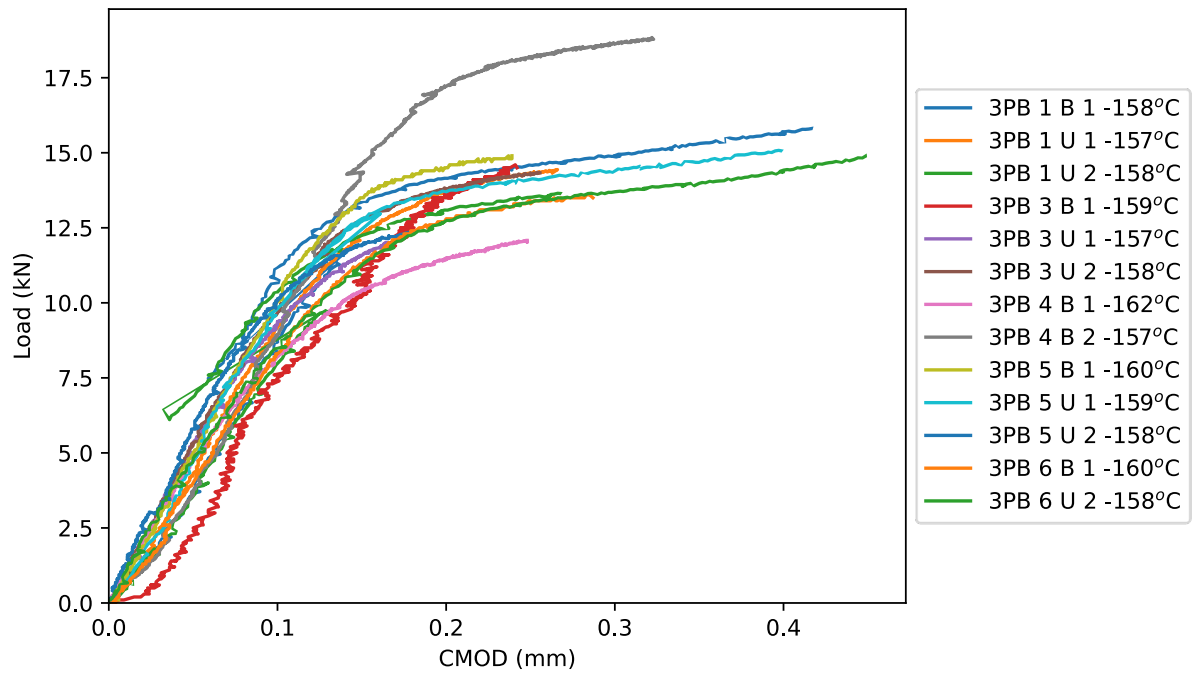


Figure 4.31: Load-CMOD of 3PB tests

Table 4.7: Experimental matrix of Uniaxial specimens

| Specimen ID | Test Temperature (°C) | Failure Load (kN) | Fatigue crack length - through thickness average (mm) | Fatigue crack length - tensile side average (mm) |
|-------------|-----------------------|-------------------|---|--|
| 3PB_1_U_1 | -157 | 1.9 | 2.4 | 2.8 |
| 3PB_1_U_2 | -158 | 2.1 | 2.6 | 2.7 |
| 3PB_1_B_1 | -158 | 2.7 | 3.4 | 3.4 |
| 3PB_3_U_1 | -157 | 1.1 | 2.4 | 2.8 |
| 3PB_3_U_2 | -158 | 1.5 | 1.6 | 2.3 |
| 3PB_3_B_1 | -159 | 1.5 | 2.9 | 3.0 |
| 3PB_4_B_1 | -162 | 1.4 | 2.2 | 2.6 |
| 3PB_4_B_2 | -157 | 1.8 | 1.8 | 2.5 |
| 3PB_5_U_1 | -159 | 2.3 | 2.1 | 2.3 |
| 3PB_5_U_2 | -158 | 1.3 | 1.8 | 2.5 |
| 3PB_5_B_1 | -160 | 1.8 | 2.1 | 2.5 |
| 3PB_6_U_2 | -158 | 2.3 | 1.5 | 2.0 |
| 3PB_6_B_1 | -160 | 1.7 | 4.5 | 3.9 |

The post fracture surface of specimen 3PB 1_U_2, shown in Figure 4.32 (a), was a characteristic example with lots of ductile tearing. Figure 4.32 (b), includes red markings denoting the ductile tearing zones, which appear to be more than 0.2mm which is considered as the threshold of tearing, for calculation of initiation fracture toughness values. Contrary to 3PB 1_U_2, specimen 3PB 6_B_1 which failed at a lower CMOD, did not appear to have ductile tearing as seen in Figure 4.33.

From the above observations and the trend observed Figure 4.31, it was decided the cut-off value for elastically failed specimens to be 0.3 mm of CMOD, except for specimen 3PB 1_U_2 which failed at a CMOD of approximately 0.25 mm but exhibited lots of tearing. The two categories consist of 5 tests for the plastic ones and the remaining 11 for the elastically failed.

The experimental results for each of the two categories separately are shown here in Figure 4.34 and Figure 4.35. Separate Load-CMOD curves for each specimen are given in Appendix 1. Friction from low to high amounts was present in most of the tests, nevertheless a trend was observed in the two categories regarding failure loads and CMODs. The differences between the elastic specimens can also be partly explained by the inherent scatter in brittle fracture.

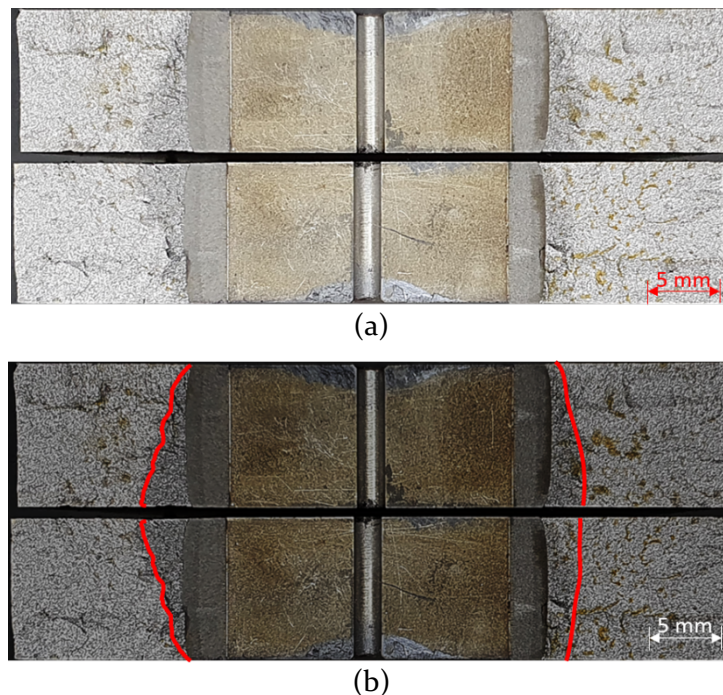


Figure 4.32: 3PB 1_U_2 post-fracture surface (a) as taken (b) with highlighted ductile tearing zones.

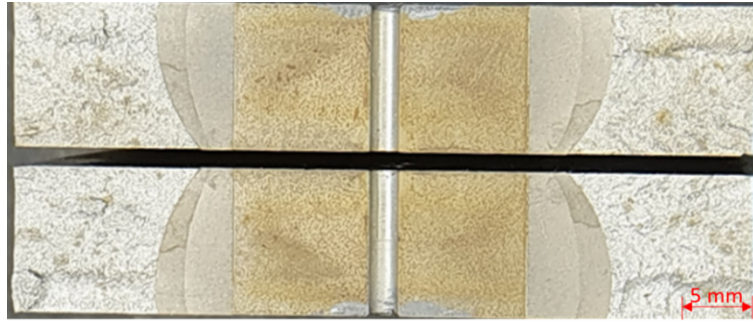


Figure 4.33: 3PB 1_U_2 post-fracture surface

Even though the tests were conducted at a nominal temperature of -160°C , which corresponds to lower shelf fracture toughness, high levels of plasticity were achieved in the plastic category specimens. This denotes that crack tip constraint of this experimental layout could be lower than what was originally intended.

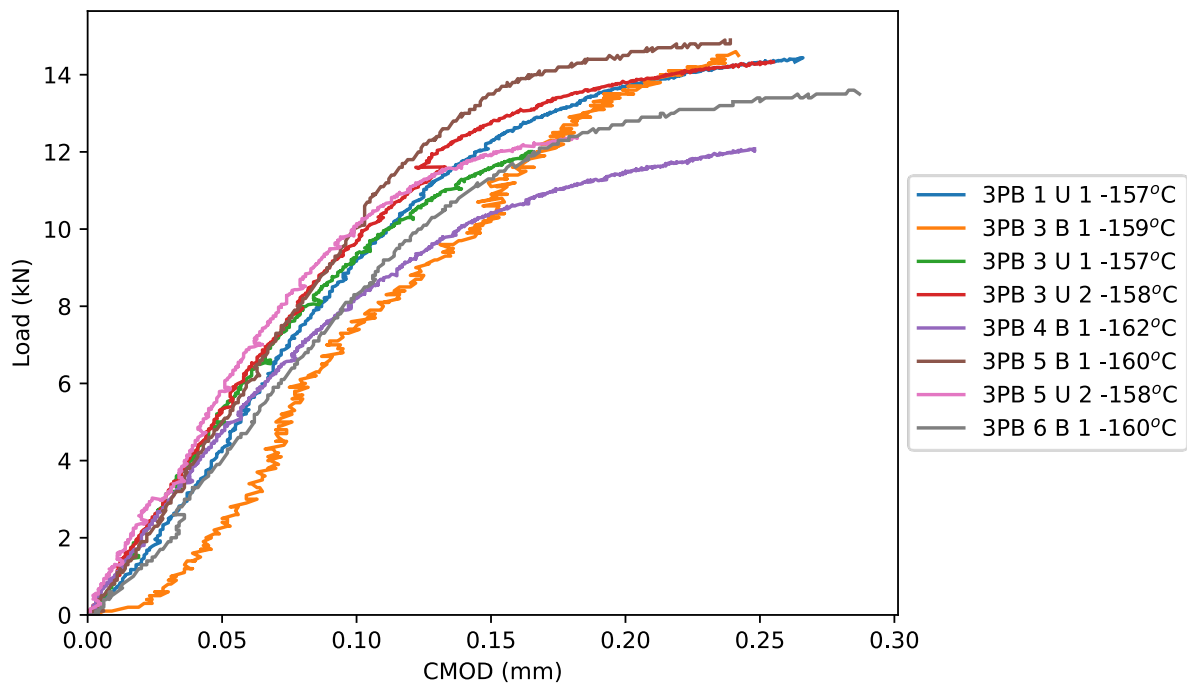


Figure 4.34: Load-CMOD curve of elastic 3PB tests

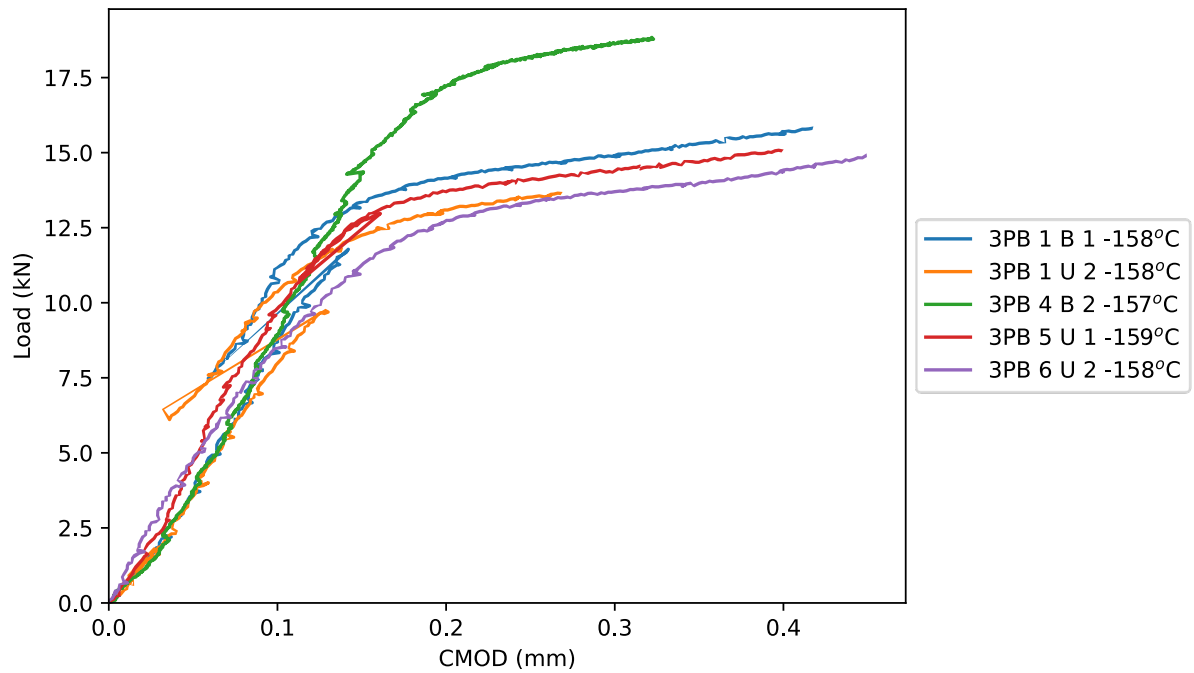


Figure 4.35: Load-CMOD curve of plastic 3PB tests

4.9.2.2 Biaxial fracture tests

Similar to the uniaxial tests, biaxial tests also included friction in many instances. This was more prominent for the 5-point bends. Given there were 4 points of contact with rollers in this setup the argument that friction originated from the rig-roller-specimen surface interactions is further supported. Here 4 specimens were rejected as having a significant amount of friction, i.e. 5PB 1_BB_1, 5PB 3_B_1, 5PB 4_BB_1, 5PB 6_BB_1.

Ten of the tests had pop-ins events during loading, shown in Table 4.8. These events were considered as the failure event. A characteristic example was that of 5PB 3_B_2, whose Load-CMOD curve is given in Figure 4.36.

The Load-CMOD curves of all the tests up to the failure events considered, are shown in Figure 4.37, while separate Load-CMOD curves of the whole experiment and until the fracture event are given in Appendix 1. The experimental matrix of the biaxial tests including the average test temperature, the failure loads, the post fracture average crack length calculated throughout the thickness and the average crack length for the tensile side is given in Table 4.9.

Table 4.8: 5-point bend failure conditions

| Specimen ID | pop-in event | CMOD > 0.5 mm |
|-------------|--------------|---------------|
| 5PB_1_B_1 | x | |
| 5PB_1_B_2 | x | |
| 5PB_1_BB_2 | | x |
| 5PB_3_B_2 | x | |
| 5PB_3_BB_2 | x | |
| 5PB_4_B_1 | x | |
| 5PB_4_B_2 | x | |
| 5PB_4_BB_2 | | x |
| 5PB_5_B_2 | x | |
| 5PB_5_BB_1 | x | |
| 5PB_5_BB_2 | x | |
| 5PB_6_B_2 | x | |
| 5PB_6_BB_2 | | x |

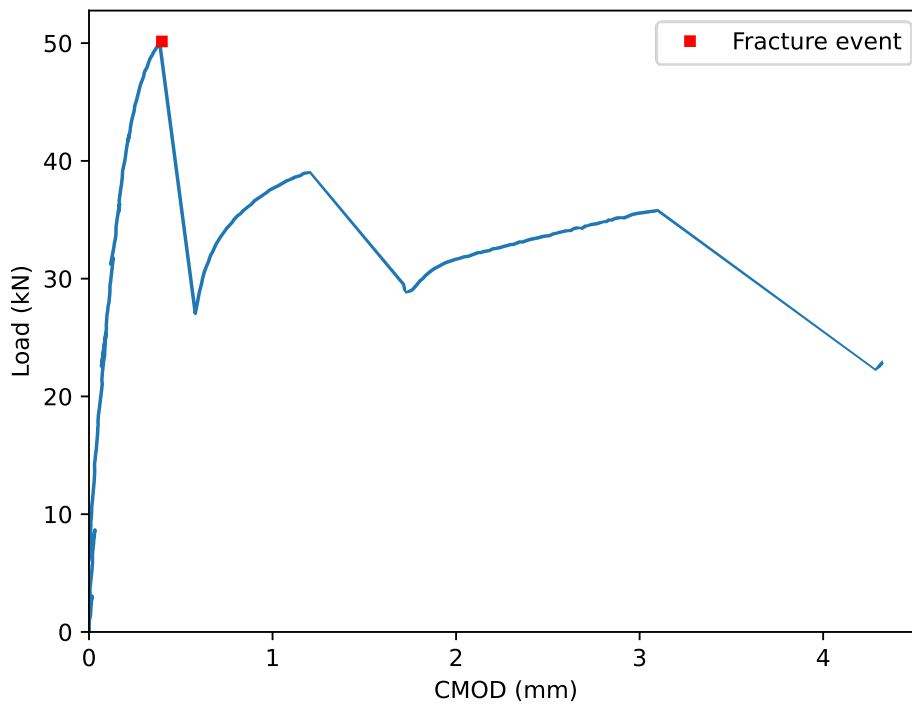


Figure 4.36: Load-CMOD of 5PB 3_B_2

Table 4.9: Experimental matrix of Biaxial specimens

| Specimen ID | Test Temperature (°C) | Failure Load (kN) | Fatigue crack length - through thickness average (mm) | Fatigue crack length - tensile side average (mm) |
|-------------|-----------------------|-------------------|---|--|
| 5PB 1_B_1 | -161 | 39.5 | 2.2 | 2.5 |
| 5PB 1_B_2 | -161 | 48.0 | 2.5 | 2.6 |
| 5PB 1_BB_2 | -161 | 56.6 | 2.7 | 2.7 |
| 5PB 3_B_2 | -162 | 50.3 | 3.4 | 3.4 |
| 5PB 3_BB_2 | -161 | 34.0 | 1.6 | 2.1 |
| 5PB 4_B_1 | -164 | 53.8 | 2.5 | 2.7 |
| 5PB 4_B_2 | -163 | 55.1 | 2.1 | 2.2 |
| 5PB 4_BB_2 | -162 | 54.6 | 2.8 | 2.9 |
| 5PB 5_B_2 | -158 | 42.2 | 2.9 | 3.1 |
| 5PB 5_BB_1 | -161 | 47.3 | 3.1 | 3.0 |
| 5PB 5_BB_2 | -162 | 48.6 | 2.3 | 2.6 |
| 5PB 6_B_2 | -162 | 45.0 | 2.4 | 2.3 |
| 5PB 6_BB_2 | -160 | 55.3 | 2.1 | 2.5 |

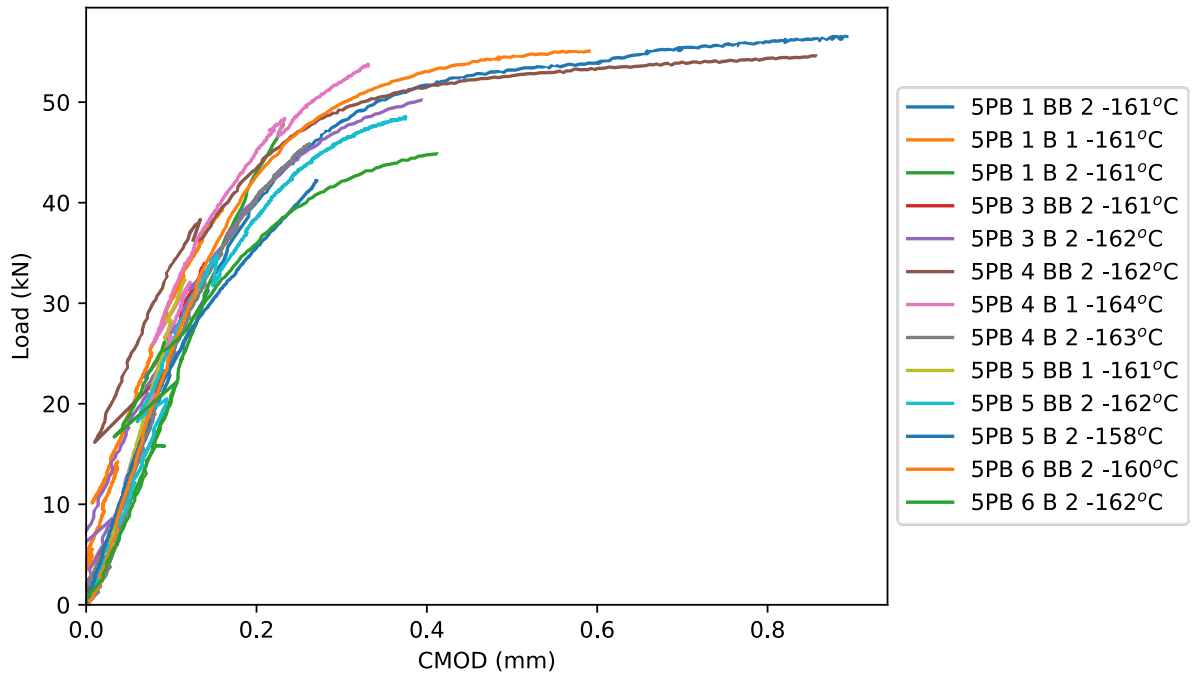


Figure 4.37: Load-CMOD of 5PB tests

Again, tests varied in the amount of plasticity reached before failure. The post fracture surface of specimen 5PB 3_B_2, shown in Figure 4.38(a), had significant ductile tearing. Figure 4.38 (b), includes red markings denoting the ductile tearing zones, which are longer

than 0.2 mm. In this case and given the pop-in event of the specimen it is not clear what amount of tearing happened prior to the pop in.

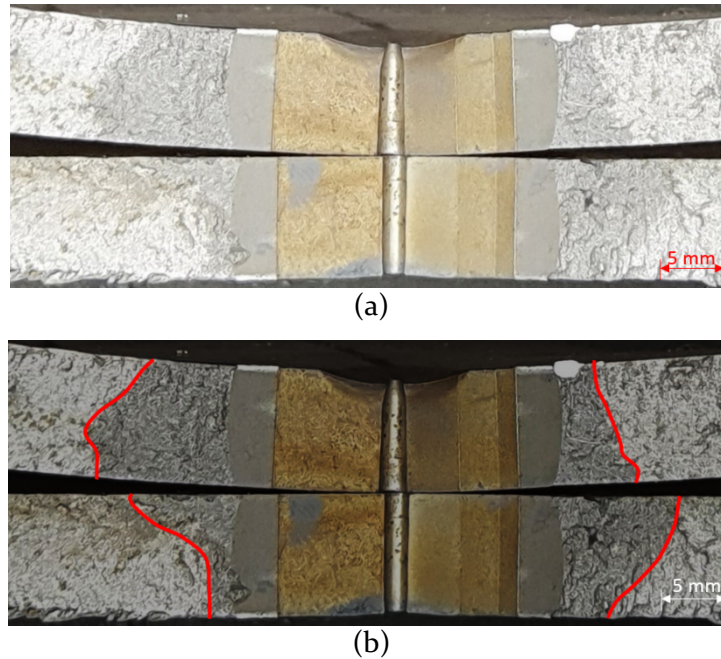


Figure 4.38: 5PB 3_B_2 post-fracture surface (a) as taken (b) with highlighted ductile tearing zones.

Even though fracture surfaces did show tearing was present, the separation between the plastically (showing lots of tearing) and elastically collapsed specimens here is made based on the trends observed in Figure 4.37. There is a clear separation between tests where the crack propagated are lower load and CMODs and these where the curve reached well into the plastic zone. The CMOD cut-off value for the separation between the two categories here was selected to be 0.5 mm.

This led to three tests falling into the plastically (showing lots of tearing) failed category, shown in Table 4.8. The remaining 14 tests were considered to have failed either in a complete brittle manner or with limited plasticity. In the cases where the pop-ins were not at a high CMOD value these tests have been considered to fail with limited plasticity. Separate graphs of the elastic and plastic failed specimens are shown in Figure 4.39 and Figure 4.40 respectively. Full curves until the final loading of the specimens are given in Appendix 1 along with pictures of the specimen post-failure and the fracture surface of each specimen.

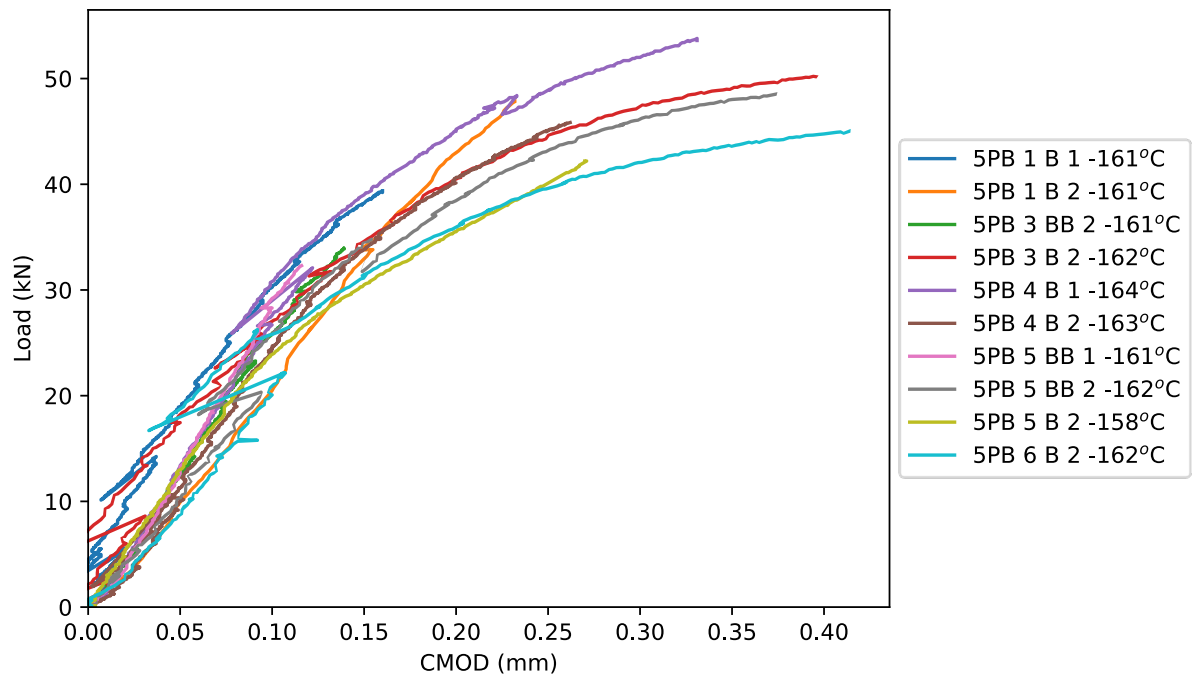


Figure 4.39: Load-CMOD curve of elastic 5PB tests

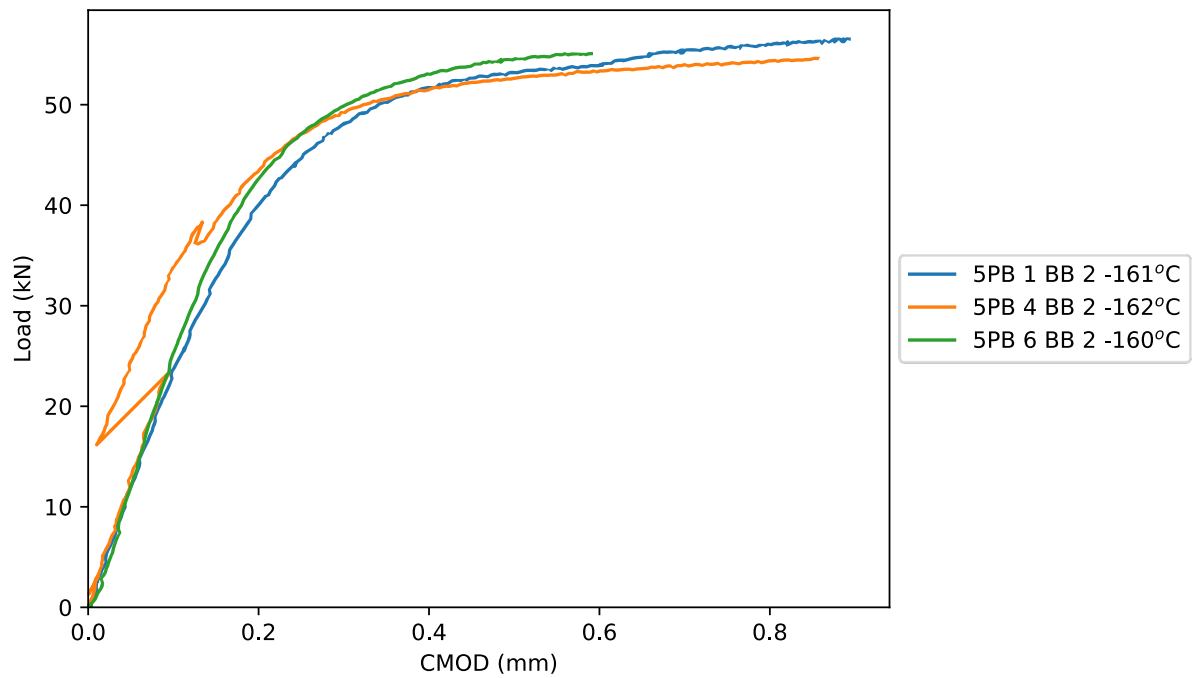


Figure 4.40: Load-CMOD curve of plastic 5PB tests

Considering the mode of fracture, the crack path did change direction during loading, with the crack exhibiting from slight curvature, observed on specimen 5PB 1_B_1 shown in Figure 4.41 (a), to the characteristic “S” shape observed in the PMMA specimens and here on specimen 5PB 1_B_2 shown in Figure 4.41 (b).

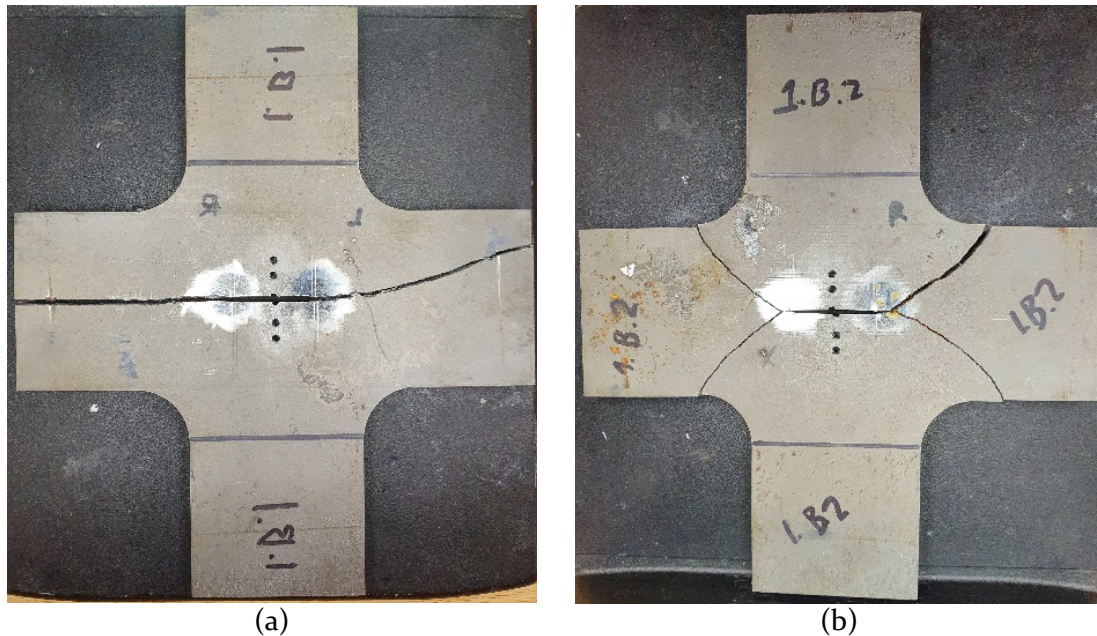


Figure 4.41: Post fracture pictures of (a) 5PB 1_B_1 and (b) 5PB 1_B_2

This confirms that biaxiality was indeed captured successfully with the experiments, however with specimens exhibiting high amounts of plasticity it is again argued that the levels of constraint captured were potentially lower than those of high constrained experiments such as C(T) specimens.

4.10 Conclusions

An experimental program has been designed to target biaxiality and its effect on constraint and failure.

Two geometries were designed, a rectangular specimen loaded in a 3-point bend and a cruciform specimen loaded in a 5-point bend. The geometries had through thickness crack and attempted to decouple surface flaw effects from biaxially induced constraint.

The experimental layout was initially validated with the use of PMMA samples. PMMA exhibited completely linear elastic behaviour breaking in a brittle manner. The fracture trajectory of the cruciform equibiaxially loaded (5-point bends) had an “S” shape, known to be an effect of biaxiality, providing confidence that it was captured from the setup.

Cruciform specimens required higher loads to fracture in comparison to the uniaxially loaded specimens due to a significant fraction of the load applied by the punch being consumed for the in-plane loading.

Steel specimens were cut out of a well characterized ferritic steel, whose fracture toughness and tensile properties were known for a wide temperature spectrum. Limited material availability allowed for thinner than PMMA specimens to be cut.

During testing, further displacement was required on steel in comparison to PMMA specimens to reach failure. To ensure safety during testing and avoid parts of the layout shooting off, a limitation on the maximum displacement was imposed. Within this displacement threshold room temperature tests showed extensive plasticity, while Load-CMOD curves were not able to reach a maximum before the test was stopped. This did not allow for further experiments at this temperature.

A single temperature that corresponded to the lower shelf of the transition curve was tested. To decide the exact temperature Charpy tests were conducted and a transition curve for this material was drafted. This in combination with the existing data on the material designated -160°C as an appropriate testing temperature, where highly constrained geometries exhibited very limited plasticity during fracture tests.

Like the PMMA specimens the fracture trajectory of the equibiaxially loaded cruciform specimens appeared to be deviating from a straight line exhibiting from slight curvature to an “S” shaped curve, ensuring that biaxiality was again captured by the experimental layout. Cruciform specimens in many cases experienced pop-in events which were treated as failure events, while the failure loads of the cruciform specimens, were as in the PMMA samples, higher than the rectangular specimens, this time, by an order of magnitude.

In both geometries tested, specimens exhibited varying levels of plasticity with some having Load-CMOD curves going way past linearity into the plastic zone and the remaining deviating very little from linear behaviour. The tests were thus separated into two categories, the ones that failed elastically, and those which had lots of ductile tearing. The separating criterion between the two categories was a specific value of CMOD chosen for each geometry with the aid of the trend of the Load-CMOD curves and the observed ductile tearing on the fracture surfaces. The existence of plasticity at such a low temperature denoted that the desired high constraint effect attempted to be captured by this setup might have not succeeded.

Chapter 5 Finite element analyses

5.1 Introduction

The innovative experimental program of Chapter 4 gave valuable insight on biaxiality's effect on failure loads and the plasticity developed, however it was not possible from experiments alone to calculate values of paramount importance like fracture toughness or constraint measures. This is due to the geometry and the loading of the specimens and in particular the cruciform specimens, for which no analytical solutions exist for the calculation of the effective fracture toughness and the structural constraint.

In pursuit of calculating stress intensity factors at failure and T-stresses for the two geometries FEA models have been developed. These values will be able to indicate the constraint effects captured with this experimental program and assist in concluding on the effect of biaxiality on through thickness flaws, i.e. when decoupled from surface flaw effects.

The following sections provide the methodology used for modelling the PMMA and steel specimens included in the experimental program and explain the modelling strategy for

the two different geometries, i.e. cruciform and rectangular specimens. Lastly, the results of the models follow for both materials.

5.2 Model methodology

5.2.1 PMMA models

5.2.1.1 Geometry

The model consists of three instances, namely

- 1) the test specimen (PMMA)
- 2) the loading punch
- 3) a boundary surface that prohibits intersection of the compressive sides of the bending along the crack front

The PMMA specimens, both rectangular and cruciform, were assumed to be symmetrical along the mid-width of the specimen and the crack front, thus a quarter was modelled, where symmetry boundary conditions were assumed in the respective planes. An overview of the FEA layout is given for the 3 and 5-point bends in Figure 5.1 and Figure 5.2 respectively.

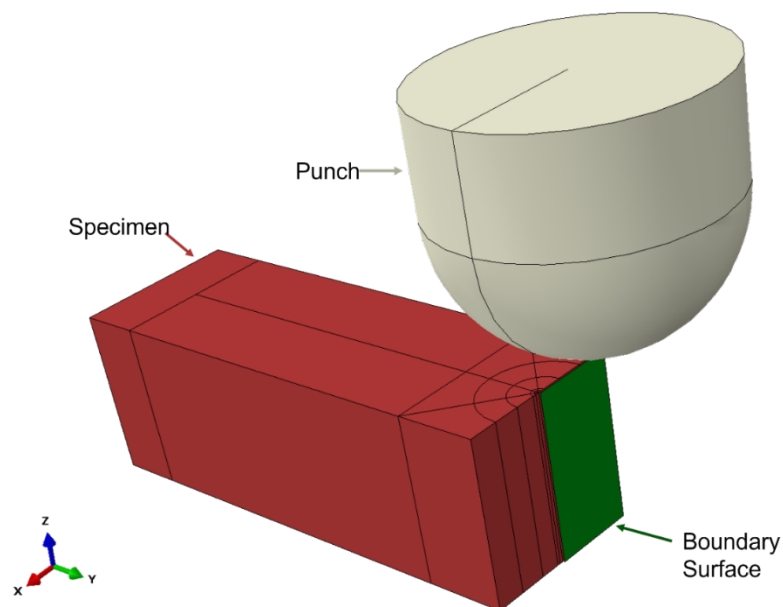


Figure 5.1: PMMA 3PB FEA Assembly

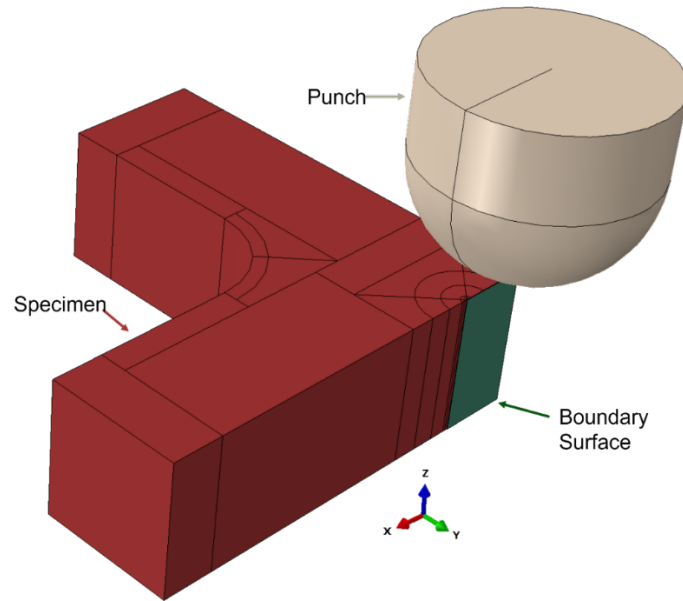


Figure 5.2: PMMA 5PB FEA Assembly

The dimensions of the PMMA test specimens in the FEA were the same given in Chapter 4 for the experiments and the crack length for all models was $2a=25$ mm (12.5 mm in the modelled quarter). The mesh of the rectangular and cruciform specimens consisted of 61344 and 147600 C3D20 quadratic hexahedral elements, shown in Figure 5.4 (a) and (b), while a focused mesh was designed around the crack tip as explained in Section 5.1.2.3. Merge convergence is ensured from the use of 25000 elements onwards, as shown in Figure 5.3 where the displacement at the tensile surface of the PMMA cruciform specimen model is shown against the number of elements used with an applied displacement of 0.87 mm by the punch.

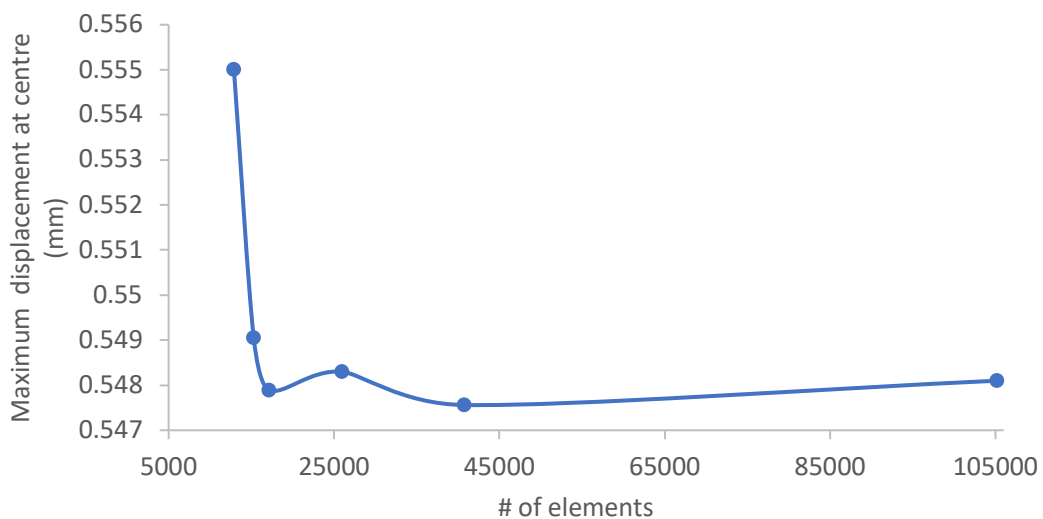
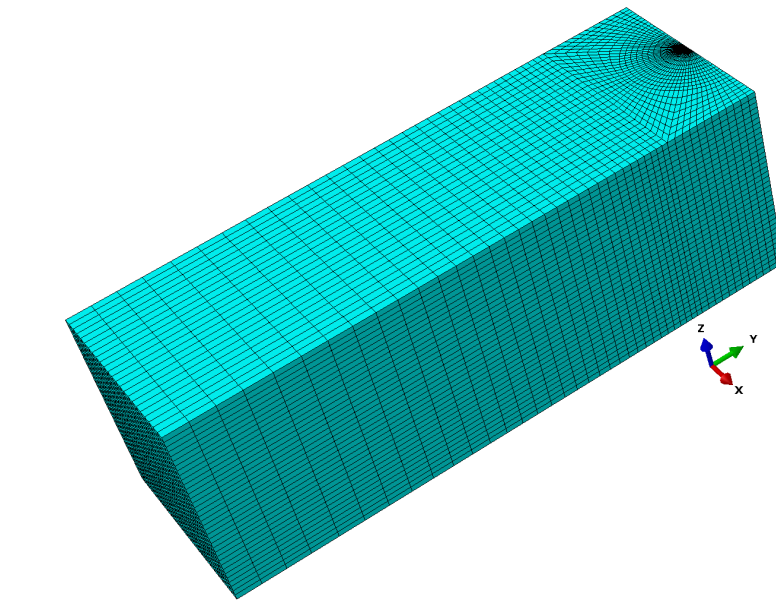


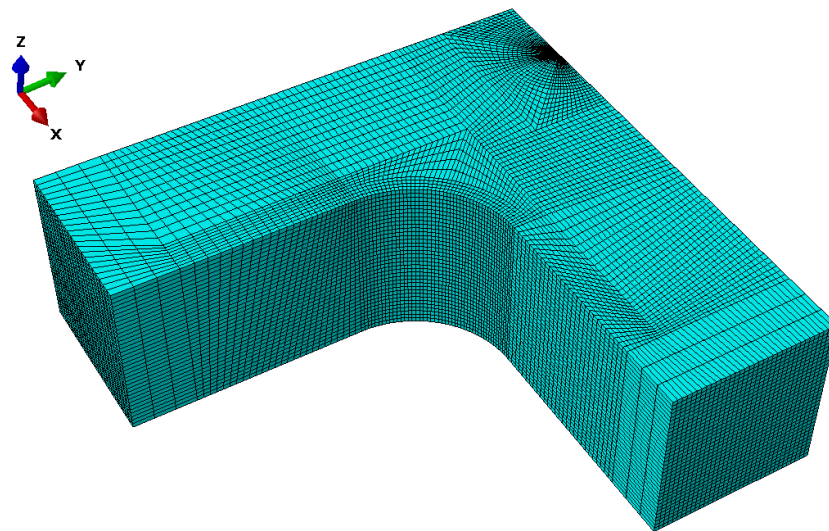
Figure 5.3: Displacement at centre of specimen vs # of elements

The semi-spherical punch was an analytic rigid shell surface with a radius of 20 mm, same as the experimental punch and required no meshing given its analytical closed form solution hence no further discussion will be made on the meshing of the punch.

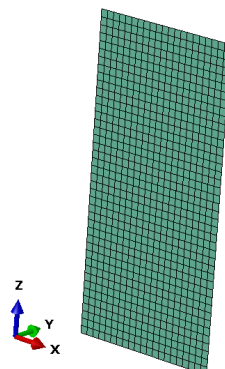
The boundary surface was a discrete rigid surface of dimensions 25 x 12.5 mm covering the modelled crack front. Its mesh consisted of 882 R3D4 linear quadrilateral elements, shown in Figure 5.4 (c). Both rigid bodies, analytic and discrete experienced no deformation during loading and required no material specification.



(a)



(b)



(c)

Figure 5.4: Meshed instances of PMMA models (a) 3PB specimen (b) 5PB specimen (c) boundary surface

5.2.1.2 Material

PMMA was considered to exhibit only linear elastic behaviour up to failure with no plasticity included. The material properties used for the elastic model were taken from literature [133] and were,

- Young's Modulus $E = 2900 \text{ MPa}$
- Poisson Ratio $\nu=0.38$

The remaining two parts of the FEA assembly were assumed as rigid bodies and did not require any material specification. Given the current runtime of the models (approximately 20-30 hours on 8 cores and 64 GB ram) adding material and meshing to the remaining 2 parts would not allow any computational and time efficiency.

5.2.1.3 Crack tip modelling

Sharp cracks have a strain singularity at the crack tip. In FEA, sharp this is commonly addressed with focused meshes. The singularity at the crack tip is incorporated in small-strain analysis with the choice the correct element types and refinement of the mesh [123]. This singularity relies on the amount of plasticity, and thus material properties, that develops during loading.

For the models developed here, a radial mesh around the crack tip was generated. At the crack tip the hexahedral elements were collapsed into wedges, shown in Figure 5.5. Given that the analyses for the PMMA specimens will be elastic, the nodes at the tip were merged to a single node. The singularity was accounted for by moving the mid-side nodes of second order elements⁶, at the crack edge, towards the crack tip at a distance of $\frac{1}{4}$ of the length of the wedge, as suggested for elastic analyses [123].

The first and second row of elements at the crack tip had a length of 0.5 mm which was then increased to 0.7 extending radially, while there were 48 elements tangentially placed along each of the semicircles. Overall, 7 contours of J-integrals were calculated, and the mesh was sufficient for the values to converge from the 3rd contour onwards.

⁶ Second order element: an element with additional midside nodes where quadratic-second order interpolation can take place for the calculation of the values at the element from its nodes.

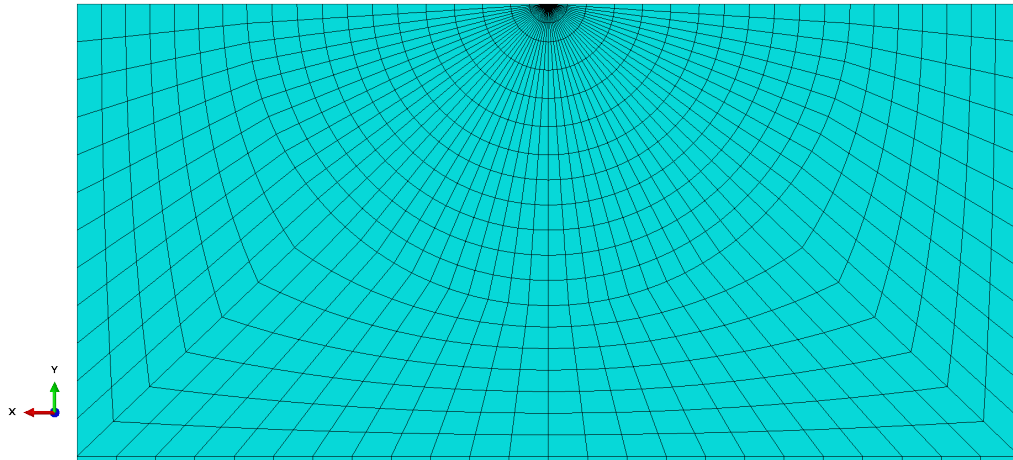


Figure 5.5: Crack-tip mesh of PMMA specimens

5.2.1.4 Boundary conditions, contact properties & loading

Both 3PB and 5PB PMMA specimens had similar boundary conditions as shown in Figure 5.6 and Figure 5.7 respectively. X and Y symmetry were assumed due to the quarter specimen modelled, not allowing displacements on the symmetry axis and relative rotations to the other two axes. The interaction with the rollers was incorporated with the use of a boundary condition at the point of contact which prohibited displacement on the Z (load) axis. As described later for the steel models the stresses developed at the roller contact were reasonable (just above yield for the steel models) and thus the mesh and the approach selected were deemed appropriate.

For the spherical punch analytical surface, a kinematically coupled reference point was defined. The point, and thus the surface, were constraint to have zero displacement along the x and y axis and any relative rotations while being allowed to move along the z axis (loading direction). Loads were applied to the specimen via application of displacement on the reference point of the punch.

For the boundary surface, it was tied to a reference point and fixed there allowing no displacement or rotations. In essence it acted as a symmetry boundary condition along the crack front which prohibited intersection between the compressive sides of the bend while allowing displacement of the PMMA surface on the tensile side of the bend.

Contact was defined between the specimen and the punch as well as the specimen and the boundary surface, while no interaction was considered between the boundary surface and the punch. The contact properties for both were a friction coefficient of 0.3 for the

tangential/shear stresses and hard-contact was used for the pressure applied in the normal direction.

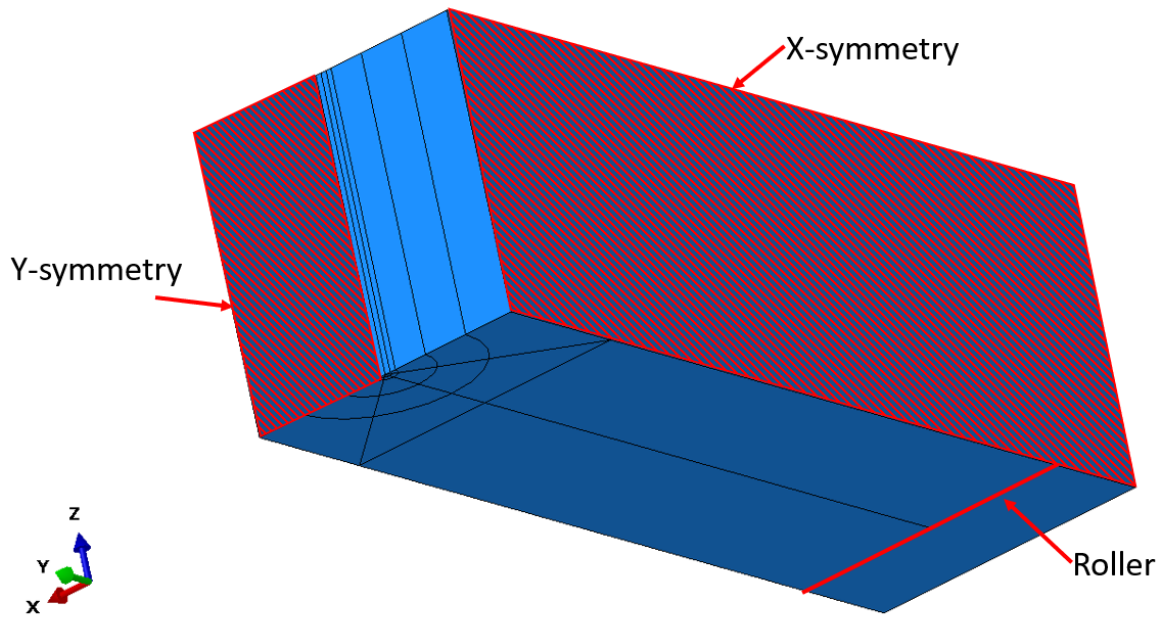


Figure 5.6: Boundary conditions of 3PB PMMA specimen

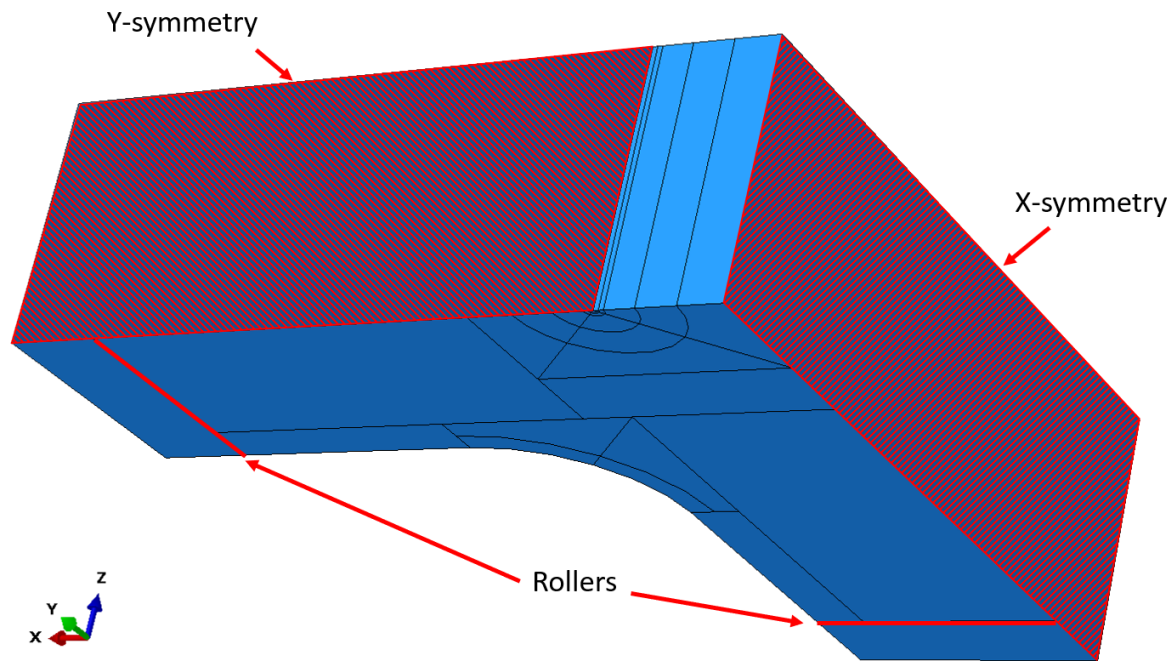


Figure 5.7: Boundary conditions of 5PB PMMA specimen

5.2.2 Steel models

5.2.2.1 Geometry

The methodology for the BS 1501-224 steel models was the same to that used for the PMMA specimens. Again, the model consisted of three geometries/parts, the test specimen, which had a thickness of 10 mm, the same semi spherical punch, which applied the load and a boundary surface that prohibited intersection of the compressive sides of the bending along the crack front with a reduced length of 10 mm to match the thickness of the specimen.

The crack length of steel specimens in the FEA was the average crack length on the tensile side of the bend, as it was measured from the optometer and presented in Appendix 1.

Given the extensive time required for the analyses of the PMMA specimens it was expected that the elastic-plastic behaviour of the steel material would extend the time for each model beyond acceptable timeframes. Considering this reduced integration elements were used for the steel models. In particular the mesh of the rectangular and cruciform specimens consisted of 19371 and 21464 C3D20R reduced integration quadratic hexahedral elements, shown in Figure 5.8 (a) and (b), while as before a focused mesh was designed around the crack tip, explained in Section 5.2.2.3. The difference on the J-integrals calculated and load-CMOD curves between reduced and full integration elements is shown for a uniaxial and a biaxial specimen loaded to failure in Figure 5.9 and Figure 5.10 respectively. The Load-CMOD curves are identical, while for the J-integral minimal differences are seen. The above render the mesh as a good balance between computational efficiency and model integrity.

The semi-spherical punch was an analytic rigid shell surface with a radius of 20 mm, same as the experimental punch and required no meshing given its analytical closed form solution.

The boundary surface was a discrete rigid surface of 10 mm length and width equal to that of the crack modelled. Its mesh consisted of 154 R3D4 linear quadrilateral elements.

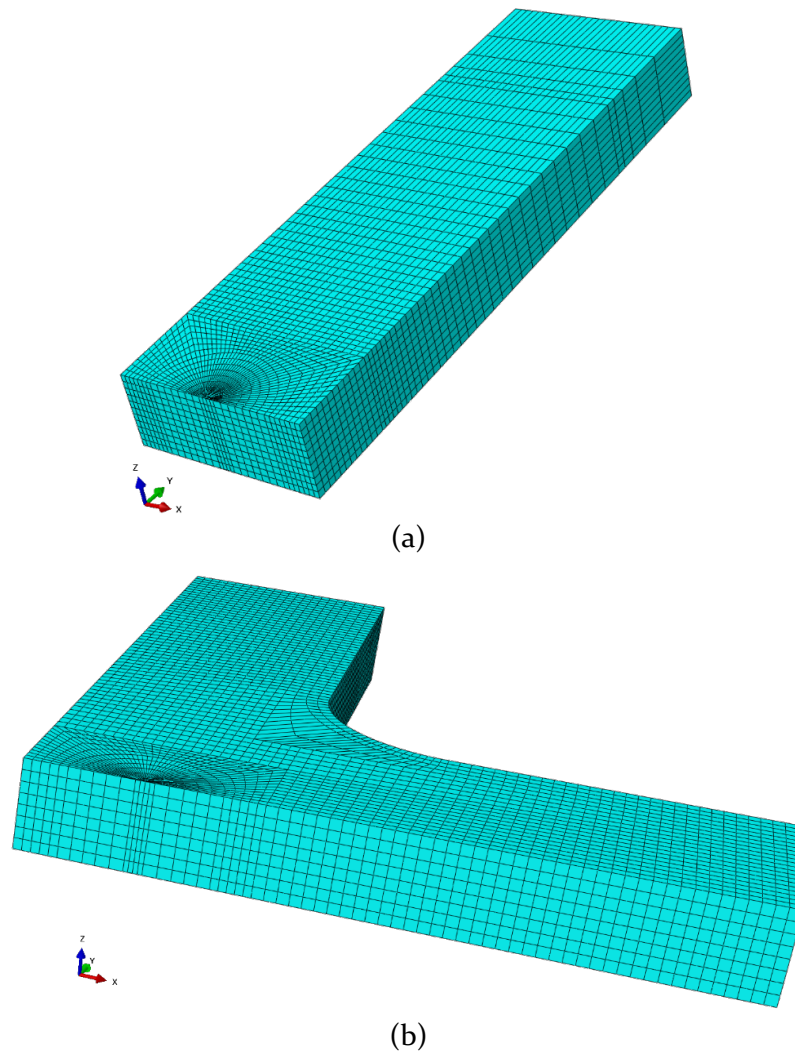
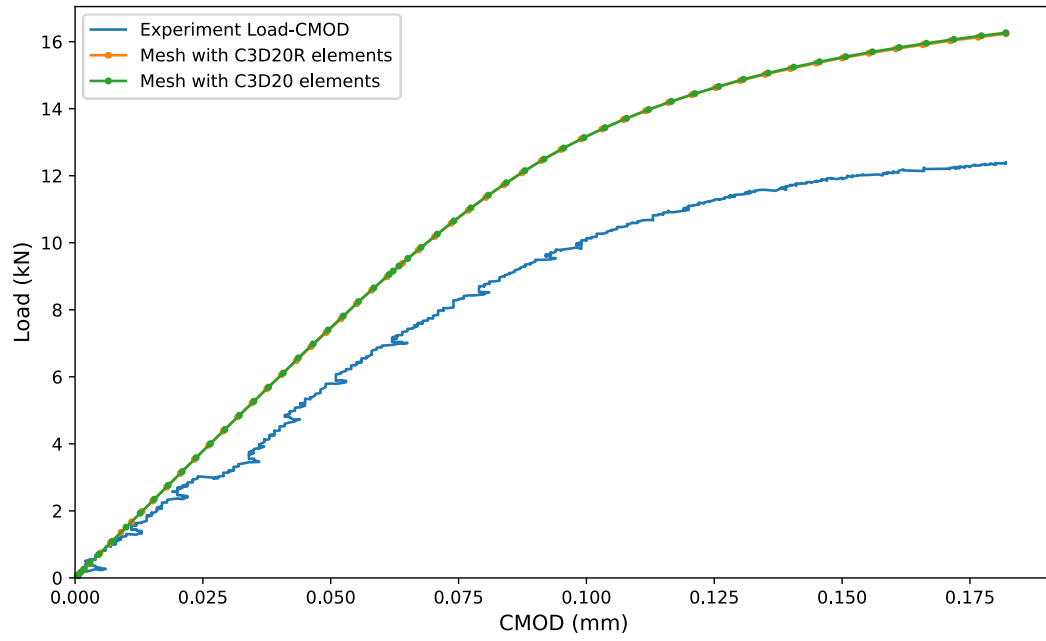
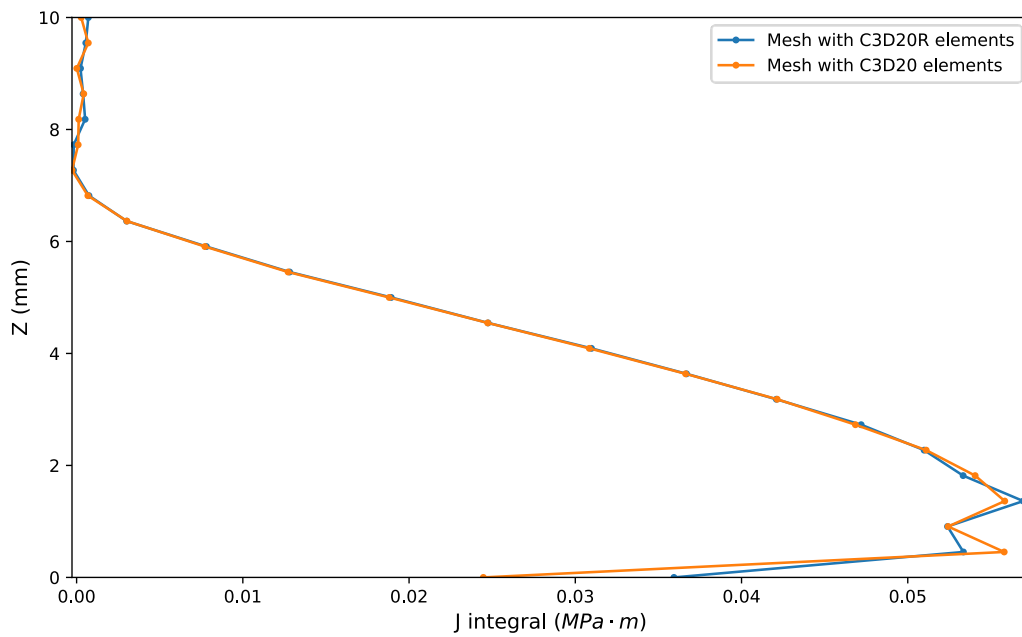


Figure 5.8: Meshed instances of steel models (a) 3PB specimen (b) 5PB specimen



(a)



(b)

Figure 5.9: Effects of element choice on (a) Load-CMOD (b) J-integral at failure calculation for specimen 3PB 5_U_2

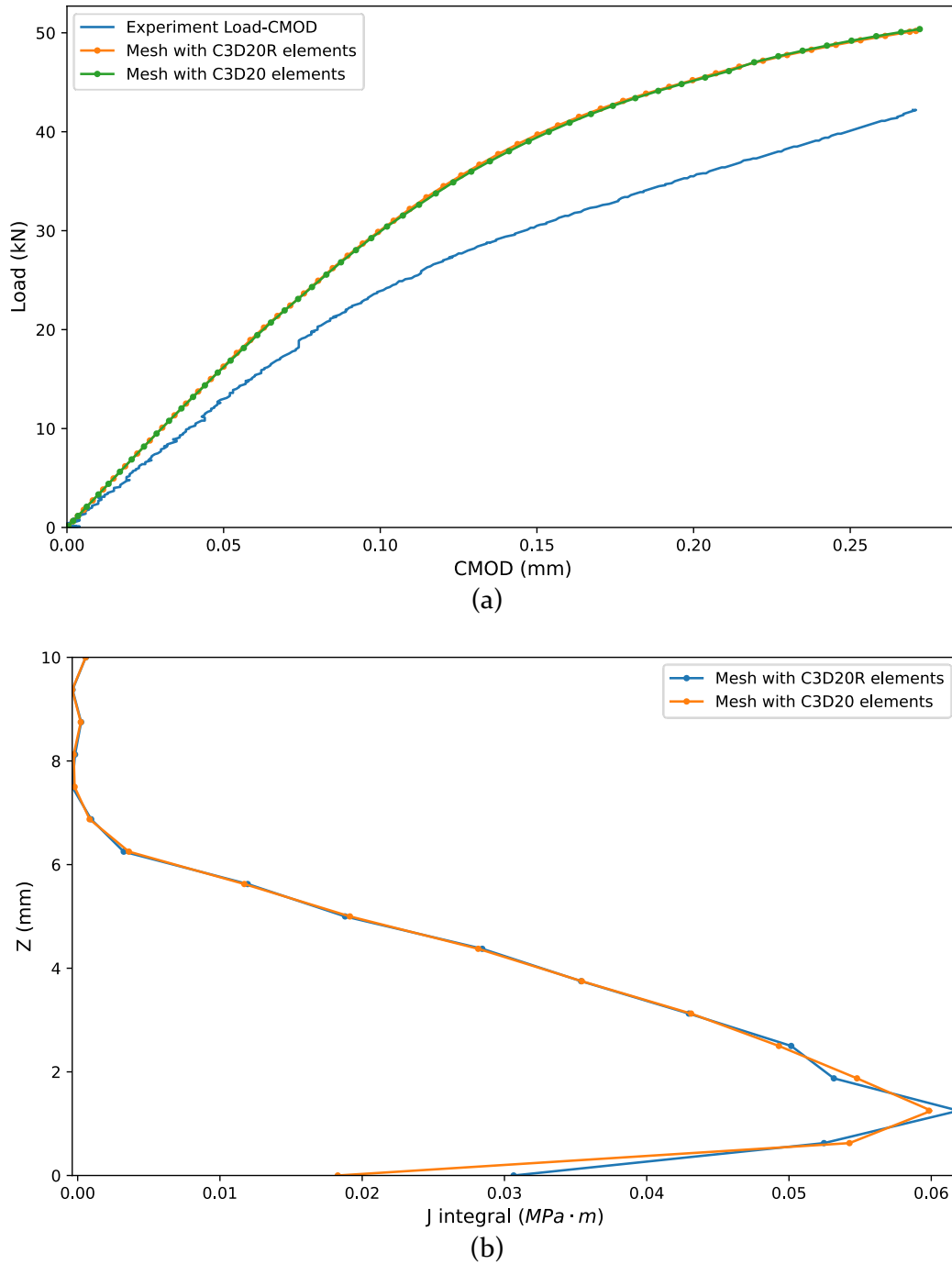


Figure 5.10: Effects of element choice on (a) Load-CMOD (b) J-integral at failure calculation for specimen 5PB 5_B_2

5.2.2.2 Material

The material properties used for the steel analyses were experimentally obtained from [126] at -160 °C. For the elastic behaviour the following properties were used:

- Young's Modulus $E = 204 \text{ GPa}$
- Poisson Ratio $\nu=0.3$

For the plastic behaviour of the specimen the exact tensile curve was taken from [126] and shown for completeness here in Figure 5.11. Here it should be noted that the tensile curve includes Lüders strains that are generally a result of tensile loading in a small specimen (such as a tensile) and not typically considered for larger specimens and components, especially under bending. Inclusion of this, results in lower crack resistance curves [134], however given the resulting model curves in the following section being higher than the experimental ones and the small Lüders plateau seen in Figure 5.11, including them is assumed to be correct.

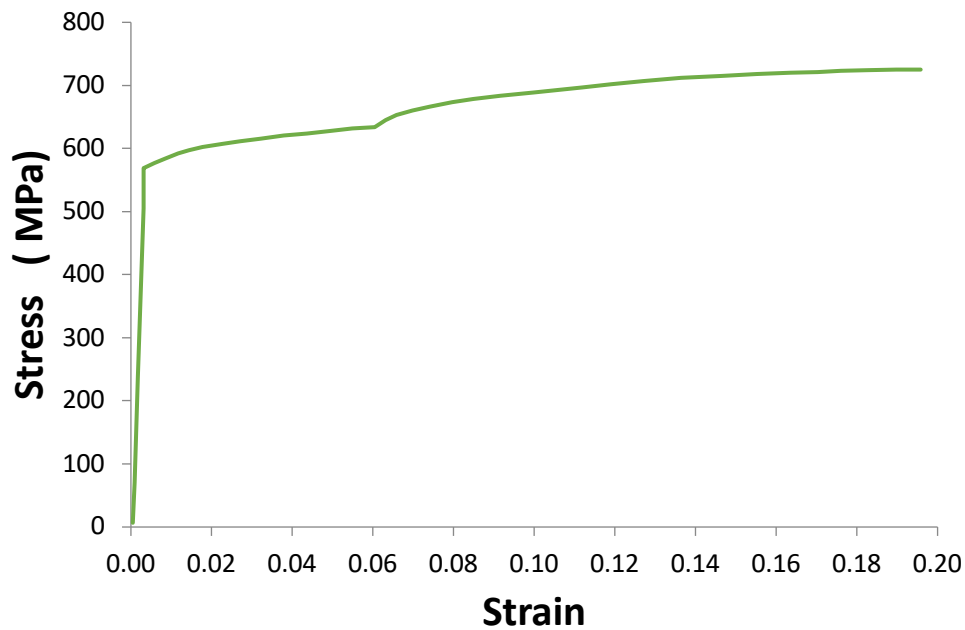


Figure 5.11: BS1501-224 28B Stress Strain Curve recreated from [126]

The remaining two parts of the FEA assembly were assumed as rigid bodies and did not require any material specification.

Regarding geometric nonlinearities, parametric analyses with the parameter that addresses that in Abaqus, i.e. nlgeom, are found in Appendix 2 and specifically in Figure A2. 10. The comparison shows that nlgeom on/off affects mostly the non-linear part of the load CMOD curve. Since specimens that go past this linear part are omitted from these analyses either choice would give accurate results. Since typically calculating J should not be considered with nlgeom on as it can lead to spurious results based on stresses near the crack-tip nlgeom was considered as off for all the analyses.

5.2.2.3 Crack tip modelling

For the steel models, a radial mesh around the crack tip was generated. At the crack tip the hexahedral elements were collapsed into wedges, shown in Figure 5.12. The nodes at the tip of the wedges/crack were merged to a single node (wedges) since elastic-plastic analyses would be run. The singularity was accounted for by moving the mid-side nodes of second order elements, at the crack edge, towards the crack tip at a distance of $\frac{1}{4}$ of the element length, as suggested for elastic-plastic analyses with a hardening material [123].

For the models developed here, a radial mesh around the crack tip was generated.

The first and second row of elements at the crack tip had a length of 0.5 mm which was then increased to 1 extending radially. There were 48 elements tangentially placed along each of the semicircles. Overall, 7 contours of J-integrals were calculated, a characteristic example of contour convergence is given for each geometry, i.e. 3PB 5_U_2 for uniaxial and 5PB 5_B_2 for biaxial specimens, in Table 5.1. There the J values calculated at the failure load are given for the depth of the crack where J is maximum (Z_{Max-J}). Table 5.1 includes the value for each contour showing that values converge from the 4th contour onwards while having less than 5% difference between them and hence the mesh is considered sufficient.

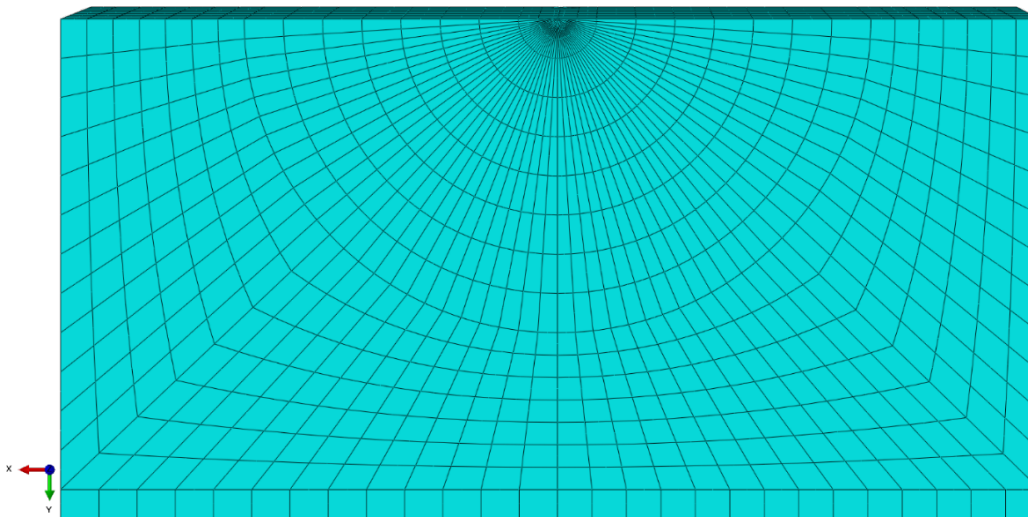


Figure 5.12: Crack-tip mesh of steel specimens

Table 5.1: J values (MPa mm) at each contour calculated at $Z_{\text{Max-J}}$ depth

| | 3PB 5_U_2 | 5PB 5_B_2 |
|-----------|-----------|-----------|
| Contour 1 | 44.79 | 59.23 |
| Contour 2 | 45.41 | 60.45 |
| Contour 3 | 46.39 | 61.64 |
| Contour 4 | 46.93 | 61.66 |
| Contour 5 | 46.96 | 61.62 |
| Contour 6 | 46.92 | 61.48 |
| Contour 7 | 46.87 | 61.48 |

5.2.2.4 Boundary conditions, contact properties & loading

The boundary conditions for the steel specimen models were the same applied to the PMMA specimens as shown in Figure 5.6 and Figure 5.7 respectively. Again, X and Y symmetry were assumed due to the quarter specimen modelled, not allowing displacements on the symmetry axis and relative rotations to the other two axes. The interaction with the rollers was incorporated with the use of a boundary condition at the point of contact which prohibited displacement on the Z (load) axis. For the model of specimen 5PB 1_BB_2, which is used for all parametric analyses shown in Appendix 2, with an applied displacement of 4.2 mm the stresses developed at the roller contact were ranging from 340 MPa on the free surface to 640 MPa (just above yield for the steel models) in the middle of the specimen at the symmetry condition. These stresses are reasonable given the high displacement applied and relate to the experiments where some plasticity was also seen at the roller interaction. This in combination with the complexity of the model deem the approach and mesh applied accurate enough for the purposes of this work.

For the spherical punch analytical surface, a kinematically coupled reference point was defined. The point, and thus the surface, were constraint to have zero displacement along the x and y axis and any relative rotations, while being allowed to move along the z axis (loading direction). Loads were applied to the specimen via application of displacement on the reference point of the punch.

For the boundary surface, it was tied to a reference point and fixed there allowing no displacement or rotations. In essence it acted as a symmetry boundary condition along the crack front which prohibited intersection between the compressive sides of the bend while allowing displacement of the PMMA surface on the tensile side of the bend.

Contact was defined between the specimen and the punch as well as the specimen and the boundary surface, while no interaction was considered between the boundary surface and the punch. After running parametric analyses, given in Appendix 2, a friction coefficient of 0.3 was used for the tangential/shear stresses, while hard contact was used for the pressure applied in the normal direction.

5.3 Modelling results

5.3.1 PMMA models

The PMMA models had displacement applied until they reached the experimental CMOD at failure. There two values were of significance, fracture toughness and T-stress values. Fracture toughness in $\text{MPa}\sqrt{\text{m}}$ values were calculated assuming plane strain conditions from the J-integral extracted from the FEA.

The modelled load-CMOD curves of the uniaxial and the biaxial PMMA experiments are shown in Figure 5.13 and Figure 5.14 respectively.

The aim of the calibration of the models was to match the elastic compliance generated from the FEA to that from the experimental Load-CMOD curves. To achieve these multiple parametric analyses were run, shown in Appendix 2 for the steel specimens, while the resulting best parameters were also used for the PMMA specimens. The parameters that were studied were the friction coefficient ranging from values of 0.1 to 0.6, displacement of the rollers with displacements ranging from -3 to 10 mm for the rollers parallel to the crack and 0 to 8 mm for the rollers perpendicular to the crack. Despite the authors best effort full matching of the elastic compliances was not achieved. The elastic compliances calculated for the experiments and FEA of the two geometries and are shown in Table 5.2. The models matched the experimental compliances by 77% and 99% for the uniaxial and biaxial cases accordingly. It is not certain why there is a 23% divergence between experimental and modelled compliance, however for the case of the PMMA specimens, material properties were taken from literature and the author argues that this could be an important reason.

For the uniaxial specimens, failure occurred at the same experimental Load and CMOD, so a single model with an applied load of 0.704 mm was sufficient to reach the failure CMOD of 0.15 mm.

For the biaxial specimens, experiment BI -1 had a non-traditional Load-CMOD curve, shown in Figure 5.14, and was disregarded. Hence a single model was developed, which with an applied displacement of 0.83 mm reached the failure CMOD of specimen BI-2 at 0.148 mm.

Table 5.2: PMMA elastic compliance in mm/kN

| | Uniaxial | Biaxial |
|--------------|----------|---------|
| Experimental | 0.115 | 0.0355 |
| FEA | 0.091 | 0.0357 |
| % Difference | 23% | 0.6% |

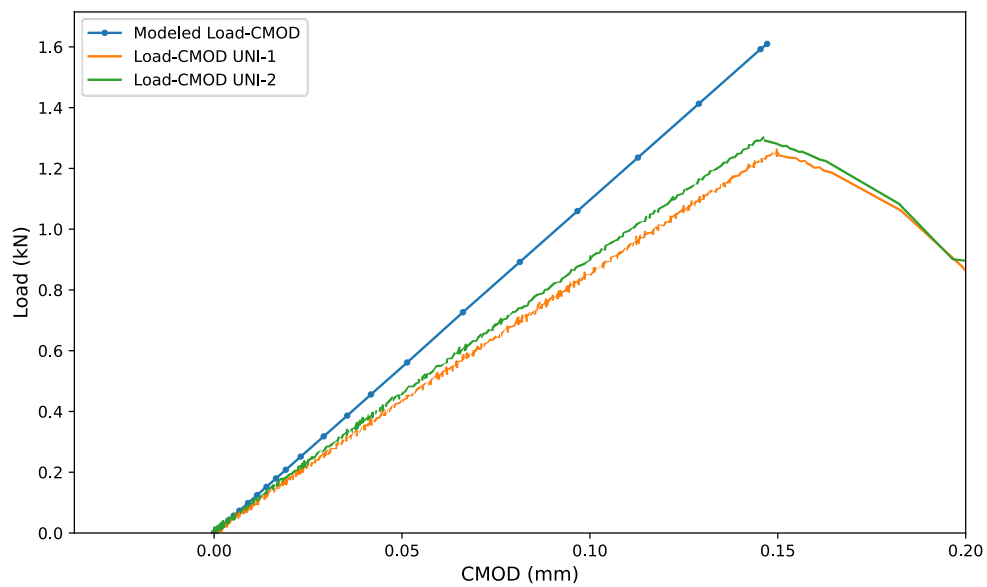


Figure 5.13: Uniaxial PMMA FEA and Experimental Load-CMOD

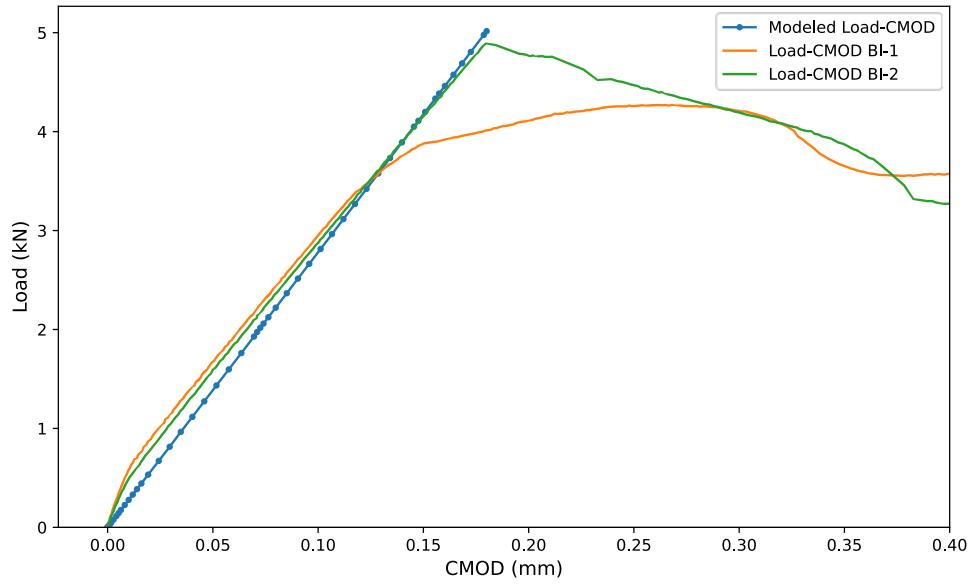


Figure 5.14: Biaxial PMMA FEA and Experimental Load-CMOD

At the final step of the model, where the failure CMOD was reached, the J-integral values along the crack front were extracted from the uniaxial and biaxial models and are given here graphically in Figure 5.15 and Figure 5.16 accordingly. While the T-stresses calculated along the Z-axis are shown in Figure 5.17 and Figure 5.18 respectively.

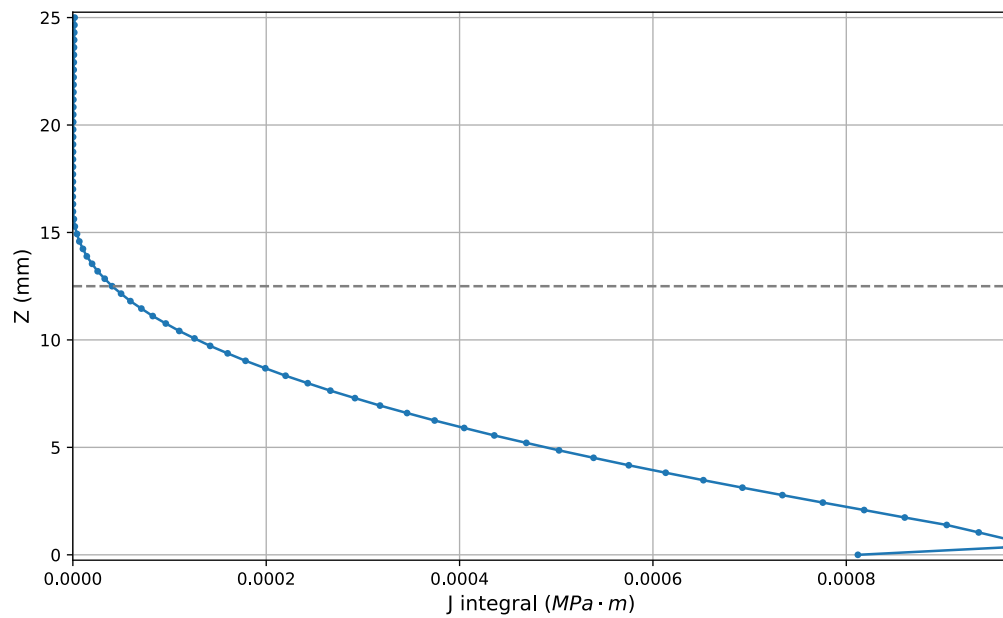


Figure 5.15: Uniaxial PMMA FEA - J-integral along crack front

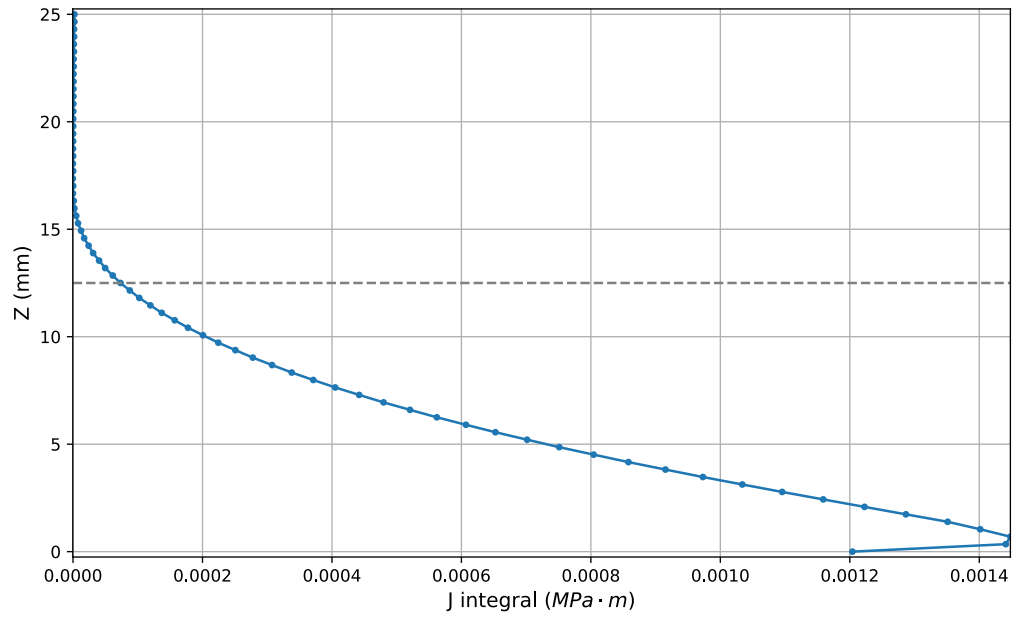


Figure 5.16: Biaxial PMMA FEA - J-integral along crack front

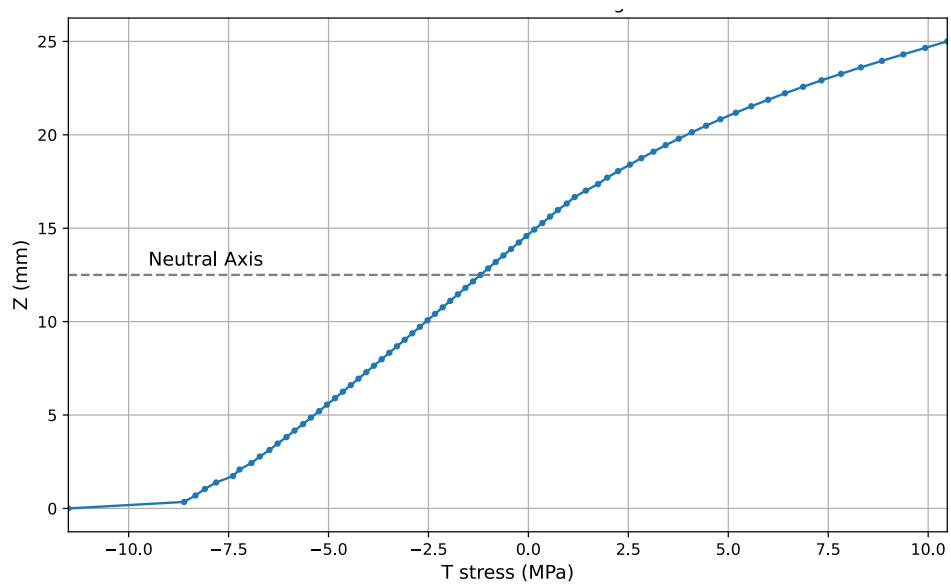


Figure 5.17: Uniaxial PMMA FEA - T-stress along crack front

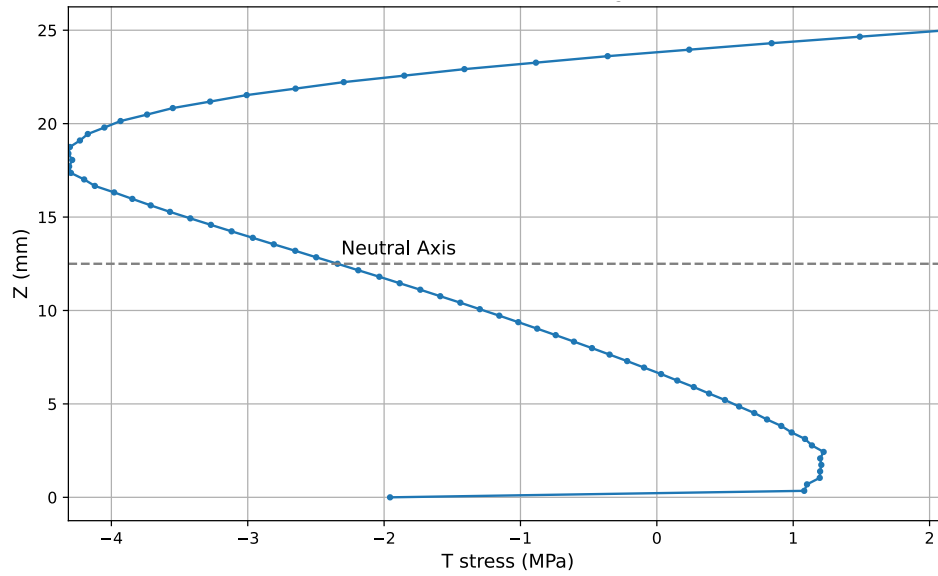


Figure 5.18: Biaxial PMMA FEA - T-stress along crack front

In the above figures, Z is the distance from the surface where the maximum tensile stresses are found. In other words, the maximum tensile stresses are located at Z=0. For both geometries the maximum J values were found at Z=0.7 mm, in Figure 5.15 and Figure 5.16 with values;

- $J_{\text{failure-uniaxial}} = 0.94 \cdot 10^{-3} \text{ MPa}\cdot\text{m}$
- $J_{\text{failure-biaxial}} = 1.43 \cdot 10^{-3} \text{ MPa}\cdot\text{m}$

These values were translated to stress intensity factor values under the assumption of plane stress since plane stress conditions occur at the surface where the crack propagation initiates. The fracture toughness values calculated are shown in Table 5.3, along with the fracture toughness calculated analytically for the uniaxial specimens using the SIF solution included in BS 7910 (M.3.1 in [71]) for plates in bending with through thickness flaws.

Table 5.3: Fracture toughness values for PMMA specimens in $\text{MPa}\sqrt{\text{m}}$

| | Uniaxial | Biaxial |
|-------------------|----------|---------|
| Analytical | 1.6 | - |
| FEA | 1.7 | 2.1 |

T-stresses were extracted from the FEA and used to calculate the structural parameter β , which is a non-dimensional form of T-stress. Here the form proposed in [27] is used, shown in Equation 5.1.

$$\beta = \frac{T_{stress}\sqrt{\pi a}}{K_I} \quad \text{Equation 5.1}$$

The β values calculated corresponded to the same Z (height) at which the maximum stress intensity factor was calculated, i.e. Z=0.7 mm and are shown in Table 5.4.

Table 5.4: Structural parameter β values calculated for PMMA specimens in MPa \sqrt{m}

| | Uniaxial | Biaxial |
|---------|----------|---------|
| β | -0.91 | 0.1 |

From Table 5.4, it was concluded that some constraint relaxation was experienced in the uniaxial specimens. Even though the difference between the two values did not seem great, it is worth revisiting Section 3.5.4.2 and Figure 3.19, where a β of value -0.633 had a significant effect on the FAL of a steel plate loaded with a biaxiality ratio of k=0.5. It is worth noting that the values of beta calculated corresponds well to that in R6 for a through-wall defect in a plate under tension, which assumes this location is equivalent to a tensile stress for a unique point. It should be noted that models here use the average crack length of the tensile side of the crack during modelling which for the PMMA specimens was relatively straight. This is due to no prior fatigue pre-cracking and gives confidence in using the β values calculated.

The fracture toughness values above did not reflect the behaviour that was expected, i.e. uniaxial specimens having lower elastic fracture toughness values than the biaxial ones. It is argued that it was due to the brittle nature of PMMA and not due to a lack of constraint effects. In particular, the lack of almost any plasticity developing, was accompanied by a lot of scatter in fracture toughness testing and it was expected that if a higher number were tested the fracture toughness values between the two configurations would converge. Additionally, the capture of constraint effects was supported by the β parameter having negative values at the case of the uniaxial specimen and denoting constraint relaxation, that when combined with higher levels of (moderate) plasticity could play an important role on the effective fracture toughness.

5.3.2 Steel models

The steel models were loaded in the same way as the PMMA ones, i.e. had displacement applied on the punch until they reached the experimental CMOD at failure. To calibrate

the models the linear part of the Load-CMOD, known as elastic compliance, was attempted to match for the experiment and the models of the two geometries.

Specimen 5PB 1_BB_2 was used as a reference given its very smooth Load-CMOD curve and its straight fatigue crack profile. Its experimental and FEA Load-CMOD are given here in Figure 5.19.

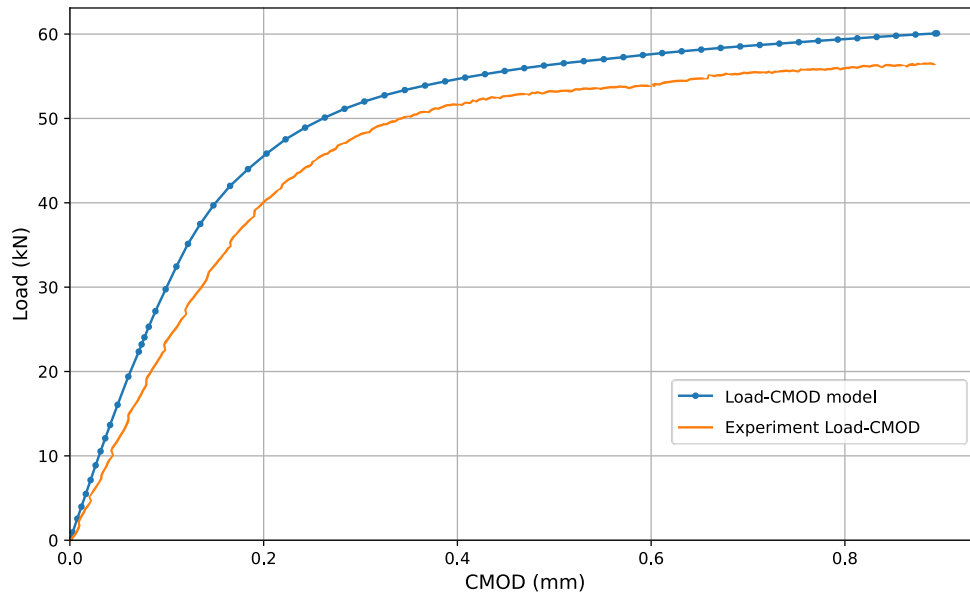


Figure 5.19: Specimen 5PB 1_BB_2; Experimental and FEA Load-CMOD curve

A lot of different parametric analyses were run to study how compliance changes, the parameters included were:

- 1) Friction coefficient
- 2) Crack Length
- 3) Roller displacement
- 4) Young's Modulus

All details of the parametric simulations and their results are presented in Appendix 2.

From the four parameters studied the only one which was able to bring the elastic part of the model's Load-CMOD curve was Young's Modulus, however that required to be decreased down to 150 GPa, which diverges significantly from the 204 GPa experimentally measured.

Given the innovative nature of experiments as well as the noise and friction that were included in many of them it was decided that the results from the FEA analyses, and

consequently the fracture toughness values calculated (from the J-integral), would be treated in a qualitative way. Hence, the modelling parameters chosen were

- 1) A friction coefficient $\mu=0.3$ between the punch and the specimen
- 2) A modelled/half crack length equal to the average of both crack sides above the neutral axis where tensile stresses were applied, as measured from the optometer
- 3) Zero roller displacement
- 4) A Young's modulus of 204 GPa

As explained in Chapter 4 some of the specimens did not break in a brittle manner but instead developed considerable amounts of plasticity that could no longer encompass the effect of biaxiality on the effective fracture toughness. The specimens that did not have a sudden crack extension as well as those rejected due to extreme conditions of friction were not analysed here. The simulated specimens are shown in Table 5.5.

Table 5.5 : Steel specimens simulated

| Biaxial Specimen ID | Uniaxial Specimen ID |
|--------------------------------|---------------------------------|
| 5PB_1_B_1 | 3PB_1_U_1 |
| 5PB_1_B_2 | 3PB_3_U_1 |
| 5PB_3_B_2 | 3PB_3_U_2 |
| 5PB_3_BB_2 | 3PB_3_B_1 |
| 5PB_4_B_1 | 3PB_4_B_1 |
| 5PB_4_B_2 | 3PB_5_U_2 |
| 5PB_5_B_2 | 3PB_5_B_1 |
| 5PB_5_BB_1 | 3PB_6_B_1 |
| 5PB_5_BB_2 | |
| 5PB_6_B_2 | |

The results extracted from the FEA were the Load-CMOD curves and the J-integral values along the crack front, shown in Appendix 3. Given the qualitative approach that the results of these analyses provided it was decided that no constraint measurements would be extracted from the FEA. Considering this T-stresses were calculated only for one representative specimen from each geometry. These analyses considered only elastic material behaviour and the specimens were loaded with the same displacement at which they reached the failure CMOD in the elastic-plastic models. The most representative specimens were 3PB_5_U_2 for the uniaxial specimens and 5PB_5_B_2 from the biaxial specimens, given their load CMOD curve including little indication of friction.

For 3PB_5_U_2 the Load-CMOD curve, J-integral and T-stress are presented in Figure 5.20 (a),(b) and (c) respectively, while for 5PB_5_B_2 these are presented in Figure 5.21. The compliances were calculated for the experimental and FEA Load-CMOD curves of these tests and are shown in Table 5.8. In comparison with the PMMA compliances, shown in Table 5.2, both of the steel geometries included an additional 20% divergence between experimental and FEA compliances. This led to an agreement between experimental and FEA of 55% for uniaxial specimens and 78% for biaxial specimens.

Table 5.6: Steel tests elastic compliance in mm/kN

| | Uniaxial | Biaxial |
|--------------|----------|---------|
| Experimental | 0.0111 | 0.0039 |
| FEA | 0.007 | 0.0031 |
| % Difference | 45% | 22% |

For both geometries the maximum J was maximum at a similar distance from the free surface of the tensile stress side of the bend, i.e. $Z=1.33$ mm for the uniaxial and $Z=1.25$ for the biaxial. The maximum J-integral values were considered as the fracture toughness J_{mat} and K_{mat} was calculated from them.

At the same distance where J was maximum the T-stresses for the two specimens were:

- $k=0$, $T_{STRESS} = -597$ MPa
- $k=1$, $T_{STRESS} = -187$ MPa

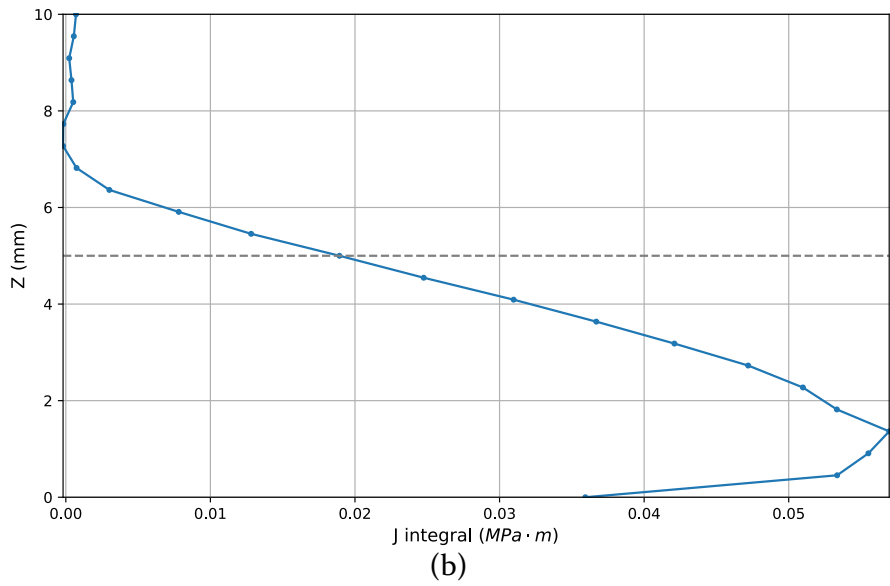
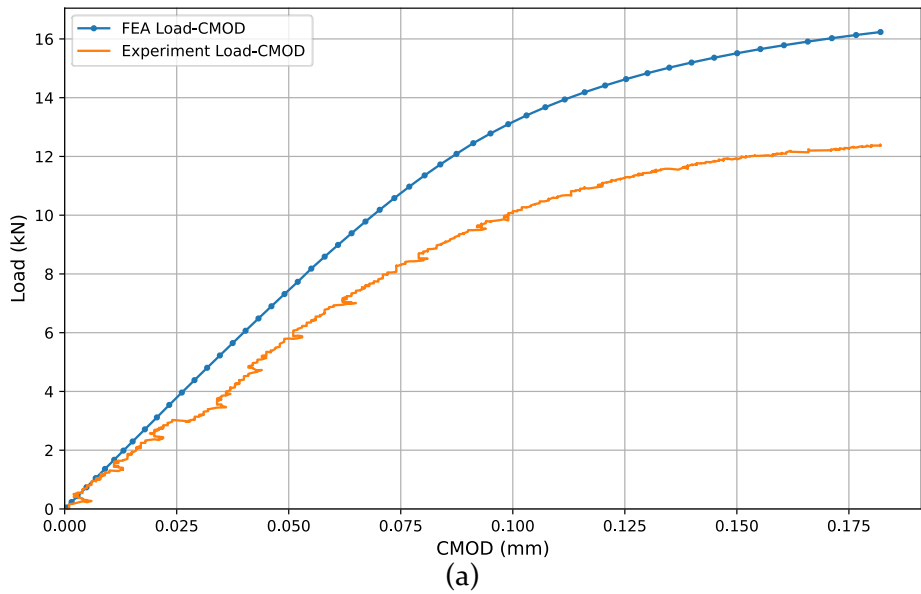
These stresses were translated to structural parameter β following Equation 5.1. The structural constraint parameters calculated are shown in Table 5.7.

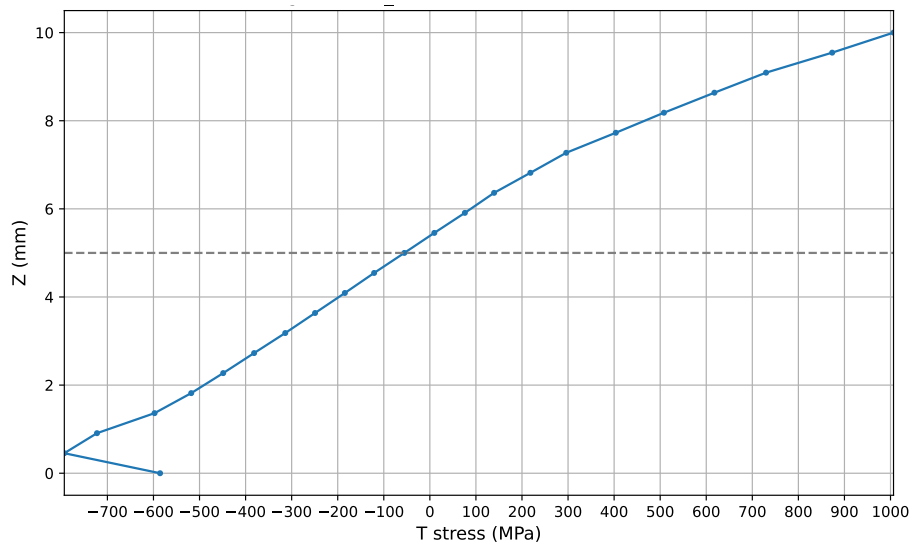
Table 5.7: Structural parameter β values calculated for steel specimens in $\text{MPa}\sqrt{\text{m}}$

| | Uniaxial | Biaxial |
|---------|----------|---------|
| β | -27.2 | -10.4 |

These values are very large in comparison to the β values calculated in Section 3.3.4.2 for the TWI biaxial plates which for $k=0,1$ had a β value of -1.154 and -0.051 respectively. These values are large enough that allow to disregard the divergence of model and experiments in arguing that the current specimens didn't achieve high levels of constraint. Given the change of the T-stress distribution from the PMMA specimens, seen in Figure 5.15 and

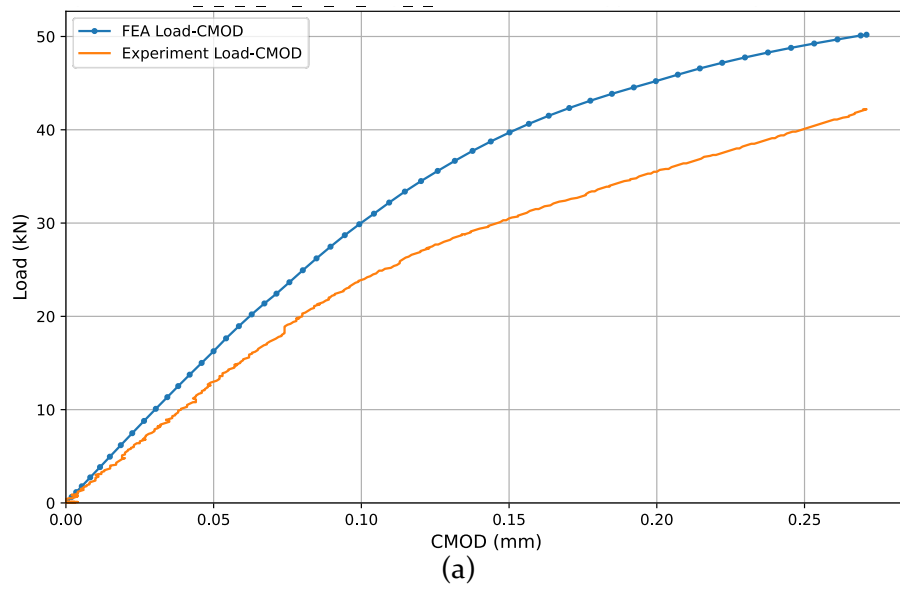
Figure 5.16, to the steel specimens, Figure 5.20 and Figure 5.21, it is believed that thickness of the specimens played an important role on the levels of constraint reached.





(c)

Figure 5.20: Specimen 3PB 5_U_2 (a) FEA and Experimental Load-CMOD curve, (b) J-integral along the crack front, (c) T-stress from elastic analysis



(a)

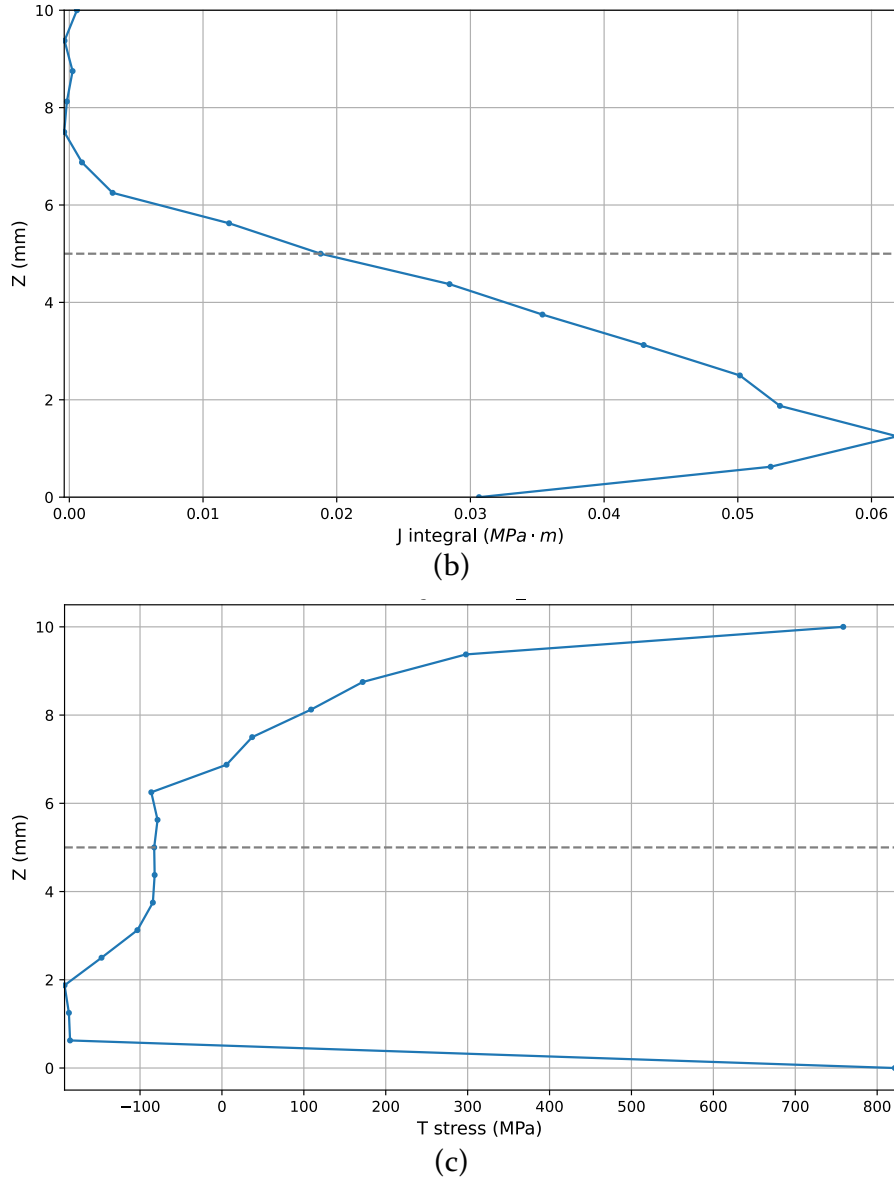


Figure 5.21: Specimen 5PB_5_B_2 (a) FEA and Experimental Load-CMOD curve, (b) J-integral along the crack front, (c) T-stress from elastic analysis

J_{mat} and K_{mat} are given in Table 5.8, along with the parameters used for each model, i.e. crack length and applied punch displacement and the desired CMOD reached in both model and experiment. From Table 5.8 the average fracture toughness values of each geometry can be calculated and are for a biaxiality ratio of:

- $k=0, K_{mat}^{k=0} = 110.88 \text{ MPa}\sqrt{\text{m}}$
- $k=1, K_{mat}^{k=1} = 128.45 \text{ MPa}\sqrt{\text{m}}$

This information is also presented graphically in Figure 5.22.

Table 5.8: FEA parameters and results

| Specimen ID | CMOD _{failure} (mm) | FEA half crack length, a (mm) | FEA applied displacement (mm) | J _{mat} FEA (MPa·m) | K _{mat} (MPa·√m) |
|-----------------|------------------------------|-------------------------------|-------------------------------|------------------------------|---------------------------|
| UNIAXIAL | | | | | |
| 3PB_1_U_1 | 0.266 | 12.79 | 1.87 | 0.0933 | 139.6 |
| 3PB_3_U_1 | 0.165 | 12.76 | 1.35 | 0.0493 | 101.5 |
| 3PB_3_U_2 | 0.255 | 12.31 | 1.85 | 0.089 | 136.3 |
| 3PB_3_B_1 | 0.242 | 13.03 | 1.74 | 0.0825 | 131.23 |
| 3PB_4_B_1 | 0.248 | 12.62 | 1.79 | 0.0855 | 133.65 |
| 3PB_5_U_2 | 0.182 | 12.49 | 1.46 | 0.0569 | 109.04 |
| 3PB_5_B_1 | 0.239 | 12.47 | 1.76 | 0.0818 | 130.65 |
| 3PB_6_B_1 | 0.287 | 13.92 | 1.9 | 0.1016 | 145.63 |
| BIAXIAL | | | | | |
| 5PB_1_B_1 | 0.16 | 12.48 | 1.08 | 0.0368 | 87.63 |
| 5PB_1_B_2 | 0.233 | 12.7 | 1.38 | 0.0535 | 105.68 |
| 5PB_3_B_2 | 0.397 | 13.19 | 1.99 | 0.0892 | 136.49 |
| 5PB_3_BB_2 | 0.139 | 12.3 | 0.98 | 0.0316 | 81.24 |
| 5PB_4_B_1 | 0.331 | 12.68 | 1.76 | 0.0758 | 125.82 |
| 5PB_4_B_2 | 0.262 | 12.15 | 1.5 | 0.0611 | 112.99 |
| 5PB_5_B_2 | 0.271 | 12.83 | 1.523 | 0.0619 | 113.7 |
| 5PB_5_BB_1 | 0.116 | 13 | 0.842 | 0.0241 | 71 |
| 5PB_5_BB_2 | 0.375 | 12.79 | 1.92 | 0.0851 | 133.3 |
| 5PB_6_B_2 | 0.414 | 12.3 | 2.08 | 0.0952 | 140.96 |

Even though the difference between the average fracture toughness values was not large there was a clear trend according to Figure 5.22 of biaxiality decreasing the effective fracture toughness. This is also supported by the decreased constraint loss of the biaxial specimens shown in Table 5.7.

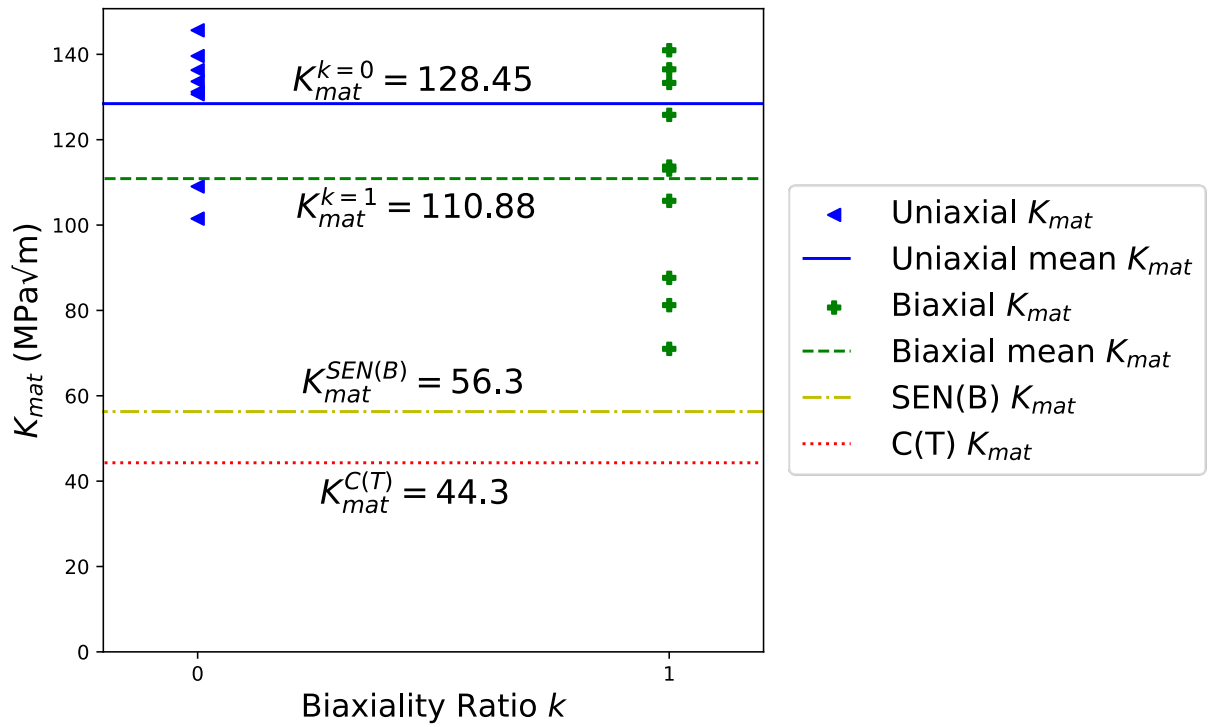


Figure 5.22: FEA derived fracture toughness values of the specimens analysed

One of the most interesting observations was that all specimens from both geometries had a stress intensity factor at failure that was significantly higher than the K_{mat} for the SEN(B) and C(T) specimens as they were tested in [126], [128]. This is also seen in Figure 5.22 where the average K_{mat} of the biaxially loaded specimens was more than twice that of both the highly constrained SEN(B) and C(T) geometries. Even though the FEA analyses deviated from the experiments, this deviation was not expected to account for the large difference.

This divergence between K_{mat} along with the structural constraint parameters calculated and the fact that all these experiments were conducted on the lower shelf, allowed to conclude that in the experimental program there were not high levels of constraint achieved.

Additional FEA modelling of the biaxial and uniaxial experiments in this work along with 10 mm thick SEN(B) and 25 mm thick C(T) specimens from this batch of steel, were conducted by Chen et al [135]. In [135] the Q fields and J fracture toughness values were calculated for the four different geometries and are shown here graphically in Figure 5.23.

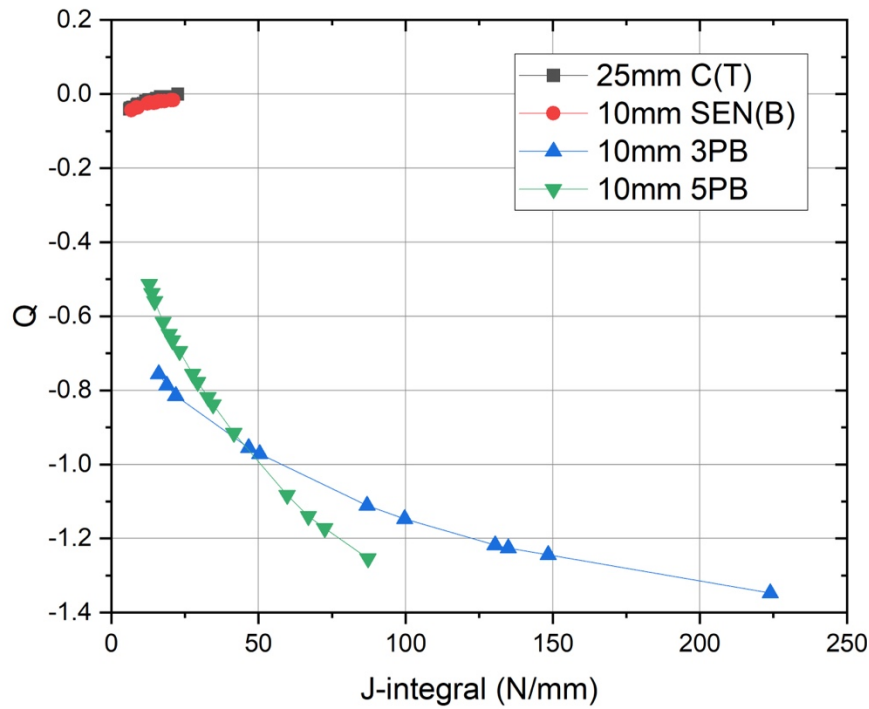


Figure 5.23: FEA derived fracture toughness values in J-Q space [135]

Figure 5.23 shows that levels of constraint had very high variation within this experimental program all of which were much lower than that observed for SEN(B) and C(T) specimens of the same or higher thickness. This can help explain the shape of the experimental Load-CMOD curves and in general the always existing but varying amount of plasticity observed throughout the experiments.

5.4 Conclusions

Three-dimensional FEA have been conducted to obtain values that could not be gathered experimentally or analytically from the specimens tested.

The PMMA FEA analyses were calibrated to match the elastic compliance of the experiments and reached good agreement for both geometries. The deviation was maximum at the case of the uniaxial specimen with 22% difference, while K_{mat} values from the uniaxial FEA agreed with the values analytically calculated, hence the model was considered accurate. Overall, from the analyses of the PMMA specimens the following are concluded:

- β structural constraint parameters calculated with the extraction of T-stresses from the FEA showed biaxially loaded cruciform specimens had a positive β ,

denoting no constraint loss as opposed to the uniaxially loaded rectangular specimens which had a negative value that could significantly enhance resistance to fracture

- Biaxiality increased the FEA calculated fracture toughness. Since constraint was captured with the biaxial tests, this was due to the brittle nature of PMMA which introduces scatter in fracture toughness testing. It is expected that a higher number of specimens tested would have converging fracture toughness values between uniaxial and biaxial tests

For the steel specimens' FEA, multiple parametric analyses were run to calibrate the model against the experiments. Calibration was based on matching the elastic compliance between the two and was achieved at 55% for uniaxial specimens and 78% for biaxial specimens, within acceptable thresholds of the parameters studied. From the steel FEA the following can be concluded:

- A trend of biaxiality decreasing the effective fracture toughness can be observed
- Both specimen geometries showed large constraint loss, which expressed in terms of structural constraint parameters were orders of magnitude larger from other available values on similar pressure vessel ferritic steels
- All uniaxially and biaxially loaded specimens had a stress intensity factor at failure that was significantly higher, almost twice, than the K_{mat} for the SEN(B) and C(T) specimens measured for this batch of material
- The large divergence between the experiments conducted in this work and the high constraint geometries tested in the past, as well as all of them having been conducted on the lower shelf, show that the experimental program here did not achieve high levels of constrained achieved
- Additional FEA comparing the uniaxial and biaxial experiments with SEN(B) and C(T) specimens of the same thickness further show varying levels of constraint that go all the way to no constraint and explain the varying plasticity of the experiments.

Chapter 6 Conclusions

6.1 Conclusions

Engineering components such as pressure vessels and piping are usually subject to pressure, and other complex loading conditions that create a multiaxial state of loading. This work aims to quantify the effect of the, commonly met, two-directional multiaxial loading known as biaxial loading on the ECA of a component and in particular the effect on failure by fracture.

Current practice in industry is to disregard this loading effect and invoke uniaxially derived values to investigate the fitness for service of a component, while the stress fields in biaxially loaded components are not uniaxial at all.

Existing research argues that assessing biaxially loaded components as uniaxial is not necessarily a safe approach, however in cases it can be not only safe but conservative, thus causing ambiguity on the importance of this effect.

As an initial approach, the author wanted to find how omitting biaxiality from ECAs affects their accuracy, which in its turn could reveal patterns that can be addressed through changing analytics equations currently used in the standards. For this, tests from multiple experimental programs from literature were analysed. These programs were not focused primarily on biaxiality and could not provide a consistent dataset to find a trend between the biaxiality ratio of a component and the accuracy of the uniaxial solutions included in the FFS standards. This made clear that any further approaches should focus solely on a biaxiality oriented set of experiments.

Following, tests from a biaxiality focused TWI experimental program were analysed. These included a combination of surface and through thickness flawed specimens loaded uniaxially and biaxially on various temperatures. With the primary focus set on fracture, the tests analysed were conducted on the lower shelf, with very limited ductility at these temperatures. The analyses showed:

- For the surface flawed specimens:
 - treating them as uniaxial was safe in all the cases considered

- equibiaxial loading resulted in the crack opening stresses reducing from the case of uniaxial loading at similar failure loads
- For the through thickness cracked specimens:
 - when analysed with an Option 3 assessment, minor differences in the interpretation of fracture toughness values were critical for the verdict of the assessment (i.e. safe or unsafe)
 - using constraint corrected Option 3 assessments require a thorough investigation of what fracture toughness values can be used, as even slightly non-conservative values led to inaccurate safe predictions

The above findings from the analyses and the lack of through thickness flawed biaxial tests in literature, steered this work towards decoupling biaxiality from flaw depth and designing an experimental program that would capture high levels of constraint through biaxially loading through thickness cracks.

This program included testing of two geometries, made from a ferritic pressure vessel steel, on the lower shelf. The geometries were a rectangular specimen loaded uniaxially in a 3-point bend and a cruciform specimen loaded equibiaxially in a 5-point bend. During the tests both geometries exhibited varying levels of plasticity, with many going way past linear elastic behaviour and exhibiting extensive ductile tearing. Hence, it was argued that high constraint was not achieved during testing.

To calculate fracture toughness and constraint parameters FEA models were developed and calibrated to allow a qualitative approach. From the analyses the following trends were observed for the,

- Fracture toughness values: these were found to be lower on average for the biaxial specimens. However, for both geometries they were significantly higher from the SEN(B) and C(T) specimen values that derived from tests on the same material and temperature
- T-stress and β structural constraint parameters: again, the same trend as the fracture toughness was followed and these were significantly large, orders of magnitude larger from those calculated for the TWI biaxial tests.

Given the varying levels of plasticity seen in the experiments and the findings from the FEA it could be safely concluded that high constraint was not achieved in this program regardless of the lower-shelf temperature at which specimens were tested.

Further analyses allowed for a comparison of the uniaxially and biaxially loaded with SEN(B) and C(T) specimens, of the same and increased thickness, in the J-Q space. There it was clearly shown that all constraint levels achieved in this experimental program were very low. They were orders of magnitude lower than both SEN(B) and C(T) specimen configurations, which regardless of the thickness difference between specimens remained within similar constraint and fracture toughness levels.

The above findings play a very important role on how biaxiality should be treated during real life applications as they support that the use of higher values of fracture toughness, when assessing components in similar loading conditions, could result to safe or even conservative predictions. Hence, given all other things equal regarding failure modes, the findings of this work add confidence that greater lifetime and load capabilities can be expected on biaxially loaded components.

6.2 Future work

It is important to keep in mind the main motivation behind the continuation of this research. Industry has been long treating constraint effects conservatively to ensure safety. This conservatism is an enabler for poor use of resources as it drives maintenance, inspection and design costs up, while not allowing for an accurate life or load capacity estimation. The following propositions aim to give a holistic and synergetic approach that will develop new data which can be triangulated with the current findings in tackling the unnecessary conservatism.

Regarding the effect of biaxiality on fracture, a lot of ground was already covered in this work, however, the ambition of the experimental program, i.e., testing throughout the fracture transition temperature spectrum and achieving high levels of constraint, was not achieved. For the latter, the plasticity developed on the lower shelf as well as the fracture toughness and constraint values calculated, in both uniaxially and biaxially loaded geometries on the lower shelf, showed that the constraint levels achieved were very low.

Additionally, something that is important but was not covered in this work is the effect of biaxiality on plastic collapse, it is crucial that more experiments are conducted on

materials and temperature combinations where a significant amount of plasticity can be met. These experiments will both help identify the gaps between the connection of the two as well as assist in validating existing analytical limit load solutions that include the effect of biaxiality. These solutions have derived from FEA analyses and experimental validation is important before they can reach implementation in industry.

It is therefore recommended that additional experimental work is conducted to quantify the effect of biaxiality on both fracture and plastic collapse. It is advised that the experimental program includes a combination of the following parameters:

1. Different thicknesses, to study the interaction of thickness (out-of-plane) and biaxiality (in-plane constraint). This allows to investigate whether the constraint levels of biaxially loaded specimens would be sensitive to thickness, as well as whether thickness increase could raise constraint to the levels seen for C(T) and SEN(B) specimens
2. Variety of temperatures:
 - a. Lower shelf temperature tests, would aim to investigate the effect of biaxiality on fracture as it was done in this program
 - b. Lower transition region temperature tests would focus on understanding the competition of ductile and brittle failure modes as temperature increases
 - c. Upper transition region to upper shelf temperature tests, would aim to identify the connection between biaxiality and plastic collapse and could act as a validation benchmark for existing analytical solutions that include biaxiality
3. Different flaw geometries and in particular a limited number of surface breaking flaws, to investigate whether higher or even lower levels of constraint can be reached with a shallow flaw.

All the above combinations would require an extensive experimental program with good planning beforehand so that enough of the same batch of material is ensured prior to its start. This might be costly, but it is of paramount importance to secure enough material not only for the current program but also for future tests that might be of importance. It

is the opinion of the author that only through a very intensive and holistic investigation can we reach a reliable quantification of the effect of biaxiality.

Additionally, the above proposed experiments would provide fertile ground for multiple FEA analyses to be conducted. Having the data points of the above experiments can allow for not only validating existing analytical and numerical solutions but also build new approaches towards quantifying biaxiality or constraint.

List of References

- [1] BSI, *BS 7910:2019 Guide to methods for assessing the acceptability of flaws in metallic structures*. BSi, 2019.
- [2] API, *API 579-1/ASME FFS-1 2016 Fitness-For-Service*. Washington, D.C.: American Petroleum Institute, 2016.
- [3] EDF Energy Nuclear Generation Ltd., Ed., *Assessment of the Integrity of Structures Containing Defects, R6 - Revision 4, as amended*. 2000.
- [4] A. Cosham, K. A. Macdonald, I. Hadley, and P. Moore, 'ECAs: Lifting the Lid of the Black Box', no. 57700, p. V05BT04A022, 2017, doi: 10.1115/OMAE2017-61889.
- [5] J. Gouveia, G. Carvalho, P. Chaves, and D. Carneiro, 'Engineering Critical Assessment of Production Pipelines in Presence of Sour Environment', presented at the 23^o Congresso Nacional de Transporte Aquaviário, Construção, Oct. 2010. doi: 10.13140/RG.2.1.1402.0965.
- [6] M. Mostafavi, D. J. Smith, and M. J. Pavier, 'Fracture of aluminium alloy 2024 under biaxial and triaxial loading', *Eng. Fract. Mech.*, vol. 78, no. 8, pp. 1705–1716, May 2011, doi: 10.1016/j.engfracmech.2010.11.006.
- [7] E. Østby and A. O. Hellesvik, 'Large-scale experimental investigation of the effect of biaxial loading on the deformation capacity of pipes with defects', *Int. J. Press. Vessels Pip.*, vol. 85, no. 11, pp. 814–824, Nov. 2008, doi: 10.1016/j.ijpvp.2008.04.009.
- [8] R. Phaal, R. M. Andrews, and S. J. Garwood, 'TWI biaxial test program: 1984–1994', *Int. J. Press. Vessels Pip.*, vol. 64, no. 3, pp. 177–190, Jan. 1995, doi: 10.1016/0308-0161(95)98940-8.
- [9] B. R. Bass, W. J. McAfee, P. T. Williams, and W. E. Pennell, 'Fracture assessment of HSST Plate 14 shallow-flaw cruciform bend specimens tested under biaxial loading conditions', Oak Ridge National Lab., TN (United States), ORNL/NRC/LTR-98/9, Jun. 1998. doi: 10.2172/296736.
- [10] W. J. McAfee, B. R. Bass, and J. W. Bryson, 'Development of a methodology for the assessment of shallow-flaw fracture in nuclear reactor pressure vessels: Generation of biaxial shallow-flaw fracture toughness data', Oak Ridge National Lab., TN (United States), ORNL/NRC/LTR-97/4, Jul. 1998. doi: 10.2172/296735.
- [11] M. Mostafavi, D. J. Smith, and M. J. Pavier, 'Reduction of measured toughness due to out-of-plane constraint in ductile fracture of aluminium alloy specimens', *Fatigue Fract. Eng. Mater. Struct.*, vol. 33, no. 11, pp. 724–739, Nov. 2010, doi: 10.1111/j.1460-2695.2010.01483.x.
- [12] F. M. Beremin, A. Pineau, F. Mudry, J.-C. Devaux, Y. D'Escatha, and P. Ledermann, 'A local criterion for cleavage fracture of a nuclear pressure vessel steel', *Metall. Trans. A*, vol. 14, no. 11, pp. 2277–2287, Nov. 1983, doi: 10.1007/BF02663302.
- [13] R. H. Dodds, T. L. Anderson, and M. T. Kirk, 'A framework to correlate a/W ratio effects on elastic-plastic fracture toughness (J_c)', *Int. J. Fract.*, vol. 48, no. 1, pp. 1–22, Mar. 1991, doi: 10.1007/BF00012499.
- [14] W. J. McAfee, B. R. Bass, and P. T. Williams, 'Shallow Flaws Under Biaxial Loading Conditions—Part I: The Effect of Specimen Size on Fracture Toughness Values Obtained From Large-Scale Cruciform Specimens', *J. Press. Vessel Technol.*, vol. 123, no. 1, p. 10, 2001, doi: 10.1115/1.1343910.
- [15] P. T. Williams, B. R. Bass, and W. J. McAfee, 'Shallow Flaws Under Biaxial Loading Conditions—Part II: Application of a Weibull Stress Analysis of the Cruciform Bend

- Specimen Using a Hydrostatic Stress Criterion', *J. Press. Vessel Technol.*, vol. 123, no. 1, p. 25, 2001, doi: 10.1115/1.1344235.
- [16] S. J. Garwood, T. G. Davey, and S. L. Creswell, 'Behaviour of A533B under biaxial loading at +70°C', *Int. J. Press. Vessels Pip.*, vol. 36, no. 3, pp. 199–224, Jan. 1989, doi: 10.1016/0308-0161(89)90003-3.
 - [17] P. S. Leever, J. C. Radon, and L. E. Culver, 'Crack growth in plastic panels under biaxial stress', *Polymer*, vol. 17, no. 7, pp. 627–632, Jul. 1976, doi: 10.1016/0032-3861(76)90282-2.
 - [18] P. S. Leever, J. C. Radon, and L. E. Culver, 'Fracture trajectories in a biaxially stressed plate', *J. Mech. Phys. Solids*, vol. 24, no. 6, pp. 381–395, Dec. 1976, doi: 10.1016/0022-5096(76)90010-7.
 - [19] N. J. I. Adams, 'Some comments on the effect of biaxial stress on fatigue crack growth and fracture', *Eng. Fract. Mech.*, vol. 5, no. 4, pp. 983–991, Dec. 1973, doi: 10.1016/0013-7944(73)90063-5.
 - [20] M. L. Williams, 'On the Stress Distribution at the Base of a Stationary Crack', *J. Appl. Mech.*, vol. 24, pp. 109–114, 1957.
 - [21] G. R. Irwin, *Fract. Mech.*, pp. 557–592, 1960.
 - [22] F. Erdogan and G. C. Sih, 'On the Crack Extension in Plates Under Plane Loading and Transverse Shear', *J. Basic Eng.*, vol. 85, no. 4, pp. 519–525, Dec. 1963, doi: 10.1115/1.3656897.
 - [23] J. Radon, P. Leever, and L. Culver, 'Fracture toughness of PMMA under biaxial stress', 1977.
 - [24] J. Eftis, N. Subramonian, and H. Liebowitz, 'Crack border stress and displacement equations revisited', *Eng. Fract. Mech.*, vol. 9, no. 1, pp. 189–210, Jan. 1977, doi: 10.1016/0013-7944(77)90063-7.
 - [25] J. Eftis, N. Subramonian, and H. Liebowitz, 'Biaxial load effects on the crack border elastic strain energy and strain energy rate', *Eng. Fract. Mech.*, vol. 9, no. 4, pp. 753–764, 1977.
 - [26] H. Liebowitz, J. D. Lee, and J. Eftis, 'Biaxial load effects in fracture mechanics', *Eng. Fract. Mech.*, vol. 10, no. 2, pp. 315–335, Jan. 1978, doi: 10.1016/0013-7944(78)90015-2.
 - [27] T. L. Anderson, *Fracture Mechanics: Fundamentals and Applications, Fourth Edition*, 4 edition. CRC Press, 2017.
 - [28] J. W. Hutchinson, 'Fundamentals of the Phenomenological Theory of Nonlinear Fracture Mechanics', *J. Appl. Mech.*, vol. 50, Dec. 1983.
 - [29] J. R. Rice, 'A Path Independent Integral and the Approximate Analysis of Strain Concentration by Notches and Cracks', *J. Appl. Mech.*, vol. 35, no. 2, p. 379, 1968, doi: 10.1115/1.3601206.
 - [30] G. Cho, *Fatigue: Core Research from TWI*. Woodhead Publishing, 2000.
 - [31] R. O. Ritchie, 'Why Ductile Fracture Mechanics?', *J. Eng. Mater. Technol.*, vol. 105, no. 1, p. 1, 1983, doi: 10.1115/1.3225613.
 - [32] N. O'Dowd and C. Shih, 'Two-Parameter Fracture Mechanics: Theory and Applications', in *Fracture Mechanics: Twenty-Fourth Volume*, J. Landes, D. McCabe, and J. Boulet, Eds. 100 Barr Harbor Drive, PO Box C700, West Conshohocken, PA 19428-2959: ASTM International, 1994, pp. 21–21–27. doi: 10.1520/STP13698S.
 - [33] W. E. Pennell, B. R. Bass, J. W. Bryson, W. J. McAfee, T. J. Theiss, and M. C. Rao, 'Biaxial loading and shallow-flaw effects on crack-tip constraint and fracture-toughness', Oak Ridge National Lab., TN (United States), CONF-940613-7, Apr. 1994. Accessed: Mar. 14, 2018. [Online]. Available:

- <https://www.osti.gov/biblio/10143212-biaxial-loading-shallow-flaw-effects-crack-tip-constraint-fracture-toughness>
- [34] W. E. Pennell, B. R. Bass, J. W. Bryson, and W. J. McAfee, 'An interim report on shallow-flaw fracture technology development', Oak Ridge National Lab., TN (United States), CONF-950740-42, Jun. 1995. Accessed: Mar. 14, 2018. [Online]. Available: <https://www.osti.gov/biblio/73023-interim-report-shallow-flaw-fracture-technology-development>
 - [35] N. P. O'Dowd and C. F. Shih, 'Family of crack-tip fields characterized by a triaxiality parameter—I. Structure of fields', *J. Mech. Phys. Solids*, vol. 39, no. 8, pp. 989–1015, Jan. 1991, doi: 10.1016/0022-5096(91)90049-T.
 - [36] N. P. O'Dowd and C. F. Shih, 'Family of crack-tip fields characterized by a triaxiality parameter—II. Fracture applications', *J. Mech. Phys. Solids*, vol. 40, no. 5, pp. 939–963, Jul. 1992, doi: 10.1016/0022-5096(92)90057-9.
 - [37] B. R. Bass, J. W. Bryson, W. J. McAfee, W. E. Pennell, and T. J. Theiss, 'Design of a cruciform bend specimen for determination of out-of-plane biaxial tensile stress effects on fracture toughness for shallow cracks', Oak Ridge National Lab., TN (United States), CONF-930803-13, Jun. 1993. Accessed: Mar. 14, 2018. [Online]. Available: <https://www.osti.gov/biblio/10162814-design-cruciform-bend-specimen-determination-out-plane-biaxial-tensile-stress-effects-fracture-toughness-shallow-cracks>
 - [38] T. J. Theiss, B. R. Bass, and J. W. Bryson, 'Experimental and analytical comparison of constraint effects due to biaxial loading and shallow-flaws', Oak Ridge National Lab., TN (United States), CONF-931118-1, Dec. 1993. doi: 10.2172/10111958.
 - [39] B. R. Bass, J. W. Bryson, T. L. Dickson, W. J. McAfee, and W. E. Pennell, 'Development of a shallow-flaw fracture assessment methodology for nuclear reactor pressure vessels', Oak Ridge National Lab., TN (United States), CONF-9609114-1, Jun. 1996. Accessed: Mar. 14, 2018. [Online]. Available: <https://www.osti.gov/biblio/266758-development-shallow-flaw-fracture-assessment-methodology-nuclear-reactor-pressure-vessels>
 - [40] W. E. Pennell, B. R. Bass, J. W. Bryson, T. L. Dickson, W. J. McAfee, and J. G. Merkle, 'Preliminary assessment of the effects of biaxial loading on reactor pressure vessel structural-integrity-assessment technology', Oak Ridge National Lab., TN (United States), CONF-960306-31, Apr. 1996. Accessed: Mar. 14, 2018. [Online]. Available: <https://www.osti.gov/biblio/217731-preliminary-assessment-effects-biaxial-loading-reactor-pressure-vessel-structural-integrity-assessment-technology>
 - [41] B. R. Bass, W. J. McAfee, P. T. Williams, and W. E. Pennell, 'Evaluation of constraint methodologies applied to a shallow-flaw cruciform bend specimen tested under biaxial loading conditions', Oak Ridge National Lab., TN (United States), ORNL/CP-96312; CONF-980708-, Jan. 1998. Accessed: Mar. 14, 2018. [Online]. Available: <https://www.osti.gov/biblio/654158-evaluation-constraint-methodologies-applied-shallow-flaw-cruciform-bend-specimen-tested-under-biaxial-loading-conditions>
 - [42] J. A. Keeney, B. R. Bass, and W. J. McAfee, 'Fracture behavior of shallow cracks in full-thickness clad beams from an RPV wall section', Oak Ridge National Lab., TN (United States), CONF-950804-2, Apr. 1995. Accessed: Mar. 14, 2018. [Online]. Available: <https://www.osti.gov/biblio/62617-fracture-behavior-shallow-cracks-full-thickness-clad-beams-from-rpv-wall-section>
 - [43] S. R. Bordet, A. D. Karstensen, C. S. Wiesner, and D. M. Knowles, 'Effects of plastic strain on cleavage fracture predictions in steel', Honolulu, Hawaii, Dec. 2001. Accessed: May 16, 2018. [Online]. Available: <https://www.twi-global.com/technical->

- knowledge/published-papers/effects-of-plastic-strain-on-cleavage-fracture-predictions-in-steel-dec2001/
- [44] P.A. Kelly, 'Stress Analysis for Plasticity', in *Solid Mechanics Part II: Engineering Solid Mechanics*, University of Auckland: Department of Engineering Science, 2012, pp. 252–259. Accessed: Apr. 17, 2018. [Online]. Available: http://homepages.engineering.auckland.ac.nz/~pkel015/SolidMechanicsBooks/Part_II/08_Plasticity/08_Plasticity_02_Stress_Analysis.pdf
 - [45] D. P. G. Lidbury *et al.*, 'Validation of constraint-based methodology in structural integrity of ferritic steels for nuclear reactor pressure vessels', *Fatigue Fract. Eng. Mater. Struct.*, vol. 29, no. 9-10, pp. 829–849, Sep. 2006, doi: 10.1111/j.1460-2695.2006.01057.x.
 - [46] R. H. Dodds, C. F. Shih, and T. L. Anderson, 'Continuum and micromechanics treatment of constraint in fracture', *Int. J. Fract.*, vol. 64, no. 2, pp. 101–133, Nov. 1993, doi: 10.1007/BF00016693.
 - [47] G. Rousselier, 'Ductile fracture models and their potential in local approach of fracture', *Nucl. Eng. Des.*, vol. 105, no. 1, pp. 97–111, Dec. 1987, doi: 10.1016/0029-5493(87)90234-2.
 - [48] S. Marie and S. Chapuliot, 'Ductile Tearing Simulation Based on a Local Energetic Criterion', *Fatigue Fract. Eng. Mater. Struct.*, vol. 21, no. 2, pp. 215–227, Feb. 1998, doi: 10.1046/j.1460-2695.1998.00017.x.
 - [49] Y. H. Wang, G. Z. Wang, S. T. Tu, and F. Z. Xuan, 'Ductile fracture prediction based on J-integral and unified constraint parameters for cracked pipes', *Eng. Fract. Mech.*, vol. 215, pp. 1–15, Jun. 2019, doi: 10.1016/j.engfracmech.2019.05.001.
 - [50] B. R. Bass, J. W. Bryson, T. J. Theiss, and M. C. Rao, 'Biaxial loading and shallow-flaw effects on crack-tip constraint and fracture toughness', Nuclear Regulatory Commission, Washington, DC (United States). Div. of Engineering; Oak Ridge National Lab., TN (United States), NUREG/CR-6132; ORNL/TM-12498, Jan. 1994. doi: 10.2172/143960.
 - [51] W. J. McAfee, B. R. Bass, J. W. J. Bryson, and W. E. Pennell, 'Biaxial loading effects on fracture toughness of reactor pressure vessel steel', Nuclear Regulatory Commission, Washington, DC (United States). Div. of Engineering Technology; Oak Ridge National Lab., TN (United States), NUREG/CR-6273; ORNL/TM-12866, Mar. 1995. doi: 10.2172/35267.
 - [52] 'Validation of Constraint-Based Assessment Methodology in Structural Integrity (VOCALIST)', Serco Assurance (UK), Contract No: FIKS CT-2000-00090, 2006. Accessed: Apr. 09, 2018. [Online]. Available: https://www.cordis.europa.eu/docs/projects/files/FIKS/FIKS-CT-2000-00090/87794261-6_en.pdf
 - [53] T. Anderson and R. Dodds, 'Specimen Size Requirements for Fracture Toughness Testing in the Transition Region', *Specim. Size Requir. Fract. Toughness Test. Transit. Reg.*, 1991.
 - [54] W. Weibull, 'A Statistical Distribution Function of Wide Applicability', *J. Appl. Mech.*, vol. 18, pp. 293–297, 1984.
 - [55] C. Ruggieri, 'Influence of threshold parameters on cleavage fracture predictions using the Weibull stress model', p. 24.
 - [56] L. Vincent, M. Libert, B. Marini, and C. Rey, 'Towards a modelling of RPV steel brittle fracture using crystal plasticity computations on polycrystalline aggregates', *J. Nucl. Mater. - J NUCL MATER*, vol. 406, pp. 91–96, Nov. 2010, doi: 10.1016/j.jnucmat.2010.07.022.

- [57] P. Forget, B. Marini, and L. Vincent, 'Application of local approach to fracture of an RPV steel: effect of the crystal plasticity on the critical carbide size', *Procedia Struct. Integr.*, vol. 2, pp. 1660–1667, Dec. 2016, doi: 10.1016/j.prostr.2016.06.210.
- [58] D. Lidbury, E. Keim, B. Marini, L. Malerba, and A. Zeghadi, *Overview of RPV sub-project of perform 60*, vol. 6. 2010. doi: 10.1115/PVP2010-25980.
- [59] K. Wallin, T. Saario, and K. Törrönen, 'Statistical model for carbide induced brittle fracture in steel', *Met. Sci.*, vol. 18, no. 1, pp. 13–16, Jan. 1984, doi: 10.1179/030634584790420384.
- [60] K. Wallin and A. Laukkanen, 'New developments of the Wallin, Saario, Törrönen cleavage fracture model', *Eng. Fract. Mech.*, vol. 75, no. 11, pp. 3367–3377, Jul. 2008, doi: 10.1016/j.engfracmech.2007.07.018.
- [61] D. Lidbury *et al.*, *PERFECT: Progress with multiscale modelling in RPV mechanics sub-project*. 2006.
- [62] A. Laukkanen and K. Wallin, 'DETERMINATION OF LOCAL APPROACH PARAMETERS ON THE BASIS OF THE "EUROCURVE" FRACTURE TOUGHNESS ROUND-ROBIN RESULTS', p. 8.
- [63] P. M. James, M. Ford, and A. P. Jivkov, 'A novel particle failure criterion for cleavage fracture modelling allowing measured brittle particle distributions', *Eng. Fract. Mech.*, vol. 121–122, pp. 98–115, May 2014, doi: 10.1016/j.engfracmech.2014.03.005.
- [64] S. R. Bordet, A. D. Karstensen, D. M. Knowles, and C. S. Wiesner, 'A new statistical local criterion for cleavage fracture in steel. Part I: model presentation', *Eng. Fract. Mech.*, vol. 72, no. 3, pp. 435–452, Feb. 2005, doi: 10.1016/j.engfracmech.2004.02.009.
- [65] C. K. Seal and A. H. Sherry, 'Predicting the effect of constraint on cleavage and ductile fracture toughness using area contour toughness scaling', *Eng. Fract. Mech.*, vol. 186, pp. 347–367, Dec. 2017, doi: 10.1016/j.engfracmech.2017.09.029.
- [66] J. R. Rice and D. M. Tracey, 'On the ductile enlargement of voids in triaxial stress fields*', *J. Mech. Phys. Solids*, vol. 17, no. 3, pp. 201–217, Jun. 1969, doi: 10.1016/0022-5096(69)90033-7.
- [67] J. W. Hancock, W. G. Reuter, and D. M. Parks, 'Constraint and toughness parameterized by T', 1993, no. 1171, pp. 21–40.
- [68] J. D. Sumpter, 'An experimental investigation of the T stress approach', *ASTM Spec. Tech. Publ.*, vol. 1171, pp. 492–492, 1993.
- [69] K. Wallin, 'Master curve analysis of the "Euro" fracture toughness dataset', *Eng. Fract. Mech.*, vol. 69, no. 4, pp. 451–481, Mar. 2002, doi: 10.1016/S0013-7944(01)00071-6.
- [70] I. Hadley and H. Pisarski, 'Materials properties for Engineering Critical Assessment: Background to the advice given in BS 7910:2013', *Int. J. Press. Vessels Pip.*, vol. 168, pp. 191–199, Dec. 2018, doi: 10.1016/j.ijpvp.2018.10.016.
- [71] BSI, *BS 7910:2013+A1:2015 - Guide to methods for assessing the acceptability of flaws in metallic structures*. BSi, 2013.
- [72] A. H. Sherry, M. A. Wilkes, D. W. Beardsmore, and D. P. G. Lidbury, 'Material constraint parameters for the assessment of shallow defects in structural components—Part I: Parameter solutions', *Eng. Fract. Mech.*, vol. 72, no. 15, pp. 2373–2395, Oct. 2005, doi: 10.1016/j.engfracmech.2004.12.009.
- [73] A. H. Sherry, D. G. Hooton, D. W. Beardsmore, and D. P. G. Lidbury, 'Material constraint parameters for the assessment of shallow defects in structural components. Part II: Constraint-based assessment of shallow defects', *Eng. Fract. Mech.*, vol. 72, no. 15, pp. 2396–2415, Oct. 2005, doi: 10.1016/j.engfracmech.2004.12.010.

- [74] C. Meek and R. A. Ainsworth, 'The effects of load biaxiality and plate length on the limit load of a centre-cracked plate', *Eng. Fract. Mech.*, vol. 147, pp. 306–317, Oct. 2015, doi: 10.1016/j.engfracmech.2015.03.034.
- [75] N. Miura and Y. Takahashi, 'Evaluation of J-integral for surface cracked plates under biaxial loading using extended reference stress method', *Int. J. Press. Vessels Pip.*, vol. 87, no. 1, pp. 58–65, Jan. 2010, doi: 10.1016/j.ijpvp.2009.11.003.
- [76] Y. Lei and P. Budden, 'Global limit load solutions for plates with surface cracks under combined biaxial forces and cross-thickness bending', *Int. J. Press. Vessels Pip.*, vol. 132–133, pp. 10–26, Aug. 2015, doi: 10.1016/j.ijpvp.2015.05.005.
- [77] M. Madia, D. Arafah, and U. Zerbst, 'Reference load solutions for plates with semi-elliptical surface cracks subjected to biaxial tensile loading', *Int. J. Press. Vessels Pip.*, vol. 119, pp. 19–28, Jul. 2014, doi: 10.1016/j.ijpvp.2014.02.004.
- [78] Y. Lei, Y. Li, and Z. Gao, 'Global limit load solutions for thick-walled cylinders with circumferential cracks under combined internal pressure, axial force and bending moment – Part I: Theoretical solutions', *Int. J. Press. Vessels Pip.*, vol. 114–115, pp. 23–40, Feb. 2014, doi: 10.1016/j.ijpvp.2013.12.002.
- [79] Y. Li, Y. Lei, and Z. Gao, 'Global limit load solutions for thick-walled cylinders with circumferential cracks under combined internal pressure, axial force and bending moment – Part II: Finite element validation', *Int. J. Press. Vessels Pip.*, vol. 114–115, pp. 41–60, Feb. 2014, doi: 10.1016/j.ijpvp.2013.12.001.
- [80] I. Hadley and P. Moore, 'Fracture case studies for validation of fitness-for-service procedures', TWI Ltd., Research Report 850/2006, May 2006.
- [81] Y. Tkach and I. Hadley, 'Reference Stress Solutions for Axial Flaws in Cylinders', TWI Ltd., 13787/1/03, Dec. 2013.
- [82] N. V. Challenger, R. Phaal, and S. J. Garwood, 'Appraisal of PD 6493:1991 Fracture assessment procedures Part I: TWI data', TWI Ltd., 512/1995, Jun. 1995.
- [83] N. V. Challenger, R. Phaal, and S. J. Garwood, 'Appraisal of PD 6493:1991 Fracture assessment procedures Part II: Published and additional TWI data', TWI Ltd., 512/1995, Jun. 1995.
- [84] A. J. Horn and A. H. Sherry, 'An engineering assessment methodology for non-sharp defects in steel structures – Part II: Procedure validation and constraint analysis', *Int. J. Press. Vessels Pip.*, vol. 89, pp. 151–161, Jan. 2012, doi: 10.1016/j.ijpvp.2011.10.015.
- [85] C.-Y. Oh, H.-S. Nam, Y.-J. Kim, R. A. Ainsworth, and P. J. Budden, 'FE validation of R6 elastic-plastic J estimation for circumferentially cracked pipes under mechanical and thermal loadings', *Eng. Fract. Mech.*, vol. 124–125, pp. 64–79, Jul. 2014, doi: 10.1016/j.engfracmech.2014.03.015.
- [86] R. D. Patel, 'Validation of R6 using finite-element analyses of cracked cylinders under thermal loading', *Nucl. Energy*, vol. 42, no. 05, pp. 257–262, 2003.
- [87] Ş. E. Eren, T. London, Y. Yang, and I. Hadley, 'Validation of Plastic Collapse Assessments Using BS 7910:2013 and R6 Procedures', presented at the ASME 2013 Pressure Vessels and Piping Conference, Jan. 2014. doi: 10.1115/PVP2013-97513.
- [88] I. Hadley, 'BS 7910:2013 in brief', *Int. J. Press. Vessels Pip.*, vol. 165, pp. 263–269, Aug. 2018, doi: 10.1016/j.ijpvp.2018.07.010.
- [89] R. A. Ainsworth, P. J. Budden, A. R. Dowling, and J. K. Sharples, 'Developments in the Flaw Assessment Procedures of R6 Revision 4 and BS7910', Aug. 2008, pp. 19–25. doi: 10.1115/PVP2003-2023.
- [90] B. R. Macejko, S. R. Kummari, and P. E. Prueter, 'Proposed Modifications to API 579 Part 3 Brittle Fracture Screening Procedures', in *Volume I: Codes and Standards*, San Antonio, Texas, USA, Jul. 2019, p. V001T01A098. doi: 10.1115/PVP2019-93207.

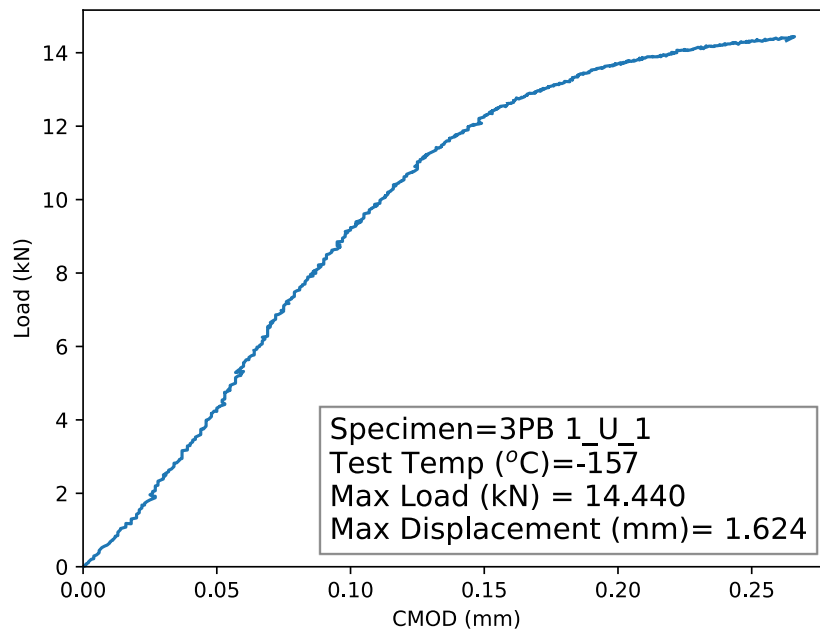
- [91] D. A. Osage and J. L. Janelle, 'API 579-1/ASME FFS-1 2007: A Joint API/ASME Fitness-for-Service Standard for Pressurized Equipment', in *Volume 1: Codes and Standards*, Chicago, Illinois, USA, Jan. 2008, pp. 777–791. doi: 10.1115/PVP2008-61796.
- [92] D. A. Osage, B. Macejko, and R. G. Brown, 'Proposed Modifications to API 579-1/ASME FFS-1 2007 Fitness-for-Service', in *Volume 1: Codes and Standards*, Anaheim, California, USA, Jul. 2014, p. V001T01A002. doi: 10.1115/PVP2014-28451.
- [93] C. Aird, 'The R6 fracture procedure: an overview and summary of recent developments', presented at the 15TH INTERNATIONAL CONFERENCE ON ENGINEERING STRUCTURAL INTEGRITY ASSESSMENT (ESIA15) + 2019 INTERNATIONAL SYMPOSIUM ON STRUCTURAL INTEGRITY (ISSI 2019), Cambridge, Under Publication.
- [94] I. Hadley, 'Validation of BS 7910:2013 and R6 Fracture Assessment Procedures: Uniaxial and Biaxial Wide Plate Tests on A533B Steel', TWI Ltd., Members Report 1107/2018, Nov. 2018.
- [95] J. Janelle, D. A. Osage, and S. J. Burkhart, 'An Overview and Validation of the Fitness-For-Service Assessment Procedures for Local Thin Areas', WRC (Welding Research Council inc.), Bulletin 505, 2005. Accessed: Mar. 31, 2020. [Online]. Available: <https://www.forengineers.org/wrc-505.html>
- [96] K. Kouzoumis, I. Hadley, and M. Mostafavi, 'Validation of BS 7910; assessing the integrity of pipes containing axial flaws', *Procedia Struct. Integr.*, vol. 13, pp. 868–876, Jan. 2018, doi: 10.1016/j.prostr.2018.12.165.
- [97] I. Hadley, K. Kouzoumis, and Y. J. Janin, 'Validation of BS 7910:2013 and R6 Fracture Assessment Procedures: Summary Report, Including Treatment of Plastic Collapse, Weld Strength Mismatch and Probabilistic Data', TWI Ltd., Cambridge, TWI industrial member report 1125/2020, 2020.
- [98] I. Sattari-Far and F. Nilsson, 'Validation of a procedure for safety assessment of cracks', The Swedish Plant Inspectorate, Stockholm, SA/FoU-RAPPORT 90/04, Jun. 1990.
- [99] I. Hadley and Y. Lei, 'Outline of the fracture clauses of BS 7910:2013', *Int. J. Press. Vessels Pip.*, vol. 168, pp. 289–300, Dec. 2018, doi: 10.1016/j.ijpvp.2018.11.004.
- [100] E. Lucon, K. Wallin, P. Langenberg, and H. Pisarski, 'The Use of Charpy/Fracture Toughness Correlations in the FITNET Procedure', in *24th International Conference on Offshore Mechanics and Arctic Engineering: Volume 3*, Halkidiki, Greece, Jan. 2005, pp. 365–368. doi: 10.1115/OMAE2005-67569.
- [101] J. Sharples and I. Hadley, 'Treatment of residual stress in fracture assessment: background to the advice given in BS 7910:2013', *Int. J. Press. Vessels Pip.*, vol. 168, pp. 323–334, Dec. 2018, doi: 10.1016/j.ijpvp.2018.11.005.
- [102] A. A. Willoughby and S. J. Garwood, 'Ductile fracture in thin section pipeline material.', TWI Ltd., Contract Report 3591/2/81, Oct. 1981.
- [103] M. Brumovsky *et al.*, 'Analysis of the applicability of fracture mechanics on the basis of large scale specimen testing', Skoda, ZJE--281, 1988. Accessed: Feb. 09, 2018. [Online]. Available: http://inis.iaea.org/Search/search.aspx?orig_q=RN:20063256
- [104] J. Faleskog, K. Zaremba, F. Nilsson, and H. Öberg, 'An Investigation of Two-and Three Dimensional Elasto-Plastic Crack Growth Experiments', in *Defect Assessment in Components- Fundamentals and Applications*, London, 1991, pp. 333–343.
- [105] D. Munz and S. Müller, 'Failure of components with surface cracks of the containment steel 15MnNi63', *Int. J. Press. Vessels Pip.*, vol. 30, no. 2, pp. 109–130, Jan. 1987, doi: 10.1016/0308-0161(87)90103-7.

- [106] Y. Takahashi, N. Miura, and K. Kashima, 'Elastic-Plastic fracture analysis of surface cracks in pipe and plate by three-dimensional Finite Element Method', *ASME PVP*, vol. 167, pp. 63–69, 1989.
- [107] A. C. Bannister and Trail, 'SUB-TASK 2.3: YIELD STRESS/TENSILE STRESS RATIO: RESULTS OF EXPERIMENTAL PROGRAMME', British Steel, RUG, UC, SINTAP/BS/25, Feb. 1999.
- [108] W. Brocks, G. Künecke, and K. Wobst, 'Stable crack growth of axial surface flaws in pressure vessels', *Int. J. Press. Vessels Pip.*, vol. 40, no. 1, pp. 77–90, Jan. 1989, doi: 10.1016/0308-0161(89)90125-7.
- [109] H. P. Keller, G. Junker, and W. Merker, 'Fracture analysis of surface cracks in cylindrical pressure vessels applying the two parameter fracture criterion (TPFC)', *Int. J. Press. Vessels Pip.*, vol. 29, no. 2, pp. 113–153, Jan. 1987, doi: 10.1016/0308-0161(87)90121-9.
- [110] I. Milne and N. Knee, 'An EGF Exercise in predicting ductile instability : Phase 2, Cracked pressure vessel', Central Electricity Generating Board, CEGB-TPRD/L/2771/N84, Jun. 1986.
- [111] C. A. Sciammarella, 'Elastic-Plastic failure analysis of pressure vessel tests', *Fract. Mech. Fourteenth Symp.*, pp. 597–616, Jan. 1985.
- [112] W. Sloterdijk, 'The influence of the yield-to-tensile ratio on deformation controlled pipeline behaviour', presented at the PRC/EPRG 10th Biennial Joint Technical Meeting on Line Pipe research, Cambridge, Nov. 1995.
- [113] G. Demofonti, G. Mannucci, D. Harris, L. Barsanti, and H.-G. Hillenbrand, 'Fracture behaviour of X100 gas pipelines by full-scale tests', Yokohama, Japan, Nov. 2002, pp. 245–261.
- [114] D. Sturm and W. Stoppler, 'Phenomenological Pipe and Vessel Burst Tests', MPA, Stuttgart, Project 1500 279, 1989.
- [115] J. Kiefner, W. Maxey, R. Eiber, and A. Duffy, 'Failure Stress Levels of Flaws in Pressurized Cylinders', Jan. 1973, doi: 10.1520/STP49657S.
- [116] M. Schödel, U. Zerbst, and C. D. Donne, 'Application of the European flaw assessment procedure SINTAP to thin wall structures subjected to biaxial and mixed mode loadings', *Eng. Fract. Mech.*, vol. 73, no. 5, pp. 626–642, Mar. 2006, doi: 10.1016/j.engfracmech.2005.10.002.
- [117] K. Kouzoumis, I. Hadley, and M. Mostafavi, 'Effect of Biaxiality on Engineering Critical Assessments', *Procedia Struct. Integr.*, vol. 17, pp. 347–354, Jan. 2019, doi: 10.1016/j.prostr.2019.08.046.
- [118] R. M. Andrews and S. J. Garwood, 'Testing of A533B under Equibiaxial Loading with a through-thickness Crack', TWI Ltd., Cambridge, 34121/1/94, Aug. 1994.
- [119] N. V. Challenger and R. M. Andrews, 'Biaxial Test Programme - Through-Thickness Cracked Uniaxial Wide Plate Test on A533B Material', TWI Ltd., Cambridge, 220682/1/96, Mar. 1996.
- [120] S. J. Garwood and R. M. Andrews, 'Testing of a further A533B wide plate under biaxial loading with a through-thickness crack - preliminary analysis', TWI Ltd., 220548/1/95, May 1995.
- [121] S. J. Garwood and T. G. Davey, 'Testing of A533B plates under biaxial loading', TWI Ltd., Cambridge, 23201/2/87, Jul. 1987.
- [122] I. Hadley and A. Horn, 'Treatment of constraint in BS 7910:2013, ISO 27306 and DNVGL-RP-F108', *Int. J. Press. Vessels Pip.*, vol. 169, pp. 77–93, Jan. 2019, doi: 10.1016/j.ijpvp.2018.11.015.
- [123] *ABAQUS/Standard User's Manual, Version 6.14*. Providence, RI, USA: Dassault Systèmes Simulia Corp., 2014.

- [124] C. Meek, 'The Influence of Biaxial Loading On The Assessment of Structures with Defects', University of Manchester, Manchester, 2017. Accessed: May 25, 2018. [Online]. Available: https://www.research.manchester.ac.uk/portal/files/61848058/FULL_TEXT.PDF
- [125] C. Meek and R. A. Ainsworth, 'Fracture Assessment of Centre-cracked Plates under Biaxial Loading', *Procedia Mater. Sci.*, vol. 3, pp. 1612–1617, 2014, doi: 10.1016/j.mspro.2014.06.260.
- [126] D. G. A. Van Gelderen, 'Effects of Load History on Low Temperature Fracture of Steels', PhD, University of Bristol, Bristol, 2016.
- [127] K. Rosahl, 'The combined effects of residual stress and warm prestressing on cleavage fracture in steels', University of Bristol, Bristol, 2012.
- [128] M. J. Balart and J. F. Knott, 'Effects of geometry and flow properties on the fracture toughness of a C–Mn reactor pressure vessel steel in the lower shelf region', *Int. J. Press. Vessels Pip.*, vol. 83, no. 3, pp. 205–215, Mar. 2006, doi: 10.1016/j.ijpvp.2005.12.001.
- [129] *ASTM E1921-17a, Standard Test Method for Determination of Reference Temperature, To, for Ferritic Steels in the Transition Range*. West Conshohocken, PA: ASTM International, 2017. [Online]. Available: www.astm.org
- [130] BSI, Ed., *BS EN ISO 148-1:2010 - Metallic materials. Charpy pendulum impact test. Test method*. 2010.
- [131] L. W. Cao, S. J. Wu, and P. E. J. Flewitt, 'Comparison of ductile-to-brittle transition curve fitting approaches', *Int. J. Press. Vessels Pip.*, vol. 93–94, pp. 12–16, May 2012, doi: 10.1016/j.ijpvp.2012.02.001.
- [132] E08 Committee, 'Test Method for Linear-Elastic Plane-Strain Fracture Toughness K_{Ic} of Metallic Materials', ASTM International. doi: 10.1520/E0399-17.
- [133] 'Material Properties of Polystyrene and Poly(methyl methacrylate) (PMMA) Microspheres'. Bangs Labs Inc. Accessed: Apr. 14, 2020. [Online]. Available: <https://www.bangslabs.com/sites/default/files/imce/docs/TSD%200021%20Material%20Properties%20Web.pdf>
- [134] S. Tu, X. Ren, J. He, and Z. Zhang, 'Effect of the Lüders plateau on ductile fracture with MBL model', *Eur. J. Mech. - A Solids*, vol. 78, p. 103840, Nov. 2019, doi: 10.1016/j.euromechsol.2019.103840.
- [135] Z. Chen, K. Kouzoumis, R. Kulka, I. Hadley, and M. Mostafavi, 'A novel unified constraint measurement for multi-axial bending specimen [CURRENTLY UNDER SUBMISSION]'.

Appendix – 1: Experimental results

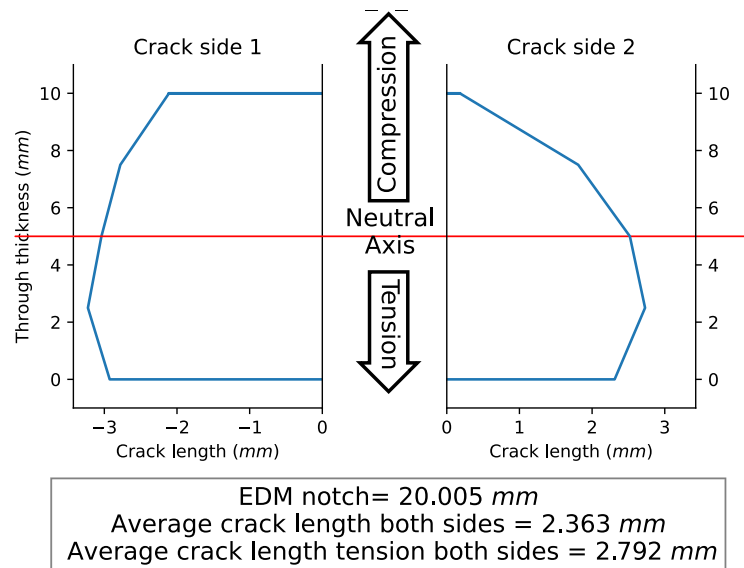
This appendix includes the detailed presentation of the results of the experimental program. For each test, the Load-CMOD curves are given along with pictures of the fracture surface post-test and a graph of the digitised post fracture crack length measurements.



(a)

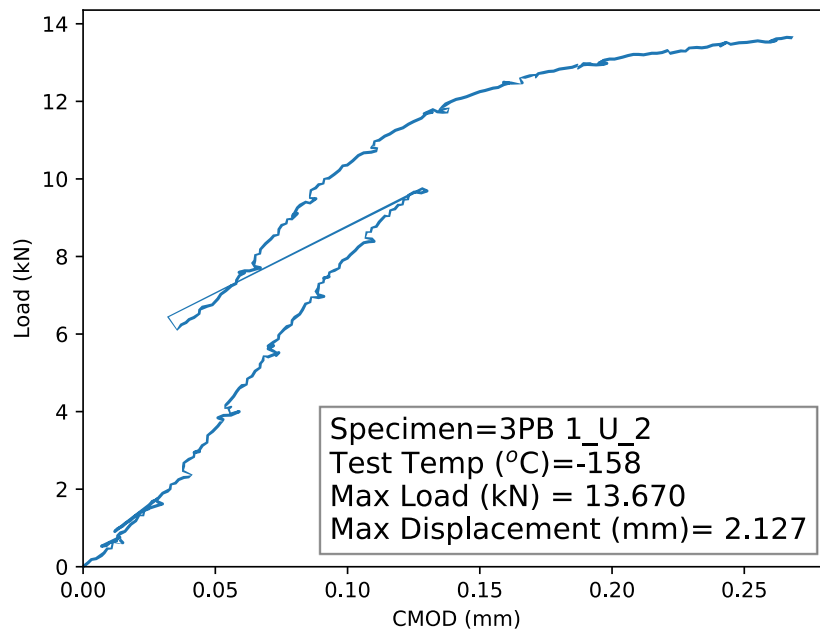


(b)



(c)

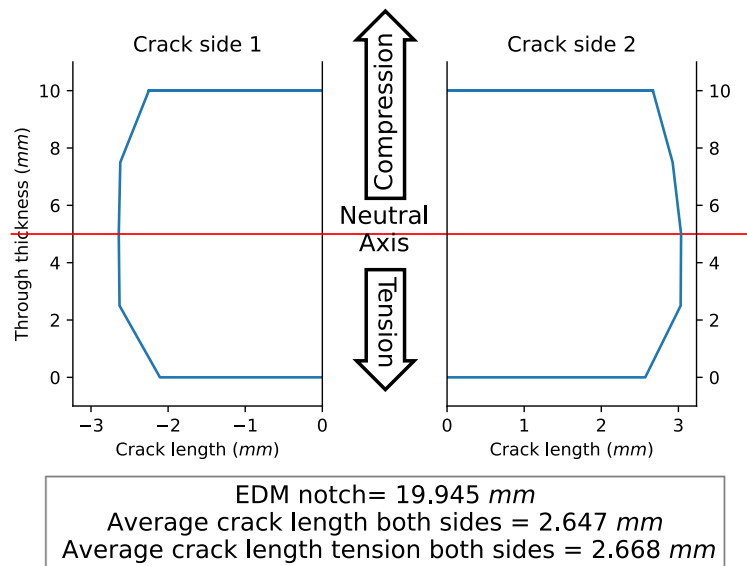
Figure A1.1: Specimen 3PB 1_U_1 (a) Load-CMOD curve, (b) fracture surface, (c) digitized fatigue crack length



(a)

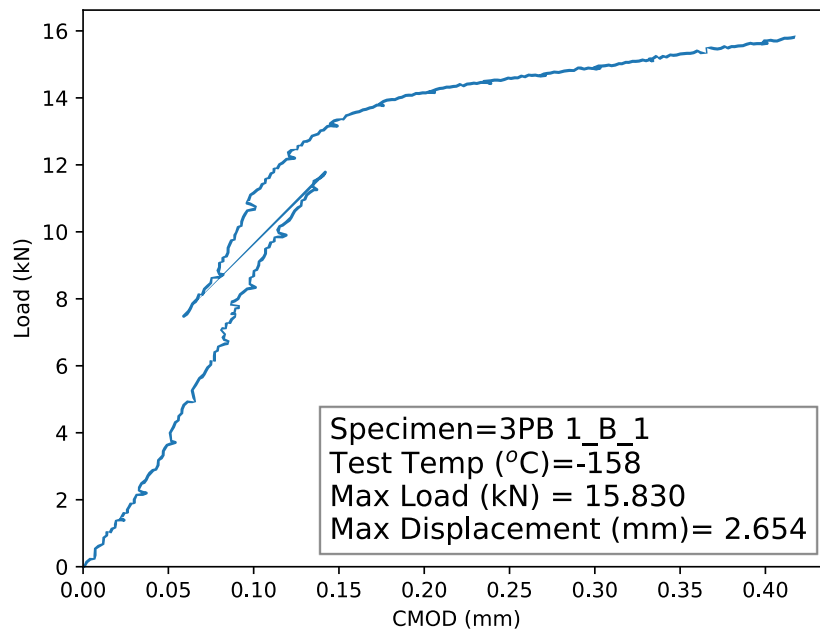


(b)

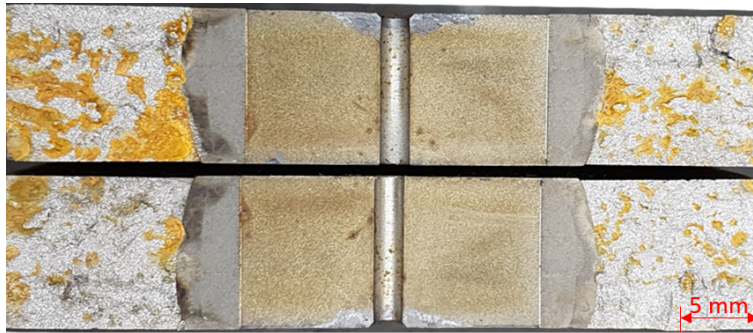


(c)

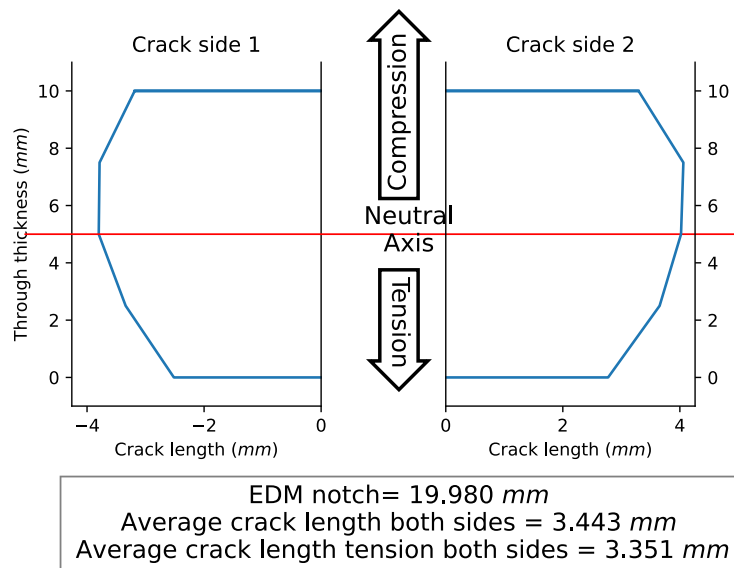
Figure A1.2: Specimen 3PB 1_U_2 (a) Load-CMOD curve, (b) fracture surface, (c) digitized fatigue crack length



(a)

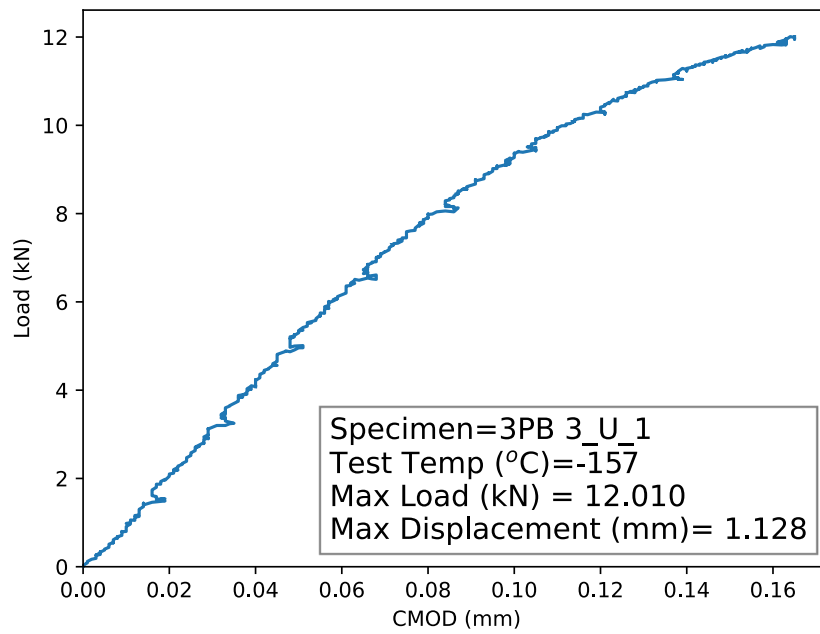


(b)

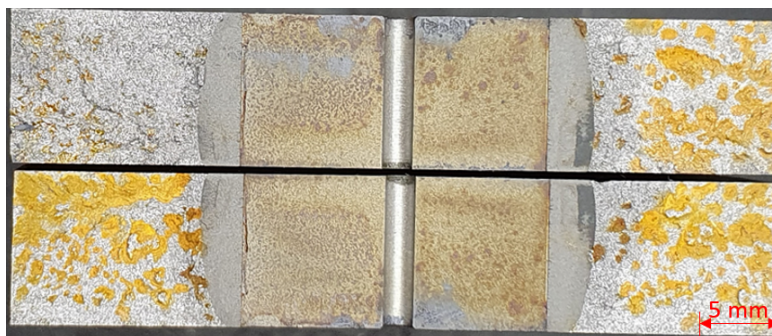


(c)

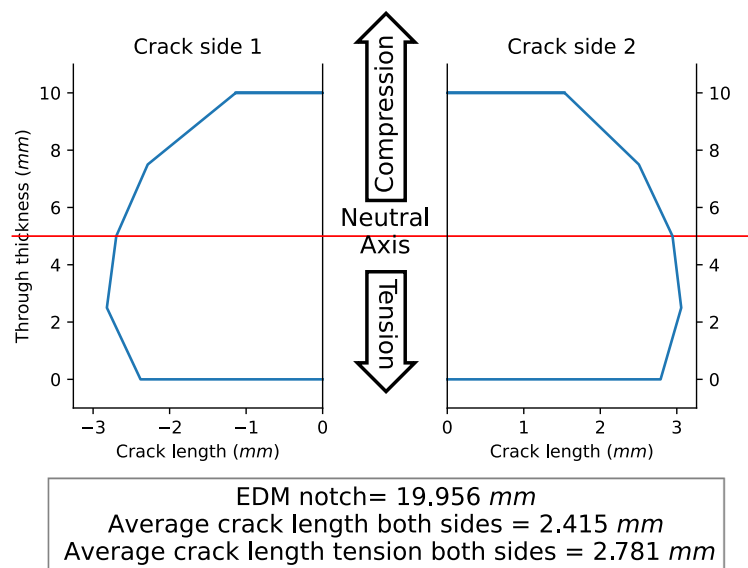
Figure A1.3: Specimen 3PB 1_B_1 (a) Load-CMOD curve, (b) fracture surface, (c) digitized fatigue crack length



(a)

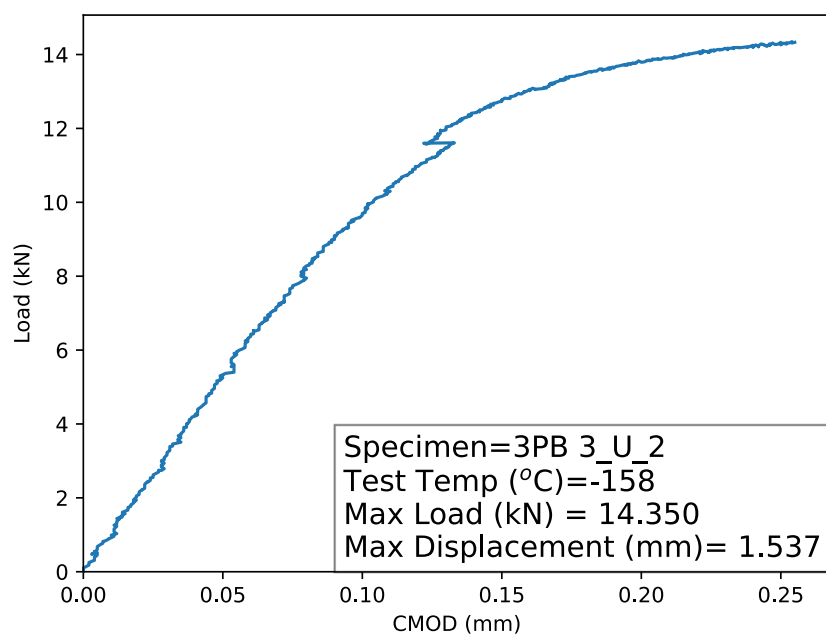


(b)

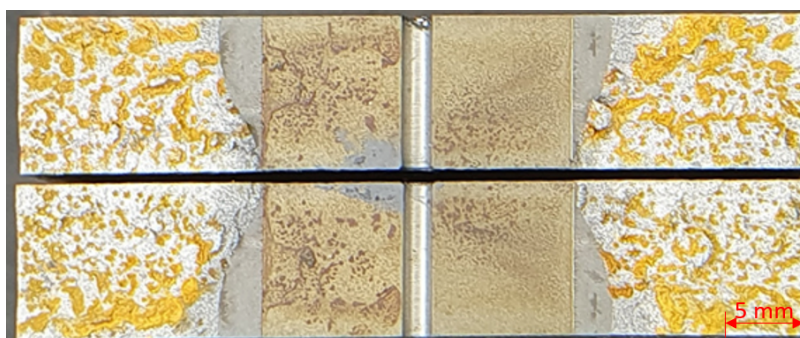


(c)

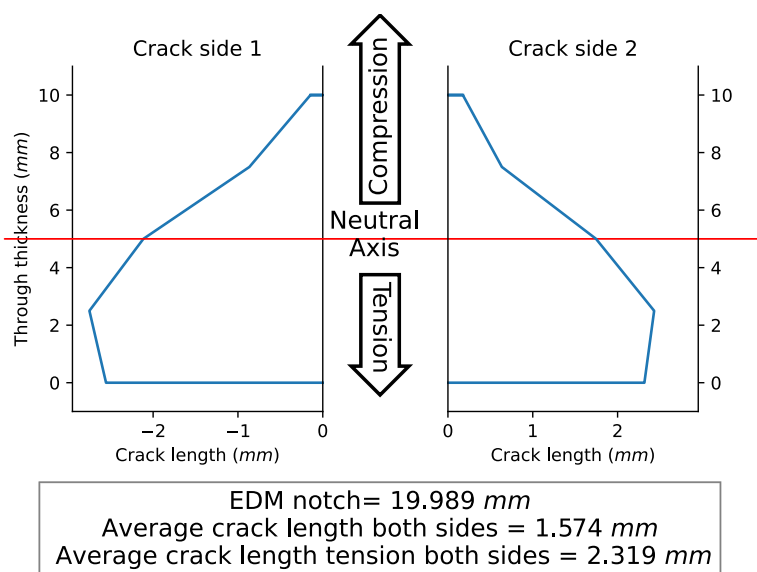
Figure A1.4: Specimen 3PB 3_U_1 (a) Load-CMOD curve, (b) fracture surface, (c) digitized fatigue crack length



(a)

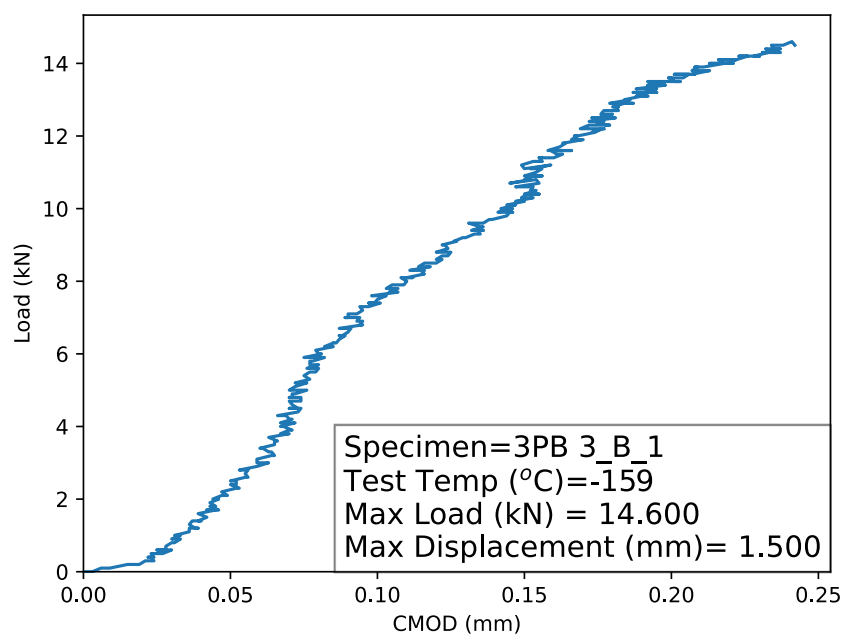


(b)

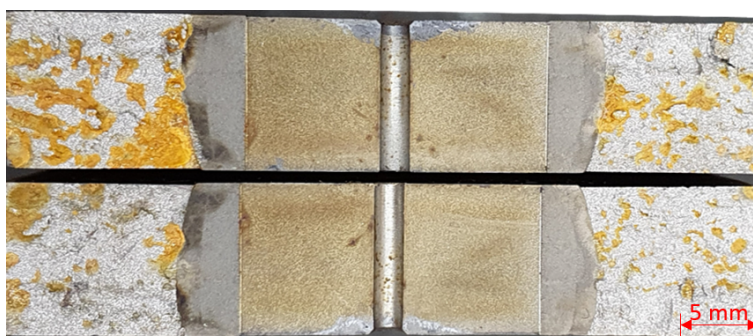


(c)

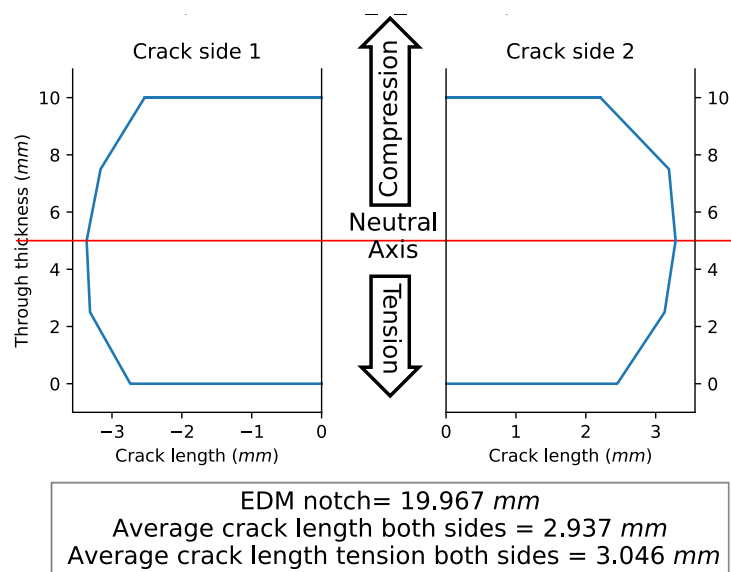
Figure A1.5: Specimen 3PB 3_U_2 (a) Load-CMOD curve, (b) fracture surface, (c) digitized fatigue crack length



(a)

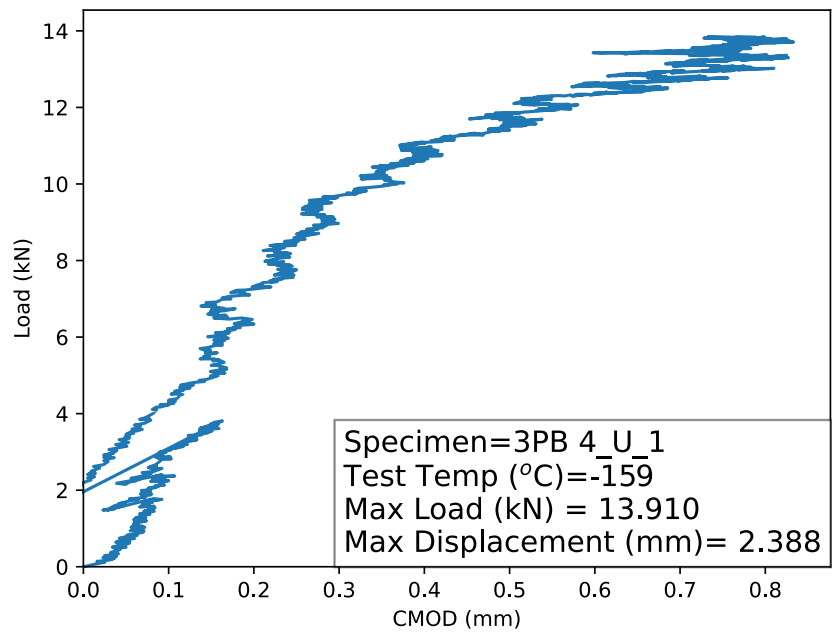


(b)

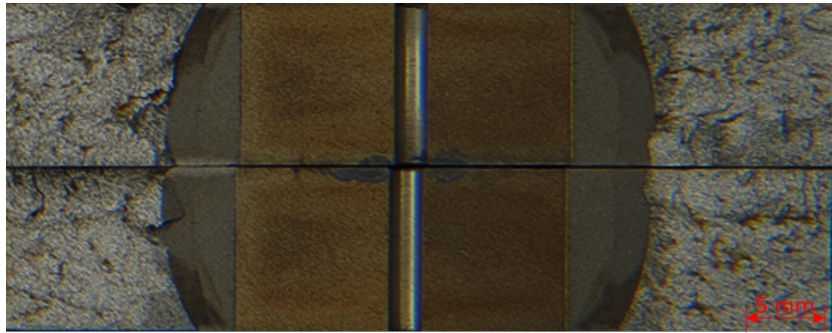


(c)

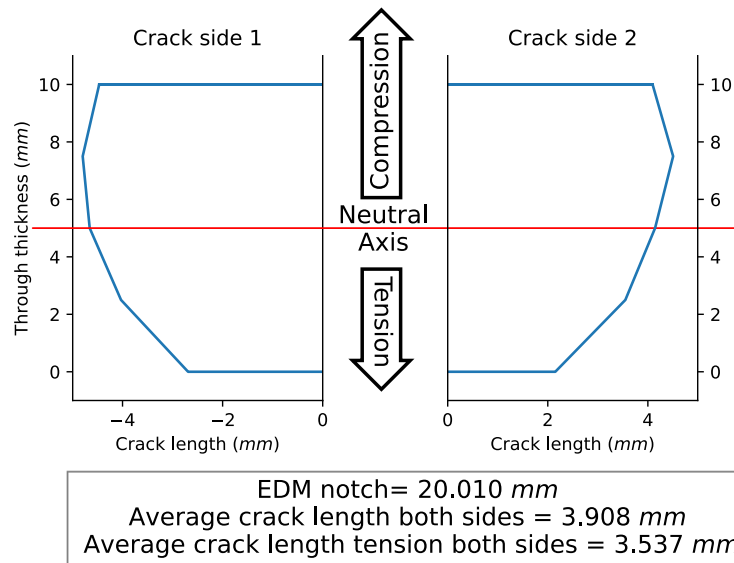
Figure A1.6: Specimen 3PB 3_B_1 (a) Load-CMOD curve, (b) fracture surface, (c) digitized fatigue crack length



(a)

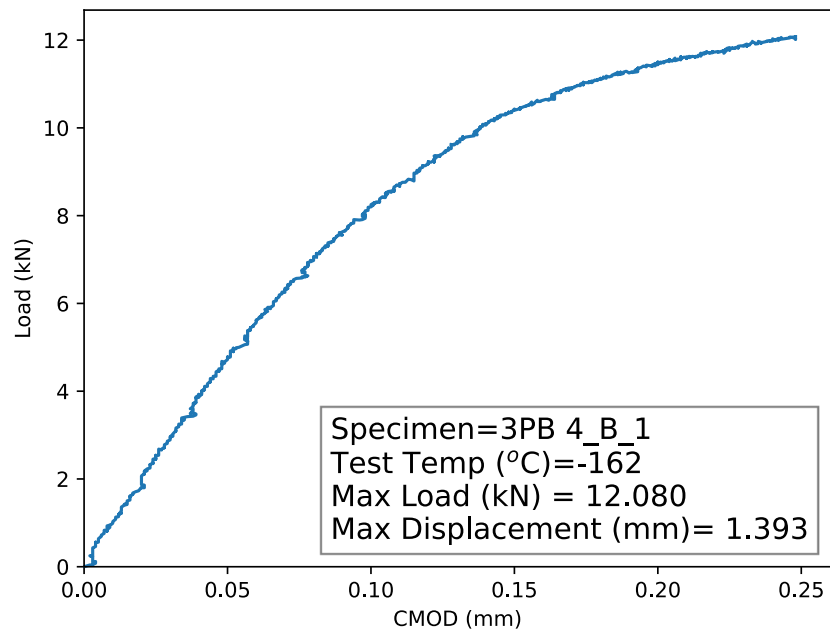


(b)

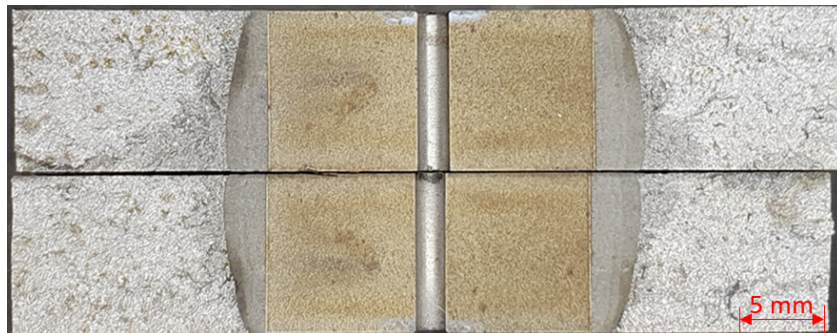


(c)

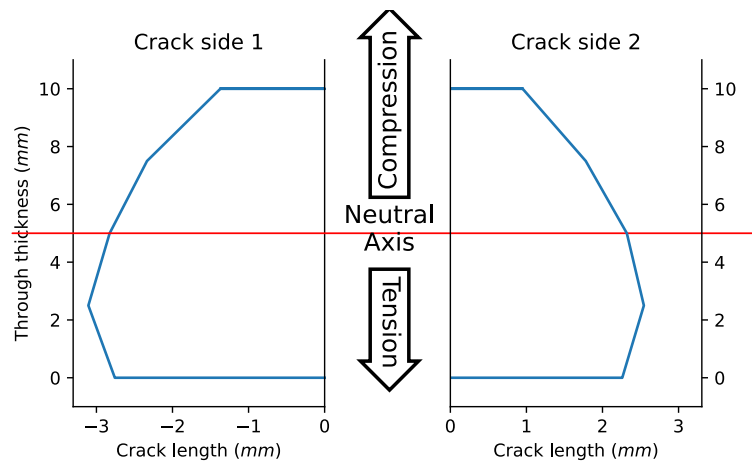
Figure A1.7: Specimen 3PB 4_U_1 (a) Load-CMOD curve, (b) fracture surface, (c) digitized fatigue crack length



(a)



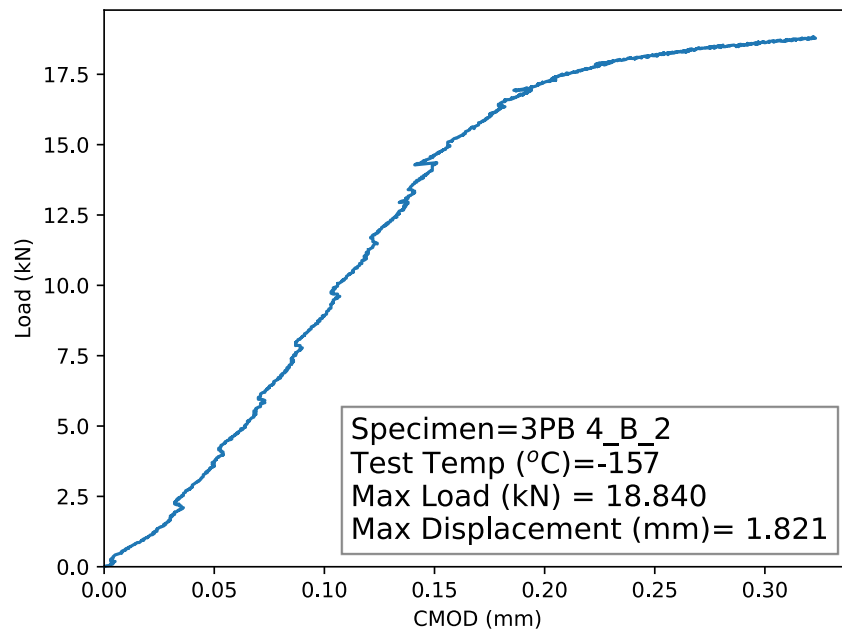
(b)



EDM notch= 19.960 mm
 Average crack length both sides = 2.225 mm
 Average crack length tension both sides = 2.636 mm

(c)

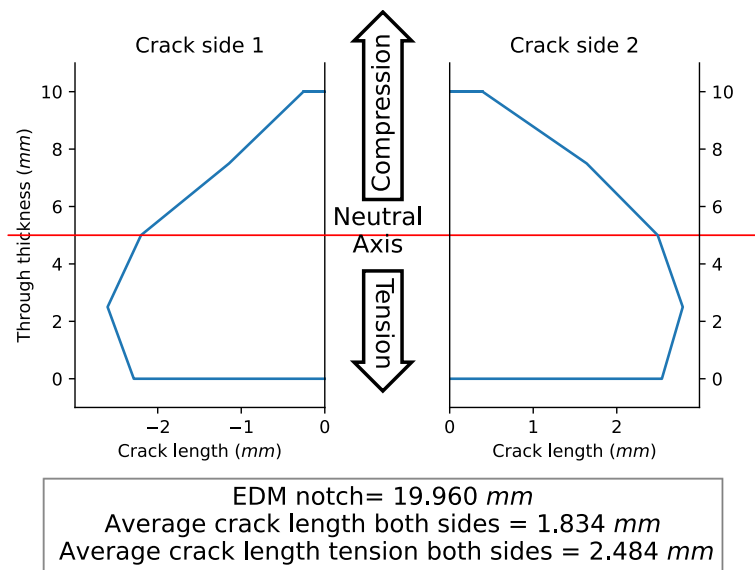
Figure A1.8: Specimen 3PB 4_B_1 (a) Load-CMOD curve, (b) fracture surface, (c) digitized fatigue crack length



(a)

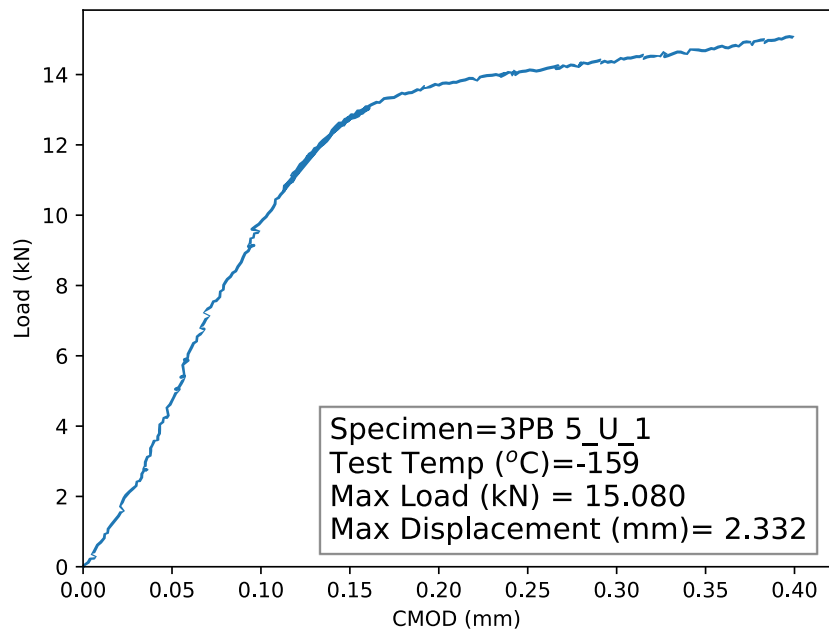


(b)

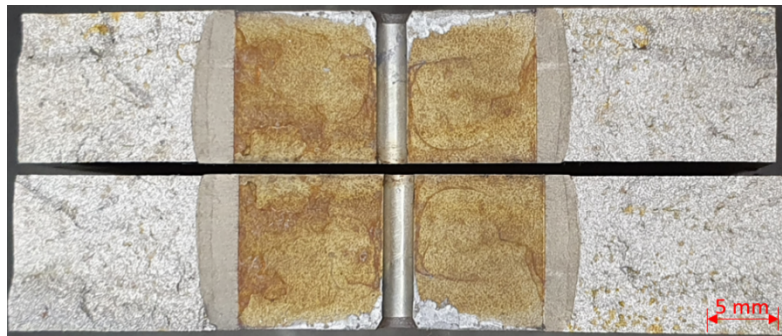


(c)

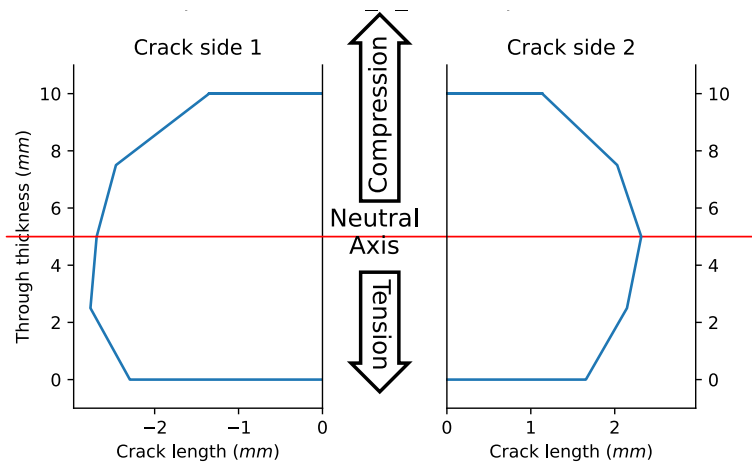
Figure A1.9: Specimen 3PB 4_B_2 (a) Load-CMOD curve, (b) fracture surface, (c) digitized fatigue crack length



(a)



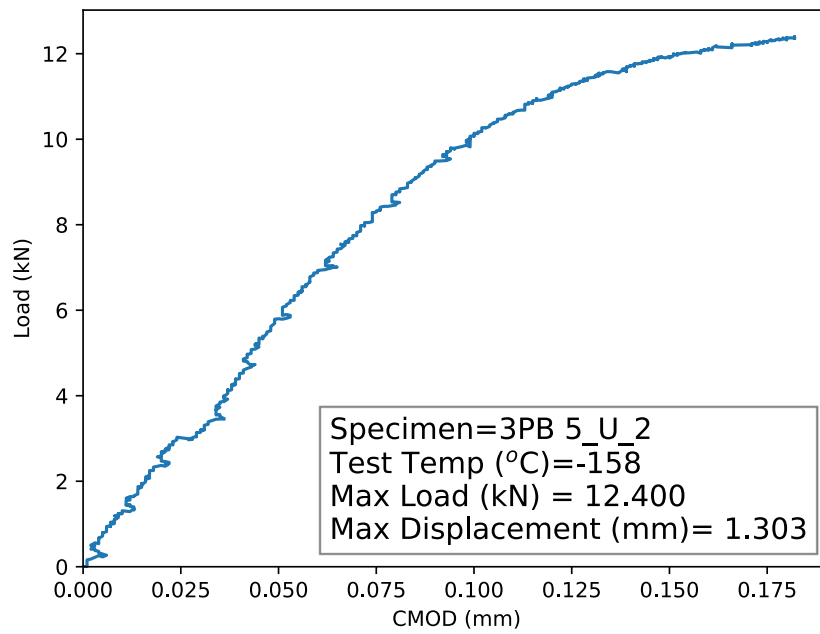
(b)



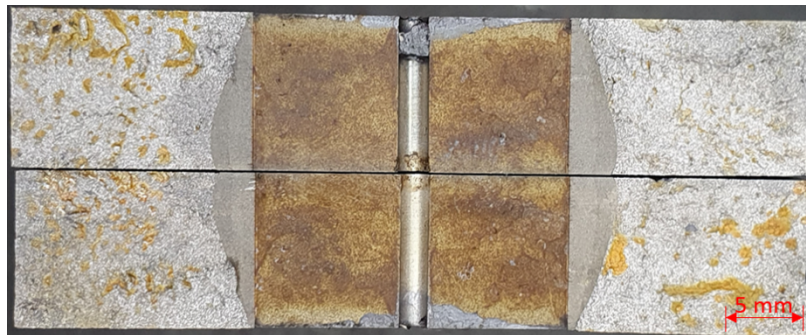
EDM notch= 20.009 mm
 Average crack length both sides = 2.085 mm
 Average crack length tension both sides = 2.312 mm

(c)

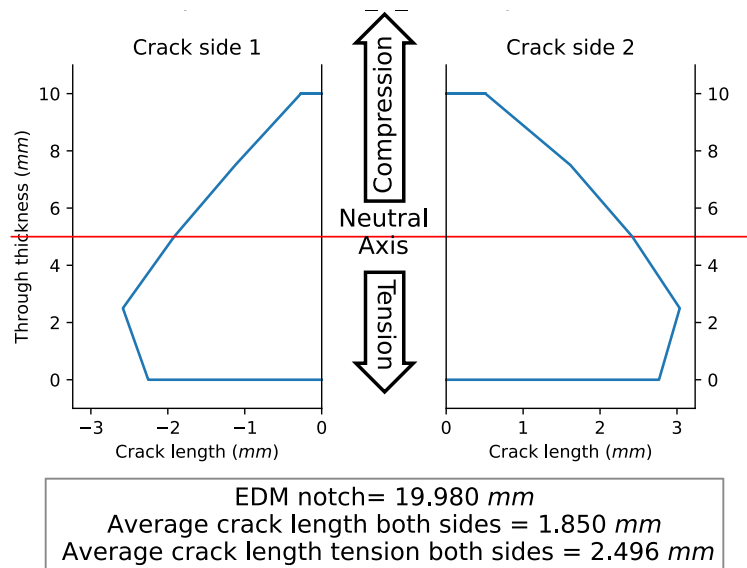
Figure A1.10: Specimen 3PB 5_U_1 (a) Load-CMOD curve, (b) fracture surface, (c) digitized fatigue crack length



(a)

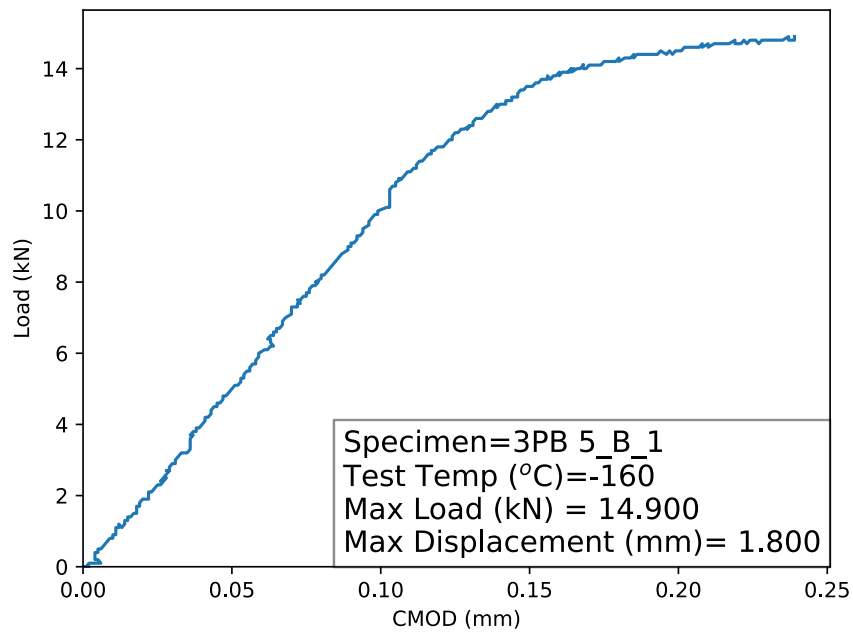


(b)

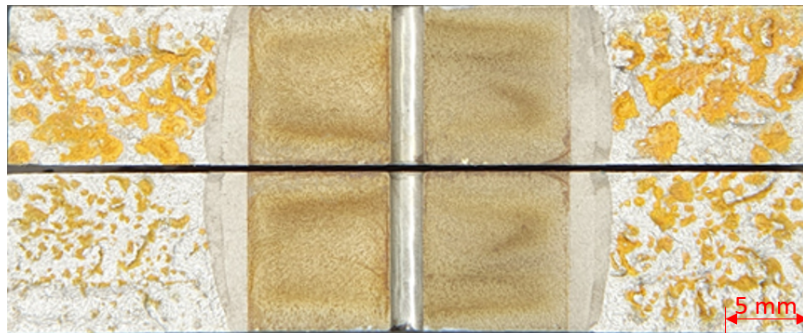


(c)

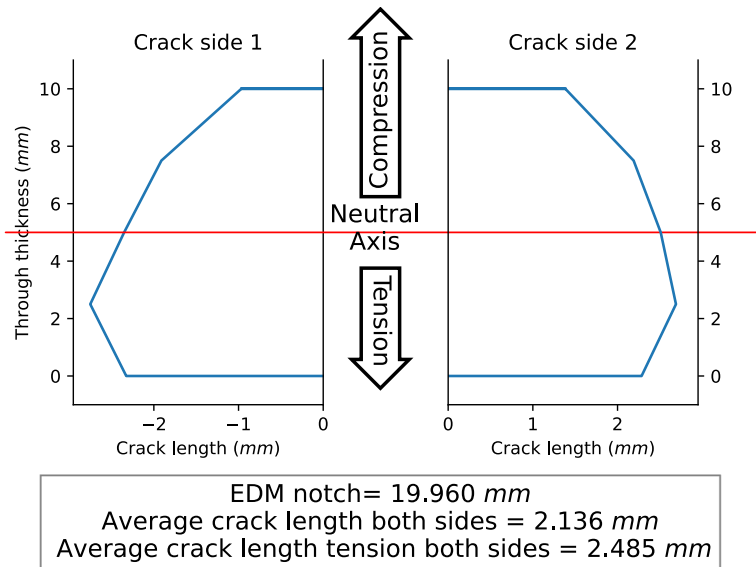
Figure A1.11: Specimen 3PB 5_U_2 (a) Load-CMOD curve, (b) fracture surface, (c) digitized fatigue crack length



(a)

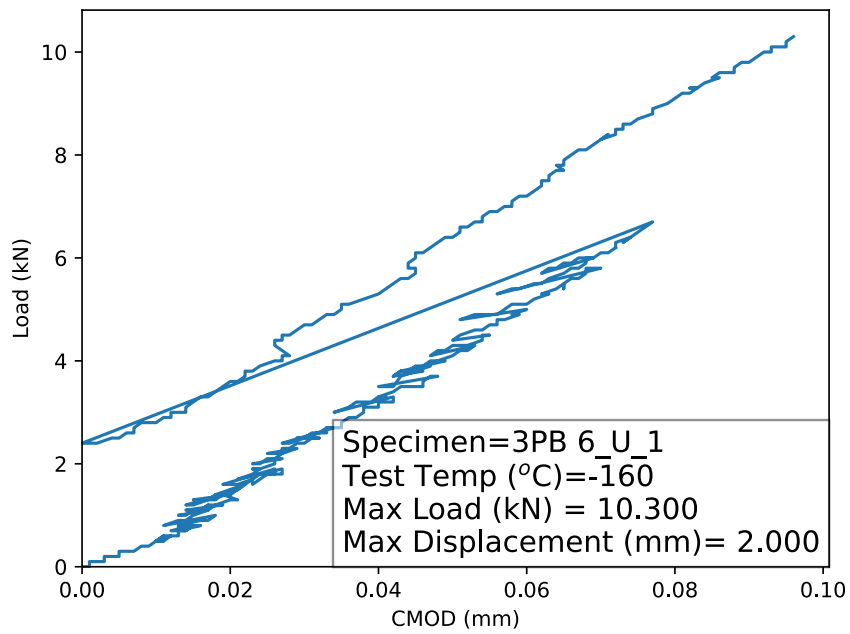


(b)

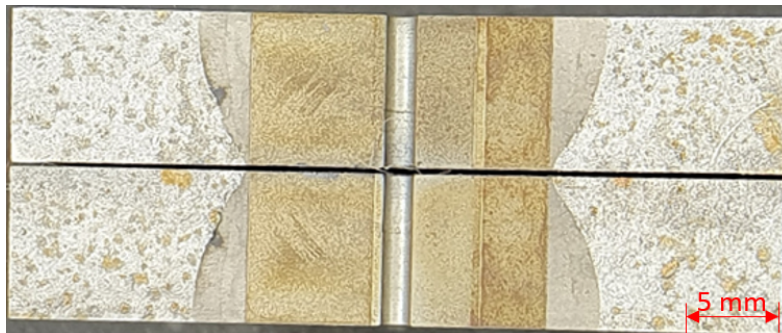


(c)

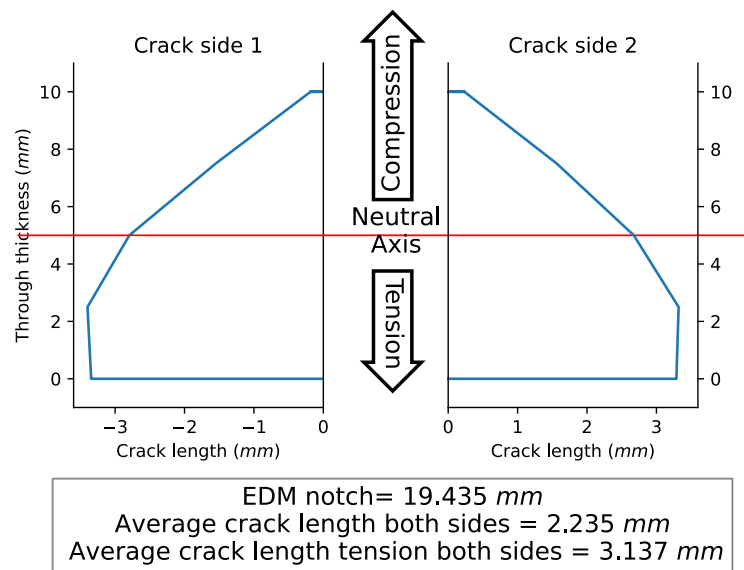
Figure A1.12: Specimen 3PB 5_B_1 (a) Load-CMOD curve, (b) fracture surface, (c) digitized fatigue crack length



(a)

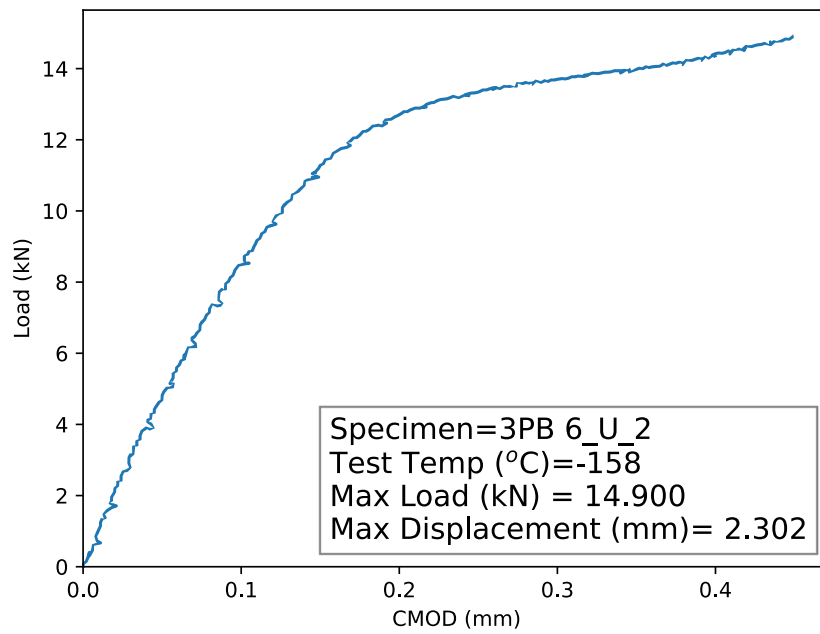


(b)

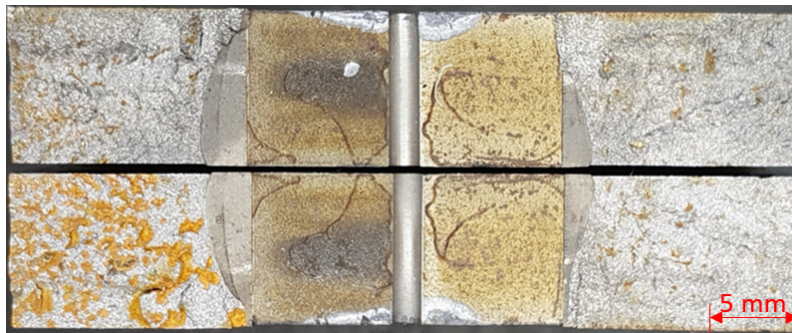


(c)

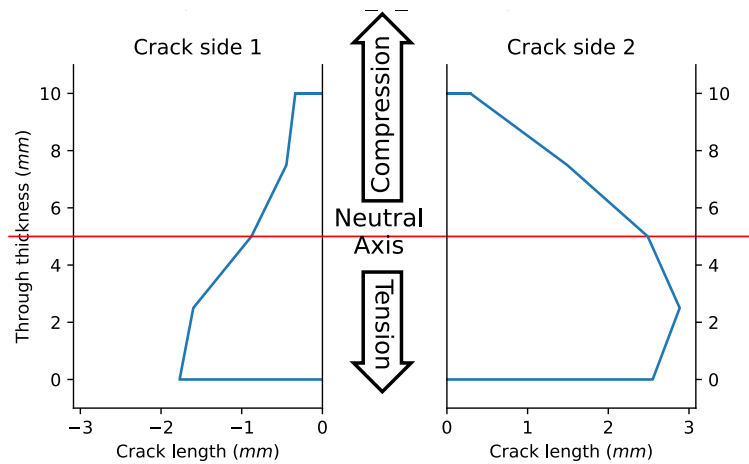
Figure A1.13: Specimen 3PB 6_U_1 (a) Load-CMOD curve, (b) fracture surface, (c) digitized fatigue crack length



(a)



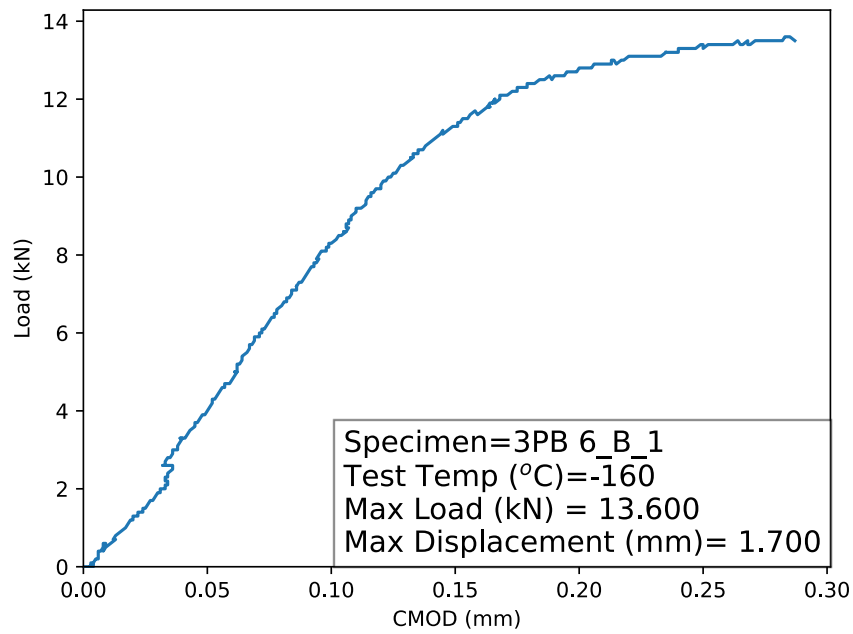
(b)



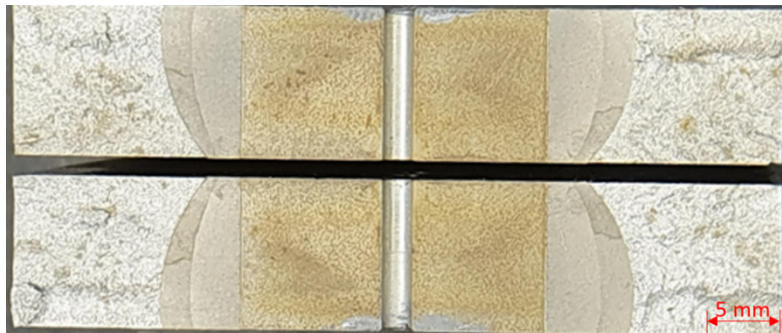
EDM notch= 19.985 mm
 Average crack length both sides = 1.474 mm
 Average crack length tension both sides = 2.029 mm

(c)

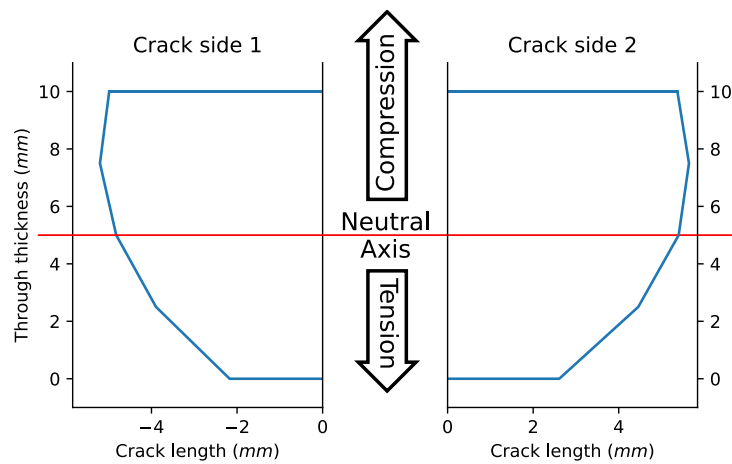
Figure A1.14: Specimen 3PB 6_U_2 (a) Load-CMOD curve, (b) fracture surface, (c) digitized fatigue crack length



(a)



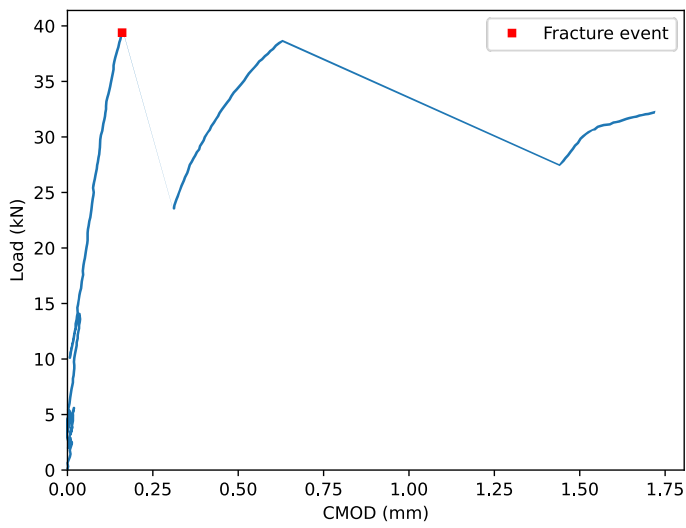
(b)



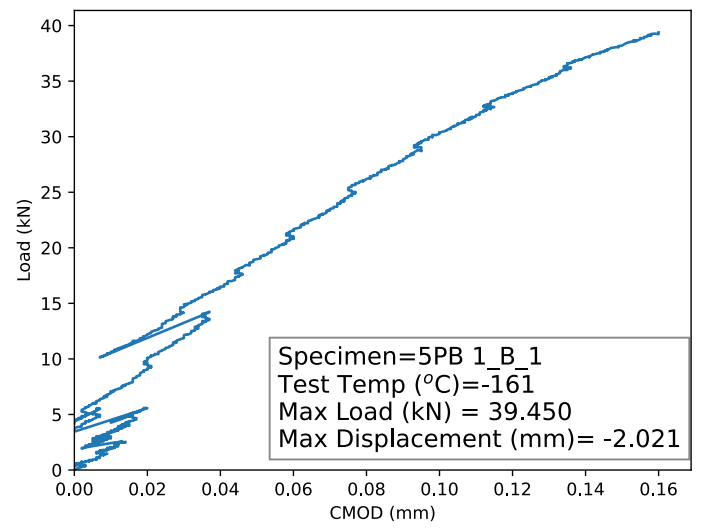
EDM notch= 20.050 mm
 Average crack length both sides = 4.456 mm
 Average crack length tension both sides = 3.893 mm

(c)

Figure A1.15: Specimen 3PB 6_B_1 (a) Load-CMOD curve, (b) fracture surface, (c) digitized fatigue crack length



(a)



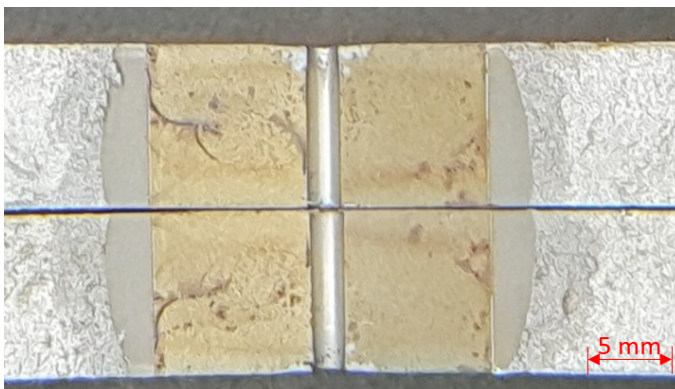
(b)



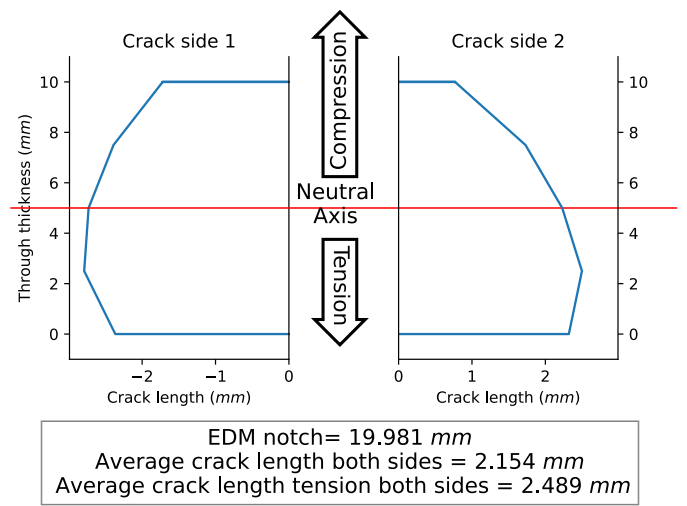
(c)



(d)

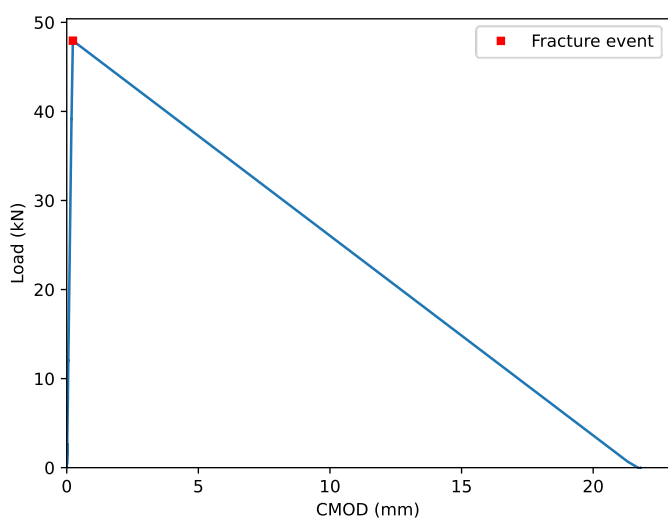


(e)

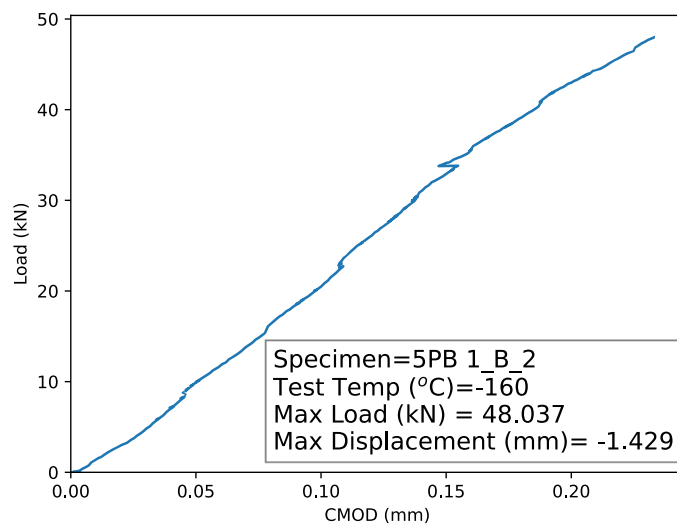


(f)

Figure A1.16: Specimen 5PB 1_B_1 (a) Full Load-CMOD curve, (b) Load-CMOD curve to fracture event, (c) post fracture top view, (d) post fracture bottom view (e) fracture surface, (f) digitized fatigue crack length



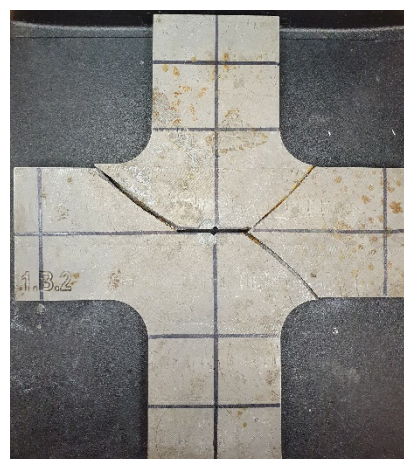
(a)



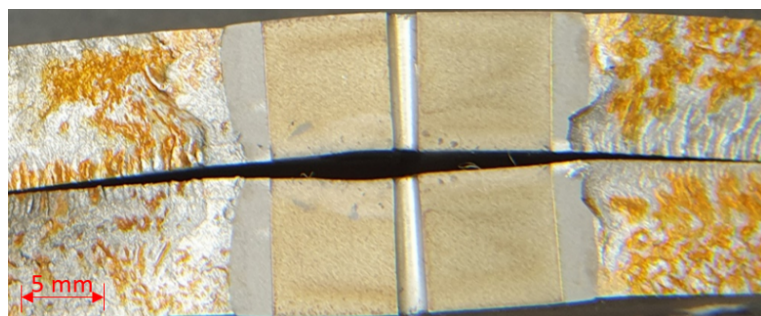
(b)



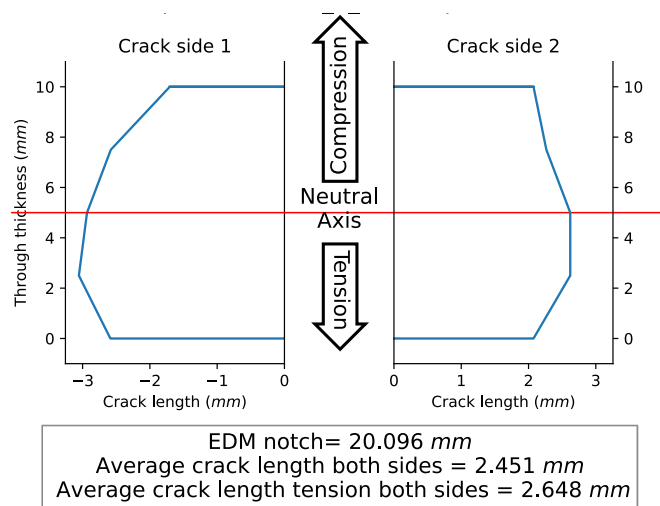
(c)



(d)

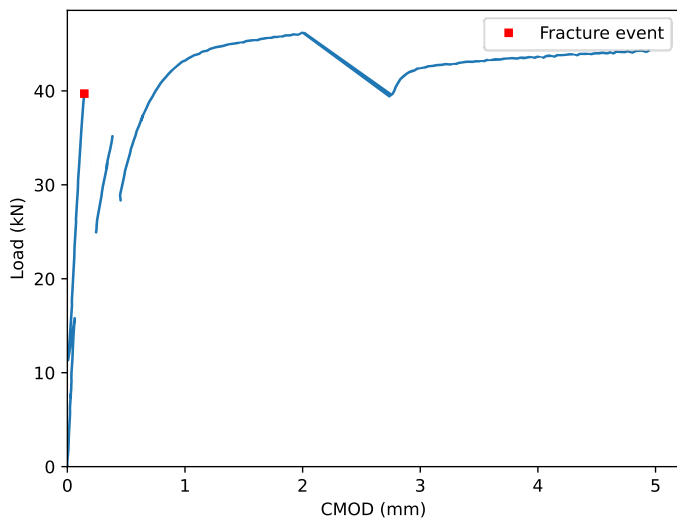


(e)

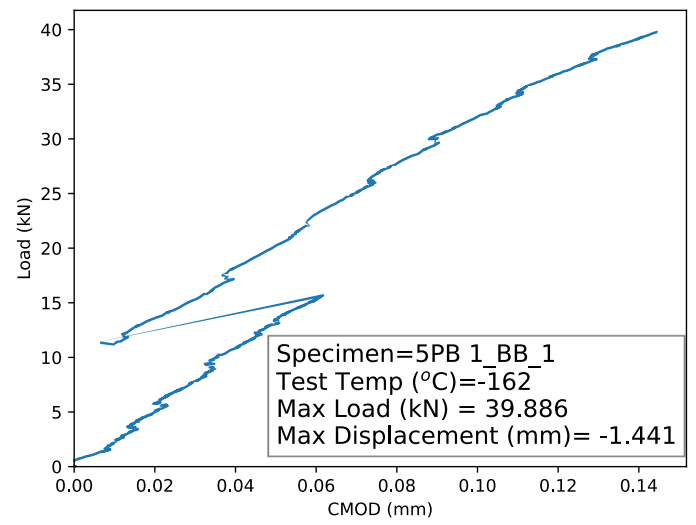


(f)

Figure A1.17: Specimen 5PB 1_B_2 (a) Full Load-CMOD curve, (b) Load-CMOD curve to fracture event, (c) post fracture top view, (d) post fracture bottom view (e) fracture surface, (f) digitized fatigue crack length



(a)



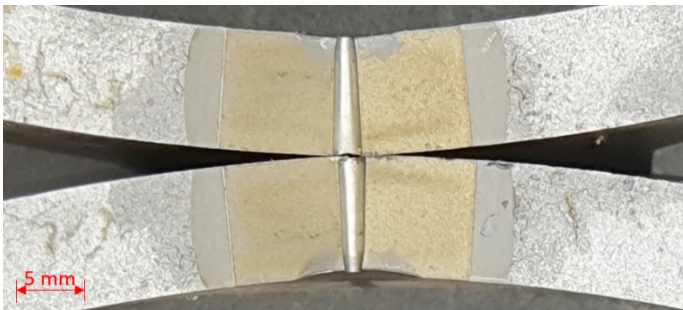
(b)



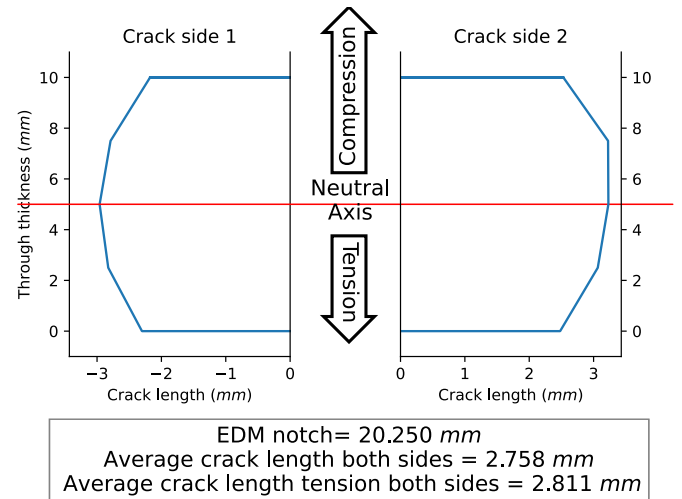
(c)



(d)

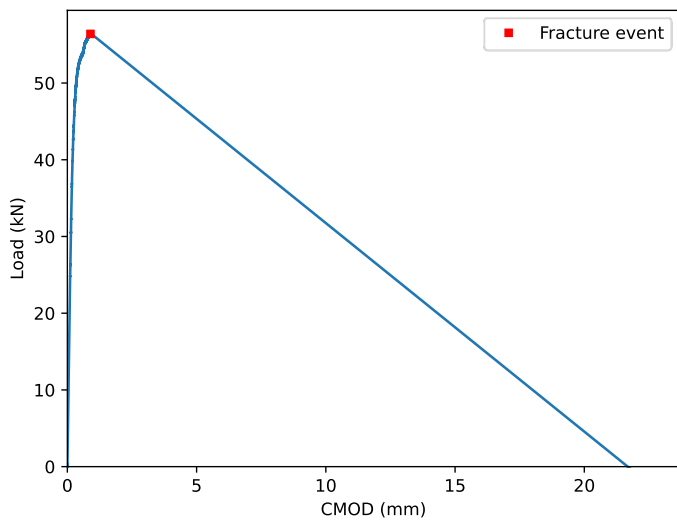


(e)

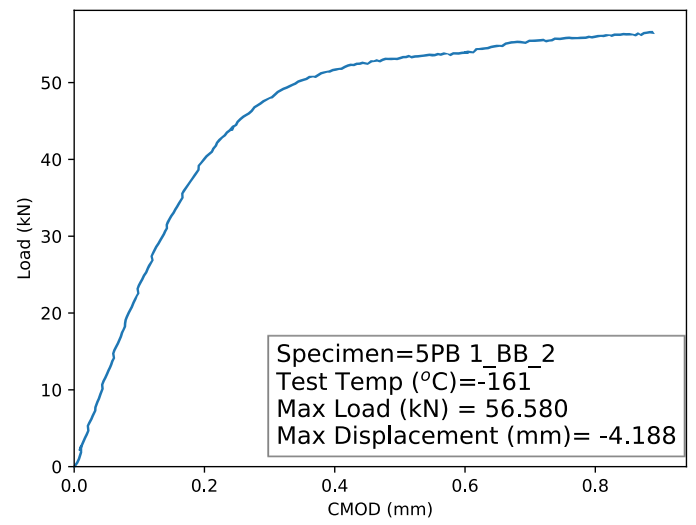


(f)

Figure A1.18: Specimen 5PB 1_BB_1 (a) Full Load-CMOD curve, (b) Load-CMOD curve to fracture event, (c) post fracture top view, (d) post fracture bottom view (e)fracture surface, (f) digitized fatigue crack length



(a)



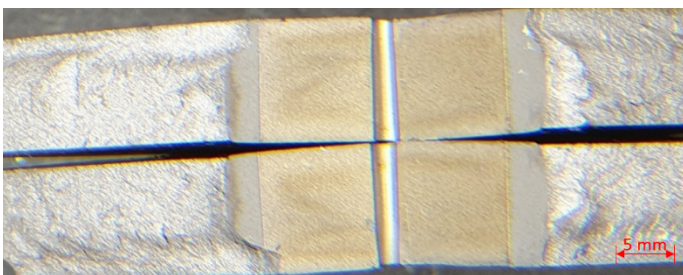
(b)



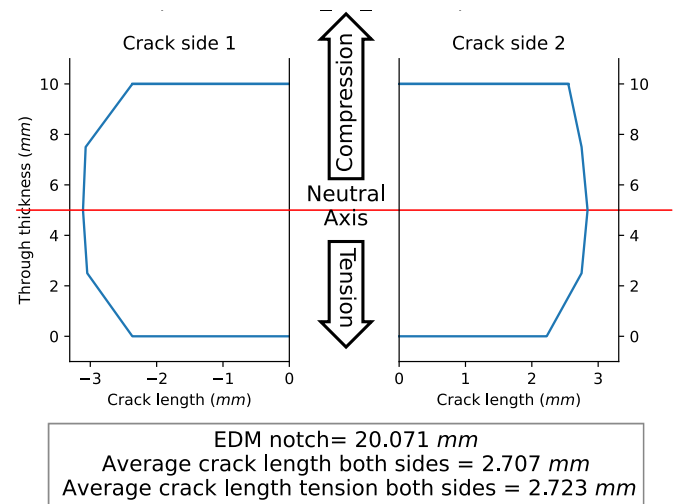
(c)



(d)

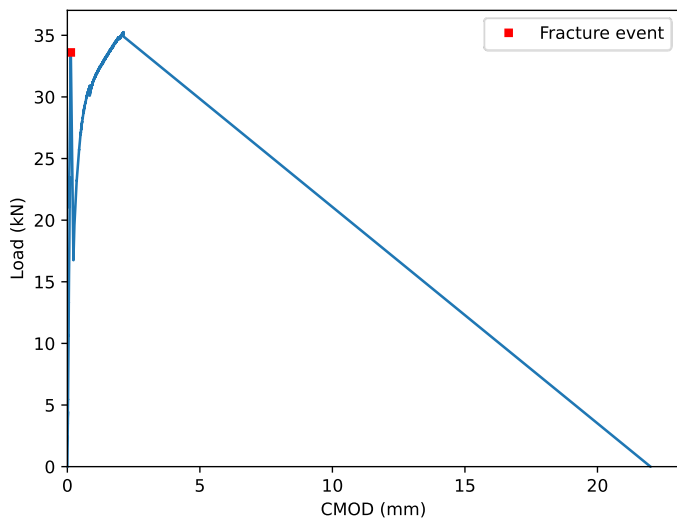


(e)

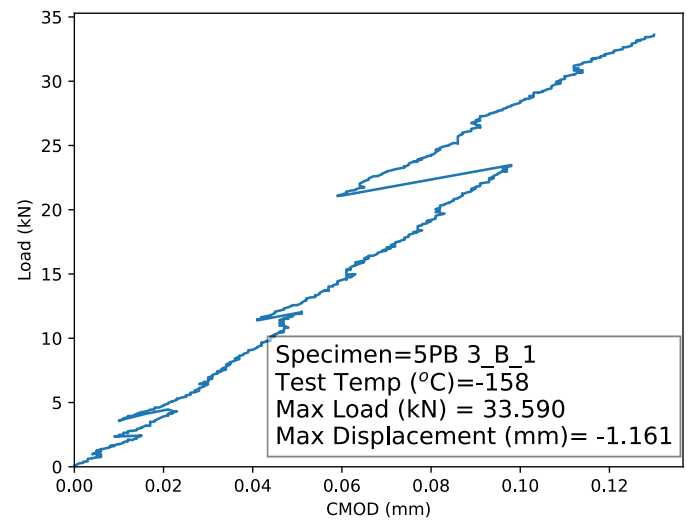


(f)

Figure A1.19: Specimen 5PB 1_BB_2 (a) Full Load-CMOD curve, (b) Load-CMOD curve to fracture event, (c) post fracture top view, (d) post fracture bottom view (e) fracture surface, (f) digitized fatigue crack length



(a)



(b)



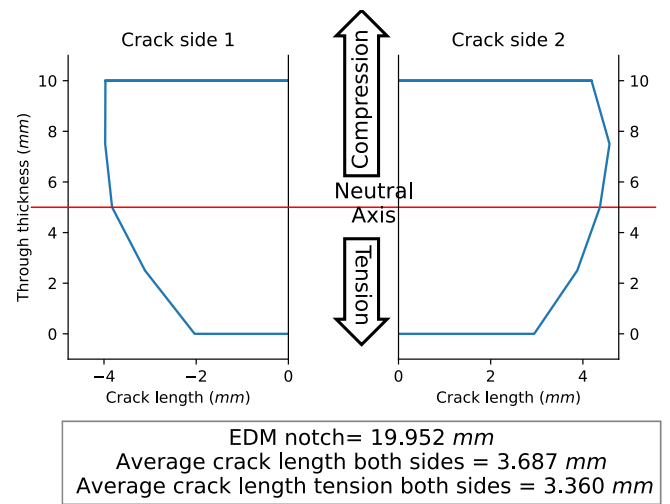
(c)



(d)

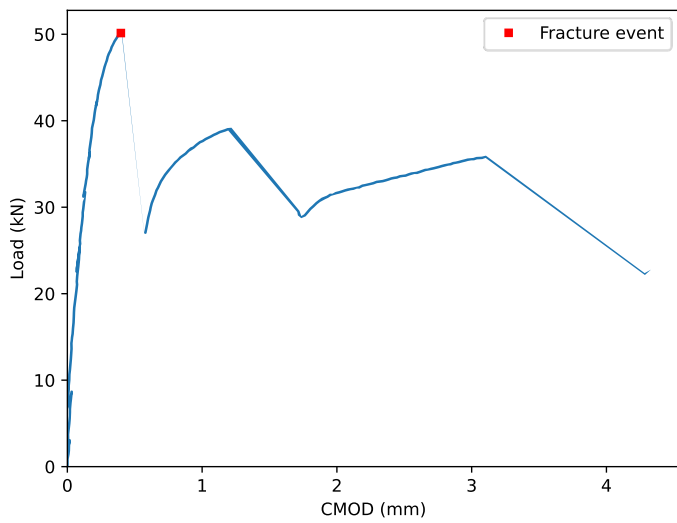


(e)

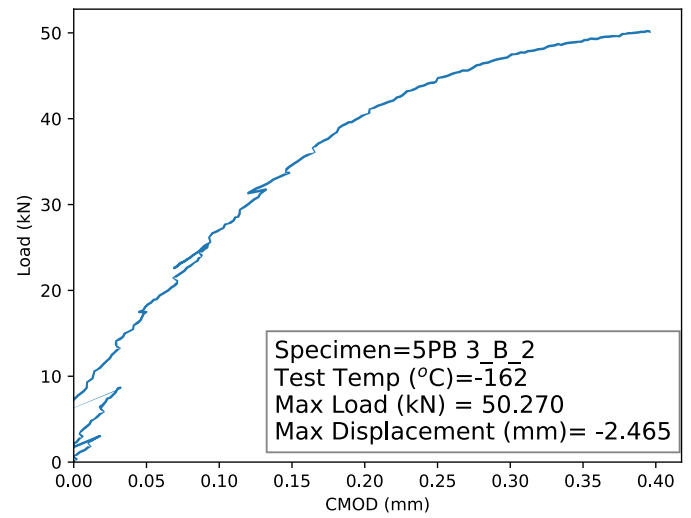


(f)

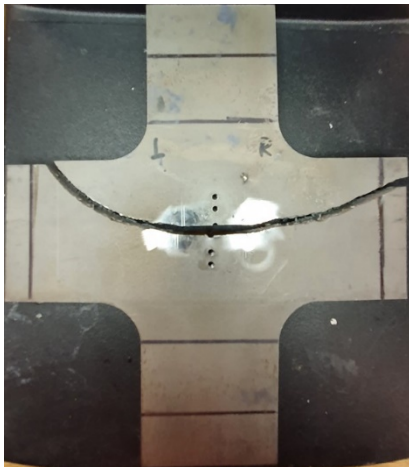
Figure A1.20: Specimen 5PB 3_B_1 (a) Full Load-CMOD curve, (b) Load-CMOD curve to fracture event, (c) post fracture top view, (d) post fracture bottom view (e) fracture surface, (f) digitized fatigue crack length



(a)



(b)



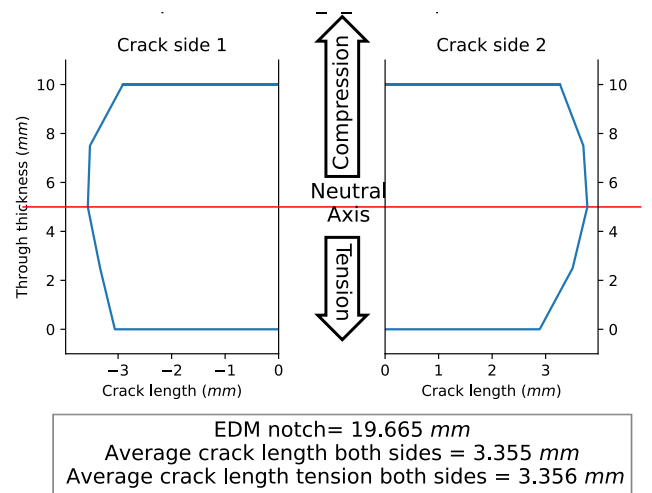
(c)



(d)

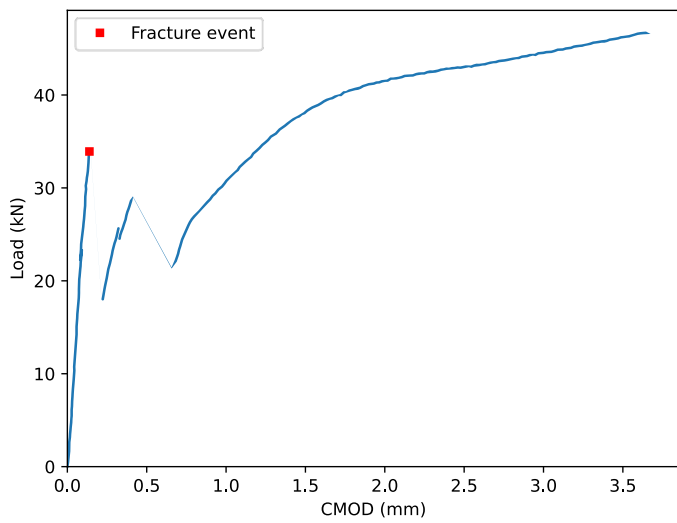


(e)

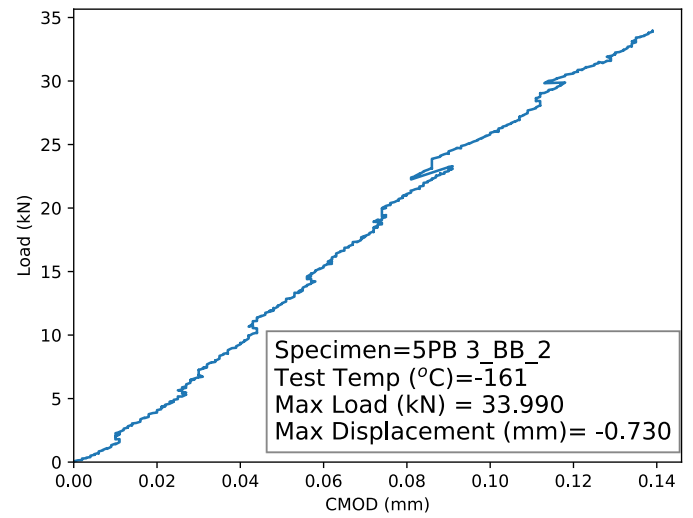


(f)

Figure A1.21: Specimen 5PB 3_B_2 (a) Full Load-CMOD curve, (b) Load-CMOD curve to fracture event, (c) post fracture top view, (d) post fracture bottom view (e) fracture surface, (f) digitized fatigue crack length



(a)



(b)



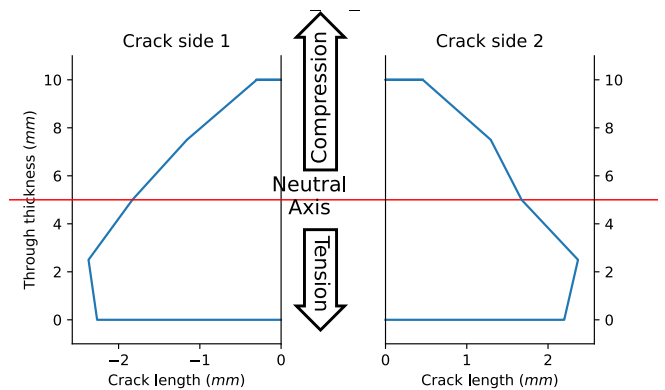
(c)



(d)



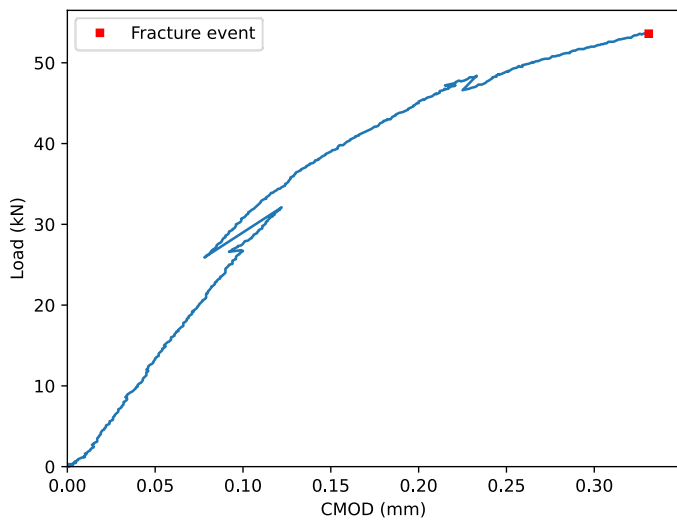
(e)



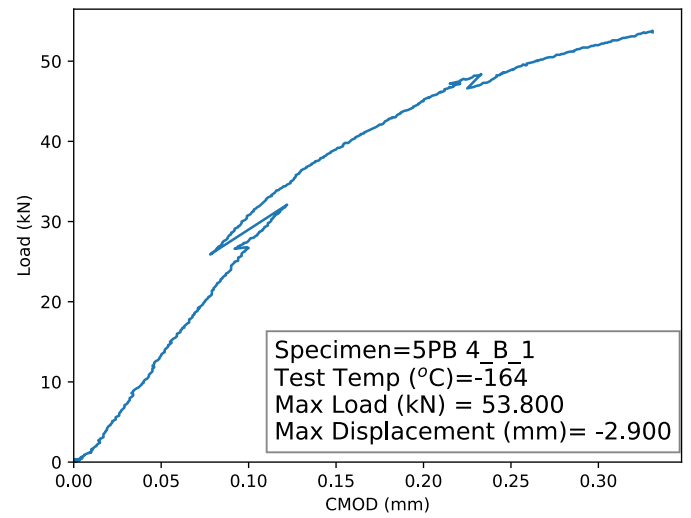
EDM notch= 20.363 mm
Average crack length both sides = 1.592 mm
Average crack length tension both sides = 2.118 mm

(f)

Figure A1.22: Specimen 5PB 3_BB_2 (a) Full Load-CMOD curve, (b) Load-CMOD curve to fracture event, (c) post fracture top view, (d) post fracture bottom view (e) fracture surface, (f) digitized fatigue crack length



(a)



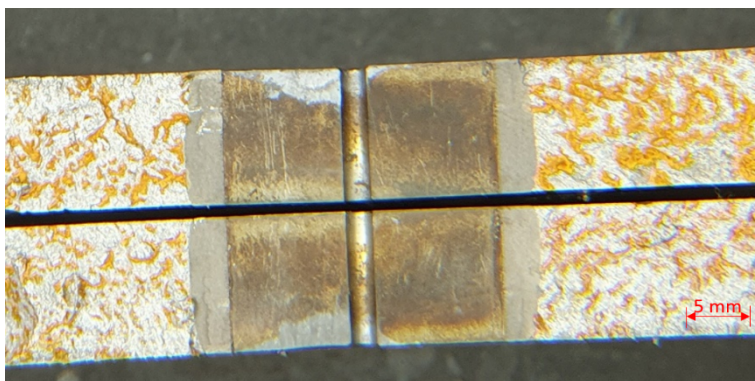
(b)



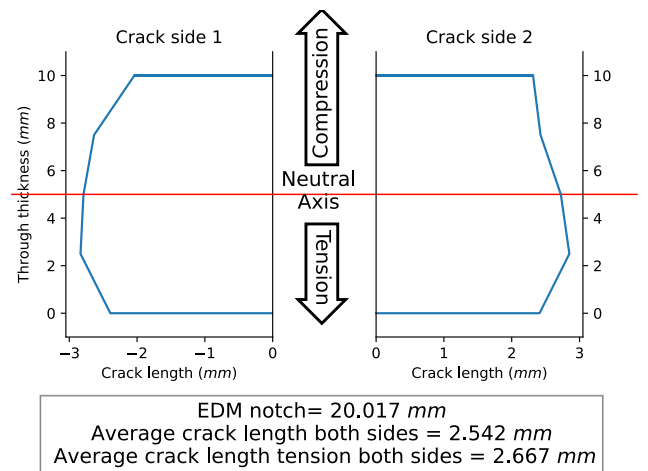
(c)



(d)

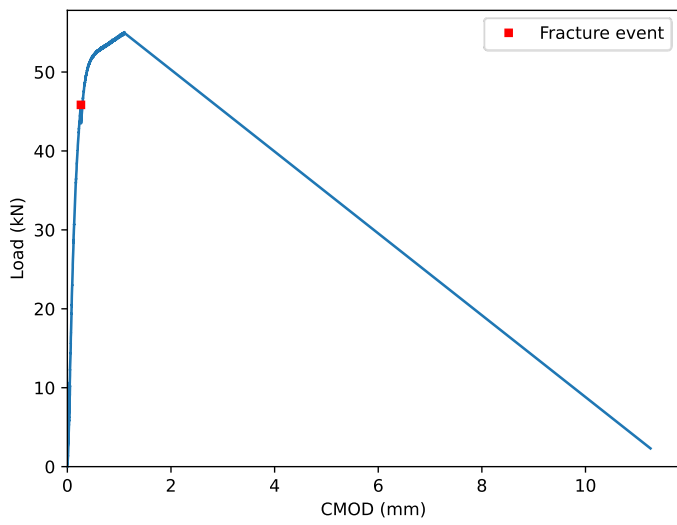


(e)

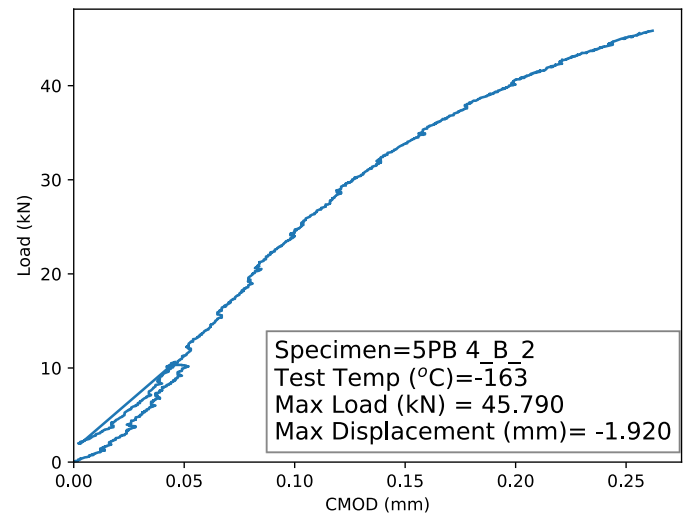


(f)

Figure A1.23: Specimen 5PB 4_B_1 (a) Full Load-CMOD curve, (b) Load-CMOD curve to fracture event, (c) post fracture top view, (d) post fracture bottom view (e) fracture surface, (f) digitized fatigue crack length



(a)



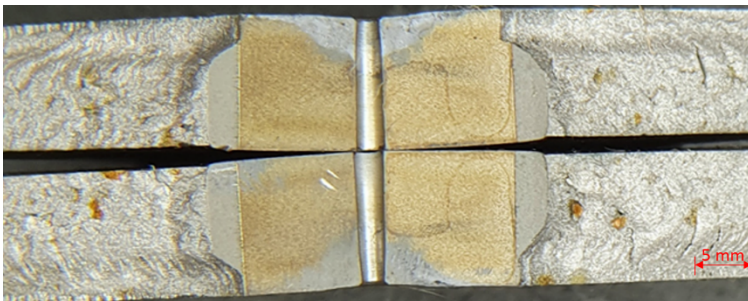
(b)



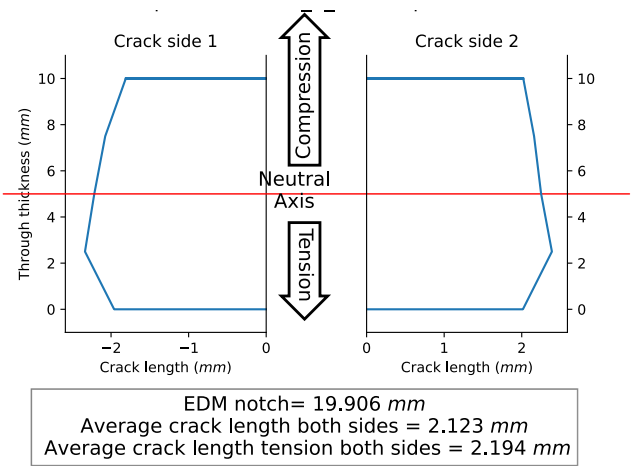
(c)



(d)

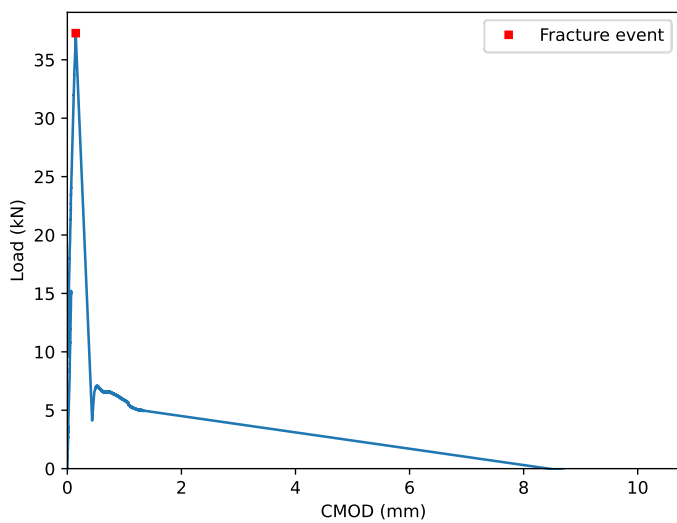


(e)

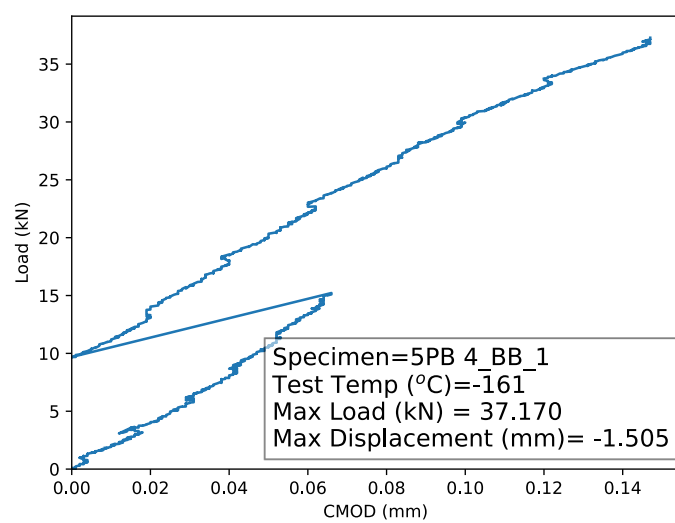


(f)

Figure A1.24: Specimen 5PB 4_B_2 (a) Full Load-CMOD curve, (b) Load-CMOD curve to fracture event, (c) post fracture top view, (d) post fracture bottom view (e) fracture surface, (f) digitized fatigue crack length



(a)



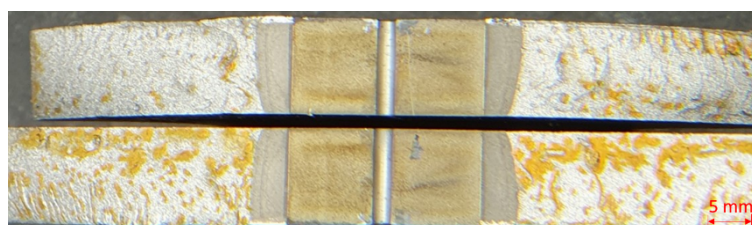
(b)



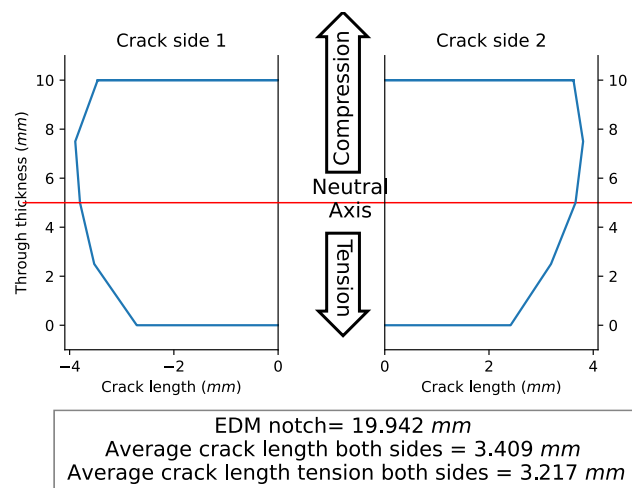
(c)



(d)

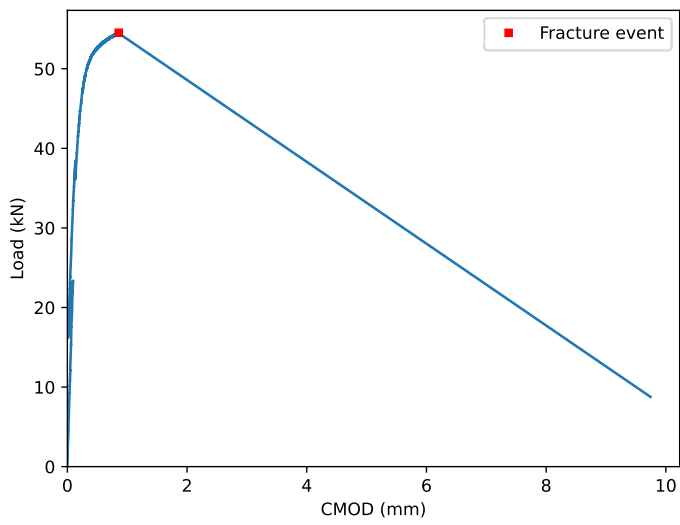


(e)

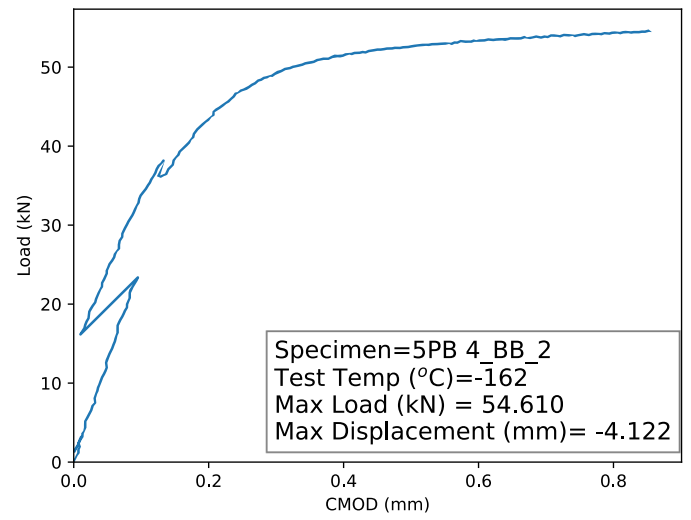


(f)

Figure A1.25: Specimen 5PB 4_BB_1 (a) Full Load-CMOD curve, (b) Load-CMOD curve to fracture event, (c) post fracture top view, (d) post fracture bottom view (e) fracture surface, (f) digitized fatigue crack length



(a)



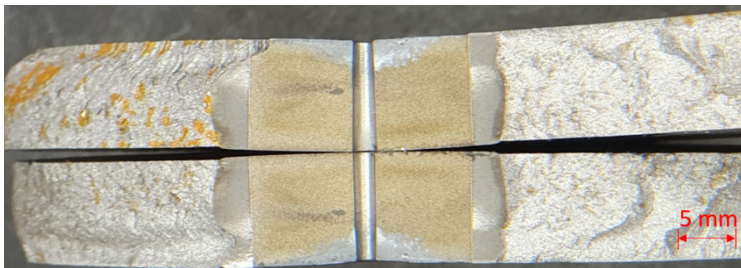
(b)



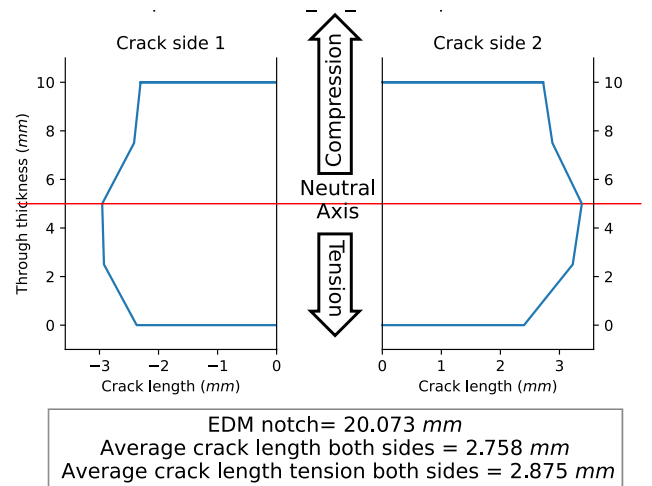
(c)



(d)

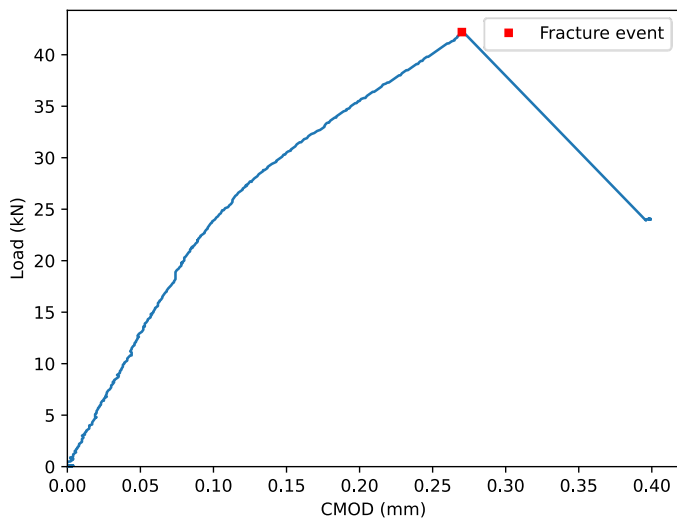


(e)

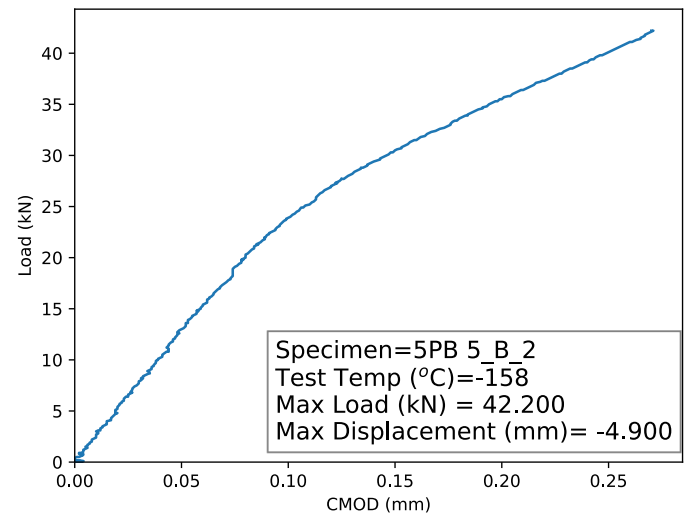


(f)

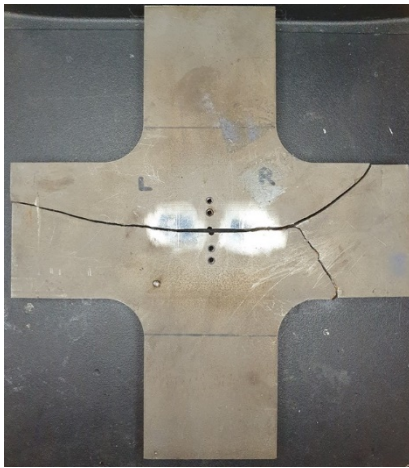
Figure A1.26: Specimen 5PB 4_BB_2 (a) Full Load-CMOD curve, (b) Load-CMOD curve to fracture event, (c) post fracture top view, (d) post fracture bottom view (e) fracture surface, (f) digitized fatigue crack length



(a)



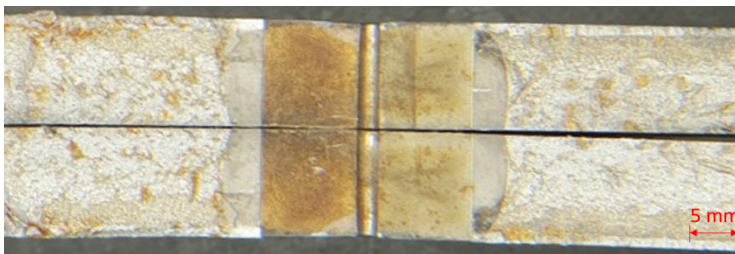
(b)



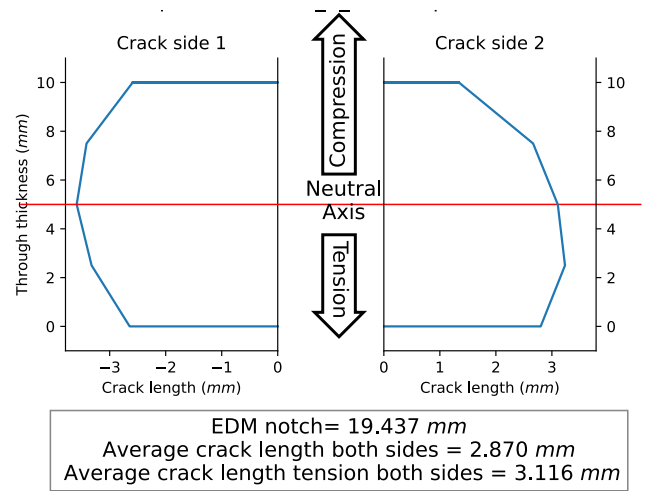
(c)



(d)

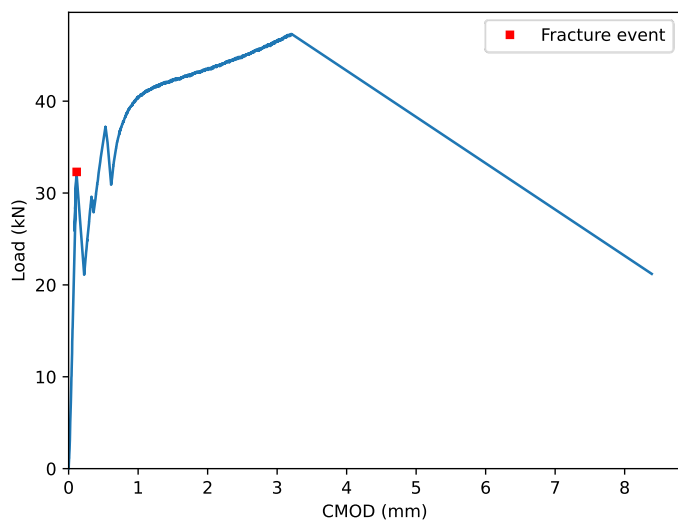


(e)

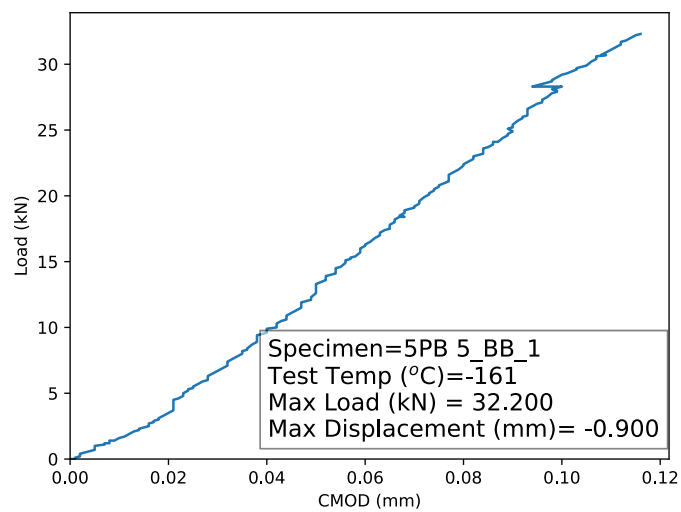


(f)

Figure A1.27: Specimen 5PB 5_B_2 (a) Full Load-CMOD curve, (b) Load-CMOD curve to fracture event, (c) post fracture top view, (d) post fracture bottom view (e) fracture surface, (f) digitized fatigue crack length



(a)



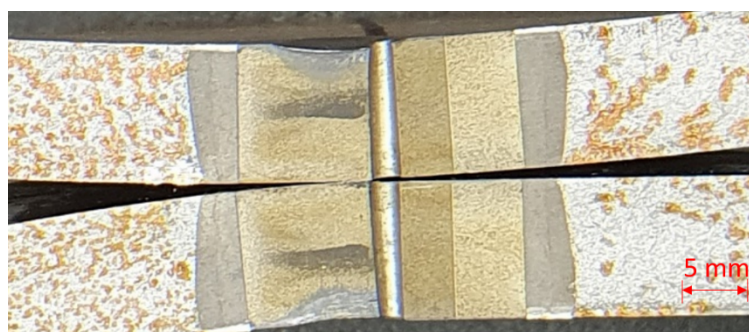
(b)



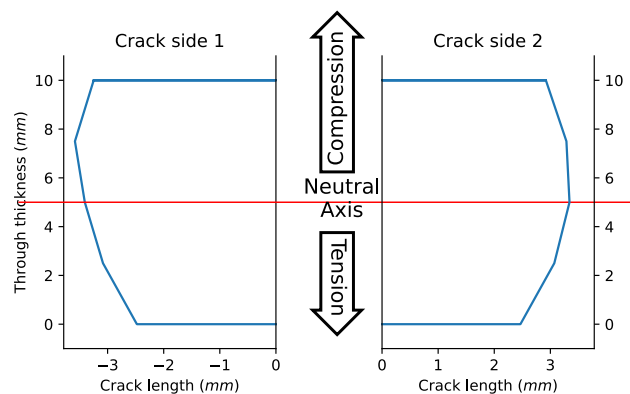
(c)



(d)

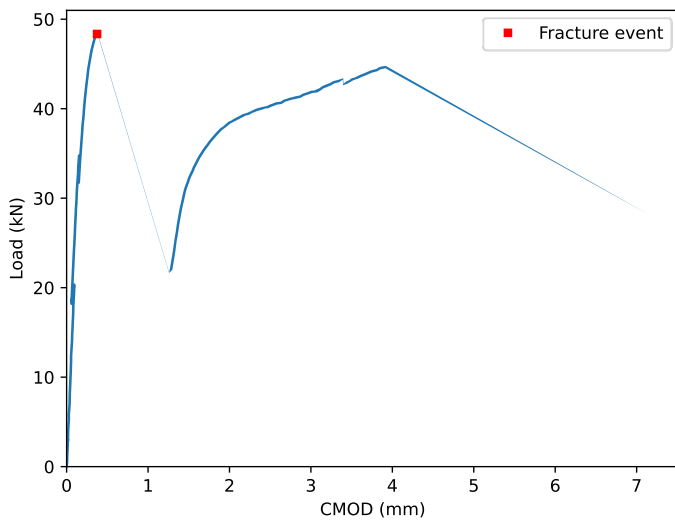


(e)

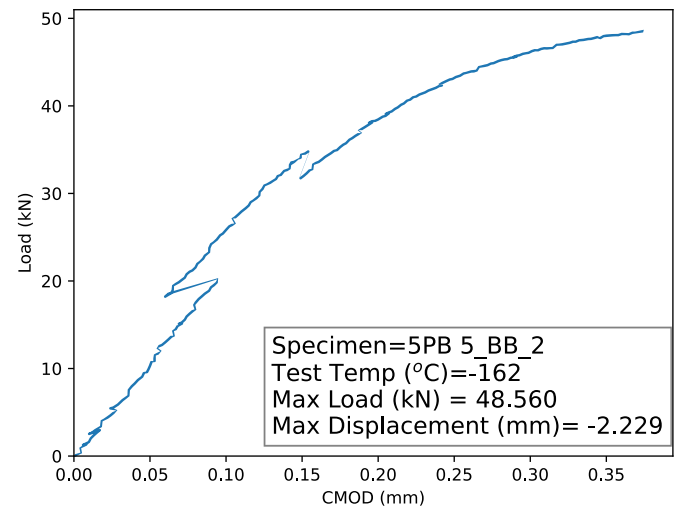


(f)

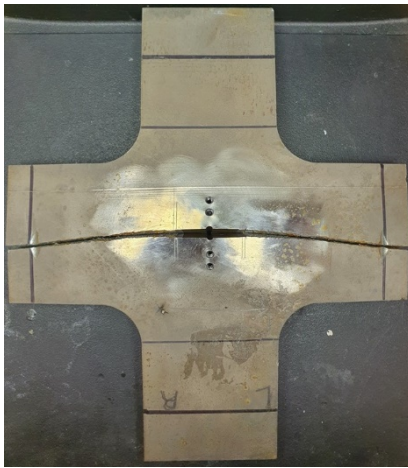
Figure A1.28: Specimen 5PB 5_BB_1 (a) Full Load-CMOD curve, (b) Load-CMOD curve to fracture event, (c) post fracture top view, (d) post fracture bottom view (e) fracture surface, (f) digitized fatigue crack length



(a)



(b)



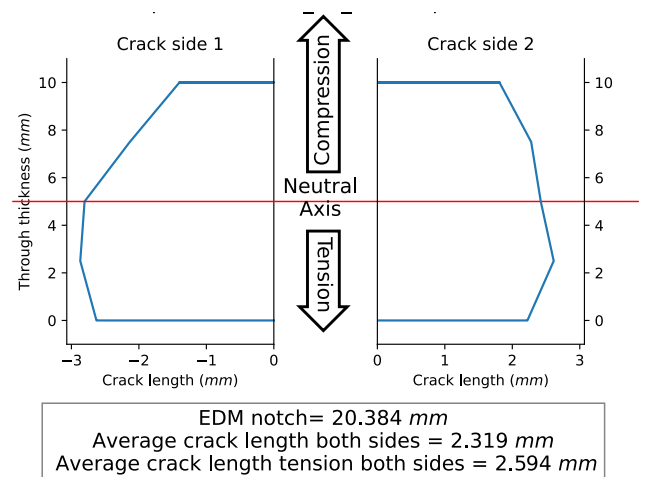
(c)



(d)

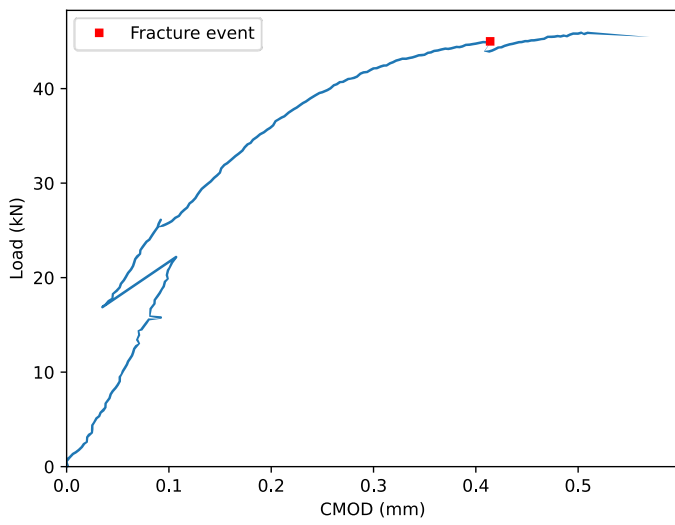


(e)

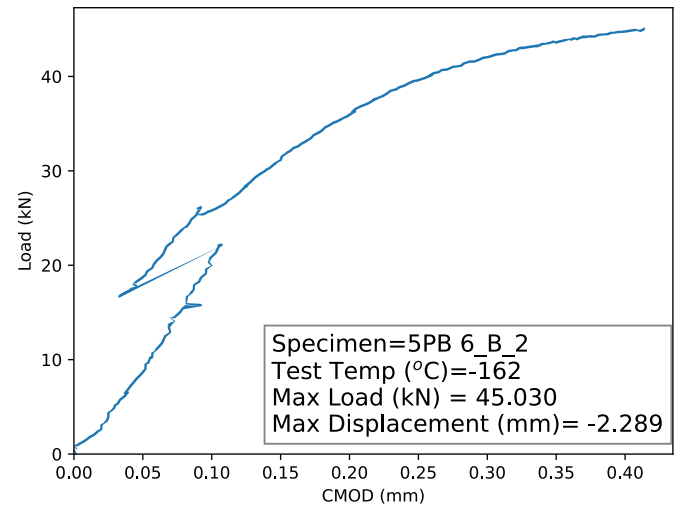


(f)

Figure A1.29: Specimen 5PB 5_BB_2 (a) Full Load-CMOD curve, (b) Load-CMOD curve to fracture event, (c) post fracture top view, (d) post fracture bottom view (e) fracture surface, (f) digitized fatigue crack length



(a)



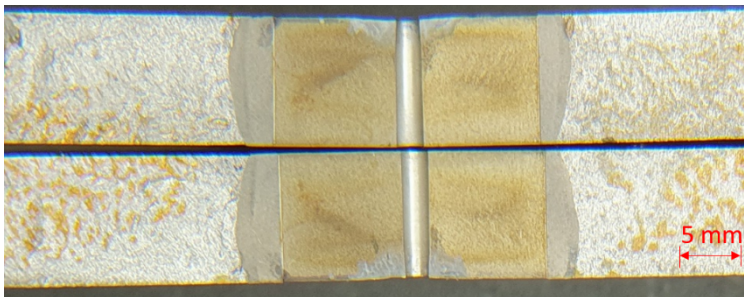
(b)



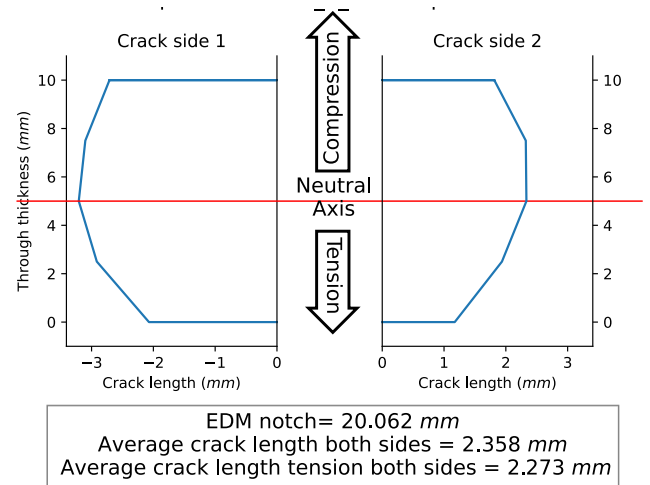
(c)



(d)

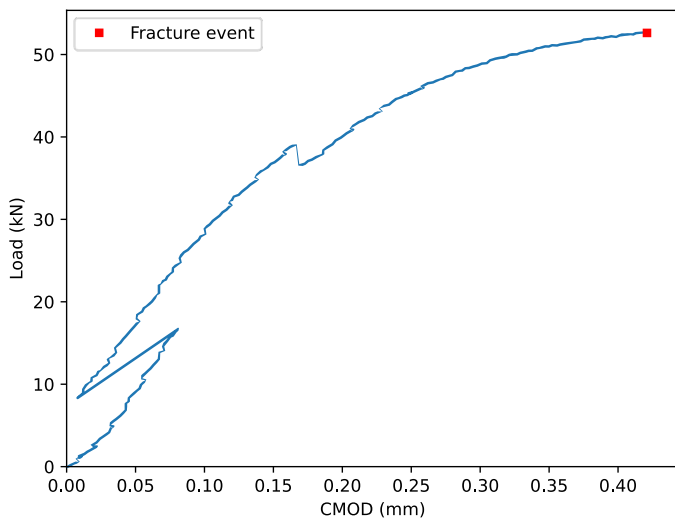


(e)

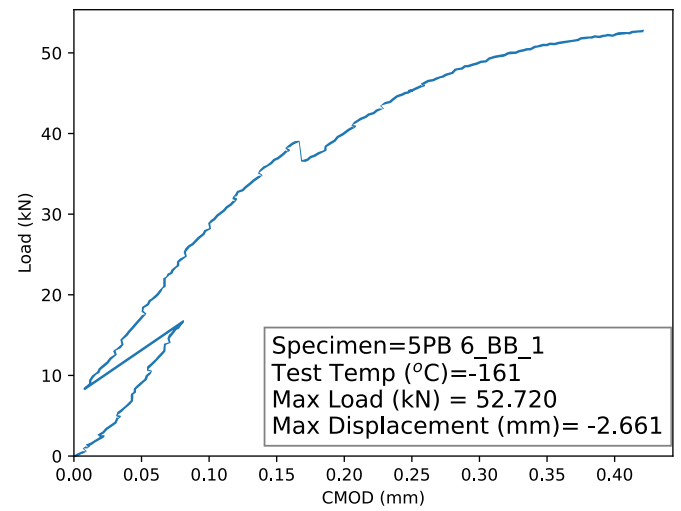


(f)

Figure A1.30: Specimen 5PB 6_B_2 (a) Full Load-CMOD curve, (b) Load-CMOD curve to fracture event, (c) post fracture top view, (d) post fracture bottom view (e) fracture surface, (f) digitized fatigue crack length



(a)



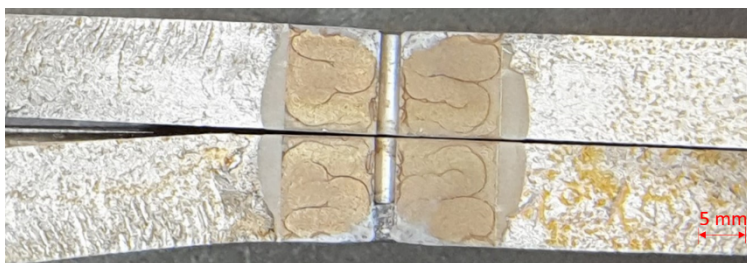
(b)



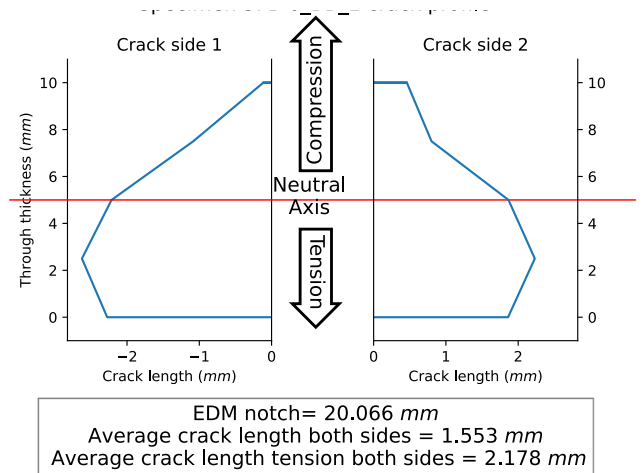
(c)



(d)

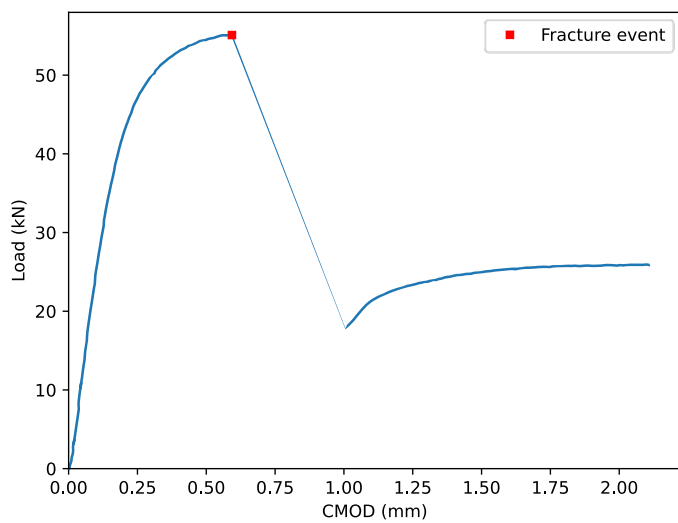


(e)

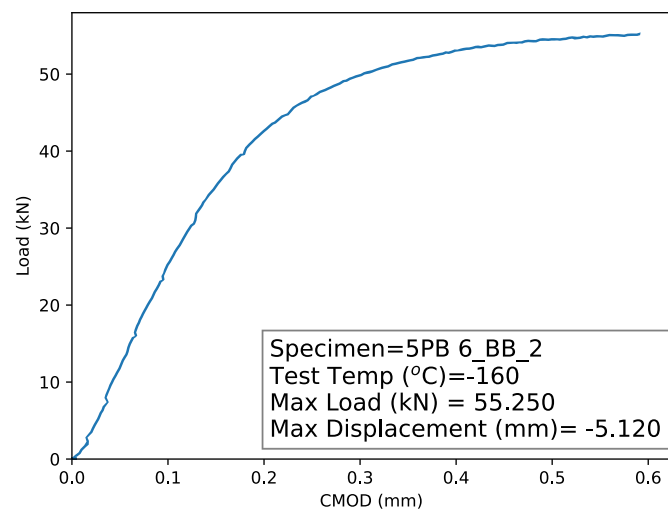


(f)

Figure A1.31: Specimen 5PB 6_BB_1 (a) Full Load-CMOD curve, (b) Load-CMOD curve to fracture event, (c) post fracture top view, (d) post fracture bottom view (e) fracture surface, (f) digitized fatigue crack length



(a)



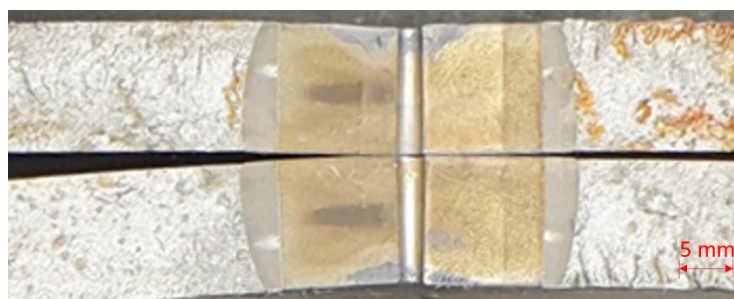
(b)



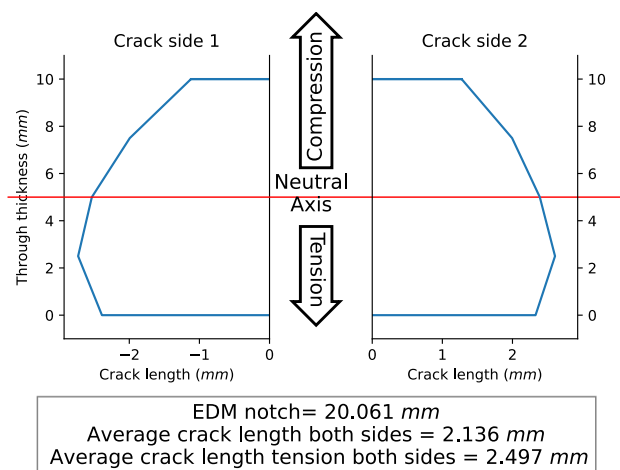
(c)



(d)



(e)



(f)

Figure A1.32: Specimen 5PB 6_BB_2 (a) Full Load-CMOD curve, (b) Load-CMOD curve to fracture event, (c) post fracture top view, (d) post fracture bottom view (e) fracture surface, (f) digitized fatigue crack length

Appendix – 2: Steel parametric FEA

This appendix includes the parametric analyses run for the validation of the steel FEA models. Biaxially loaded test specimen 5PB_1_BB_2 was assumed to have the representative behaviour of the average test given its smooth Load-CMOD curve (lack of noise in the data) and the straight fatigue pre-crack profile achieved. Details on this experiment are given graphically in Appendix 1

The best modelling parameters were

- 5) A friction coefficient $\mu=0.3$ between the punch and the specimen
- 6) A modelled/half crack length $a=12.76$ mm as measured from the optometer
- 7) An applied displacement of 4.188 mm from the loading punch
- 8) A Young's modulus of 204 GPa, as measured experimentally at -160°C

The results of the model against the experimental Load-CMOD with the use of the best parameters are given in the following graph

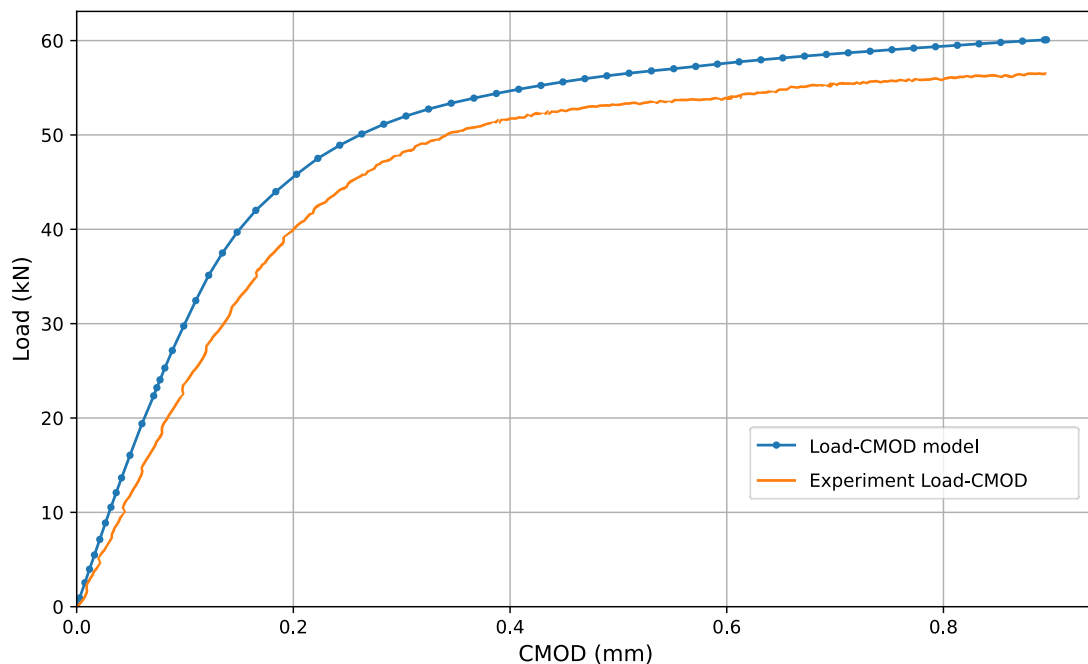


Figure A2. 1: 5PB_1_BB_2 Experimental and FEA Load CMOD – best modelling parameters

Following are the analyses that investigate the effect of different parameters

Effect of friction coefficient

Overall 4 different friction coefficients were used, shown in Table A2. 1.

Table A2. 1: Friction coefficient of parametric study parameter values

| <u>Punch Friction coefficient μ</u> |
|--|
| 0.6 |
| 0.4 |
| 0.3 |
| 0.2 |
| 0.1 |

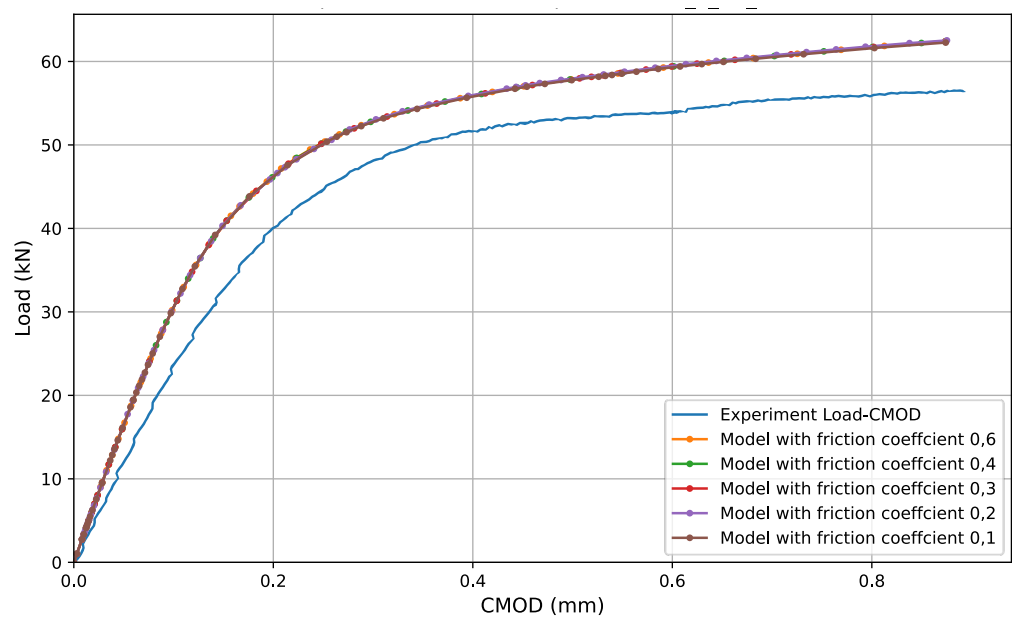


Figure A2. 2: 5PB_1_BB_2 Friction coefficient parametric FEA vs Experimental Load-CMOD

From the results shown in Figure A2. 2, within the reasonable threshold of friction coefficients for steel contact it played almost no effect on the overall behaviour of the specimen.

Effect of crack length

To rule out the effect of the minor tunnelling observed from fatigue pre-cracking on the validity of the model and to check the sensitivity of compliance with crack-length different crack lengths were assumed in the analyses, shown in Table A2. 2.

Table A2. 2: Crack length parametric study parameter values

Half Crack length a (mm)

10

11

12.76 (actual length)

14

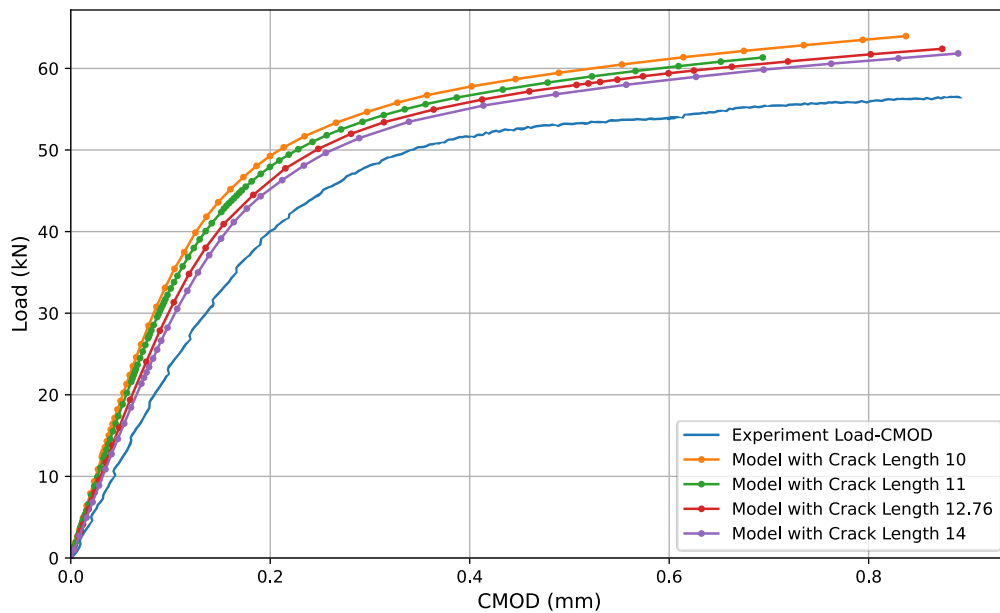


Figure A2. 3: 5PB_1_BB_2 Crack length parametric FEA vs Experimental Load-CMOD

From the results shown in Figure A2. 3, compliance changed with crack length as expected however even for extreme half crack-length of 14 mm compliance did not reach the experimental data.

Effect of roller displacement

Given that the experiment was novel and conducted with significant time constraints, minor displacement of the specimen could have been present during the experimental setup. In light of this, 5 different roller displacement scenarios were run to study the sensitivity of the model.

The 4 rollers that were in contact with the specimen are divided into two categories,

9) Rollers parallel to the crack, where the crack opening load was applied

10) Rollers perpendicular to the crack, where the in-plane loading was applied

The different displacement values for the cases are shown in Table A2. 3 while the results for each case are shown in Figure A2. 4 to Figure A2. 8.

Table A2. 3: Roller Displacement parametric study parameter values

| Applied displacement in mm | |
|----------------------------|--------------------------------|
| Rollers parallel to crack | Rollers perpendicular to crack |
| CASE 1 | |
| 3 | 0 |
| 1 | |
| 0.1 | |
| 0 | |
| -0.1 | |
| -1 | |
| -3 | |
| CASE 2 | |
| 0 | 0 |
| 4 | |
| 6 | |
| 8 | |
| 10 | |
| CASE 3 | |
| 0 | 0 |
| | 2 |
| | 4 |
| | 6 |
| | 8 |
| CASE 4 | |
| 8 | 0 |
| | 2 |
| | 4 |
| | 6 |
| | 8 |
| CASE 5 | |
| 10 | 0 |
| | 2 |
| | 4 |
| | 6 |
| | 8 |

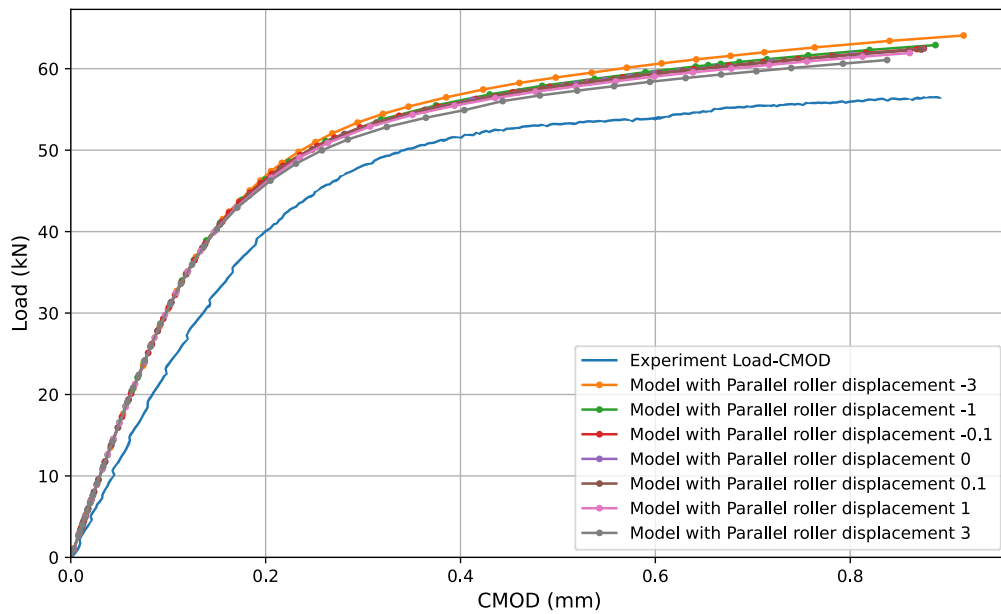


Figure A2. 4: Roller displacement parametric study FEA vs experimental Load-CMOD - Case 1

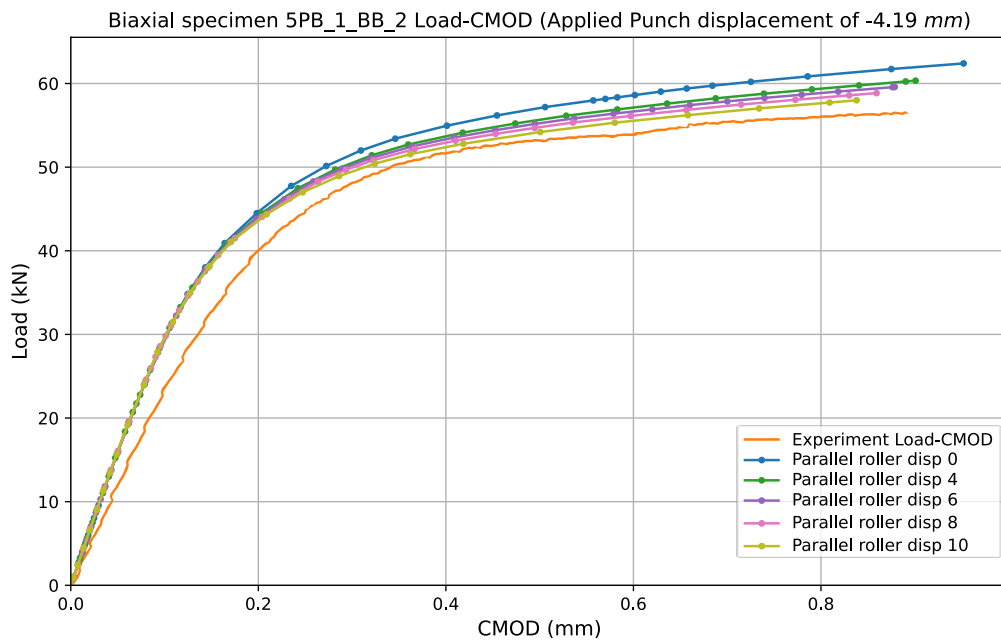


Figure A2. 5: Roller displacement parametric study FEA vs experimental Load-CMOD - Case 2

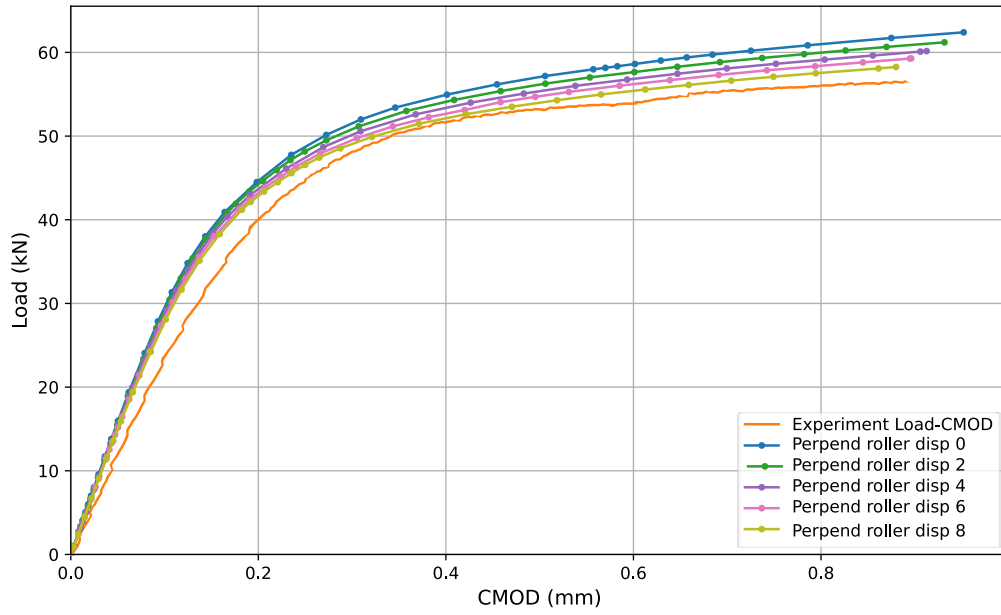


Figure A2. 6: Roller displacement parametric study FEA vs experimental Load-CMOD - Case 3

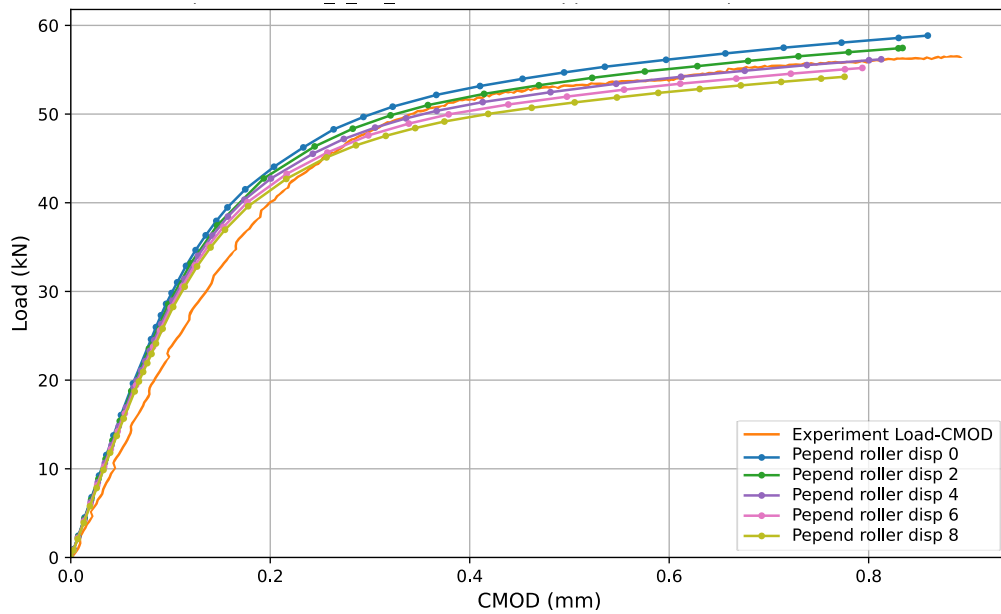


Figure A2. 7: Roller displacement parametric study FEA vs experimental Load-CMOD - Case 4

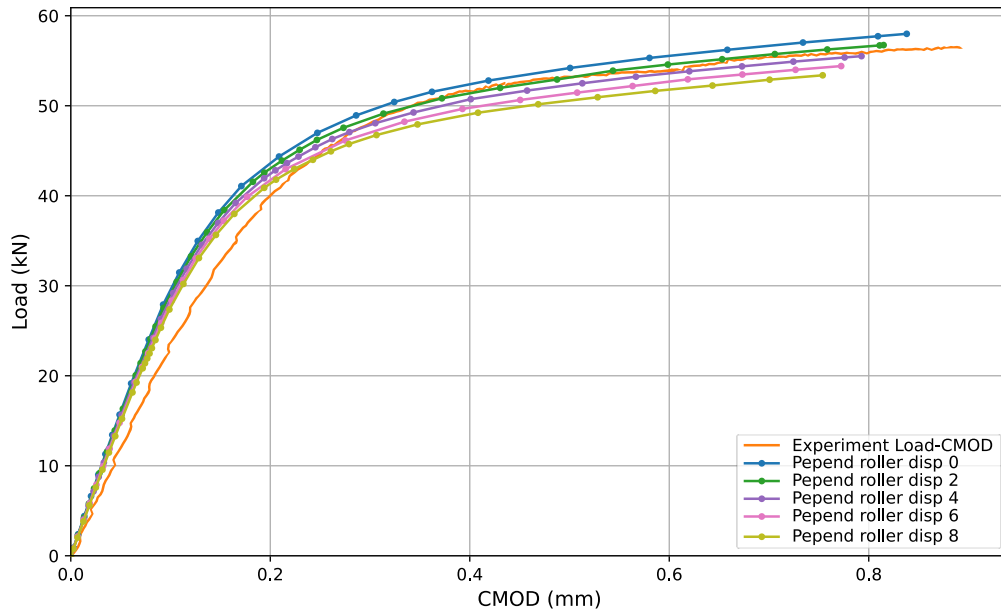


Figure A2. 8: Roller displacement parametric study FEA vs experimental Load-CMOD – Case 5

The results that Load-CMOD changes with applied roller displacement, in particular displacement of the rollers parallel to the crack have an effect only on the plastic part of the curve, while compliance is mostly affected by displacing the rollers perpendicular to the crack. However, even in Case 5, with a displacement of parallel rollers by 10 mm and of perpendicular rollers by 8 mm the desired compliance is not reached. Such displacements are considered to be extreme and not present in any of the experiments conducted and it is concluded that the roller positioning cannot correct the mismatch between models and experiments.

Effect of Young's Modulus

Knowing that elastic compliance is directly affected by the material properties and in particular the Young's modulus selected, parametric analyses with different Youngs moduli were run to check the sensitivity of the model. The parameter values are shown in Table A2. 4 and the results of the analyses in Figure A2. 9.

Table A2. 4: Elastic modulus parametric study parameter values

| Young's modulus E (GPa) |
|-------------------------|
| 150 |
| 170 |
| 180 |
| 192 |
| 204 (at -160°C) |

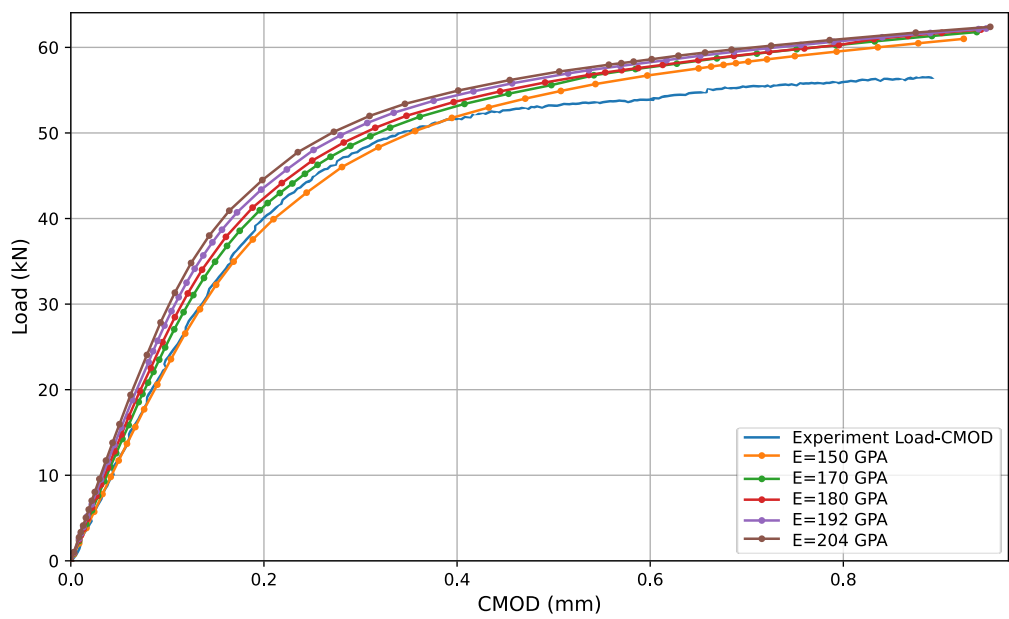


Figure A2. 9: Elastic modulus parametric study FEA vs experimental Load-CMOD

As expected, elastic compliance is sensitive to the E used. For the model compliance to reach the experimentally measured compliance the elastic modulus needs to decrease to 150 GPa. This value is not representative of a mild ferritic steel, and it is concluded that this parameter cannot be altered to match the experimental with the modelled Load-CMOD values.

Effect of geometry nonlinearity

Given that plasticity is included in the simulations a comparison two analyses were run considering geometric nonlinearity (nlgeom=on) or disregarding it (nlgeom=off). The results are shown in Figure A2. 10 below, where geometric nonlinearities slightly increase the Load CMOD curve, however this is in the zone where significant tearing is beginning. In this experimental program occurrences of significant tearing are disregarded from the analyses, hence either choice of nlgeom is acceptable.

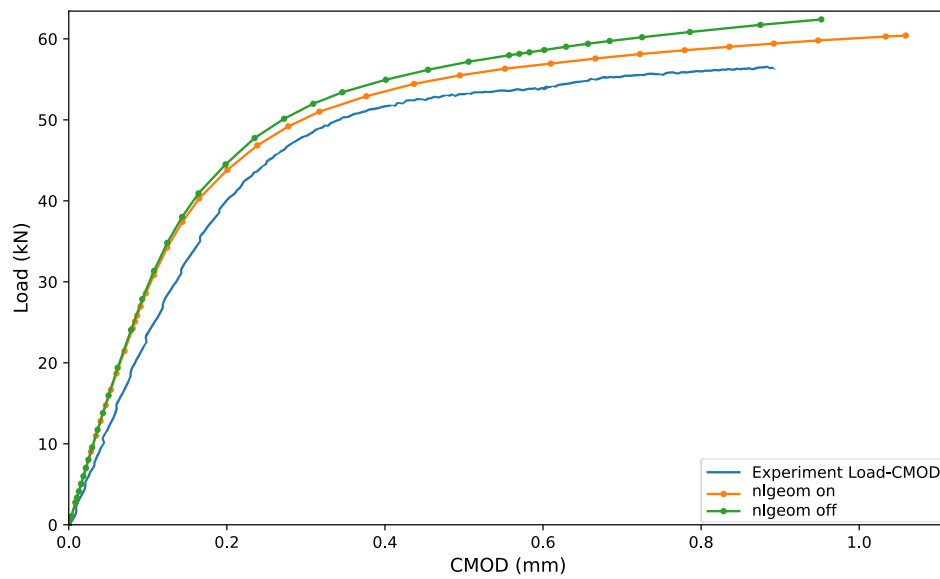


Figure A2. 10: Geometric nonlinearity parametric study FEA vs experimental Load-CMOD

Appendix – 3: Steel FEA results

This appendix contains all the results of the simulated steel biaxial/cruciform and uniaxial/rectangular specimens.

Uniaxial – 3 Point Bend FEA results

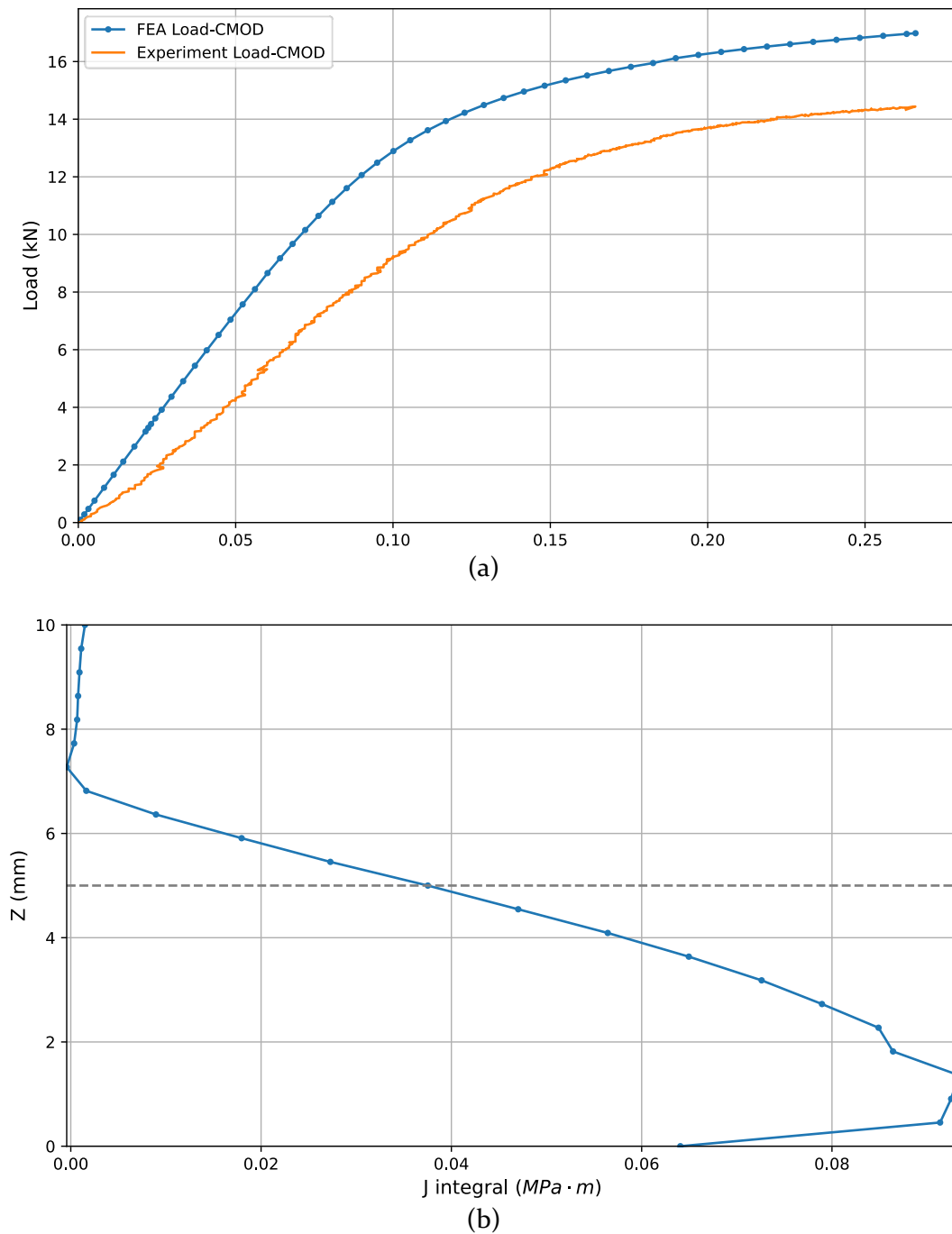
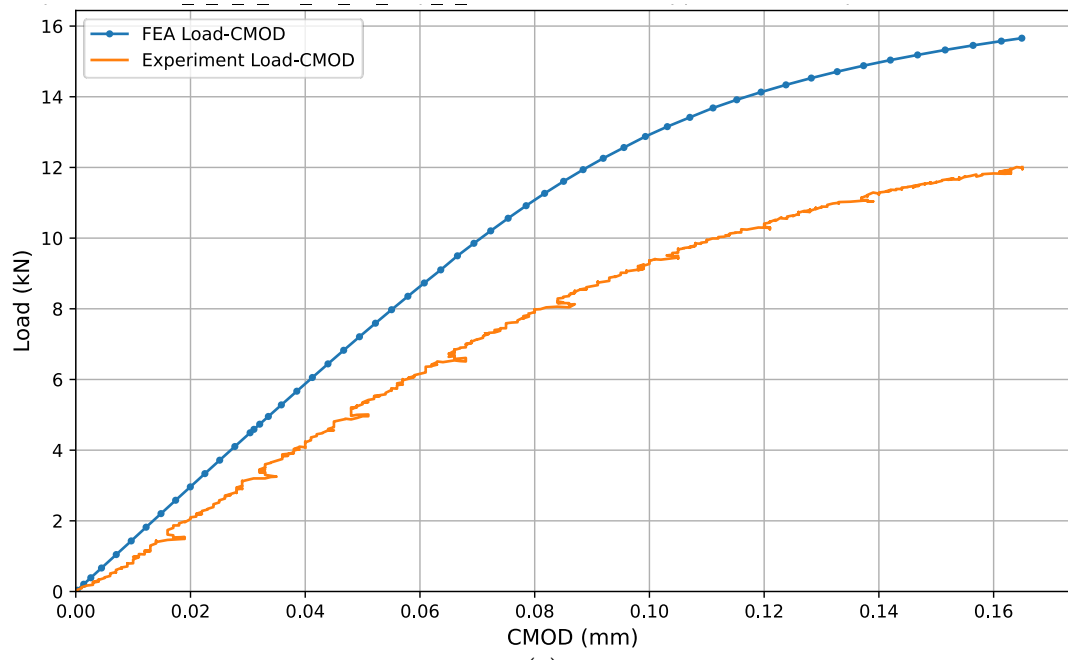
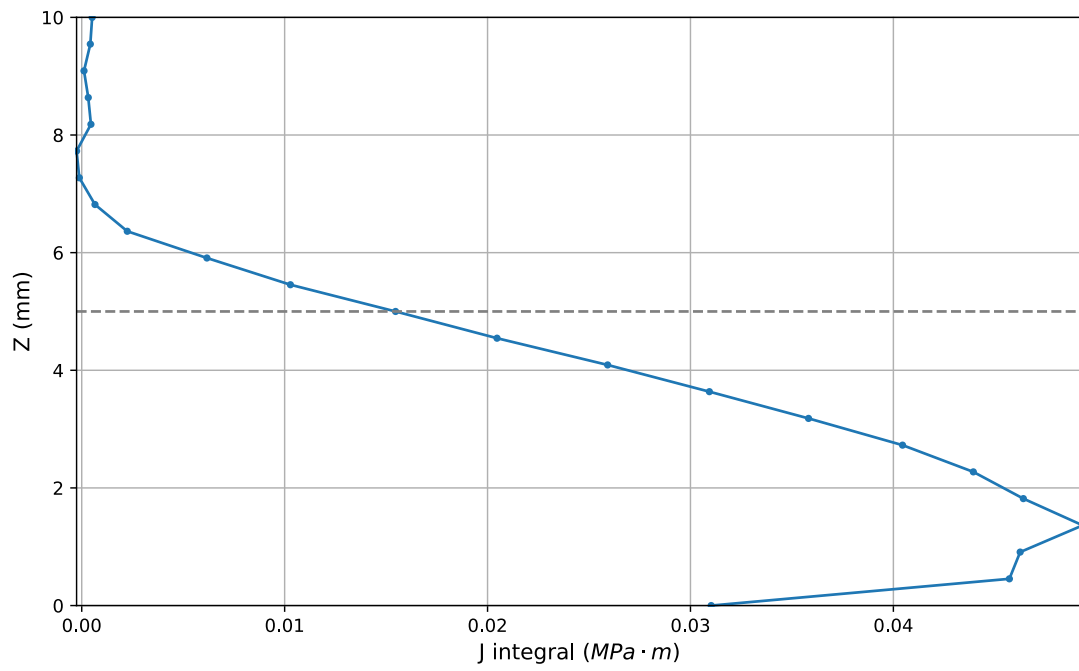


Figure A3. 1: Specimen 3PB 1_U_1 (a) FEA and Experimental Load-CMOD curve, (b) J-integral along the crack front



(a)



(b)

Figure A3. 2: Specimen 3PB 3_U_1 (a) FEA and Experimental Load-CMOD curve, (b) J-integral along the crack front

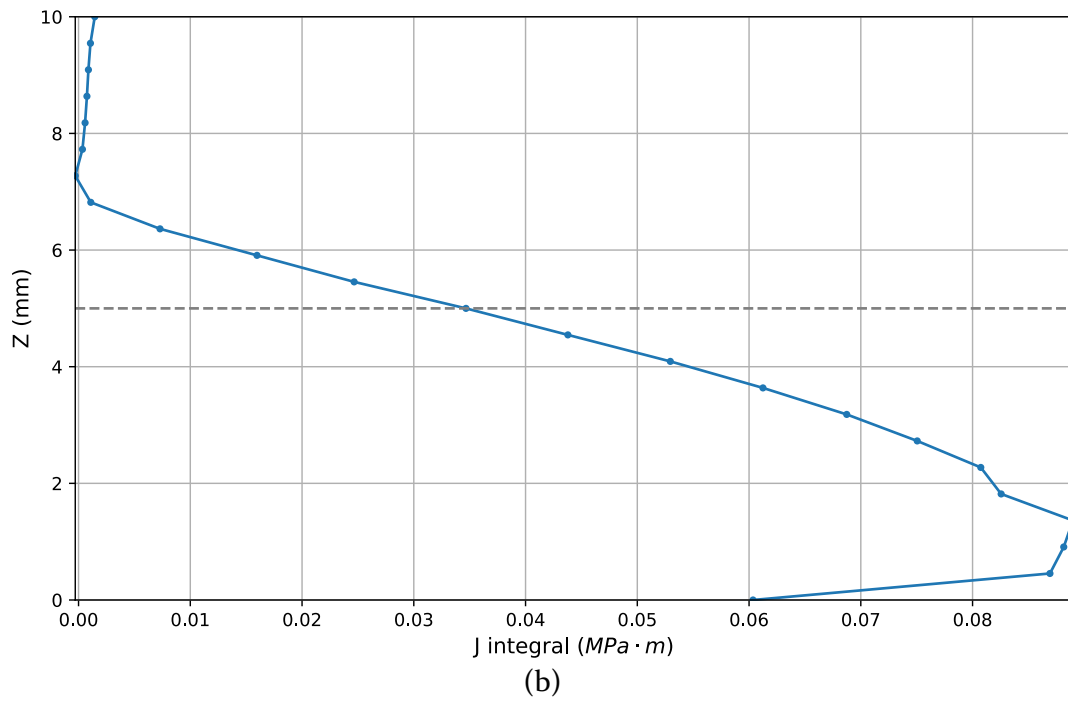
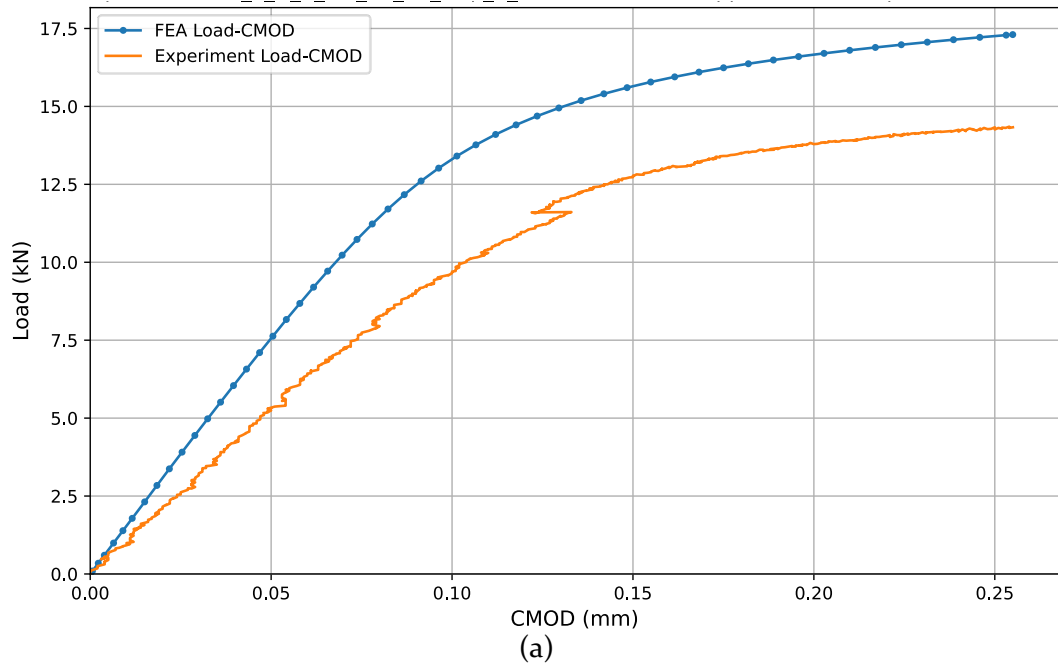


Figure A3. 3: Specimen 3PB 3_U_2 (a) FEA and Experimental Load-CMOD curve, (b) J-integral along the crack front

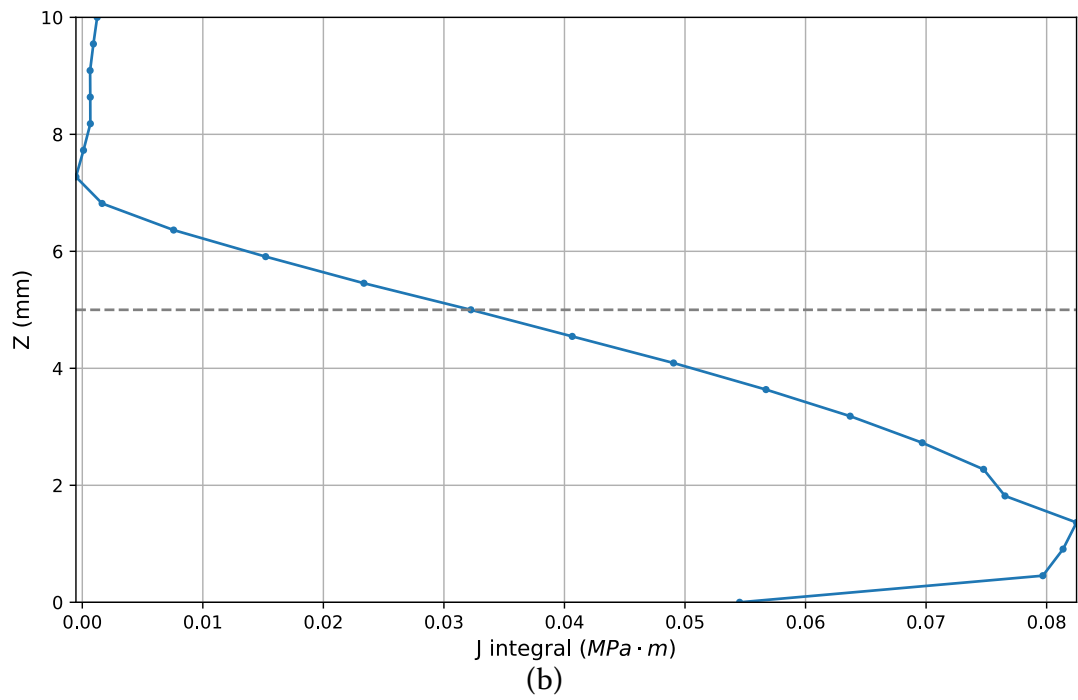
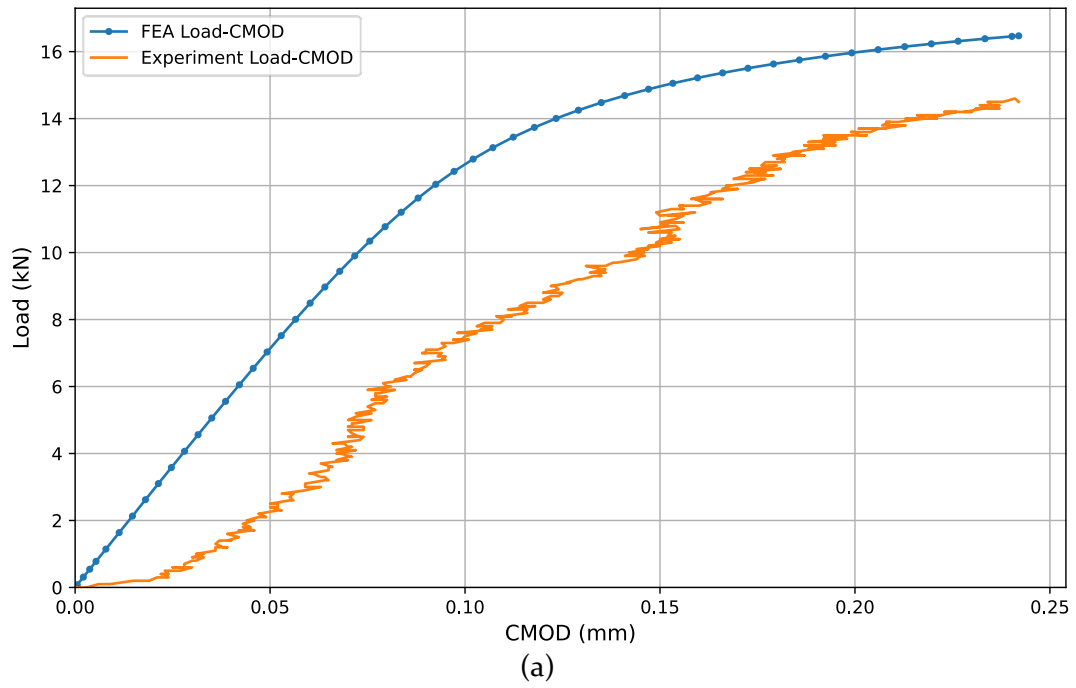


Figure A3. 4: Specimen 3PB 3_B_1 (a) FEA and Experimental Load-CMOD curve, (b) J-integral along the crack front

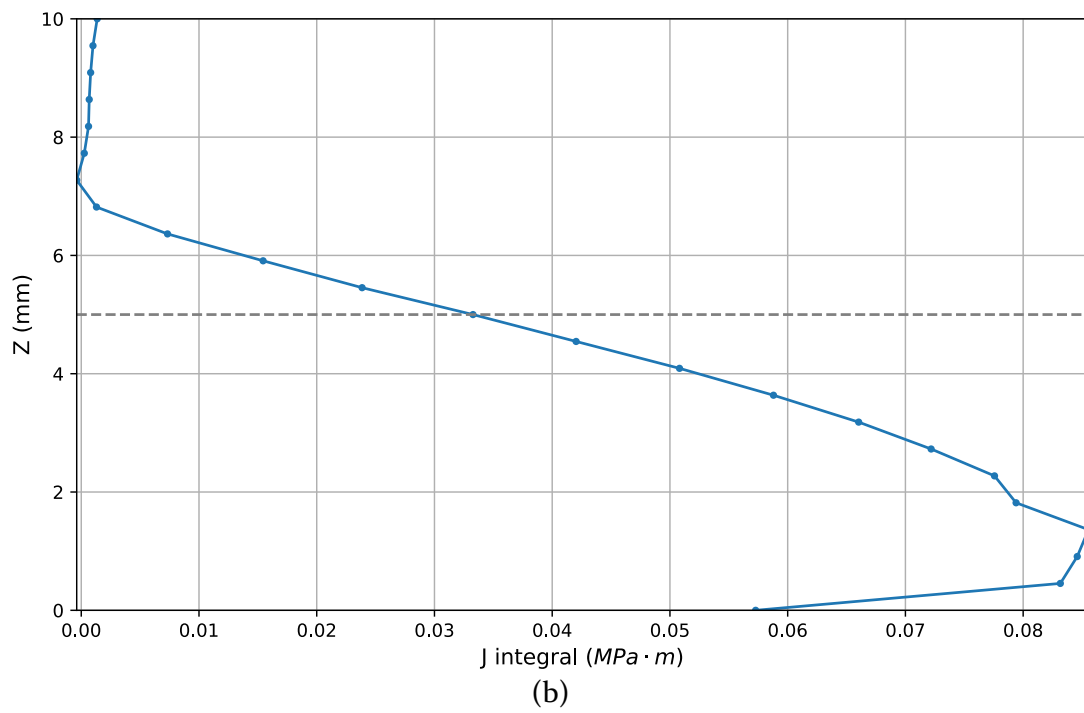
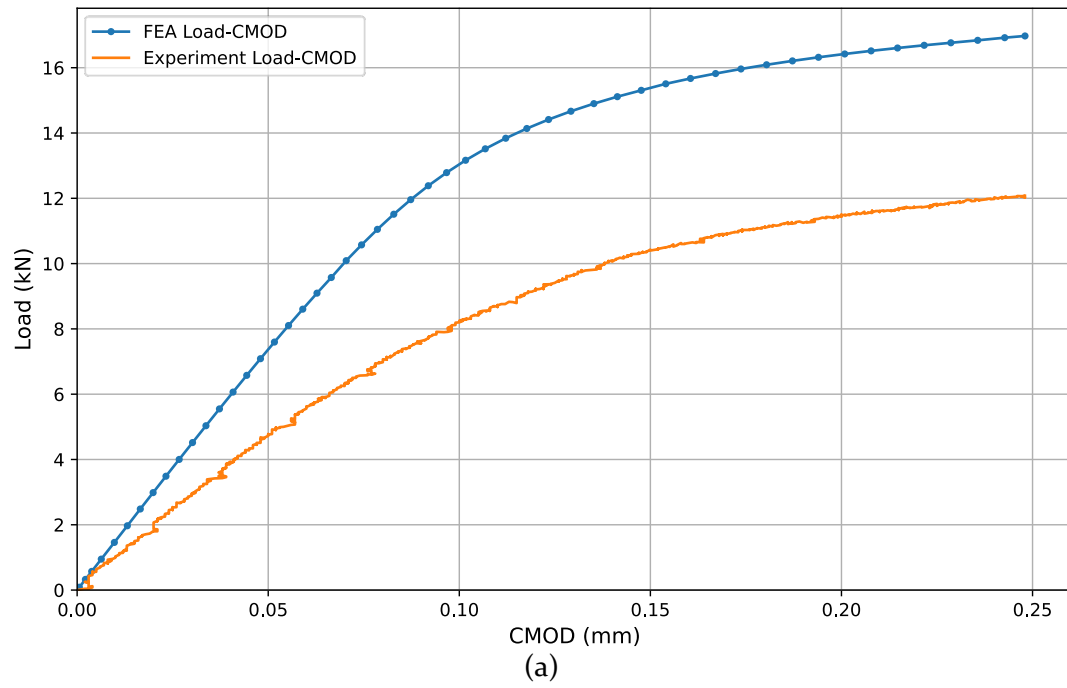


Figure A3. 5: Specimen 3PB 4_B_1 (a) FEA and Experimental Load-CMOD curve, (b) J-integral along the crack front

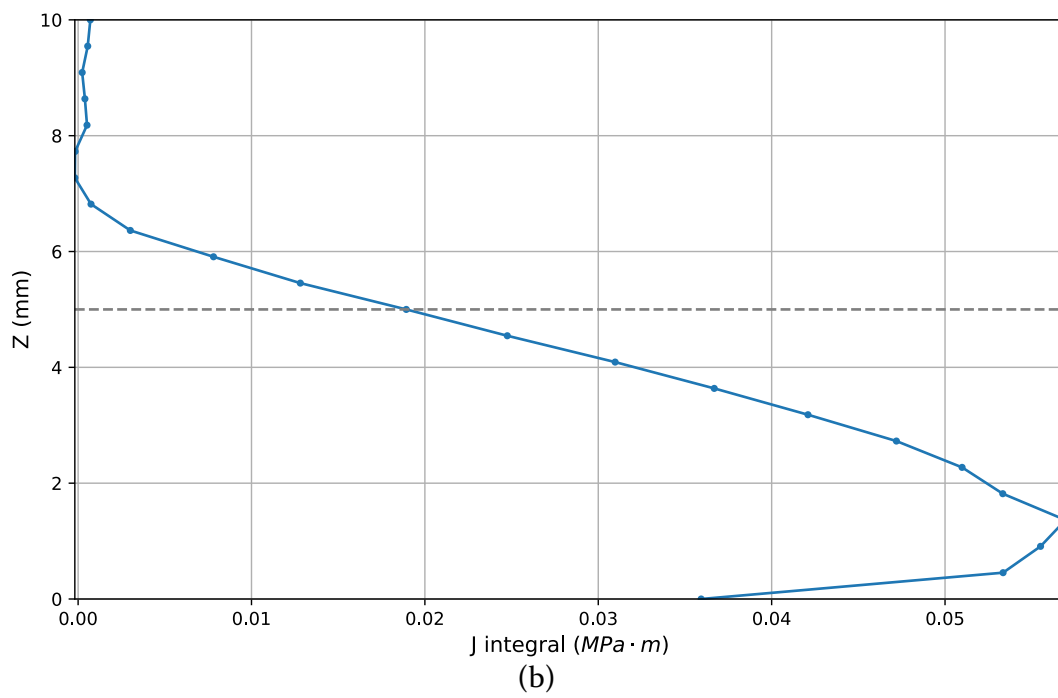
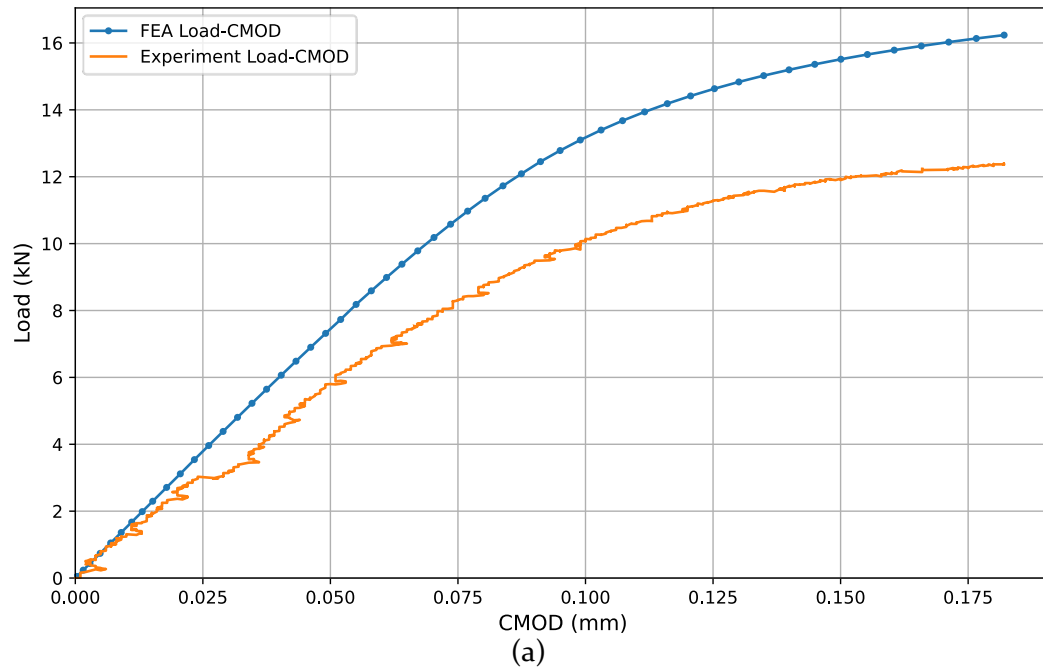


Figure A3. 6: Specimen 3PB 5_U_2 (a) FEA and Experimental Load-CMOD curve, (b) J-integral along the crack front

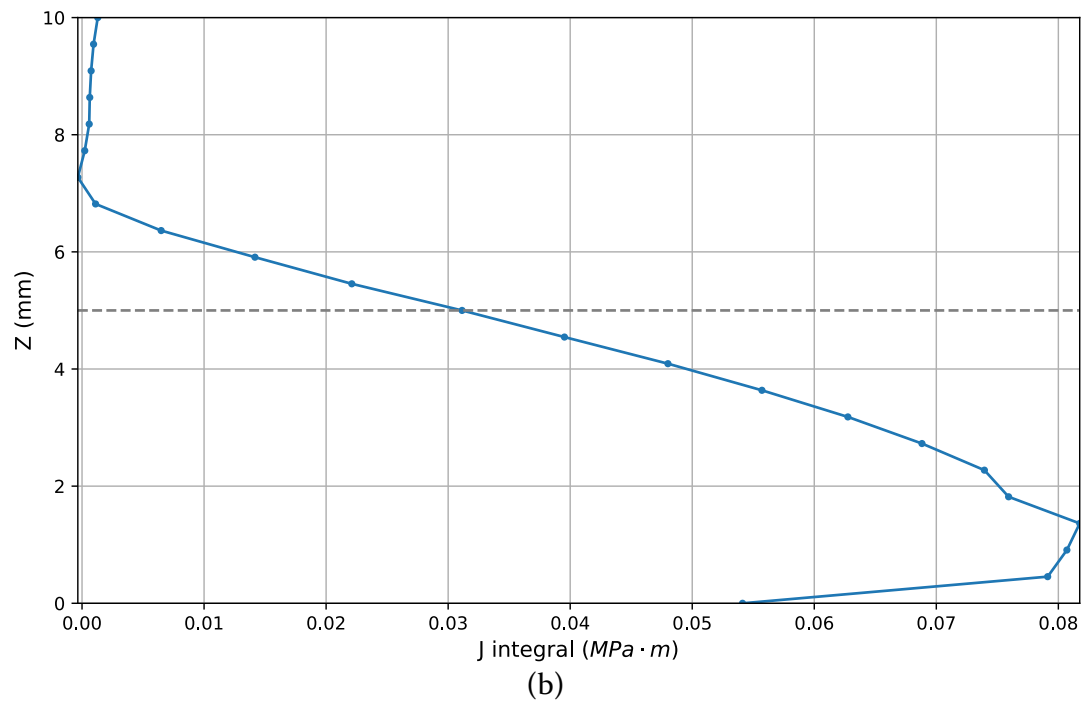
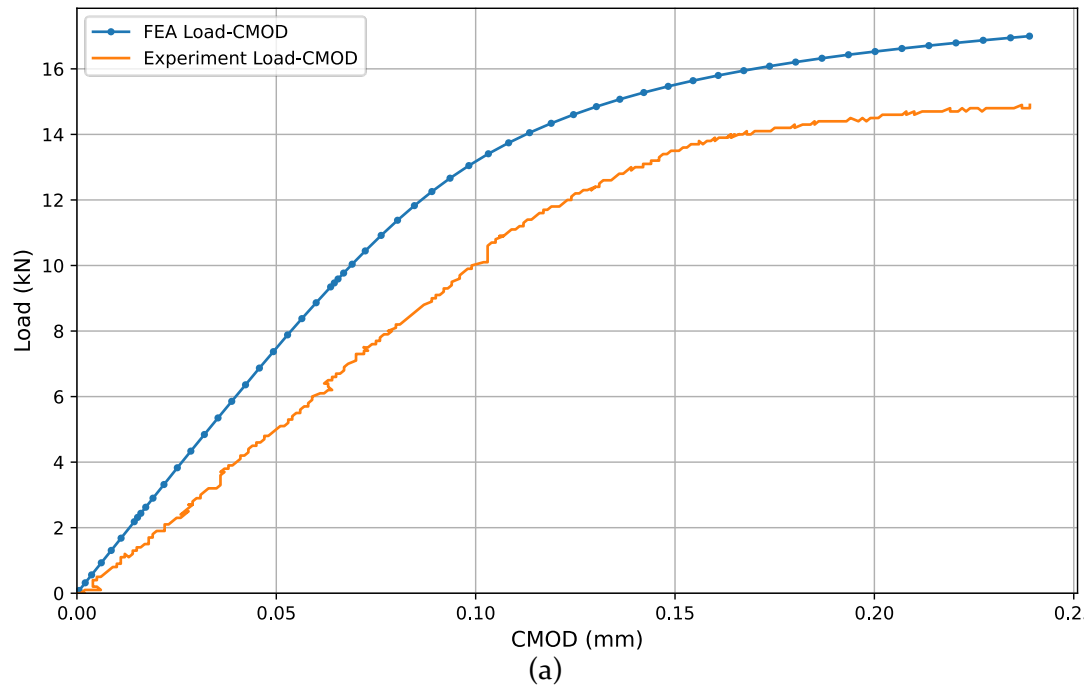


Figure A3. 7: Specimen 3PB 5_B_1 (a) FEA and Experimental Load-CMOD curve, (b) J-integral along the crack front

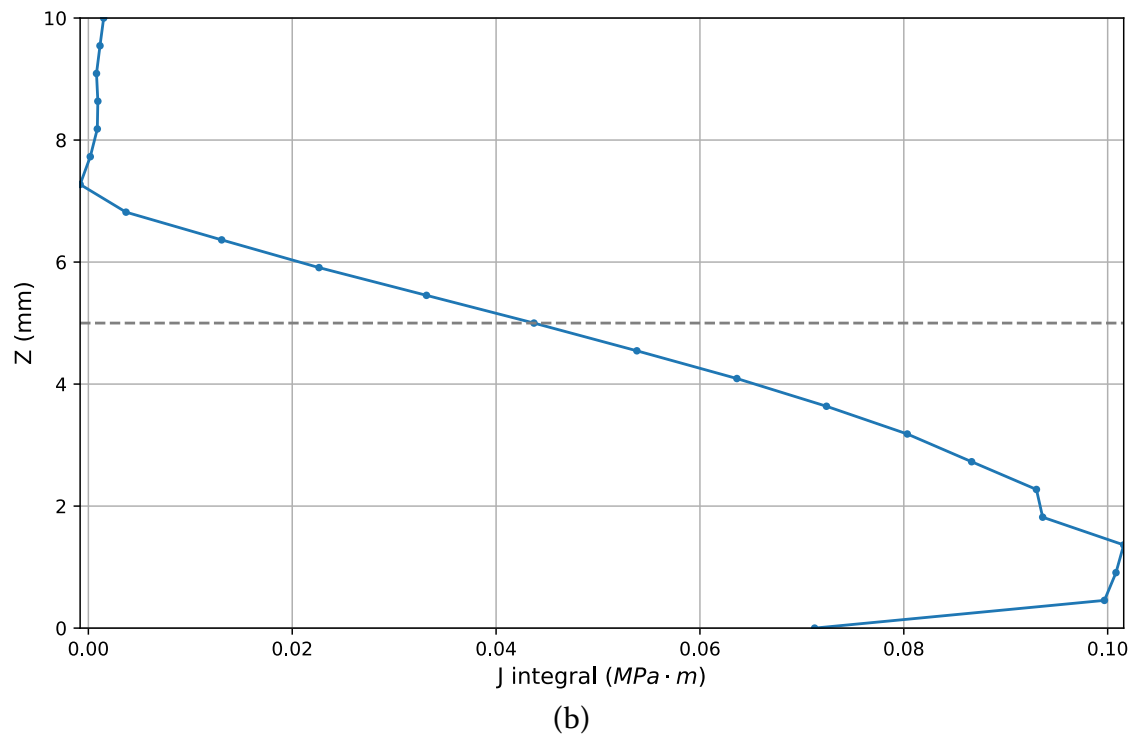
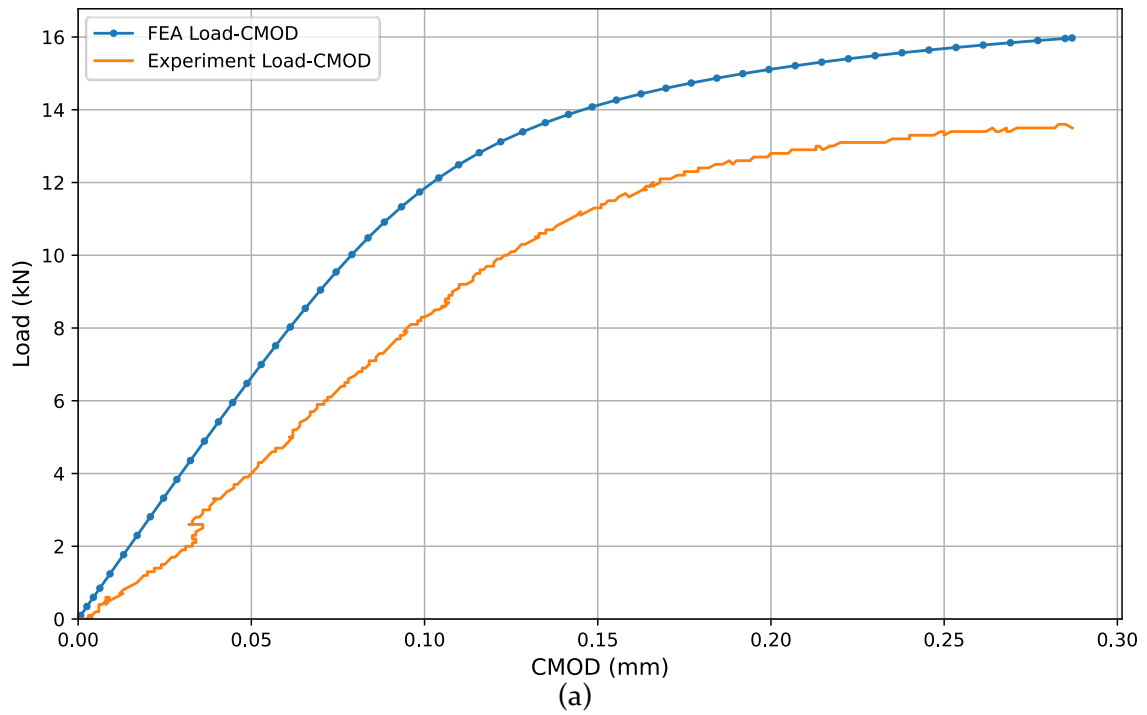


Figure A3. 8: Specimen 3PB 6_B_1 (a) FEA and Experimental Load-CMOD curve, (b) J-integral along the crack front

Biaxial – 5 Point Bend FEA results

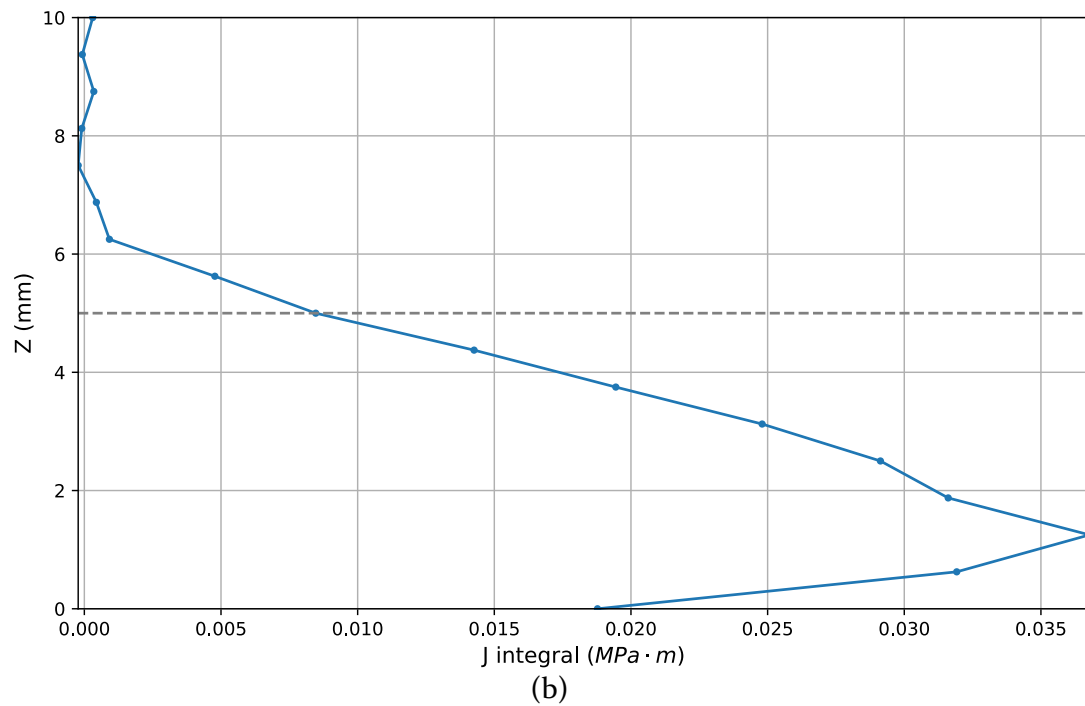
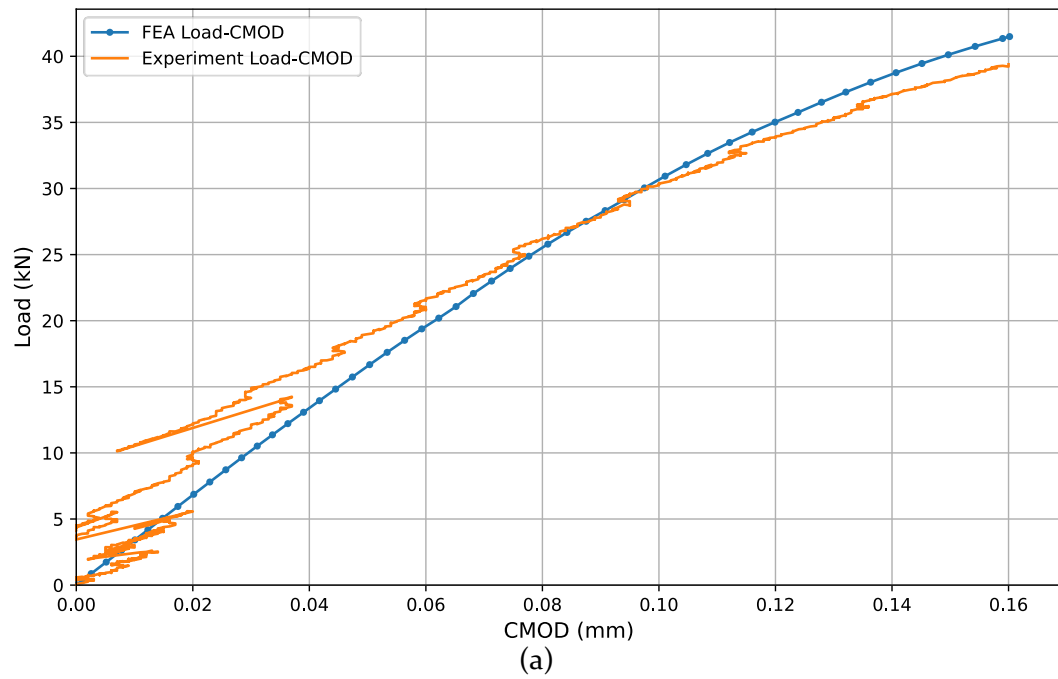
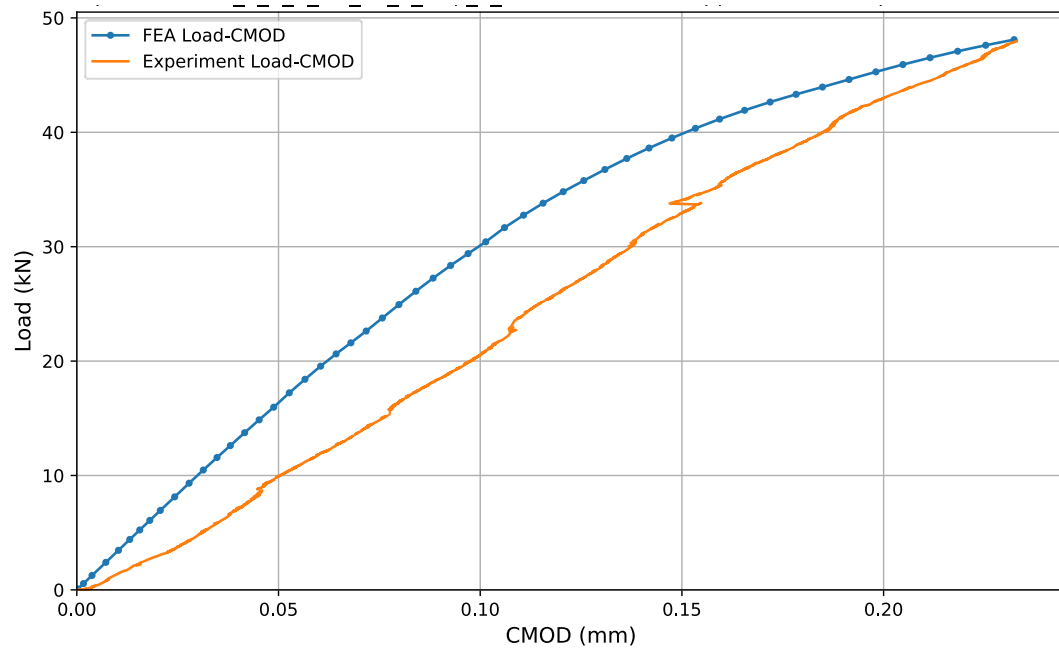
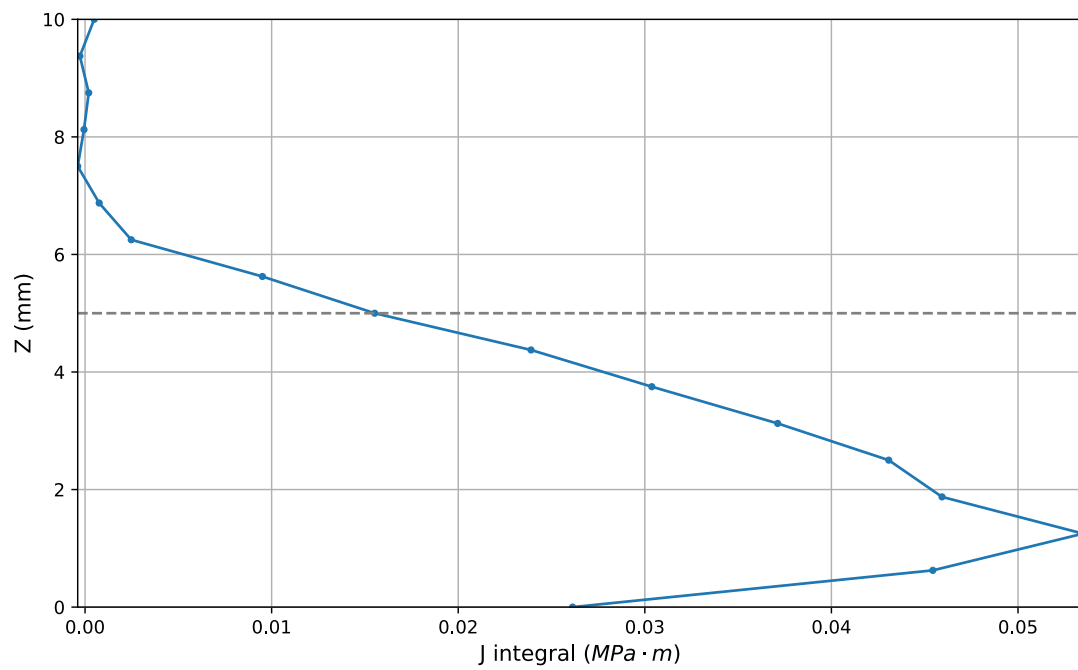


Figure A3. 9: Specimen 5PB 1_B_1 (a) FEA and Experimental Load-CMOD curve, (b) J-integral along the crack front



(a)



(b)

Figure A3. 10: Specimen 5PB 1_B_2 (a) FEA and Experimental Load-CMOD curve, (b) J-integral along the crack front

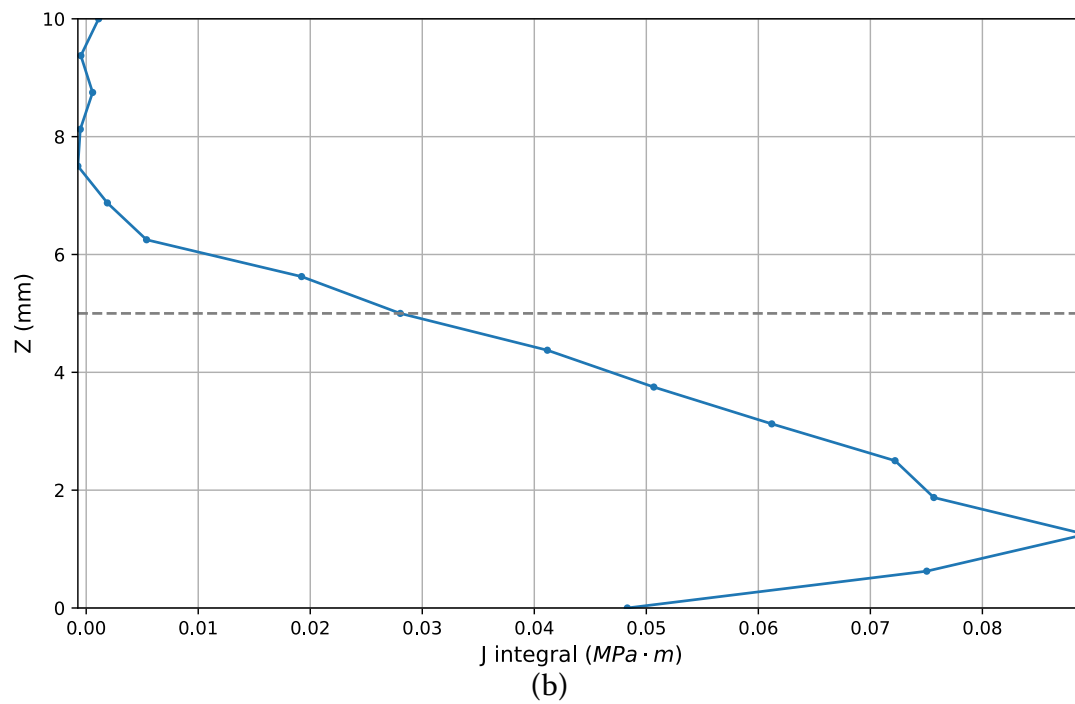
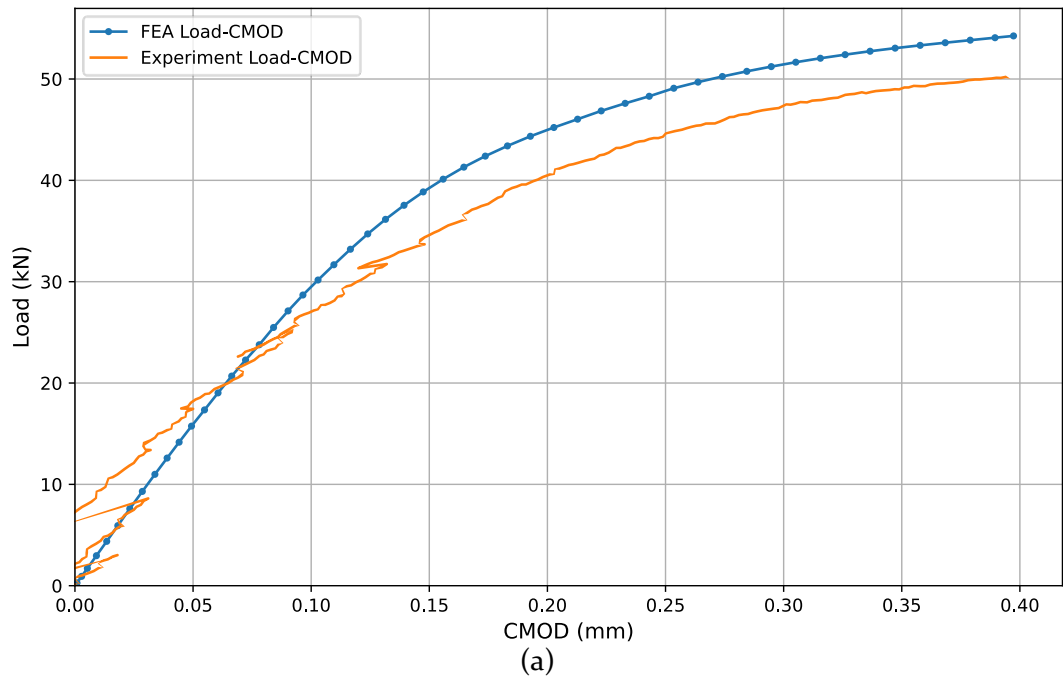


Figure A3. 11: Specimen 5PB 3_B_2 (a) FEA and Experimental Load-CMOD curve, (b) J-integral along the crack front

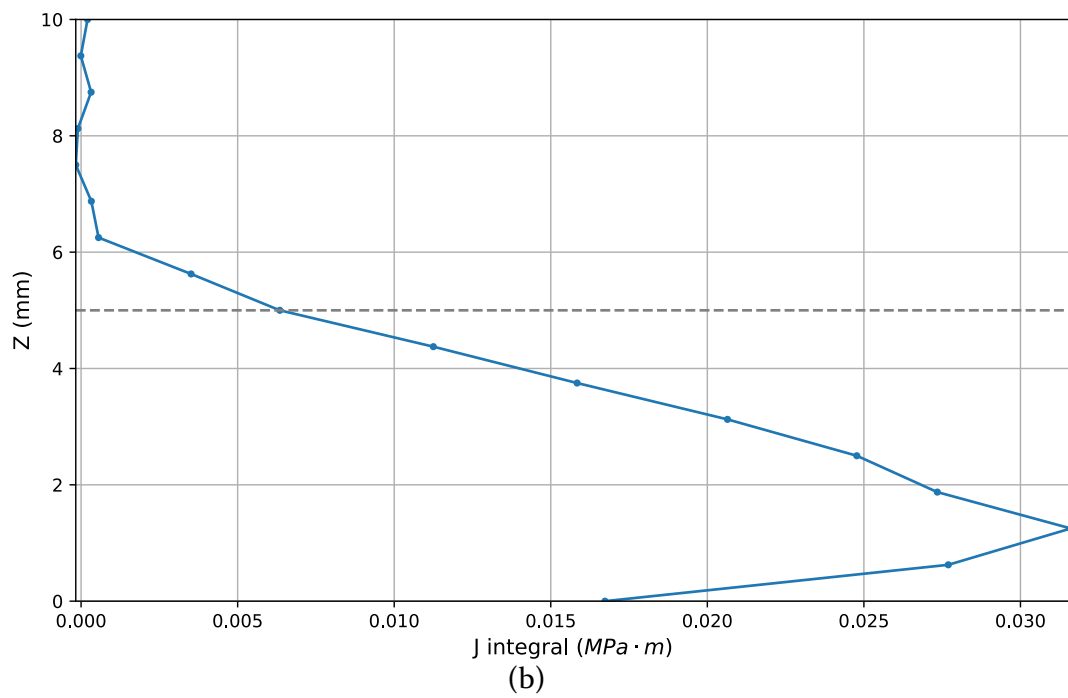
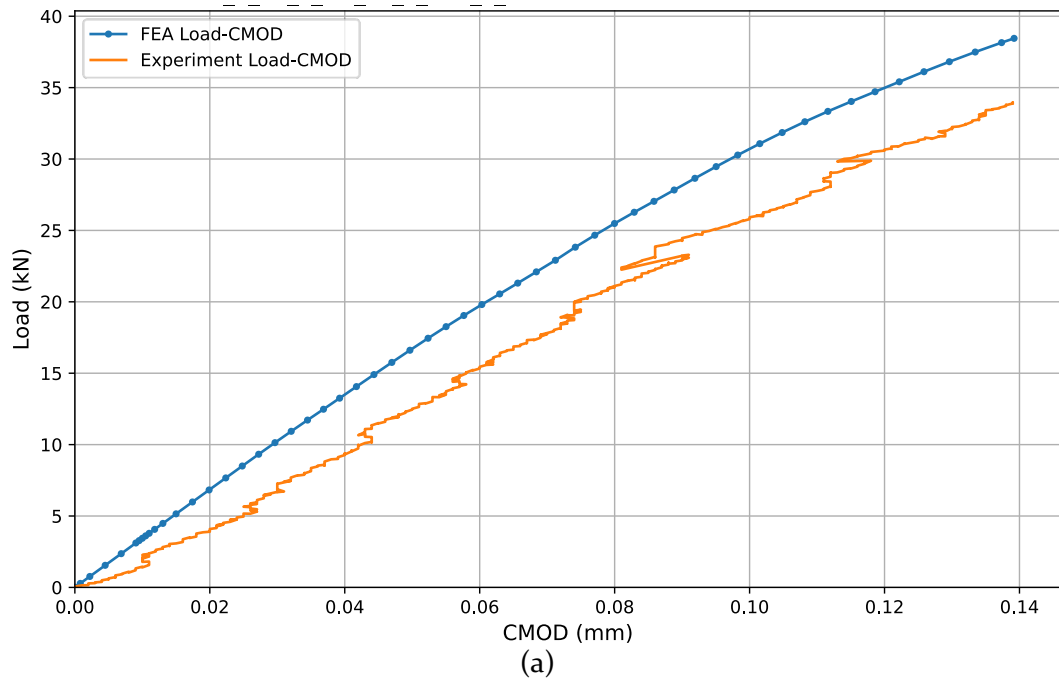


Figure A3. 12: Specimen 5PB 3_BB_2 (a) FEA and Experimental Load-CMOD curve, (b) J-integral along the crack front

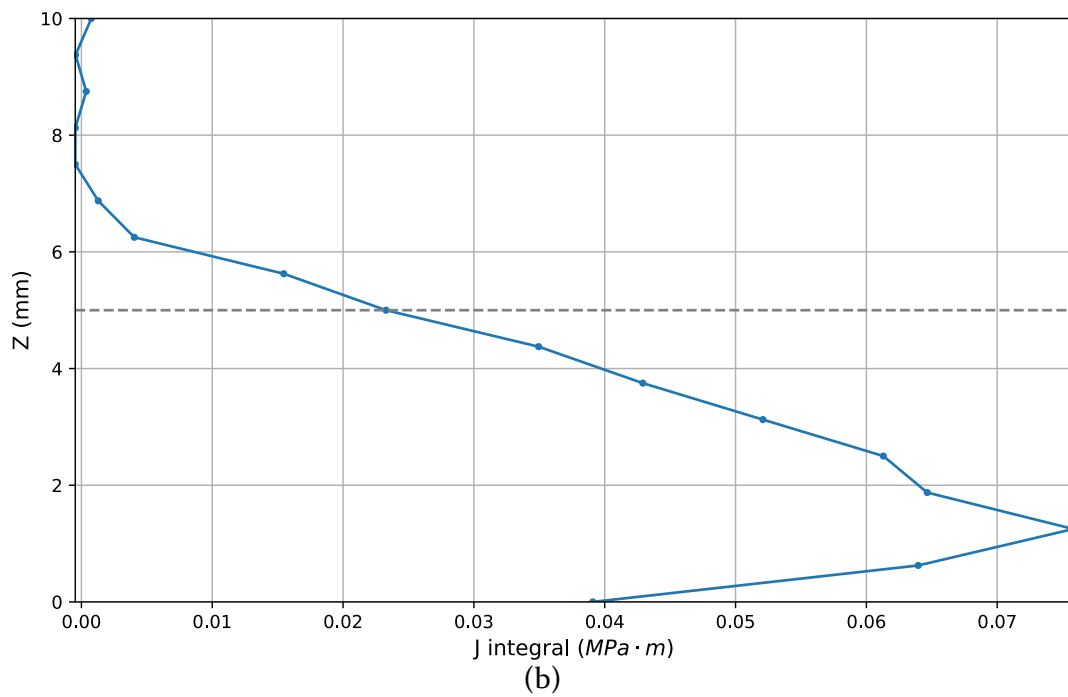
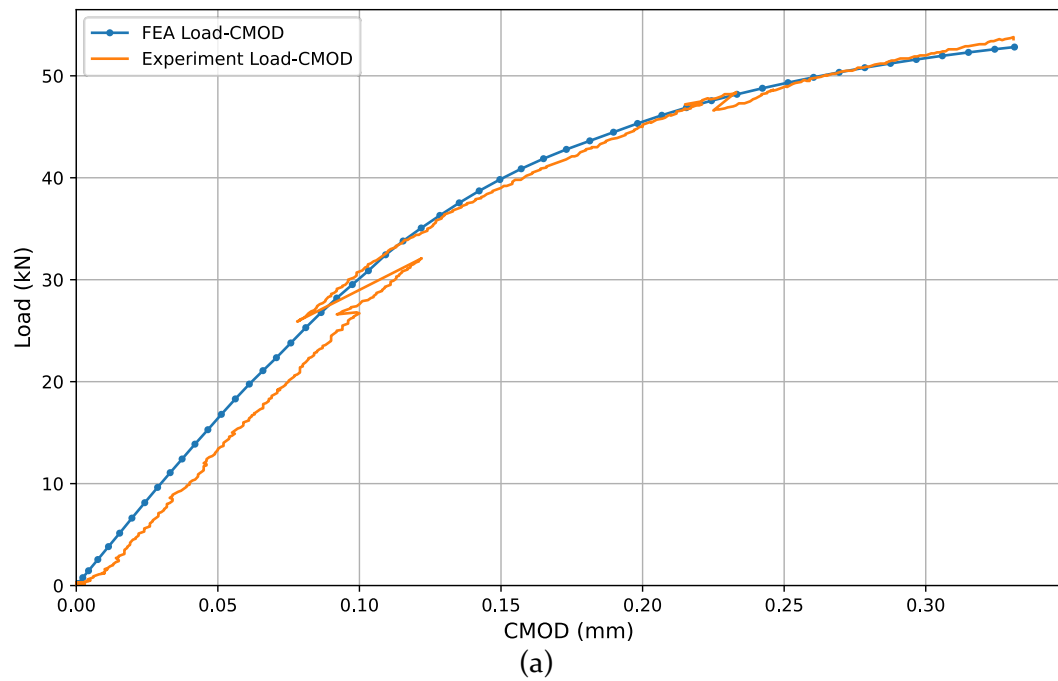


Figure A3. 13: Specimen 5PB 4_B_1 (a) FEA and Experimental Load-CMOD curve, (b) J-integral along the crack front

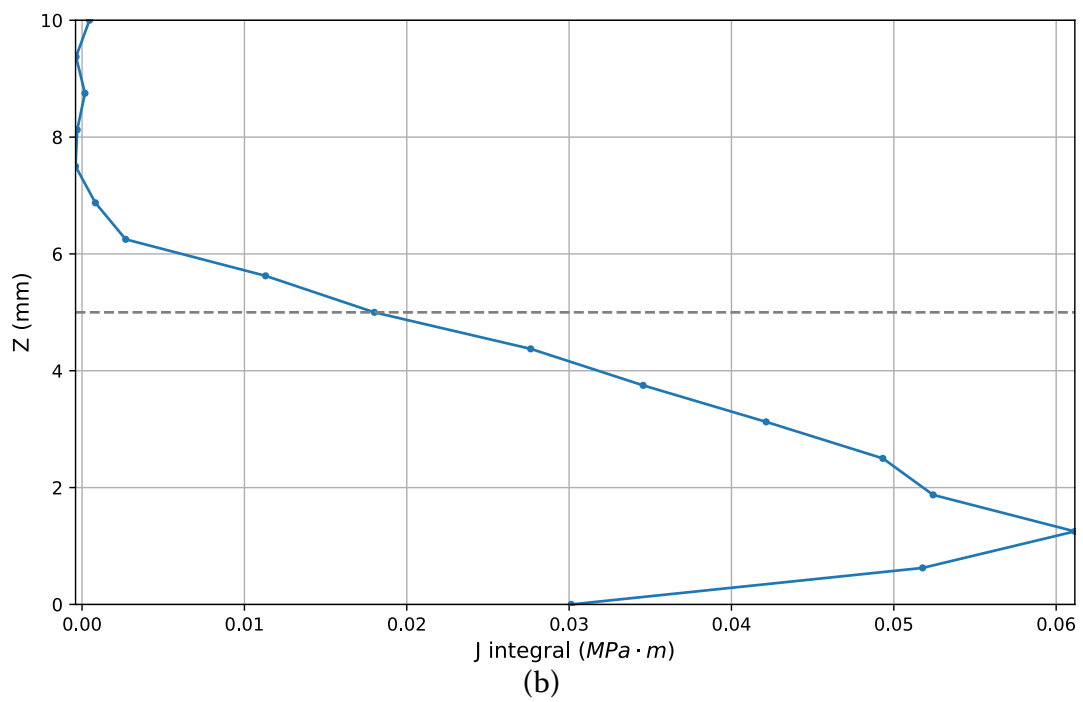
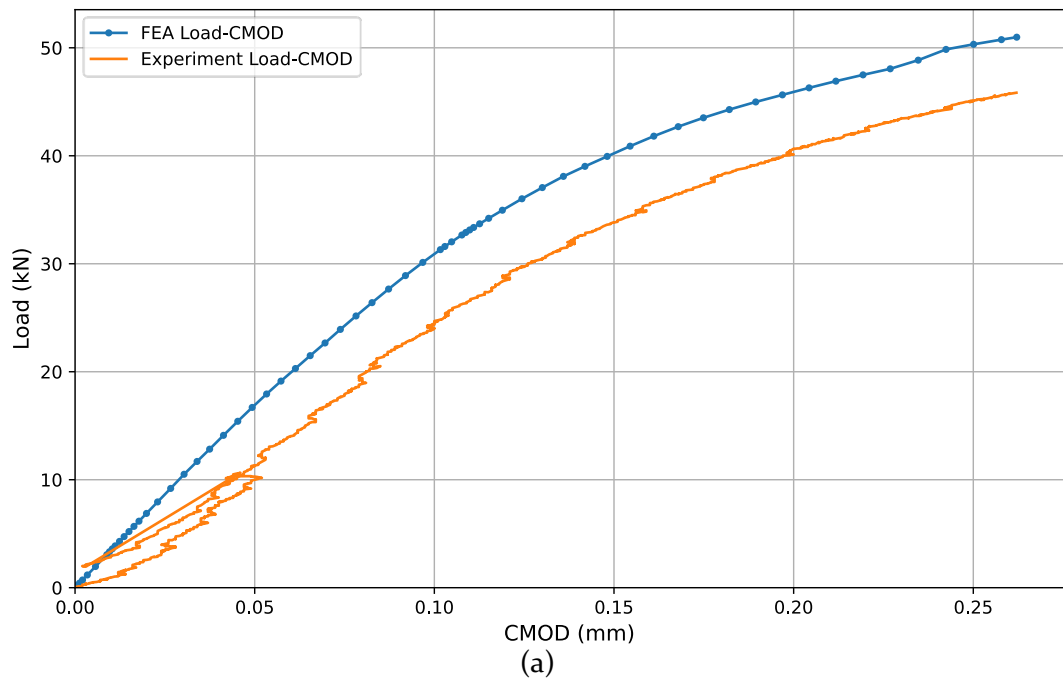


Figure A3. 14: Specimen 5PB 4_B_2 (a) FEA and Experimental Load-CMOD curve, (b) J-integral along the crack front

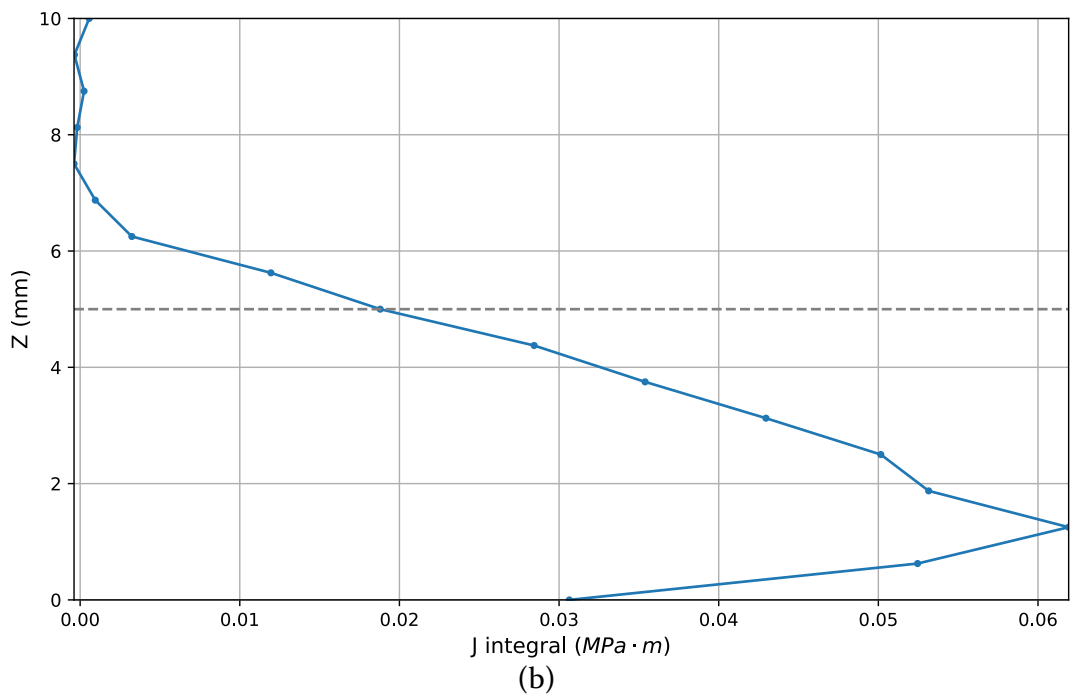
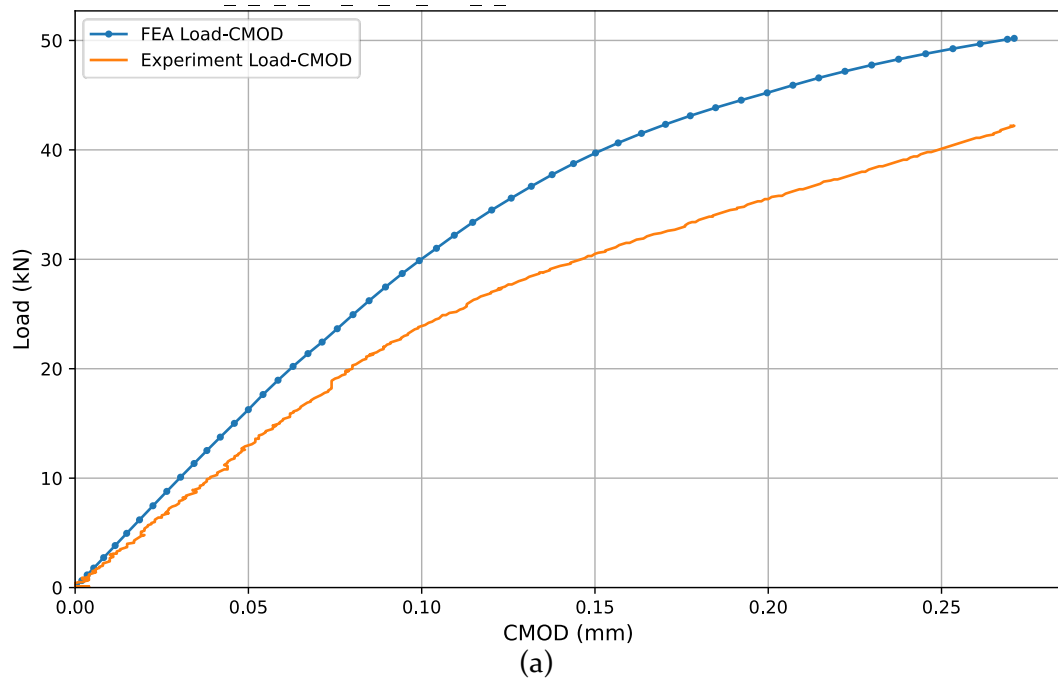


Figure A3. 15: Specimen 5PB 5_B_2 (a) FEA and Experimental Load-CMOD curve, (b) J-integral along the crack front

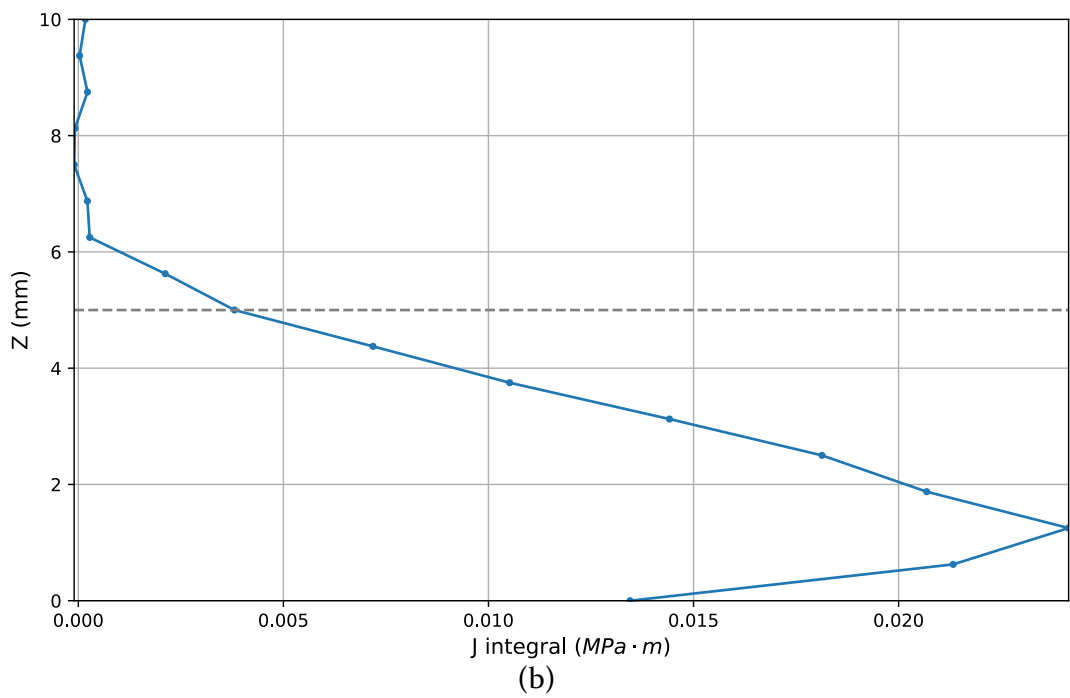
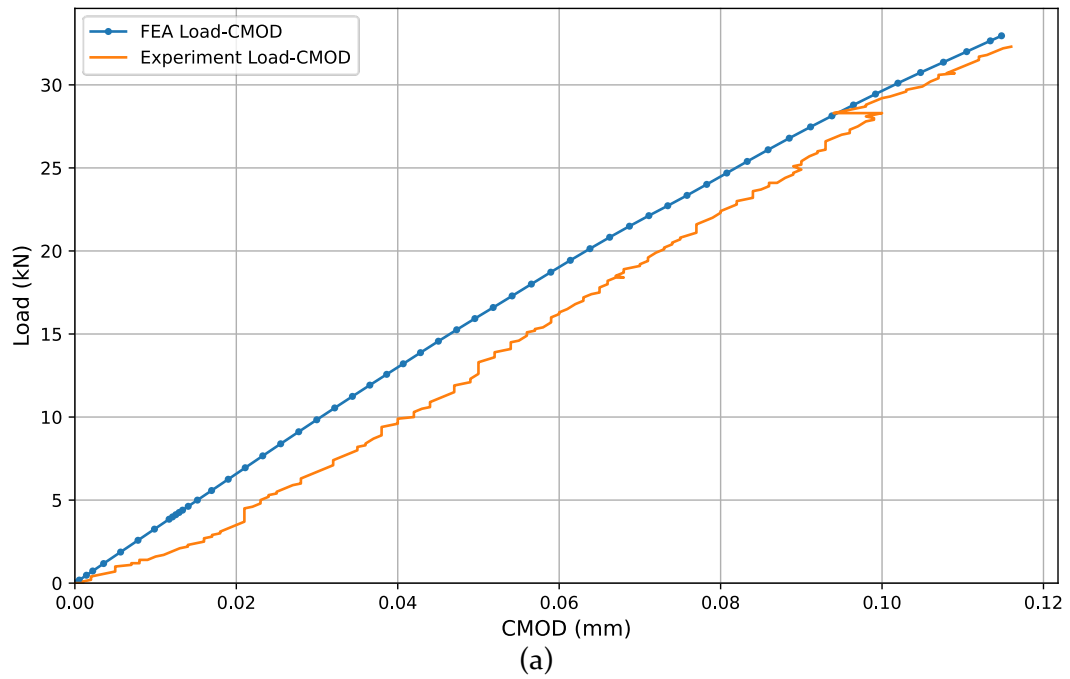


Figure A3. 16: Specimen 5PB 5_BB_1 (a) FEA and Experimental Load-CMOD curve, (b) J-integral along the crack front

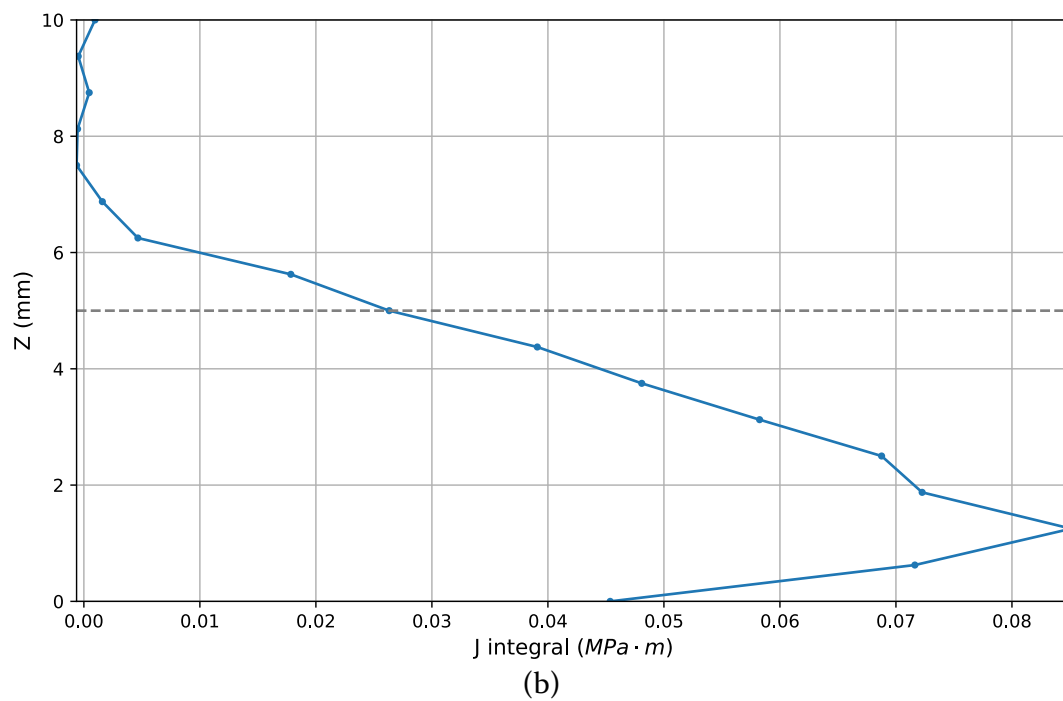
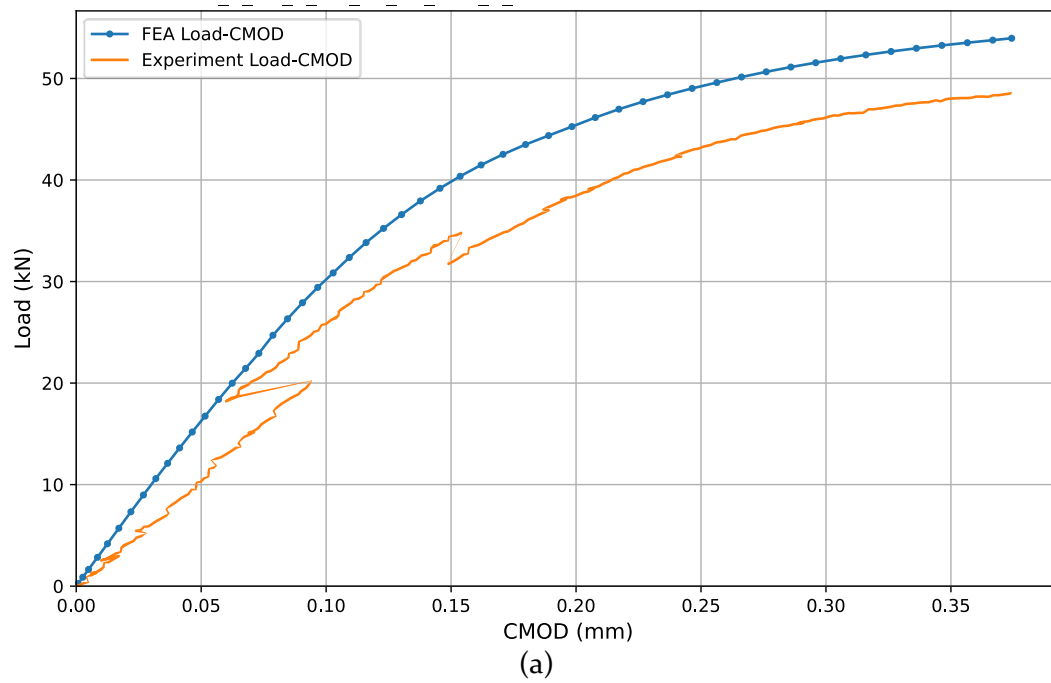
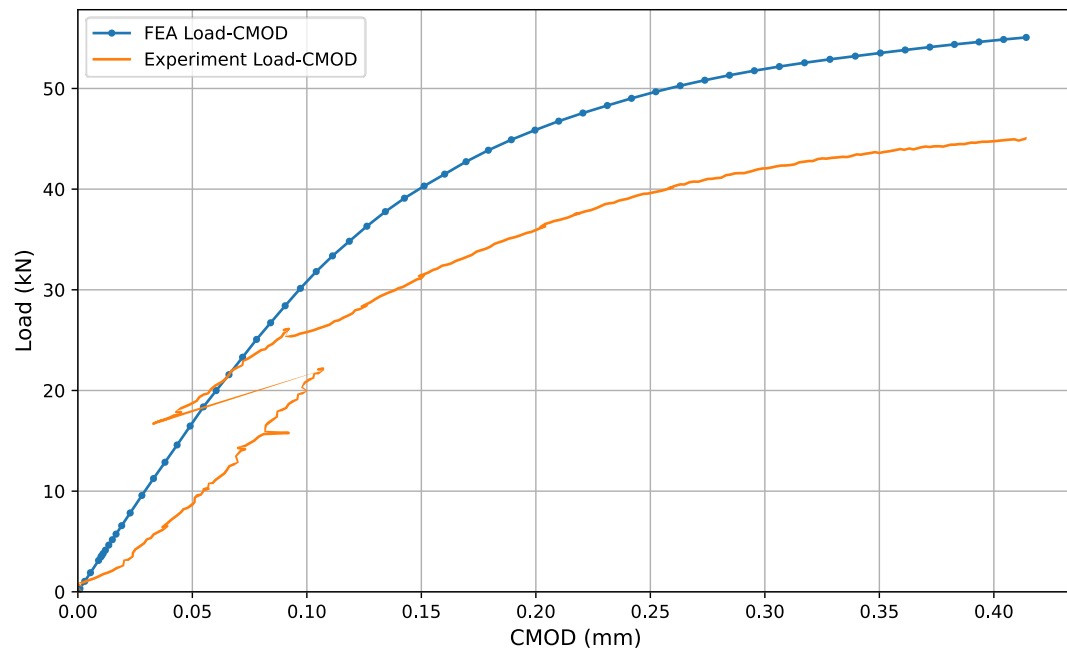
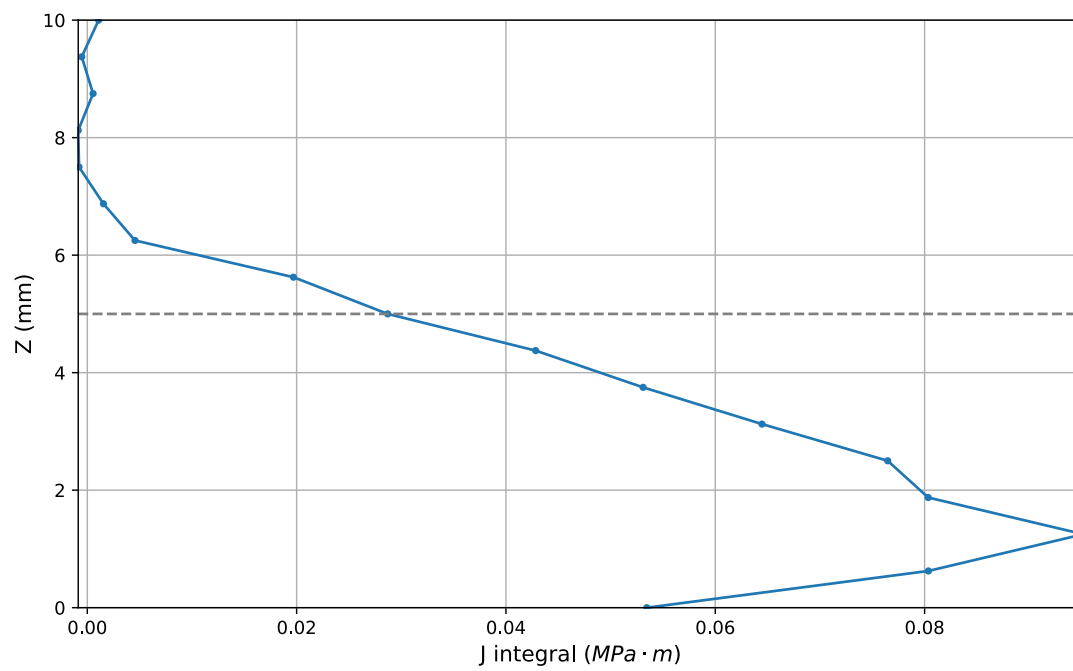


Figure A3. 17: Specimen 5PB 5_BB_2 (a) FEA and Experimental Load-CMOD curve, (b) J-integral along the crack front



(a)



(b)

Figure A3. 18: Specimen 5PB 6_B_2 (a) FEA and Experimental Load-CMOD curve, (b) J-integral along the crack front